Novel Diagnostics and Therapeutic Approaches for Supratentorial Ependymoma

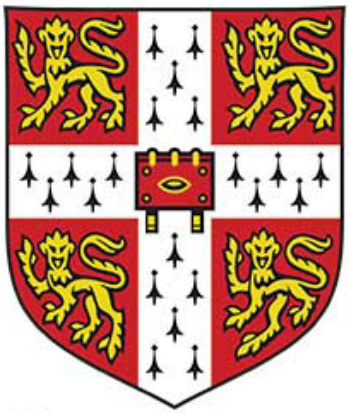

Lisa Ruff

Christ's College

Cancer Research UK Cambridge Institute

University of Cambridge

This dissertation is submitted for the degree of

Doctor of Philosophy

January 2021

This thesis is dedicated to my family and loved ones.

Declaration

This thesis is the result of my own work and includes nothing which is the outcome of work done in collaboration except as declared in the Preface and specified in the text. It is not substantially the same as any that I have submitted, or, is being concurrently submitted for a degree or diploma or other qualification at the University of Cambridge or any other University or similar institution. I further state that no substantial part of my dissertation has already been submitted, or, is being concurrently submitted for any such degree, diploma or other qualification at the University of Cambridge or any other University or similar institution. In accordance with the guidelines of the Degree Committee for the Faculties of Clinical Medicine and Veterinary Medicine, this thesis does not exceed the prescribed limit of 60,000 words and contains fewer than 150 figures.

Lisa Ruff

January 2021

Abstract

Title: Novel Diagnostics and Therapeutic Approaches for Supratentorial Ependymoma

Author: Lisa Ruff

Ependymoma is the third most common paediatric brain tumour. These tumours are incurable in up to 40% of cases. Previously classified as a single disease by histological criteria, ependymomas are now grouped into nine molecular subgroups, three in each compartment of the central nervous system. The largest subgroup of supratentorial ependymoma, initially identified by our lab in 2014, is characterised by a fusion of *C11orf95* and *RELA*, or less commonly, YAP1. The C11orf95-RELA fusion protein acts as a potent driver of oncogenesis in mouse models, and patients with this form of the disease have a particularly poor prognosis. Here, I describe research to develop a new diagnostic antibody for C11orf95-RELA-fusion ependymoma as well novel therapeutic approaches to treat the disease.

Antibodies raised against the C11orf95-RELA fusion epitope were selected through phage-display and tested in immunoblot and immunohistochemistry assays before lead immunoglobulins were subjected to affinity maturation via ribosome display. Affinity-matured candidates were assessed for their diagnostic potential in immunoblot analysis blotting, proteomic assays and immunohistochemistry on human and mouse tissue.

Novel treatment approaches included the screening of chemical entities with known and unknown targets, with a novel PLK1 inhibitor being established for *in vivo* preclinical testing. Screens of FDA-approved drugs produced candidate drugs for repurposing. As these compounds display unfavourable blood-brain barrier penetrability, they were combined with a local delivery system. For this, a biodegradable hydrogel system was optimised and implemented into a multimodality treatment regimen for ependymoma mouse models.

The release of a selection of compounds was tested *in vitro* and *in vivo* resulting in the selection of gemcitabine-loaded hydrogels as a novel treatment for preclinical efficacy studies.

Collectively, this thesis presents approaches for facilitated diagnosis of fusion-positive tumours and present novel drug delivery systems and novel therapeutic compounds in a currently poorly treatable tumour.

Acknowledgements

First and foremost, I would like to thank my supervisor Professor Richard Gilbertson for his mentorship and guidance over the last four years. Thank you also for teaching me how to always see the bigger picture and for your highly contagious excitement for research. I am very grateful for the opportunity to work on such exciting and challenging projects in a highly stimulating environment like your lab.

Secondly, I would like to thank the lab members, past and present, notably Eric, Claire, Katie, Amir, Sabrina, Erica, Deanna, Helen, Birgit and Sandra for making the lab such a fun place to work. You have been great colleagues and friends and helped me grow as a person and a scientist. Thank you especially to Birgit for the excellent handover of projects at the very beginning of my PhD and for all your support and mentorship during my first year. I further wish to specifically thank Sabrina and Erica for being the best surgery assistants I could have asked for and for spending countless hours in the animal facility with me.

A very special shoutout goes to my best lab friend- Robert Kupp. Thank you so very much for making this experience more fun than I could have ever imagined and for all the great times inside- and outside of the lab!

My project has been hugely collaborative and I would therefore like to thank all my collaborators in laboratories in the US, Germany and the UK, who have made working on my projects even more enjoyable. Within the scope of my drug development projects, I first wish to thank Anang Shelat and Jamie Jarusiewicz from St Jude Children's Research Hospital, United States, for all their help in the NCE project. Secondly, I wish to thank Bob Boyle, Stuart Travers, Meriel Major and Kyla Grimshaw from Sentinel Oncology for enabling me to work with such exciting new compounds.
The antibody project would not have been possible without the enthusiastic and motivated members from the Antibody Alliance Laboratory. I wish to thank particularly Maria Groves, Mark Austin, Stuart Haynes and Denice Chan for all the productive discussions regarding our project and for hosting me in their lab and teaching me antibody affinity maturation.

I am very grateful to Ulrich Schüller for providing long-sought human ependymoma tissues, and for welcoming me into his lab at the UKE, Hamburg, Germany and thereby allowing me to carry out my most desired experiments within my antibody project.

I thoroughly enjoyed working with Chris Parkins and Paraskevi Kasapidou from Professor Oren Scherman's lab on the hydrogel project and would like to thank them for all their help, passion and the insightful discussions, which had a tremendous impact on the project progression.

Throughout the course of my PhD, I also used the many Core Facilities at CRUK Cambridge Institute and would therefore like to thank all the Core staff in particular from the BRU, Proteomics, Histopathology- and PKB Core for their help and support. Moreover, I would like to thank Alice McKay for all her help with the MTAs, without which my collaborative projects would not have been possible. I further acknowledge Cancer Research UK for funding my PhD studentship and CureSearch, the Mathile- and the SOHN foundation, whose funding has enabled many of the experiments described in this thesis.

I am incredibly grateful for my amazing friends in both Germany and Cambridge. Thanks to my German friends from childhood and university for always ensuring I get a great break from life in the bubble Cambridge and helping me put things into perspective, when science proved to be challenging once again. Thanks to my friends at Christ's College for making unforgettable memories with me during various rowing sessions, formal dinners and MCR events. A special thanks to Sophia for all the great trips we took, the best dinners in College and at our house and always having an open door for me!

I would also like to thank my most wonderful family. Thank you to Mama, Papa, Anna, Annette, Wolfgang and everyone else for your continuous support and love and encouragement and for always believing in me. You are loved greatly.

Last but certainly not least, I am thankful to my partner Sebastian. Thank you for all your love, patience and support throughout the last years and for the multiple scientific discussions. I am looking forward to more adventures.

Table of Contents

1. Introduction **1**

1.1. Paediatric brain tumours **1**

1.2. Ependymoma **2**

1.2.1. Ependymomas comprise nine discrete molecular subgroups 3

1.2.2. Oncogenes and tumour suppressor genes of supratentorial ependymomas 5

1.2.3. C11orf95-RELA fusion-positive supratentorial ependymoma 6

1.2.3.1. Diagnosis of C11orf95-RELA subgroup tumours requires sophisticated molecular technologies 9

1.3. Standard of care treatment for ependymomas comprises maximum resection surgery and radiation therapy **9**

1.3.1. Role of chemotherapy for the adjuvant treatment of ependymoma remains controversial 11

1.4. Drug development for brain tumours presents a challenge **13**

1.5. The blood brain barrier limits brain tumour treatment **14**

1.5.1. Novel drug delivery methods for the treatment of brain tumours 15

1.6. Aims of Thesis **17**

2. Generation of novel candidate diagnostic antibodies for C11orf95-RELA fusion-positive ependymoma **19**

2.1. Attributions **19**

2.2. Introduction **19**

2.2.1. Antibodies are part of the adaptive immune response in humans 19

2.2.1.1. Structure of Immunoglobulin G 20

2.2.2. Development of monoclonal antibodies 21

2.2.2.1. Affinity maturation via ribosome display 23

2.2.3. Antibodies and cancers 25

2.2.3.1. Diagnostic antibodies for cancer fusion proteins 25

2.3. Methods **27**

2.3.1. *In vitro* cell culture methods 27

2.3.1.1. Cell culture 27
2.3.1.2. Isolation of mouse neural stem cells 29
2.3.1.3. Transduction of cells 30
2.3.2. Mouse and human tissue 30
2.3.2.1. Mouse models and husbandry 30
2.3.2.2. Orthotopic mouse models 31
2.3.2.3. Mouse tissue samples 32
2.3.2.4. Human tissue samples 32
2.3.3. Molecular and biochemical assays 34
2.3.3.1. SDS-Page and Immunoblot Analysis 34
2.3.3.2. Nuclear Extraction 35
2.3.3.3. Immunoprecipitation 35
2.3.4. Tissue staining methods 36
2.3.4.1. Immunohistochemistry 36
2.3.5. Techniques performed by AAL 43
2.3.5.1. Peptide design for phage display assay 43
2.3.5.2. Phage display and selection of single chain variable fragments 46
2.3.5.3. Conversion of single chain variable fragments into mature monoclonal immunoglobulins 46
2.3.5.4. Homogenous time-resolved fluorescence binding screens 47
2.3.5.5. Affinity maturation via ribosome display 47
2.3.5.6. Epitope competition assay 48
2.4. Results 49
2.4.1. Phage display selections identify candidate C11orf95-RELA^{Fus1}-specific single chain variable fragments 49
2.4.1.1. Crude scFv fail to recognize C11orf95-RELA^{Fus1} protein in immunoblot assays and require conversion to monoclonal IgGs 49
2.4.1.2. Immunoblot analysis identifies lead monoclonal antibodies against C11orf95-RELA^{Fus1} proteins 52
2.4.1.3. Testing C11orf95-RELA^{Fus1}-specific IgGs in immunohistochemistry analysis reveals candidate IgGs for affinity maturation 54
2.4.1.4. C11orf95-RELA^{Fus2}-targeting antibodies do not appear to be binding to C11orf95-RELA^{Fus2} according to immunoblot analysis 56

2.4.2. Affinity maturation of lead parental clones using ribosome display 59
2.4.3. Analysis of affinity matured candidate antibodies in a variety of assays determines selection of three lead antibodies 59
2.4.3.1. Selected affinity matured antibodies produce distinct staining pattern on mouse tissue in immunohistochemistry assays 60
2.4.3.2. Antibody testing in molecular assays demonstrates fusion-specific selectivity of candidate IgGs 62
2.4.4. Immunohistochemistry analysis of lead antibodies on human tissue sections reveals ambiguous staining patterns in fusion-negative ependymoma 66

2.5. Discussion 70

2.6. Supplementary Material 76

3. Comprehensive drug screens identify novel compounds that selectively target ependymoma cells 79

3.1. Attributions 79

3.2. Introduction 79

3.2.1. Drug development approaches for cancer 79
3.2.2. Novel chemical entities and natural products are commonly used in target-agnostic approaches 81
3.2.2.1. Atropisomerism in drug development 82
3.2.3. Novel compounds with known mechanisms of action are screened in target-informed approaches 82

3.3. Material and Methods 85

3.3.1. *In vitro* methods 85
3.3.1.1. Cell culture 85
3.3.1.2. *In vitro* dose-response drug screens 85
3.3.1.3. *In vitro* radiation of cells 86
3.3.2. *In vivo* methods 87
3.3.2.1. Mouse models and husbandry 87
3.3.2.2. Orthotopic allografts of mouse tumours 87
3.3.2.3. Bioluminescent imaging of allograft tumours 87
3.3.2.4. *In vivo* maximum tolerated dose studies 87
3.3.2.5. *In vivo* preclinical efficacy study of lead compound 88

3.3.2.6. Collection of brains and haematoxylin and eosin staining 89
3.3.3. Data analysis 89
3.3.4. Workflow of project 90
3.4. Results 91
3.4.1. *In vitro* drug screens of novel compounds and natural products with unknown mechanisms of actions 91
3.4.1.1. *In vitro* drug screens of aminopyrimidine scaffold analogues reveal candidate drugs for further development 91
3.4.1.2. Selection of natural products do not exhibit ependymoma-specific activity 96
3.4.2. Novel PLK1 inhibitors are promising candidates as novel therapeutics for supratentorial ependymoma 99
3.4.2.1. Systemic delivery studies of lead PLK1 inhibitor compound in ependymoma mouse models 102
3.4.2.2. SOL288-atropisomer SOL686 is highly active against ependymoma cells *in vitro* 105
3.4.2.3. Systemic delivery of SOL686 in mouse ependymoma models is not toxic 109
3.5. Discussion 111
3.6. Supplementary Material 116
4. Hyaluronic acid-based hydrogels as a novel drug delivery method for ependymoma 123
4.1. Attributions 123
4.2. Introduction 123
4.2.1. The role of repurposed compounds in the quest for a brain tumour cure 124
4.2.2. Local drug delivery systems for the treatment of brain tumours include injectable hydrogels 126
4.2.3. Hyaluronic acid-based hydrogels as novel drug delivery methods for the treatment brain tumours 127
4.3. Methods 129
4.3.1. *In vitro* assays 129

4.3.1.1. Cell culture 129
4.3.1.2. Drug treatment and cell viability studies 129
4.3.2. Hydrogel assays 129
4.3.2.1. Hydrogel preparation and drug loading 129
4.3.2.2. FITC labelling of polymer 130
4.3.2.3. Time-release basket assays 130
4.3.2.4. Drug release basket assays 131
4.3.2.5. Sample preparation for UHPLC-MS 131
4.3.3. *In vivo* studies 132
4.3.3.1. Mice used and husbandry 132
4.3.3.2. Orthotopic allografts and xenografts 132
4.3.3.3. Bioluminescence imaging 133
4.3.3.4. Preclinical efficacy studies of systemic fluvastatin 133
4.3.3.5. Preclinical neurosurgery and post-op care 134
4.3.3.6. Preclinical neurosurgery and hydrogel injection 135
4.3.3.7. Brain Sample collection and Haematoxylin & Eosin staining 136
4.3.3.8. Fluorescent imaging of mouse brains 136
4.3.3.9. Pharmacokinetic studies 136
4.3.4. Data analysis 137
4.3.5. Workflow of project 137
4.4. Results 140
4.4.1. Anticancer and non-oncology drugs identified as lead compounds for drug repurposing 140
4.4.1.1. Systemic delivery of fluvastatin does not have an effect on tumour growth or overall survival in ependymoma models 144
4.4.2. Establishing a hyaluronic acid-based hydrogel as novel delivery technique for ependymoma models *in vitro* 147
4.4.2.1. Confirmation of hydrogel-based drug-release of gemcitabine, fluvastatin and rigosertib over time *in vitro* 147
4.4.2.2. Gemcitabine and fluvastatin released from hydrogels inhibit ependymoma neurosphere formation *in vitro* 151
4.4.3. Implementation hydrogel-based delivery into preclinical standard of care neurosurgery 155

4.4.3.1. Injection of unloaded hydrogels into post-resection cavities is not toxic and does not affect tumour recurrence 155
4.4.3.2. Identification of challenges associated with hydrogel delivery in post-resection cavities 156
4.4.4. Optimisation of resection surgery to overcome challenges for hydrogel delivery 158
4.4.4.1. Optimisation of cavity size and hydrogel volume injected into post-resection cavity 159
4.4.4.2. Control of haemorrhage during resection surgery involves combination of haemostatic agents and PBS washes 160
4.4.4.3. Retention of gel within resection cavity achieved through sealing the resection cavity with artificial dura 164
4.4.5. Utilization of drug-loaded hydrogels as local delivery technique post-surgical resection in ependymoma models *in vivo* 165
4.4.5.1. *In vivo* pharmacokinetic studies reveal gemcitabine as the candidate drug for repurposing in hydrogels 165
4.4.5.2. Preclinical efficacy study of gemcitabine-loaded hydrogel reveals trend of efficacy for hydrogel-based delivery of gemcitabine 168
4.5. Discussion 170
4.6. Supplementary Data 180
5. Conclusion 185
6. Patent application 189
6.1. Patent application for antibodies targeting C11orf95-RELA^{Fus1} 189
References 191

List of Tables

Table 2.1: Overview of cell lines used *in vitro*. 28
Table 2.2: Overview of cell lines used for orthotopic implants. 32
Table 2.3: List of human ependymoma tissue samples. 33
Table 2.4: Overview of single chain variable fragments by AAL. 38
Table 2.5: Overview of mature parent IgGs targeting C11orf95-RELA^{Fus1} by AAL. 39
Table 2.6: Overview of mature parent IgGs targeting C11orf95-RELA^{Fus2} by AAL. 41
Table 2.7: List of affinity matured monoclonal IgGs targeting C11orf95-RELA^{Fus1} by AAL. 42
Table 2.8: Overview of commercial antibodies used for immunohistochemistry, immunoblotting and immunoprecipitations. 43
Table 2.9: Overview of amino acid sequences for each synthetic peptide. 44
Table 2.10: Values of HTRF competition assay for clones competing with C0040034. 76
Table 2.11: Values of HTRF competition assay for clones competing with C0040036. 76
Table 2.12: Overview of peptide specificity of affinity matured clones derived from C0040034 lineage. 77
Table 2.13: Overview of peptide specificity of affinity matured clones derived from C0040036 lineage. 77
Table 3.1: Overview of cell lines used in *in vitro* drug screens. 86
Table 3.2: Overview of drug plate numbers, compound names, dilution factors, and concentration ranges for aminopyrimidine analogues. 116
Table 3.3: Overview of dilutions for novel compounds by Sentinel Oncology. 118
Table 3.4: Overview of statistical analysis of dose-response curves of mouse ependymoma cell lines vs. human ependymoma cell line in candidate NCEs. 119
Table 3.5: Overview of statistical analysis of dose-response curves of mouse ependymoma cell lines vs. human ependymoma cell line in Sentinel Oncology compounds. 120
Table 4.1: Overview of mass-spectrometry calibration standards for gemcitabine, fluvastatin and rigosertib. 132

Table 4.2: Overview of mouse and human cells used for allografts and xenografts. 133
Table 4.3: Overview of drugs contained in the post-operative care drug mix. 135
Table 4.4: Overview of dose-response concentrations for repurposed drugs. 180
Table 4.5: Overview of IC_{50}s for all drugs tested against variety of ependymoma cell lines. 181
Table 4.6: Overview of IC_{10}, IC_{50} and IC_{90} for gemcitabine and fluvastatin values for mSEP-CR(+) and mSEP-CR(-)^{EPHB2} cells. 181

List of Figures

Figure 1.1: Classification of molecular subgroups of ependymoma. 4
Figure 1.2: C11orf95-RELA-positive supratentorial ependymoma are a result of chromothripsis on chromosome 11q. 7
Figure 1.3: C11orf95-RELA^{Fus} drive aggressive ependymoma in mouse models and patients. 8
Figure 1.4: Structure of blood-brain barrier and local delivery techniques for the treatment of brain tumours. 16
Figure 2.1*:* Structure of monoclonal Immunoglobulin G. 21
Figure 2.2: Overview of Ribosome Display Affinity Maturation. 24
Figure 2.3: Structures and amino acid sequences of synthetic peptides used for phage display, binding assays and ribosome display. 45
Figure 2.4: Screening of scFv candidate for C11orf95-RELA^{Fus1} recognition in immunoblot assays. 51
Figure 2.5: Immunoblot analysis of reformatted C11orf95-RELA^{Fus1}-targeting IgGs. 54
Figure 2.6: Immunohistochemistry analysis of lead C11orf95-RELA^{Fus1}-targeting IgGs on mouse supratentorial ependymoma tissue. 56
Figure 2.7: Immunoblot analysis of C11orf95-RELA^{Fus2}-targeting IgGs. 58
Figure 2.8: Selection of affinity-matured IgGs show nuclear-specific staining pattern on fusion-positive mouse tumour tissues. 61
Figure 2.9: Immunoprecipitation and immunoblot analysis of candidate antibodies on mouse and human cell lysates. 64
Figure 2.10: Immunoprecipitation and immunoblot analysis of IgG151, 154 and 159 on mouse nuclear fractions. 66
Figure 2.11: Immunohistochemistry analysis of lead antibodies on human supratentorial ependymoma tissues. 68
Figure 2.12: Immunohistochemistry analysis of lead antibodies on human posterior fossa ependymoma tissues. 69
Figure 3.1: Structure of aminopyrimidine scaffold. 91
Figure 3.2: Overview of IC_{50} values for new chemical entities tested *in vitro*. 93
Figure 3.3: Selection of lead aminopyrimidine analogues identified in mid-throughput drug screen. 96

Figure 3.4: Dose-response curves of natural products tested in ependymoma cell lines. 98
Figure 3.5: Novel compounds with known mechanisms are highly active in ependymoma cells *in vitro.* 101
Figure 3.6: *In vivo* studies of novel PLK1 inhibitor compound SOL288. 105
Figure 3.7: Effects of atropisomers SOL685 and SOL686 over time. 107
Figure 3.8: Combination therapy of irradiation with SOL atropisomers. 108
Figure 3.9: Maximum-tolerated dose study of SOL686 determines dose for future preclinical efficacy studies. 110
Figure 4.1: Overview of hydrogel as a local drug delivery in a preclinical mouse hospital. 128
Figure 4.2: Overview of workflow for establishment of hydrogels as novel drug delivery in ependymoma models. 139
Figure 4.3: Activity of repurposed drugs against ependymoma cell lines *in vitro*. 141
Figure 4.4: Dose-response curves for drugs selected for repurposing. 143
Figure 4.5: Systemic delivery does not have any effect on tumour growth or survival in ependymoma *in vivo* models. 147
Figure 4.6: Release of gemcitabine, fluvastatin and rigosertib over time. 151
Figure 4.7: Effect of gemcitabine released from hydrogels on ependymoma cells *in vitro*. 153
Figure 4.8: Effect of fluvastatin released from hydrogels on ependymoma cells *in vitro.* 154
Figure 4.9: Hydrogel injection into surgical resection activities does not affect tumour growth or survival. 156
Figure 4.10: Overview of challenges in hydrogel-based drug delivery post-resection. 158
Figure 4.11: Overview of gel volume injected into post-resection cavity. 159
Figure 4.12: Optimisation of resection surgery technique to resolve challenges regarding hydrogel delivery. 163
Figure 4.13: Utilization of artificial dura to close of resection cavity. 164
Figure 4.14: Pharmacokinetics for gemcitabine, fluvastatin and rigosertib released from hydrogels in post-resection cavities. 167
Figure 4.15: Preclinical efficacy study with gemcitabine-loaded gels shows trend of extended survival. 169

Figure 4.16: Expression analysis of PDGFRα/β, ALK, CDK in ependymoma cell lines. 182
Figure 4.17: Expression analysis of Hyaluronidases 1,2,3 and 6 in ependymoma cell lines. 183

Acronyms and abbreviations

AAL- Antibody Alliance Laboratory

ALK- Anaplastic Lymphoma Kinase

BBB- Blood-Brain Barrier

BLI- Bioluminescence Imaging

BSA- Bovine Serum Albumin

C11orf95-RELA^{Fus}- C11orf95-RELA fusion

C11orf95-RELA^{Fus1}- C11orf95-RELA fusion 1

C11orf95-RELA^{Fus2}- C11orf95-RELA fusion 2

CB8- Cucurbit[8]uril

CDK- Cyclin-Dependent Kinases

CED- Convection Enhanced Delivery

CNS- Central Nervous System

DIPG- Diffuse Intrinsic Pontine Glioma

Da- Dalton

DIV0- Day *in vitro* 0

DIV1- Day *in vitro* 1

DMEM- Dulbecco's Modified Eagle Medium

EGF- Epidermal Growth Factor

ELISA- Enzyme-Linked Immunosorbent Assay

EPHB2 – Ephrin type-B Receptor 2

Fab- antigen-binding Fragment

FDA- U.S Food and Drug Administration

FFPE- Formalin-Fixed Paraffin Embedded

FISH- Fluorescence In situ Hybridisation

FITC- Fluorescein Isothiocyanate

Fv- variable Fragment

FGF- Fibroblast growth factor

FRET- Fluorescence Resonance Energy Transfer

GTR- Gross Total Resection

HA- Hyaluronic Acid

HeLa- Henrietta Lachs human epithelial cervical carcinoma

HMGR- Hydroxy-3-methylglutaryl-Coenzyme A Reductase

HPLC-High-Performance Liquid Chromatography

HTRF- Homogenous Time-Resolved Fluorescence

Ig- Immunoglobulin

IgG- Immunoglobulin G

IHC- Immunohistochemistry

IP- Immunoprecipitation

mNSC- mouse Neural Stem Cells

MMOA- Molecular Mechanism Of Action

MOI- Multiplicity Of Infection

MS- Mass Spectrometry

mSEP-CR(+)- mouse Supratentorial Ependymoma C11orf95-RELA fusion-positive cells

mSEP-CR(-)^{RTBDN}- mouse Supratentorial Ependymoma C11orf95-RELA fusion-negative, RTBDN-driven cells

mSEP-CR(-)^{EPHB2}- mouse Supratentorial Ependymoma C11orf95-RELA fusion-negative, EPHB2-driven cells

NATPRO- Natural Product

NCE- Novel Chemical Entity

NTR- Near Total Resection

OS- Overall Survival

PBS- Phosphate Buffered Saline

PBST- Phosphate Buffered Saline with 1% Tween

PBD- Polo Box Domain

PD- Pharmacodynamic

PDGFRα/β - platelet-derived growth factor receptor α and β

PDX- Patient Derived-Xenograft

PF-EP- Posterior Fossa Ependymoma

PFS- Progression-Free Survival

PK- Pharmacokinetic

PLK1- Polo-Like Kinase1

RIPA- Radioimmunoprecipitation

RT- Radiation Therapy

RTBDN- Retbindin

Rsx- Resection

scFv- single chain variable Fragment

ST-EP- Supratentorial Ependymoma

STR- Subtotal Resection

TE- Tris-EDTA buffer

TBS- Tris Buffered Saline

TBST- Tris Buffered Saline with 1% Tween

UHPLC- Ultra-High-Performance Liquid Chromatography

UL- Unloaded Hydrogel

V_H- Variable Heavy chain

V_L- Variable Light chain

WHO- World Health Organisation

xSEP-CR(+)- human Supratentorial Ependymoma C11orf95-RELA fusion-positive cells

1. Introduction

1.1. Paediatric brain tumours

Cancer describes the malignant growth of cells with unrestrained proliferation and local and metastatic invasion that can arise in tissues throughout the human body. It is one of the leading causes of mortality worldwide, accounting for 1 in every 6 deaths. In children aged 0-14years, it is the second-leading cause of death[1]. Each year, ~1,900 and ~11,000 children are diagnosed with cancer in the United Kingdom and the United States, respectively[2,3]. In children, tumours of the central nervous system (CNS) are the most prevalent form of solid cancer and account for 18-26% of all paediatric tumours[4–6]. Among them, brain tumours are the leading cause of cancer-related death in children[5].

Advances in technologies and molecular biology have furthered our understanding of brain tumours over the last fifteen years by prompting the identification of cells of origin, driver oncogenes and molecular targets, resulting in the identification of specific tumour subgroups[7,8]. Simultaneously, advances in surgery and adjuvant therapies have greatly improved prognoses for paediatric patients harbouring tumours such as low-grade glioma and medulloblastoma[9]. However, for particularly aggressive tumour types such as diffuse intrinsic pontine glioma (DIPG) or high-grade glioma, prognosis remains poor[9–11]. Treatment varies according to tumour type, location and patient age. Maximum safe resection surgery, if possible, constitutes the initial treatment[12]. This is generally followed by adjuvant radiation therapy (RT) and chemotherapy, depending on the tumour type[11]. However, in very young children, RT is often delayed to avoid long-term side effects that include cognitive sequelae or endocrine dysfunctions [13–17]. Proton-based irradiation has been introduced to reduce the damage caused by radiation to normal surrounding structures[18]. In tumours like medulloblastoma, the inclusion of chemotherapy into standard of care regimens has played a crucial role in the improvement of survival. However, in ependymoma, the benefit of chemotherapy remains controversial[19–22].

1.2. Ependymoma

Ependymomas are the third most common form of childhood brain tumour and remain incurable in up to 40% of cases [23,24]. They are primary tumours of the CNS arising in all three compartments- the supratentorial region, the posterior fossa and the spinal cord. In children, intracranial ependymoma account for 90% of all ependymomas, with approximately 60% arising in the posterior fossa[25].

Ependymal tumours were originally thought to be one disease and were classified by the World Health Organisation (WHO) into grades I, II and III depending on their anaplasia grade[26]. Histopathologically, grade II and III tumours are characterised by ependymal rosettes, which are defined by a central lumen surrounded by tumour cells. They also frequently display perivascular pseudorosettes- a perivascular nuclei-free zone surrounded by radially positioned tumour cells[27].

The predictive value of histological grading is limited. In 1989, Ross *et al.* reported limited correlation between histopathology grade and clinical outcome[28]. Some of the first genetic studies of ependymoma identified allelic loss of chromosome 22q as a common feature[29–33]. In 1999, Ebert *et al.* discovered that, besides allelic loss of chromosome 10q and 22q, spinal ependymomas frequently harbour NF2 mutations. These mutations were exclusively observed in ependymomas in the spine, first suggesting clear biological differences among ependymomas from different locations[34]. One of the first gene expression analysis studies then correlated gene expression patterns with ependymomas of differing grades and location, and a comparative genomic analysis revealed a direct link between genomic imbalances and clinical outcome[35,36]. These data led to the emerging concept that ependymomas from different compartments are distinct entities[28,36,37]. This was confirmed when our lab identified radial glia cells as candidate stem cells of ependymoma that displayed regionally distinct transcriptomes that matched ependymomas from the corresponding region of the CNS[37,38]. Since then, studies involving whole genome sequencing and RNA sequencing have identified nine, regionally discrete molecular subgroups for ependymoma[39].

1.2.1. Ependymomas comprise nine discrete molecular subgroups

Following extensive research by several groups, nine distinct ependymoma subgroups have been identified[36–38,40]. Each CNS compartment is thought to give rise to three tumour subgroups, which are further distinguished by their molecular profile (Figure 1.1). These subgroups are characterised by different oncogenes, age distributions and varying prognoses[41]. Intracranial ependymomas occur either in the supratentorial (ST) or posterior fossa (PF) compartment. Both compartments have one sub-ependymoma subgroup (ST-EP-SE, PF-EP-SE). Tumours arising in the hindbrain are classified as posterior fossa anaplastic ependymoma A and B (PF-EP-A; PF-EP-B). The remaining ST subgroups are ST-EP-YAP1 and ST-EP-CR, each characterised by unique fusion proteins. In ST-EP-YAP1, YAP1 is fused to either MAMLD1 or FAM118B and acts as a potent driver of oncogenesis. In ST-EP-CR, tumour formation is driven by C11orf95-RELA fusion (C11orf95-RELA^{Fus})[39,40]. Of all nine ependymoma subgroups, only PF-EP-A and ST-EP-CR are associated with poor prognoses, with 10-year overall survival (OS) rates of 50% (Figure 1.1)[41]. Since each tumour subgroup displays different clinical outcomes following conventional treatment, it is likely that each subtype will need individual treatment approaches [40,42–44].

Recent studies have reported fusion-negative ependymoma subgroups to be more heterogenous than previously conceived. Already in 2018, Fukuoka *et al.* reported that the supratentorial sub-ependymomas, which do not feature the C11orf95-RELA fusion protein, are a heterogenous group of tumours harbouring different fusions such as *YAP1* fusions, *EP300-BCORL1* or *FOXO1-STK24* fusions[45]. These tumours could not be allocated to any of the previously established molecular profiles in the methylation classifier.

This was further corroborated by Zschernack *et al.* in 2021, who also reported that the fusion-negative supratentorial ependymoma subgroup is heterogenous, with tumours featuring fusions of C11orf95 to MAML2 or NCOA1. As for the ependymoma cases reported by Fukuoka *et al.*, the ependymoma samples could not be matched to any established methylation profiles[46].

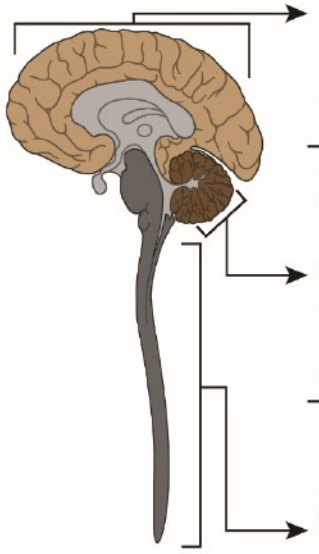

	Molecular subgroup	Age group	Gender distribution	Prognosis	Genetics	Histopathology
Supratentorial (ST-)	SE	adults	m > f	good	balanced	subependymoma (WHO I)
	EPN-YAP1	children	m < f	good	focal aberrations Chr. 11; *YAP1*-fusion	(anaplastic) ependymoma (WHO II/III)
	EPN-RELA	children and adults	m > f	poor	aberrations Chr. 11; chromothripsis; *RELA*-fusion	(anaplastic) ependymoma (WHO II/III)
Posterior Fossa (PF-)	SE	adults	m > f	good	balanced	subependymoma (WHO I)
	EPN-A	children	m > f	poor	balanced	(anaplastic) ependymoma (WHO II/III)
	EPN-B	children and adults	m < f	good	CIN	(anaplastic) ependymoma (WHO II/III)
Spine (SP-)	SE	adults	m = f	good	6q deletion	subependymoma (WHO I)
	MPE	predominantly adults	m = f	good	CIN	myxopapillary ependymoma (WHO I)
	EPN	predominantly adults	m > f	good	CIN; *NF2* mutation	(anaplastic) ependymoma (WHO II/III)

Figure 1.1: Classification of molecular subgroups of ependymoma. Ependymomas arise along the craniospinal axis in the central nervous system. Nine different subgroups have been identified, all characterised by distinct outcomes, age distributions, prognosis, genetics and histopathological grades (Pajtler *et al.* 2015[41]).

1.2.2. Oncogenes and tumour suppressor genes of supratentorial ependymomas

ST-EP have been studied extensively. Using whole genome *in vivo* screens, we have identified several tumour suppressor and oncogenes including *INK4a*, ephrin type-B receptor 2 (Ephb2) and retbindin (Rtbdn)[37,38,47]. The *INK4a/Arf* locus encodes $p16^{INK4a}$, a direct inhibitor of cyclin D-dependent kinases CDK4 and CDK6, both of which play an important role in cell cycle progression[48]. Thus, loss of *INK4a/Arf* (*INK4a/Arf*$^{-/-}$) results in uncontrolled cell proliferation, which renders it a tumour suppressor gene whose deletion is also observed in a variety of other cancers[49].

In normal cells, EPHB2 plays a crucial role in axon guidance, cell adhesion and motility[50,51]. EPHB2 overexpression has been reported in breast cancer and glioma, where it has been shown to promote cell invasion[52–54]. The transformative oncogenic capacities of EPHB2 have further been confirmed by our lab and others. Orthotopic implantation of *INK4a*$^{-/-}$ mouse neural stem cells (mNSC) expressing Ephb2 into the cortices of mice induced tumour formation[37,38,55].

RTBDN is an additional oncogene of ST-EP and was first described by Mohankumar *et al.* in 2015[47]. While its function remains unknown, RTBDN displays transformative potential by efficiently driving tumorigenesis in mice that harbour *RTBDN*-overexpressing *INK4a*$^{-/-}$ cells[47,56]. As described in the next section, the most significant finding among supratentorial oncogenes was the discovery of the C11orf95-$RELA^{Fus}$ fusion oncogene[40].

1.2.3. C11orf95-RELA fusion-positive supratentorial ependymoma

The ST-EP-CR subgroup driven by the C11orf95-RELA^{Fus} fusion was first described by our lab in 2014[40]. It comprises 70% of all ST-EP and was officially recognised as a distinct tumour entity by the WHO in their "Classification of Tumours of the Central Nervous System" in 2016[40,57].

Whole genome sequencing of intracranial ependymomas revealed frequent structural variations on chromosome 11 in ST-EP (Figure 1.2A) versus the relatively silent genomes of PF-EP. These variations are caused by a genomic event called chromothripsis, a catastrophic mutational event frequently observed in cancers[58,59]. First discovered in 2011 in samples of chronic lymphocytic leukaemia, chromothripsis describes the shattering and subsequent rearrangement of a chromosome, or part of one[60]. In >70% of ST-EP, chromothripsis of chromosome 11q results in the fusion of *C11orf95* and *RELA,* two genes that are usually separated by 73 genes (Figure 1.2B). While the function of *RELA*, also referred to as p65*,* is well characterised as the principal effector of NF-κB signalling, the function of C11orf95 remains unknown[61]. Transcription of the fusion gene produces the fusion protein C11orf95-RELA, of which seven different splice variants have been described (Figure 1.2C). The two most frequent account for more than 70% and 24%, respectively, and, are henceforth referred to as (C11orf95-RELA^{Fus1}) and (C11orf95-RELA^{Fus2})[40]. Spontaneous nuclear translocation of the fusion protein triggers an aberrant gene expression programme in tumour cells[40,62]. Elevated expression levels of L1CAM (cell adhesion molecule L1) are also detected in ST-EP-CR tumours[40]. Immunohistochemical (IHC) analysis demonstrates a distinct nuclear staining pattern for active RELA (NF-κB p65) and L1CAM in ST-EP-CR (Figure 1.2D).

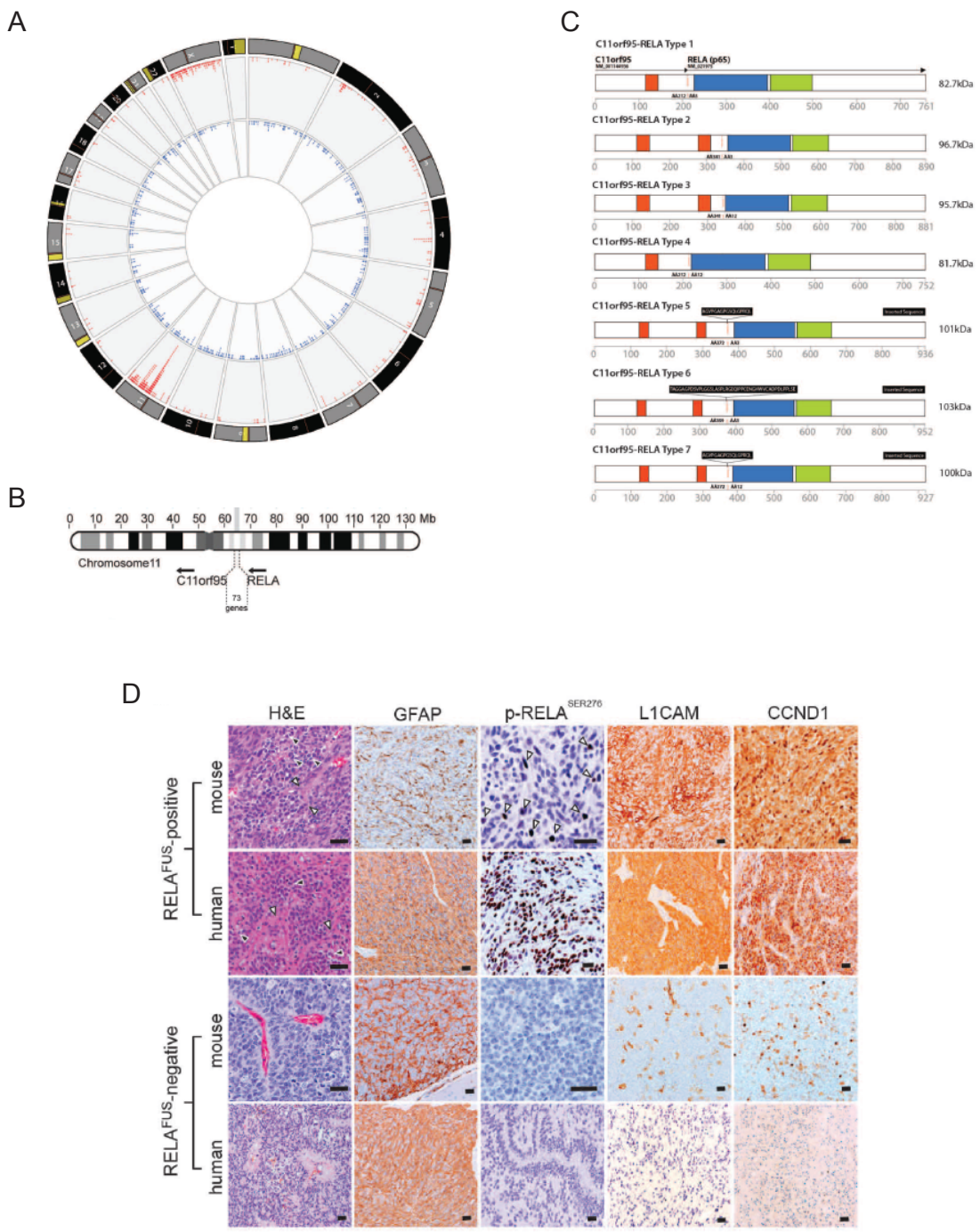

Figure 1.2: C11orf95-RELA-positive supratentorial ependymoma are a result of chromothripsis on chromosome 11q. A. Circos plot depicts structural variations across genome for supratentorial (red) and posterior fossa ependymomas (blue). **B.** Structure of chromosome 11 prior to chromothripsis. **C.** Overview of seven different splice variants of C11orf95-RELA fusion. **D.** Immunohistochemistry analysis of C11orf95-RELA^{Fus}-positive tumours (Taken from Parker *et al.* 2014[40]).

The oncogenic potential of C11orf95-RELA^{Fus} was confirmed in orthotopic implant models of *INK4a-/-* mNSCs overexpressing C11orf95-RELA^{Fus1} and C11orf95-RELA^{Fus2} that generated tumours rapidly in recipient mice[40,62]. Conversely, mNSC transduced with wild-type (WT) partner genes failed to generate tumours[40]. Oncogenic activity of C11orf95-RELA^{Fus1} and C11orf95-RELA^{Fus1} has since been reproduced by several groups utilizing different mouse models[62–64].

Retrospective analysis of patient survival data further confirmed that expression of C11orf95-RELA^{Fus} in human tumours negatively correlates with 10-year OS (<50% OS; Figure 1.3B&C)[39].

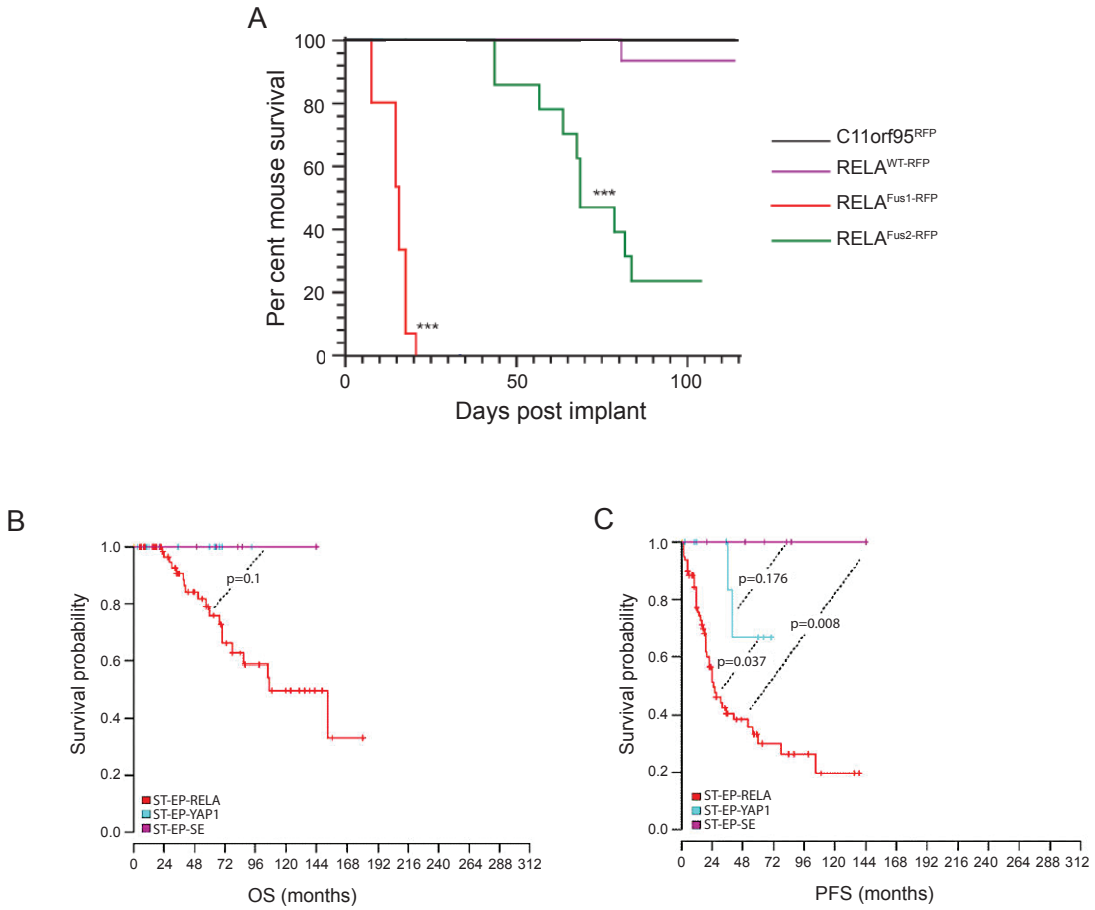

Figure 1.3: C11orf95-RELA^{Fus} drive aggressive ependymoma in mouse models and patients. A. Survival curves of mice implanted with *Ink4a-/-* NSCs overexpressing C11orf95-RELA^{Fus1}, C11orf95-RELA^{Fus2}, RELA^{WT}, C11orf95^{WT} (*** P<0.0001, Log-rank test relative to control NSC). **B** Kaplan-Meier survival curves for overall survival (OS) **C.** Kaplan-Meier survival curve for progression-free survival (PFS). (Adapted from Parker *et al.* 2014, Pajtler *et al.* 2015[39,40]).

1.2.3.1. Diagnosis of C11orf95-RELA subgroup tumours requires sophisticated molecular technologies

Accurate diagnosis of ST-EP-CR tumours is important if we are to develop new treatments for this aggressive subtype of ependymoma. Currently, diagnosis of the subgroup requires sophisticated approaches such as break-apart FISH (Fluorescence In Situ Hybridisation), RNA sequencing or methylation profiling[40,65]. These relatively expensive and technically complex methods are not widely available, thereby rendering diagnosis of these tumours problematic. IHC is more widely available, making it a more easily implemented alternative. Our lab and others have demonstrated a nuclear IHC staining of RELA or cell staining with L1CAM in ST-EP-CR[40]. Consequently, several groups have used these markers as surrogate IHC markers of direct molecular diagnosis of the fusion[40,66–69]. However, these IHC stains are not perfect and can yield false positive and negative results[68,70–72]. Therefore, its unique epitope structure C11orf95-RELA^{Fus} suggests this might represent an ideal diagnostic marker for IHC. The generation of candidate C11orf95-RELA^{Fus1} antibodies is described (Chapter 2).

1.3. Standard of care treatment for ependymomas comprises maximum resection surgery and radiation therapy

A retrospective, multi-centre analysis study reported a poor 10-year OS for paediatric ependymoma patients of 50 ± 5%, with a 39 ± 5 % chance of relapse within 5 years[73]. Hence, there is a great need for new treatment options to improve the survival of children with ependymomas. Despite the recent advances in molecular subgrouping of ependymoma, the standard of care treatment regimen has not changed over 40 years and its mainstay treatment remains as resection surgery followed by RT[43]. Despite efforts to develop effective chemotherapy regimens, most clinical trials have produced negative results (see 1.3.1)[74–76].

Various studies have reported the extent of surgical resection to positively correlate with OS. Patients undergoing gross-total resection (GTR) or near-total resection (NTR) have a significantly higher chance of prolonged progression-free survival (PFS) than patients receiving subtotal resection (STR)[75,77–79]. It was further demonstrated

that addition of RT in patients receiving STR has a beneficial effect on OS[78]. It is usually administered in the form of local fractionated RT with children receiving between 54 and 59.4Gy[23,80]. While in medulloblastoma patients, RT is avoided in children below the age of three, for ependymoma patients, adjuvant RT is given as early as 12-18months of age[23,81]. Particularly young patients that are not enrolled for RT due to their age or other factors such as parental indecision, receive surgery followed by chemotherapy with RT delayed 1-2 years or until tumours progress. This treatment strategy was tested in the clinical trial ACNS0121, in which three different treatment strategies were compared: 1) GTR + observation, 2) GTR + RT, 3) STR + chemotherapy, followed by a second surgery and RT in case of a relapse. The inclusion of irradiation was recommended in the treatment of most ependymoma subgroups[82]. This finding was corroborated by data from a recent study collecting survival data of relapsing patients. Here, it was shown that patients receiving chemotherapy alone have the poorest OS upon recurrence with an average of 19.3 months, compared to patients subjected to irradiation or surgical resection with OS values of 29.1 and 24.2months respectively[83].

The importance of including the molecular subgroup into the analysis of patients' survival data was emphasised in 2016, when Ramaswamy *et al.* found that, while radiation post-resection adds a survival benefit in PF-EP-A patients, gross-total resection without adjuvant RT is efficient for the treatment of PF-EP-B patients[44]. Hence, to help develop subgroup-specific treatment regimens, subsequent studies have introduced survival analysis according to subgroup[84,85].

Besides the extent of surgical resection and the molecular subgroups, several markers have been associated with poor prognosis[25,79,86]. Location of the tumour, high mitotic activity and necrosis were associated with decreased OS in patients with spinal or intracranial ependymoma[87]. Moreover, chromosome 1q gain, high expression of Ki67 and low expression of H3K27me3 have all been correlated with relapse and poorer survival in intracranial ependymoma patients[43,79,86]. Absence of p16 and elevated levels of pAKT and Ki67 were further linked to poor outcome in PF-EP patients[88], Some of these markers have been suggested as potential therapeutic targets but more studies will be necessary to investigate how these tailored treatments will affect survival outcomes in ependymoma patients.

1.3.1. Role of chemotherapy for the adjuvant treatment of ependymoma remains controversial

For over four decades, numerous clinical trials have tested various multiagent regimens in the context of standard of care treatment. However, the benefit of chemotherapy in management of ependymoma patients remains to be verified[89,90]. Early clinical trials between 1975 and 1992 initiated by the Children's Cancer Group (CCG; CCG942, CCG921) tested the effect of multiagent modalities consisting of 3 or 8 drugs respectively, on survival. Neither of these studies demonstrated any survival benefit[74,89]. In order to delay irradiation in children aged 3 and below, a number of subsequent trials tested the administration of chemotherapy post-surgery, during which a maximum PFS of 42% could be achieved[22,80,91]. More recent studies have focused on combination therapy mainly consisting of cisplatin, cyclophosphamide, etoposide and vincristine. For example, the currently active phase III trial ACNS0831 (NCT01096368) compares three treatment arms, of which two comprise post-RT observation and post-RT chemotherapy containing the compounds listed above. The third treatment arm involves neoadjuvant chemotherapy and second-look surgery, a treatment regimen recommended in the preceding trial ACNS0121[82,92]. The SIOP Ependymoma II (NCT02265770) trial, a European multi-centre study, assesses a similar treatment regimen to the one applied in ACNS0831[11]. As of December 2020, both studies (NCT01096368 and NCT02265770) are still active but have not reported assessing the outcomes of specific ependymoma subgroups. This is due to the fact that the ependymoma subgroups were only defined during the course of these studies.

Due to their distinct origins, molecular profiles and varying prognoses, each subtype of ependymoma is likely to require different treatment[43]. While subgroup-specific therapies are not available in the clinic yet, several groups are now investigating potential targets and therapeutic approaches. Witt *et al.* have reported elevated levels of PD-L1 in ST-EP and therefore suggested a potential susceptibility to immunotherapy for these tumours[93]. The NOTCH pathway has also been implicated as a target in C11orf95-RELA^{Fus}- and YAP^{Fus}-positive ST-EP [64,94].

The suggestion of a tailored treatment approach targeting ependymoma-specific biomarkers was further supported by Ferguson *et al.* in 2018, as they showed that ependymoma overexpress proteins involved in DNA-repair and chemoresistance, thereby rendering them more resistant towards established chemotherapeutics such as anti-metabolites[95].

Moreover, the predominantly local recurrence of ependymoma, which mostly represent the same subgroup as the primary tumour, suggests that these recur from remaining tumour cells surrounding the surgical site following GTR[39]. As relapse generally does not occur within months but years, these remaining tumour cells might be dormant at the time of imaging post-surgery. Due to their halted cell cycle, dormant cancer cells are not susceptible to treatment with anti-proliferative agents (reviewed in [96]). Hence, adjuvant chemotherapeutic treatment of ependymoma after GTR using cytotoxic compounds will be ineffective.

All these factors need to be considered when developing new treatment approaches against intracranial ependymoma. Thus, current clinical trials focus on the treatment of recurrent ependymoma and include novel therapeutic approaches such as administration of immunotherapy, the use of a monoclonal antibodies and the intratumoural injection of an oncolytic virus (NCT01795313, NCT02774421 and NCT02457845, respectively).

1.4. Drug development for brain tumours presents a challenge

Drug development for brain tumours has proven to be extremely challenging[97]. Although more than 2000 brain tumour trials are registered at clinicaltrials.gov, only six drugs are currently approved for brain tumours treatments. One of the confounding factors in brain tumour drug development is the blood-brain barrier (BBB) (see section 1.5)[98]. This physical barrier tightly regulates substances in the blood stream from entering into the brain. Only drugs with specific properties are able to cross the BBB (see section 1.5)[99]. Although it is possible to design drugs with BBB penetrating properties, pharmaceutical companies often avoid this to prevent unwanted side effects when developing chemotherapies for cancers of peripheral tissues.

Accurate modelling of treatment regimens at the preclinical stage plays a key role in successful drug development. Many treatments fail the transition from the preclinical to the clinical stage, which could either be due to them being tested as monotherapies or the use of an incorrect preclinical model[97,100]. In the clinic, patients receive multimodal treatment regimens consisting of maximum safe resection, radiation and chemotherapy[11]. Hence, novel tumour treatments should be tested in the same context in preclinical studies. In order to ensure that novel treatment regimens are tested accurately, our lab has established a so-called preclinical mouse hospital. Here, brain tumour mouse models are subjected to the same treatment regimens patients receive in the clinic. Moreover, it is combined with newly developed mouse models representing distinct tumour subgroups[101]. This approach is particularly powerful when it is combined with mouse models that accurately reproduce the biology and treatment response of the corresponding human tumour subtypes[39,40,62,102–107].

Genomic and transcriptomic profiling studies have identified a number of highly overexpressed or unique molecules specific for the distinct subgroups that could be exploited for targeted therapeutics[104,108–110]. Based on these insights, drug screens, which present the initial step in drug development, can be tailored towards specific tumour subgroups and their genotypes[111–113]. They are distinguished into target-agnostic and target-based screening approaches[114].

Among others, our lab has performed numerous high-throughput drug screens, testing over a million compounds for their efficacy in brain tumour cells. These screens comprised novel structures, drugs approved by the U.S Food and Drug Administration (FDA), or a combination thereof[47,101,115] (Nimmervoll *et al.* unpublished). These led to the identification of a selection of novel structures and licensed drugs, which were studied as part of this thesis (Chapter 2).

1.5. The blood brain barrier limits brain tumour treatment

Traditionally, chemotherapeutic agents are delivered systemically either via the oral route or by injection into the blood stream[19,116,117]. Systemically administered drugs for brain tumours are presented with the BBB as a hurdle, as the BBB prevents most molecules such as toxic metabolites or xenobiotics from entering the brain[118]. The BBB is formed by endothelial cells, pericytes and astrocyte end-feet (Figure 1.4). Endothelial cells are inter-connected via tight junctions, which restrict the flow of hydrophilic or large molecules from the blood into the brain via the paracellular route[119]. Thus, molecules can only penetrate into the brain through ion channels, active transporters or by cellular diffusion[120,121]. The latter is restricted to molecules below a certain size limit. While the exact nature of molecules that can diffuse through the BBB is debated, it is reported to be those sized <400-600 Dalton (Da) and lipophilic[98,99,122]. Chemotherapeutic drugs currently used for the treatment of brain tumours often either have short half-lives (temozolomide) or do not exhibit favourable BBB penetration properties (paclitaxel)[123,124]. Penetration of paclitaxel has been shown to be improved by inhibiting the ABCB1 receptor[125]. Also referred to as P-glycoprotein (P-gp), this drug-efflux transporter, amongst others, is highly expressed on the luminal membranes of endothelial cells[119]. It is also expressed in a variety of tumour cells, where it efficiently mediates drug-efflux and thereby contributes to multidrug resistance in these tumours[126–128].

The importance of the BBB as a barrier to brain tumour therapy is exemplified by recent demonstration that the highly curable WNT-medulloblastoma has a leaky BBB, rendering them particularly susceptible to chemotherapy[129]. While ependymoma are characterised by an aberrant vasculature, there is no evidence that these tumours

have a leaky BBB[130,131]. Instead, transcriptomic analysis revealed expression of P-gp and multidrug resistance proteins, leading to the hypothesis that ependymoma are characterised by an intact blood-tumour barrier[132].

In order to treat brain tumours with an intact BBB, alternative approaches have been developed to circumvent it and enable direct delivery into the brain or the primary tumour site[133].

1.5.1. Novel drug delivery methods for the treatment of brain tumours

Different strategies have been developed to circumvent or disrupt the BBB[134]. An increase in barrier-permeability is achieved through the application of focused ultrasound, laser, electrohyperthermia and nanoparticles[135,136]. Methods to deliver drugs directly into the brain include convection enhanced delivery (CED), implantable biodegradable polymer wafers and hydrogels[121,137–139] (Figure 1.4). CED describes the delivery of drugs through an implantable catheter, often connected to either an infusion pump or a reservoir on the skull, also referred to as an Ommaya reservoir[139].

Wafers are impregnated with chemotherapeutical compounds, while hydrogels can be synthesised specifically to incorporate the anticancer drug and release it at a desired rate[140]. Following resection surgery, wafers and hydrogels are implanted into post-resection cavities where they release the anticancer compound into the surrounding tissue[137,140]. Carmustine-loaded wafers (Gliadel®) have been approved for the treatment of GBM since 1996[140]. Although they add a marginal survival benefit in GBM patients, they have been associated with side effects such as intracranial infection or seizures in several studies[141]. The use of Gliadel® remains controversial, with a retrospective review of nineteen studies deeming them not recommendable due to the high complication rate, while another study examining over 400 patients did not find any differences between patients with or without carmustine wafer therapy[142,143].

Ommaya reservoirs, which have been tested repeatedly in children, have also been associated with post-implantation infections[144–148]. As a result of these disadvantages, there is a need for the development of novel, more favourable drug delivery methods.

Recently developed hyaluronic-based hydrogels present a promising alternative to currently available local delivery methods. Due to their hyaluronic acid backbone, these gels are fully biodegradable and can further be tailored specifically with regards to cargo loading and drug release rates[149]. Thus, they present a novel injectable drug delivery method for adjuvant chemotherapy following resection surgery in brain tumour patients. Chapter 3 describes the optimisation and application of these gels in *in vitro* and *in vivo* ependymoma models.

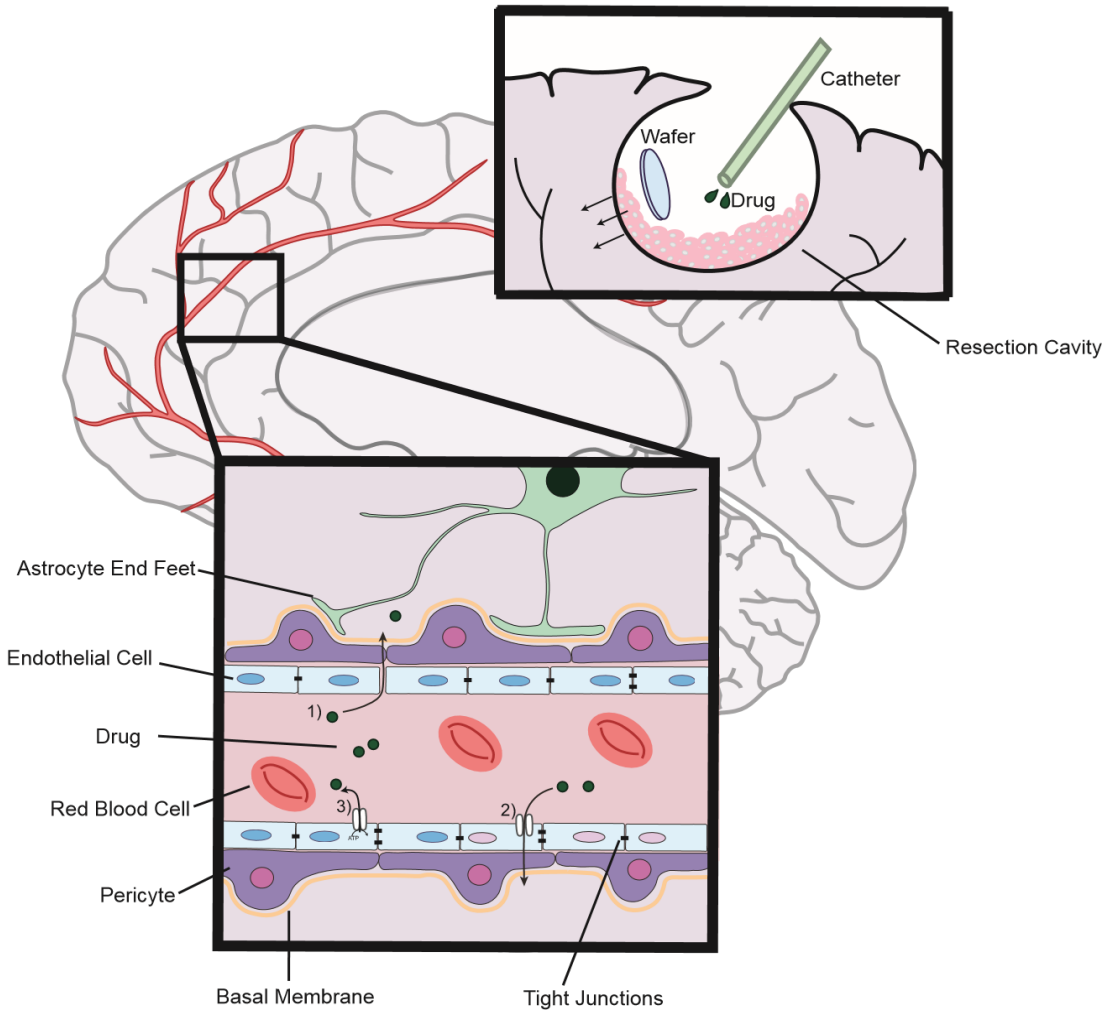

Figure 1.4: Structure of blood-brain barrier and local delivery techniques for the treatment of brain tumours. Blood brain barrier consists of endothelial cell layer, pericytes and astrocyte end feet. Small, lipophilic drug influx occurs via diffusion (1) or active transporters (2), while efflux is mainly mediated by ATP-pumps (3). Local drug delivery techniques include the implantation of wafers and catheters into the cavity following maximal safe surgical resection (adapted from [134,139]).

1.6. Aims of Thesis

Rationale: Supratentorial ependymoma driven by C11orf95-RELA^{Fus} are aggressive tumours associated with poor prognosis. Accurate diagnosis is therefore particularly important for appropriate subsequent clinical management of the patients and development of new treatments. However, there is a lack of widely available routine diagnostic methods for these tumours. Due to its exclusive expression in ST-EP-CR tumours, the C11orf95-RELA^{Fus} protein presents a unique target for diagnostics and therapeutics. To facilitate widely available, accurate diagnostic of ST-EP-CR tumours, a novel C11orf95-RELA^{Fus}-targeting antibody for the use in routine IHC was developed.

Furthermore, standard of care treatment of ependymoma has not changed over the last 40 years, with over one-third of ependymoma remaining incurable. Hence, there is an unmet need for novel therapeutic regimens. Different approaches for therapeutic development include *de novo* drug development and repurposing of drugs. As most FDA-approved drugs selected for repurposing harbour unfavourable BBB properties, delivery to the tumour site has to occur via a local drug delivery method.

The aims and objectives of this thesis are:

1. Generation of an C11orf95-RELA^{Fus1}-targeting diagnostic antibody to help accelerate acute diagnostic of fusion-positive supratentorial ependymoma in the clinic
2. Identification of active novel compounds to be pursued in the development of a novel therapeutic specific for supratentorial ependymoma
3. The development of a novel drug delivery system in combination with repurposed drugs to treat supratentorial ependymoma

2. Generation of novel candidate diagnostic antibodies for C11orf95-RELA fusion-positive ependymoma

The work described in this chapter is part of a patent application. Please see 6.1 for more details.

2.1. Attributions

Several steps of the antibody development were carried out by the Antibody Alliance Laboratory (AAL). These include phage display screening, selection of single chain variable fragments via homogenous time-resolved fluorescence assays as well as conversion to mature monoclonal immunoglobulins as described in 2.3.2. The affinity maturation of parental clones was led by Denice Chan from AAL and I assisted for parts of the affinity maturation rounds 3-5. Epitope competition assays were further carried out by the AAL lab. Work carried out by AAL staff is identified in each section of this chapter. Co-immunoprecipitations and immunoblots in Figure 2.9 were performed by Robert Kupp.

2.2. Introduction

This chapter describes the development of candidate C11orf95-RELA^{Fus}-targeting antibodies, designed for diagnostic application in the clinic. To date, the exact diagnosis of C11orf-RELA^{Fus} proteins in patient samples requires sophisticated approaches such as break-apart FISH, RNA sequencing or methylation profiling, which are not widely available[71,150]. Hence, antibodies that detect C11orf-RELA^{Fus} protein in routine immunohistochemistry could facilitate accurate, widely available, diagnosis of supratentorial ependymoma subgroup.

2.2.1. Antibodies are part of the adaptive immune response in humans

Antibodies play an important role in the human response against pathogens. Immune responses triggered by the human immune system are broadly distinguished into two

types: the innate immune response and the adaptive immune response[151]. During the latter, activated B-lymphocytes are responsible for the production of antibodies[152].

When exposed to foreign pathogens, cells of the innate immune response recognise conserved structures on the microbial surfaces shared by a large number of pathogens via a range of pattern recognition receptors and can process and subsequently present the foreign antigens to cells of the adaptive immune system[153]. Upon antigen presentation by antigen-presenting cells and stimulation through cytokines secreted by T-cells, B-lymphocytes can mature into antibody-secreting plasma cells[154]. These can produce five different types of immunoglobulins (Igs): IgM, IgG, IgA, IgE, IgD. IgMs are expressed on naïve B-cells and are therefore considered natural antibodies, which are germ-line encoded. Upon maturation of the B-lymphocyte, IgMs are switched to other isotypes with higher binding affinity via a process called somatic hypermutation[155–157]. IgGs are the most prevalent antibody in the serum and can further be differentiated into four subclasses: IgG1, IgG2, IgG3 and IgG4[158].

2.2.1.1. Structure of Immunoglobulin G

Generally, IgGs are heterodimers containing two 50kDa heavy chains and two 25kDa light chains consisting of either κ chains or λ chains connected through disulphide bridges[151]. On these chains, amino-terminal domains (N-terminus) harbour “variable” (V) amino acid sequences, while the fragments closer to the carboxy-terminus (C-terminus) contain “constant” (C) sequences. The variable domains are linked via joining segments (J) and through alternative splicing of V(D)J exons a wide range of variable sequences can be generated, thereby producing a large number of diverse antibodies[151]. On mature immunoglobulins, the antigen-binding fragment (Fab) consists of variable and constant regions of heavy (V_H, C_H) and light (V_L, C_L) chains[158]. Variable domains of these are also termed variable fragments (Fvs) and single chain variable fragments can be generated (scFvs) by linking the VH and the VL through a flexible peptide linker. These present one of the smallest unit required for antigen-binding[159]. The remaining constant regions of the heavy domain below the two Fab domains form the Fc region (Figure 2.1).

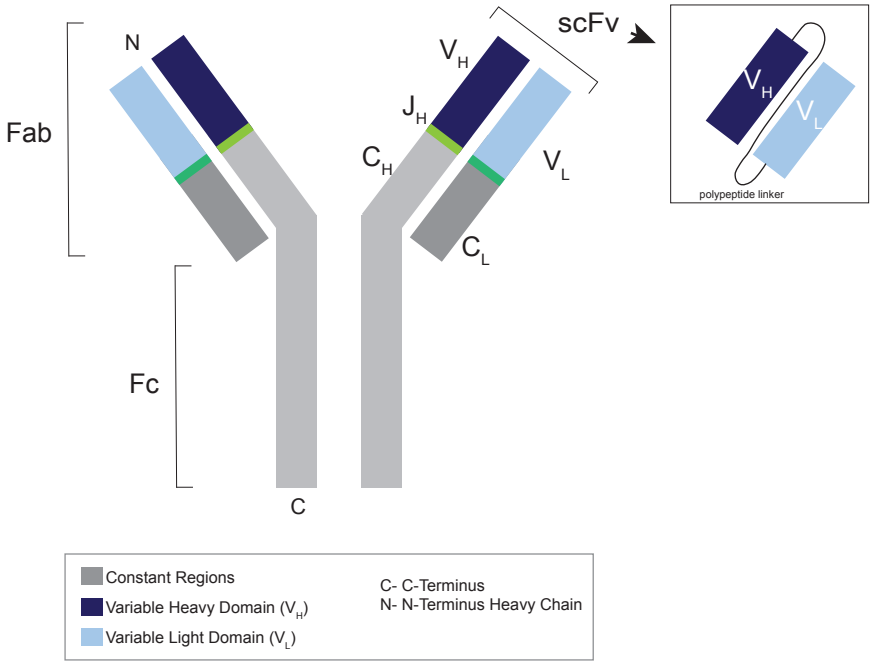

Figure 2.1*:* Structure of monoclonal Immunoglobulin G. Simplified structure of monoclonal Immunoglobulin G. Y-shaped immunoglobulin is a heterodimer of heavy and light chains connected via disulphide bonds. Variable and linked constant regions of heavy and light chain form the antigen-binding fragment (Fab). Remaining constant regions of the heavy domain form the Fc. Single chain variable fragments (scFvs) present the smallest antigen-binding fragment and are comprised of variable light and heavy chain fragments that can be linked via a polypeptide linker for the use in technical applications such as phage-display or as therapeutics (adapted from[158,160]).

2.2.2. Development of monoclonal antibodies

In modern medicine, engineered antibodies are extremely versatile and can be utilized as therapeutics or function as diagnostic tools[161]. Originally, antibodies were produced through the immunization of animals with the first such antibody published in 1890[162]. This was followed by the development of the hybridoma technique by Köhler and Milstein, which involved the fusion of a murine immortal myeloma cell with murine spleen cells[163]. One of the limitations of this technique was that it produced mouse immunoglobulins, which, upon repeated dosing in human patients, can induce a human anti-mouse antibody reaction[164–166]. Hence, chimera antibodies consisting of

human and mouse immunoglobulin fragments were developed to reduce immunogenicity of the therapeutic antibodies (reviewed in [167]).

Phage display is now commonly used to produce human antibodies (reviewed in [168]). It includes the presentation of human antibody fragments on the surface of a bacteriophage, predominantly a filamentous M13 phage, which is usually achieved by fusing a gene encoding the phage's minor coat protein III (gene III) to genes encoding the fragment-presenting peptides[169–174]. It has been shown that expression of these fusion proteins is most successful when cloned into another plasmid. This plasmid contains promoter, replication signal, resistance marker and packaging information of the filamentous phage. *Escherichia coli (E. coli*) are routinely used to clone large numbers of the fusion genes after they have been infected with the phagemid plasmid via a so-called helper phage, such as M13KO7[26]. Expression in the periplasmic space of the bacteria further allows for proper folding of the protein[176–178]. However, as the *E. coli* folding machinery is unable to process large fragments, only small fragments such as scFvs, Fabs or variable heavy domains can be folded properly[179]. Following successful production of antibody fragment-presenting phages, phage display selection is performed.

The protocol comprises five steps with the first one being the combination of phage display libraries with the antigen of interest. Antigens are either directly adsorbed to the bottom of a well or immunotube or are immobilised via streptavidin capture using biotinylated antigen. Following the binding of the antibody fragment with the highest affinity, non-binders are washed away. Phages bound to antigens are released either via enzymatic digestion or dilute acids or bases. Amplification of eluted phages is achieved through the use of bacteria. Selections are then used for consecutive rounds of phage display, each round with decreased antigen concentration, to ultimately select antibodies displaying the highest affinity for the antigen of interest[177,179,180]. Culture supernatants can further be screened in enzymatic based assays such as the enzyme-linked immunosorbent assay (ELISA) to confirm antigen-binding of selection outputs[171,181].

Phage display can be performed with a range of libraries including synthetic or patient-derived naïve or immunised libraries[182]. The latter are generated from samples of previously immunised donors, while naïve libraries are produced with blood from unimmunised donors[171,183].

2.2.2.1. Affinity maturation via ribosome display

Antibody affinity for a protein of interest can be improved through iterative cycles of either phage display or ribosome display[184]. The biggest advantage of these techniques is, that they allow affinity maturation to be performed *in vitro* exclusively. While ribosome display can also be applied to improve protein stability or select antigen-binding peptides, it is most commonly used for affinity maturation. If a selection of antibodies is to be matured, ribosome display is preceded by random mutagenesis of the linear scFv sequence of the respective antibodies. Error prone PCR mutagenesis is applied to induce minor mutations in the sequence that might increase affinity[180,182]. These novel sequences are then transcribed into mRNA, which, in turn is translated into peptides by eukaryotic cell free systems such as rabbit reticulocyte lysates or prokaryotic systems such as *E. coli* S30 ribosomes. Due to a stem-loop sequence and a missing STOP codon in the mRNA sequence, ribosomes are stalled and upon stabilizing of the translation complex, a so-called genotype (mRNA)-phenotype (peptide) linkage is observed (reviewed in[185]). Biotinylated antigens are then added to the mRNA-ribosome-protein complex, enabling the displayed scFv to bind to its target antigen. Subsequently, bound complexes are captured by streptavidin-coated magnetic beads and non-binders are removed through several washing steps. Finally, RT-PCR is used to convert mRNA to cDNA, which in turn is amplified through PCR and purified via gel extractions. Output DNA is then used for additional rounds of ribosome display (Figure 2.2)[186]. In order to enrich for scFvs with higher affinity, ribosome display is commonly performed 3-5 times with decreasing antigen-concentrations[187].

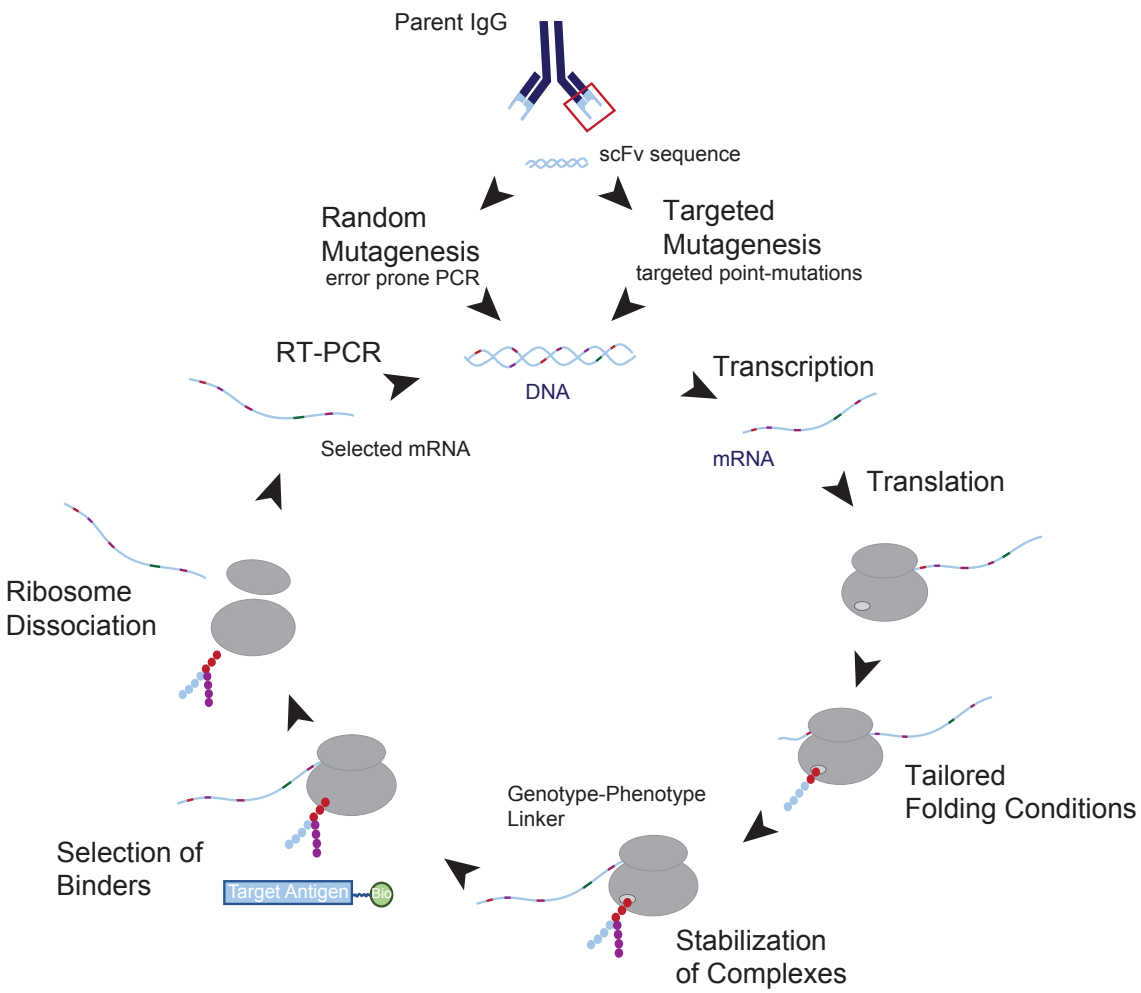

Figure 2.2: Overview of Ribosome Display Affinity Maturation. Overview of the ribosome display cycle. When a parent immunoglobin has been selected for affinity maturation, its single chain variable fragment sequence is subjected to ribosome display. First, DNA is transcribed into mRNA. This is followed by translation using S30 ribosomes under specifically tailored folding conditions that enable stabilization of the mRNA-Ribosome-peptide complex. Following exposure to the biotinylated target antigen, bound complexes are captured using streptavidin-coated beads. Captured complexes are dissociated and selected mRNA is reverse transcribed into cDNA and amplified before selection outputs are used for successive rounds. Generally, 3-5 rounds of ribosome display with decreasing antigen concentrations are recommended for optimal affinity maturations (adapted from [167,186]).

2.2.3. Antibodies and cancers

Antibodies can play different roles when targeting cancer. Due to technological progress over the last decades, antibodies can be used in a range of therapeutic or diagnostic applications. In the field of immunotherapies, antibodies can be utilized in different types of therapy like antibody-drug conjugation, immunotoxins or radioimmunoconjugates. For these, they are either coupled to a cancer-specific drug, a cytotoxic drug or a radionuclide, respectively[188]. The FDA approved the antibody rituximab as the first monoclonal therapeutic antibody for leukaemia. Its use has since been extended to lymphoma and was followed by the development of a series of cancer-immunotherapeutics[189].

Technical advances have further led to the development of a range of antibody-based assays for diagnostic purposes. These include the ELISA, that can be used to detect and measure concentrations of cancer-associated proteins or antigens in serum samples of patients[190–192]. In line with the most recent advances in early diagnostics, ELISAs can also be used to detect circulating tumour antigens[192–194]. However, with regards to costs and practicality, immunohistochemistry (IHC) is a superior method. Used as a standard diagnostic tool since the late 1970s, IHC has recently also been utilized to predict outcome, most-suitable therapy or therapy-response of tumours through the application of specific biomarkers[195]. These are referred to as prognostic markers and, depending on the tumour type, can be a single marker or an array of markers, so-called biomarker panels[196–199]. They include markers for proteins commonly upregulated in cancers such as Ki67 or p53 but also tumour-specific markers like the oestrogen receptor and progesterone receptor used in breast cancer diagnoses[197,198,200].

2.2.3.1. Diagnostic antibodies for cancer fusion proteins

Over the last years, extensive research into cancer cell genomes has allowed the identification of driver mutations and genes that are either frequently mutated in various tumours or specific to cancer types or tumour subgroups. Some of the cancer genes identified are fusion genes which are the result of genomic rearrangements[60,201]. These fusions are commonly found in subtypes of lymphoma,

leukaemia or sarcoma[202]. Synovial sarcoma, for example, is characterised by SS18-SSX fusions, which were previously found to present a potential therapeutic target[203]. In 2020, Baranov *et al.* reported the development of the first fusion protein-specific diagnostic antibodies targeting SS18-SSX in synovial sarcoma. This rabbit monoclonal antibody had been generated through the immunization of a rabbit with a synthetic peptide harbouring the SS18-SSX fusion site[204].

Our lab previously identified the C11orf95-RELA^{Fus} as the driver oncogene in 70% of ST-EP[40]. The subgroup featuring this fusion is associated with a particularly poor prognosis of 10-year PFS rates of only 20%[39]. Hence, accurate diagnosis is crucial for the clinical management of patients. As C11orf95-RELA^{Fus} is exclusively expressed in ST-EP-CR, it harbours both prognostic and diagnostic potential. Due to its unique fusion epitope, it further presents the most suitable target for antibody development[40,43]. This was utilized in the generation of a diagnostic antibody targeting C11orf95-RELA^{Fus1}, described in this chapter.

2.3. Methods

2.3.1. *In vitro* cell culture methods

2.3.1.1. Cell culture

A variety of murine ependymoma cell lines (mSEP-CR[-]^{EPHB2}, mSEP-CR[-]^{RTBDN}, mSEP-CR[+]), a mouse neural stem cell line (mNSC) and a human ependymoma cell line (xSEP-CR[+]), which had previously been generated in our lab were used for the work described in this chapter[38,40,47]. Mouse ependymoma cell lines were generated by infecting neural stem cells (NSCs) isolated from *Ink4a/Arf*$^{-/-}$ mice retroviruses encoding either *RTBDN*, *EPHB2*, and *C11orf95-RELA*^{Fus1} ependymoma oncogenes (Table 2.1)[38,40]. Upon tumour formation in mice, they display genomic and histologic similarities to primary ST-EP. MNSCs were isolated either from brains of CD1® mice (unpublished) or *Ink4a/Arf*$^{-/-}$ mice (see 2.3.1.2). The patient derived-xenograft (PDX) model was generated by implanting tumour cells derived from a human C11orf95-RELA^{Fus} -positive ependymoma (xSEP-CR[+]) into the brains of immunocompromised mice[101].

Cells were cultured in ultra-low attachment 75 cm^2 culture flasks in serum-free neurobasal media containing 2mM L-glutamine, 1x N2 supplement, 1x B27 supplement, penicillin-streptomycin (2%) (all from Gibco)[39,40]. Culture media was further supplemented with 20ng/mL recombinant human epidermal growth factor (EGF), 20 ng/mL recombinant human basal fibroblast growth factor (FGF; both Miltenyi Biotec) and 45µg/mL bovine serum albumin (BSA; Sigma-Aldrich). The use of serum-free Neurobasal media in combination with human EGF, FGF and BSA had been identified as the optimised culture as described by Taylor et al. 2005[37]. Cells were cultured at 37°C in a humidified atmosphere of 5% CO_2 and passaged every 3-6 days using StemPro® Accutase (Gibco). Spheres were dissociated into single cells by filtering them through a 40µm cell strainer. After centrifugation at 450g for 5min, cells were resuspended in 1mL media and counted using the Cellometer Auto T4 Bright Field Cell Counter (Nexcelom Bioscience).

Furthermore, HeLa (human epithelial cervical carcinoma) cells were used to generate a cell line stably expressing C11orf95-RELA^{Fus2} (see 2.3.1.3) (henceforth referred to

HeLa^{Fus2}). They were cultured in Dulbecco's Modified Eagle Medium (DMEM; Gibco) with 10% FBS (Gibco) and penicillin-streptomycin (1%). HeLa^{Fus2} cells were cultured in 75cm^2 flasks and passaged every 3-6 days per trypsinization (0.05% Trypsin-EDTA for 5min; Gibco).

Table 2.1: Overview of cell lines used *in vitro*.

Name	Species	Cell of Origin	Ependymoma Transgene	Tumour
mSEP-CR(+)[40]	*Mus musculus*	*INK4a/Arf*$^{-/-}$ neural stem cells	*C11orf95-RELA*^{Fus1}	ST-EP
mSEP-CR(-)[RTBDN, 47]	*Mus musculus*	*INK4a/Arf*$^{-/-}$ neural stem cells	*RTBDN*	ST-EP
mSEP-CR(-)[EPHB2, 38]	*Mus musculus*	*INK4a/Arf*$^{-/-}$ neural stem cells	*EPHB2*	ST-EP
mNSC	*Mus musculus*	CD1® nude mouse neural stem cells	-	-
INK4a/Arf$^{-/-}$, [37]	*Mus musculus*	*INK4a/Arf*$^{-/-}$ neural stem cells	-	
xSEP-CR(+)[101]	*Homo sapiens*	Patient-derived xenograft cells	C11orf95-RELA^{Fus}	ST-EP
HeLa^{Fus2}	*Homo sapiens*	HeLa- cervical cancer cell line	*C11orf95-RELA*^{Fus2}	ST-EP

ST-EP- Supratentorial Ependymoma

2.3.1.2. Isolation of mouse neural stem cells

Ink4a/Arf$^{-/-}$ neural stem cells were isolated from the cortex of a four-week-old female mouse, following euthanasia and dissection of the brain and cortex[37]. Using a scalpel, the cortex was then minced into small pieces and incubated with neurobasal media containing 1mg/mL Collagenase (Thermo Fisher) and Hyaluronidase (Sigma Aldrich) each for 20min at 37°C. After centrifugation at 1000rpm for 5min, cells were resuspended using a 2mL serological pipette and a 1000µl Eppendorf pipette and subsequently strained through a 40µm filter to obtain single cells. Cells were spun down at 1000rpm for 5min, resuspended in media and cultured in ultra-low attachment flasks in neurobasal media as described for neural stem cells in 2.3.1.1.

2.3.1.3. Transduction of cells

To generate a human cell line expressing C11orf95-RELA^{Fus2} HeLa cells were transduced with a lentivirus encoding *C11orf95-RELA$^{Fus2-GFP}$*. For this, HeLa cells ($5x10^5$ cells) were plated on 100mm dishes on *in vitro* day 0 (DIV0). On day *in vitro* one (DIV1), cells were transduced with C11orf95-RELA$^{Fus2-GFP}$ lentivirus at a multiplicity of infection (MOI) of 1-2, allowing one-two virus particles per cell. To enhance transduction efficiency, polybrene infection/ transfection reagent (1:1000; Millipore) was added. Transduced cells were cultured at 37°C and 5% CO_2 for 48h before being split according to protocol and subjected to flow cytometry to sort for GFP$^+$ cells, as these represented successfully transduced cells. GFP$^+$ HeLa cells were then cultured as described above for four to ten more passages. Cell pellets of ~2million cells for protein extractions were frozen down post-transduction for passages 4-10 for further downstream experiments.

Cells used for orthotopic implants were transduced with a lentiviral vector (vCL20SF2-Luc2a YFP) expressing a luciferase reporter and a YFP tag. Cells were cultured as described for mouse ependymoma cells in 2.3.1.1 and upon reaching ~70% confluency, 200µl-500µl of virus were added to cells grown in ultra-low attachment T75 flasks. Successful transfection was confirmed either by fluorescent microscopy or by bioluminescent imaging using the XENOGEN IVIS 200 (Caliper Lifesciences). For this, cells were seeded in ultra-low attachment 6 well plates and 3min prior to imaging, 200µl of D-Luciferin (PerkinElmer) were added per well.

2.3.2. Mouse and human tissue

2.3.2.1. Mouse models and husbandry

Eight- to ten-week-old mice of the immunodeficient CD1® nude strain by Charles River (strain code 086) were purchased and housed at the CRUK Cambridge Institute in compliance with the UK Home Office license (license No. P6787677F). Housing occurred under pathogen-free conditions in groups of 2-5 mice per cage on a 12h light cycle in air-filtered racks with laboratory chow and water *ad libitum*.

2.3.2.2. Orthotopic mouse models

Mouse ependymoma cells (mSEP-CR[+], mSEP-CR[-]^{RTBDN}) resuspended in 5µl Matrigel® (Corning) were implanted orthotopically into the cerebral cortex of brains of eight- to twelve-week-old mice of the immunocompromised CD1® nude strain (strain code 086, Charles River). Table 2.2 gives an overview of cell lines used for allografts listing their origin, oncogenes, cell number injected and the tumour subgroup they represent.

All surgeries were carried out applying aseptic surgery technique was throughout the whole procedure. Mice were anaesthetized with isoflurane (4-5% induction, 1.5% O_2) and injected subcutaneously with 100µl buprenorphine (0.3mg/mL) before fixed in a stereotactic frame (Kopf, Model 902) for surgery. Lubrithal™ eye gel (Dechra) was applied on the eyes and scalp was cleaned using a cotton swab with iodine followed by 70% ethanol. A skin incision right of the midline was made to expose the skull. Using sterile cotton-tipped applicators, the periosteum was removed to further reveal the midline and lambda. Using a dental drill with a 0.7mm burr, a cranial window (~2mm x 2mm) was drilled around ~2mm right of the midline and 3mm up from lambda. Sterile phosphate-buffered saline solution was used to irrigate the window and was dried up using sterile cotton-tipped applicators. A sterile, ice-cooled 25µl Hamilton syringe was used to draw up 5µl of Matrigel® cell suspension. The syringe was fixed in a stereotactic applicator and cells were injected into the cortex at a depth of 2.5mm. The needle was left in place for 30 seconds to avoid cell reflux and was removed slowly. Any blood was dried up using sterile cotton-tipped applicators and the wound was closed with 3-4 stitches using 6-0 coated VICRYL RAPIDE™ sutures (Ethicon).

Table 2.2: Overview of cell lines used for orthotopic implants.

Cell line	Origin	Cell of origin	Oncogene	Tumour subgroup	Cell no. injected /mouse
mSEP-CR (+)[40]	*Mus musculus*	*Ink4a/Arf*$^{-/-}$ NSC	*C11orf-95-RELA*	ST-EP-CR	50,000
mSEP-CR (-)^{RTBDN}, [47]	*Mus musculus*	*Ink4a/Arf*$^{-/-}$ NSC	*RTBDN*	ST-EP-CR(-)	10,000

ST-EP-CR- C11orf95-RELA fusion-positive supratentorial ependymoma; ST-EP-CR(-) C11orf95-RELA fusion-negative supratentorial ependymoma

Mouse brains harbouring mSEP-CR(+) and mSEP-CR(-)^{RTBDN} tumours were dissected and fixed in neutral buffered formalin for 24h followed by submersion in 70% ethanol for 24-72h prior to paraffin embedding, which was performed by the Histopathology core.

2.3.2.3. Mouse tissue samples

Sections of formalin-fixed paraffin-embedded (FFPE) mouse brains were prepared by the histopathology core at the Cancer Research UK Cambridge Institute. Sagittal brain sections were cut with 5µm thickness and mounted on glass slides. The first section of each block was stained for Haematoxylin and Eosin (H&E) by the core.

2.3.2.4. Human tissue samples

Ethical approval was obtained for the use of human tumour sections and is covered under HBREC.2020.13. Human tumour sections covered under this REC number were kindly provided by Professor Ulrich Schüller from UKE Hamburg, Germany. The study involving these tissues was considered a retrospective study on anonymized tissue sections.

Table 2.3: List of human ependymoma tissue samples.

Hamburg Sample Number	Tumour Subgroup	Diagnosis confirmed in the Schüller lab by:
N2875/18 1B	ST-EP-CR	850K, FISH, RT-PCR
E56/2003 B	ST-EP-CR	850K, FISH, RT-PCR
3226/17	ST-EP-CR	RT-PCR
E300/15 1B	ST-EP-CR	RT-PCR
N223/70	ST-EP-CR	RT-PCR
E527/06	ST-EP-CR	RT-PCR
E1170/06	ST-EP-CR	RT-PCR
E142/05	ST-EP-CR	850K, RT-PCR
N13/5	ST-EP-CR	850K, RT-PCR
E1014/12	ST-EP-CR	RT-PCR
E225/94	ST-EP-CR	IHC (NF-κB p65)
94/645	ST-EP-CR	RT-PCR
E545/10	ST-EP-CR	IHC
E 1349/08	PF-EP-A	850K
E 1180/10 C	PF-EP-A	850K
N/3373/18	PF-EP-A	850K
E 30/91	PF-EP-A	850K
E 498/02	PF-EP-A	850K
N/24/17 2B	PF-EP-A	850K
N/509/12	PF-EP-A	850K
E 821/05	PF-EP-A	850K
N3430/17	PF-EP-A	IHC

ST-EP-CR- C11orf95-RELA fusion-positive Supratentorial Ependymoma; PF-EP-A- Posterior Fossa Ependymoma subgroup A; 850K- 850K methylation array; FISH- Fluorescence In-Situ Hybridisation; RT-PCR- Reverse Transcription Polymerase Chain Reaction; IHC- Immunohistochemistry;

2.3.3. Molecular and biochemical assays

2.3.3.1. SDS-Page and Immunoblot Analysis

Mouse ependymoma cells mSEP-CR(-)^{RTBDN}, mSEP-CR(-)^{EPHB2} mSEP-CR(+) as well as mouse NSC and human HeLa ^{Fus2} and HeLa cells were cultured in their respective media, passaged and counted as described in 2.3.1.1. Cell pellets of about 2-3 million cells were snap frozen for immunoblotting. For protein extraction, cell pellets were mixed with radioimmunoprecipitation (RIPA) assay buffer (ThermoFisher) containing protease inhibitors (1:100; ThermoFisher) and incubated on ice for 15min. Subsequently, samples were sonicated in 3 cycles with 30sec on, 10sec off using the Bioruptor® (Diagenode) followed by rotation at 4°C for 20min to allow for proper cell lysis. Alternatively, cells were only rotated at 4°C for 25min at 30rpm. Following 10min of centrifugation at 14,800rpm, protein concentrations were measured using the infrared (IR)-based spectrometer Direct Detect® (Millipore). For immunoblot analysis, 10-40µg of protein cell lysate were used. Samples were prepared with NuPage 1x LDS sample buffer and 1x sample reducing agent and were incubated at 70°C for 10min before loaded onto a 4-12% Bis-Tris gel. ECL Rainbow molecular weight marker (VWR) or Page Ruler^{TM} Plus Prestained Protein Ladder (Fisher) were used as molecular weight markers and 1x NuPage^{TM} MOPS-SDS running buffer (Thermo Fisher Scientific) was used to fill up the gel tank. Gel electrophoreses was run at 120-145V for 1.5-2h, was followed by protein transfer onto nitrocellulose membranes using the iBlot Dry Blotting System (Thermo Fisher Scientific).

Following blocking of the membranes in Odyssey Blocking Buffer (Licor Biosciences), they were incubated with primary antibodies at 4°C overnight. See Table 4.8 for commercial primary antibodies used and Tables 4.4-4.7 for candidate AAL IgGs. All primary antibodies were made up in Odyssey blocking buffer diluted in phosphate buffered saline (PBS) (1:2). After incubation with the primary antibodies, membranes were washed in PBS containing 0.1% Tween-20 (1x PBST). Subsequently, membranes were incubated in secondary antibodies anti-rabbit IRDye 680 and anti-mouse IRDye 800 (1:15,000; Licor Biosciences) for 60min. Nitrocellulose membranes were then washed with PBS-T followed by one 5min washing step in PBS prior to

scanning the blots using the Odyssey CLx infrared technology imager (Li-Cor Biosciences). Images were taken using the Image Studio 4.0 software.

2.3.3.2. Nuclear Extraction

All cell lines were cultured in their respective media, passaged and counted as described in 2.3.1.1. Cell pellets of ~5-7 billion cells were snap frozen and stored in -80°C until processed further. Pellets were lysed in appropriate amounts of protease inhibitors (ThermoFisher) diluted in immunoprecipitation (IP) wash buffer (20mM Tris-HCl, 150mM NaCl, 0.2mM EDTA, 1% Triton-X) and cytoplasmic extraction reagent I (CER I, ThermoScientific) was added followed by vortexing to resuspend pellet. After incubating for 10min on ice, cell extraction reagent II (CER II) was added, tubes were vortexed for 5min and incubated on ice for another 10min. Samples were spun down at 14,800rpm for 5min at 4°C, the cytoplasmic fraction in the supernatant was transferred to a clean tube and samples were stored at -80°C. The pellet was resuspended in nuclear extraction reagent (NER), followed by a 15sec vortex before samples were placed on ice and vortexed for 15sec every 10min for 40min. After an additional 10min spin at 4°C and 14,800rpm, the nuclear extract containing supernatant was transferred to a new tube and samples were either used directly for IP or stored at -80°C until processed further.

2.3.3.3. Immunoprecipitation

Whole cell lysates or nuclear extracts prepared as described in 2.3.3.2 and 2.3.3.3 were used for IPs. For pre-clearing of lysates, Pierce™ Protein A/G magnetic beads (Thermo Scientific) were washed with BSA solution (1%BSA in PBS) 3 times and 30µl of beads resuspended in PBS were used per sample. Following 1h of rotation at 4°C, protein concentrations were measured using the infrared-based spectrometer Direct Detect® (Millipore). For IP samples, ~50µg of protein were mixed with PBS and IP wash buffer and incubated in rotation with 5-10µg of primary antibody at 4°C overnight. Following primary antibody incubation, 100µl of BSA-washed magnetic Protein A/G beads were added per sample and probes were rotated at 4°C for 2h for beads-capture. Ten washing cycles of Protein-IgG-beads complexes were performed using

IP wash buffer and subsequently resuspended in loading buffer. Beads' dissociation was achieved through an incubation at 75°C using a thermocycler for 10min incubation period. Finally, samples were loaded onto SDS-gels and SDS page and immunoblots were performed as described above in 2.3.4.2.

2.3.4. Tissue staining methods

2.3.4.1. Immunohistochemistry

IHC was performed on both, mouse and human brain sections. For mouse tissue sections, 5µm FFPE tissue sections were automatically dewaxed and rehydrated. Antigen retrieval was performed either by proteolytic-induced epitope retrieval using proteinase K (37°C for 10min) or heat-induced epitope-retrieval at 126°C for 10 min using either Tris-EDTA (TE; pH 9.0) or sodium citrate buffer (SC; pH 6.0). Heat-induced epitope-retrieval using either TE or SC buffers produced the best staining results and was therefore chosen for most of the stainings (as indicated in figure legends). The Novolink polymer kit was used for further preparation of the tissue according to the Manufacturer's instructions omitting the step with the post-primary solution (Novolink Polymer DS, Leica). Primary antibodies were diluted in Tris-buffered saline (TBS) supplied with 1% Tween 20 (1xTBST, Sigma-Aldrich) + 10% goat serum and incubated for 1h at room temperature. Tables 2.4-2.8 list all scFvs and primary antibodies used, with details of manufacturers, host species, concentrations, applications they were used in and the respective dilutions. In control stains, the presence of C11orf95-RELA^{Fus1} was detected using an NF-κB p65 antibody from Cell Signalling Technology. The C11orf95-RELA^{Fus1} specific rabbit IgGs were at different dilutions (1:10, 1:50, 1:100, 1:200, 1:500). DAB substrate was used for detection.

IHC performed on human tissue sections from ependymoma patients was performed by me in the laboratory of Professor Ulrich Schüller in Hamburg, Germany. First, 2µm sections of FFPE tissue were dewaxed, rehydrated and subjected to heat-induced epitope-retrieval using sodium citrate buffer (pH 6.0) before continuing the staining using the Novolink polymer kit according to the manufacturer's instructions but omitting the step with the post-primary solution (Novolink Polymer DS, RE7140-CE).

Primary antibodies were diluted in TBST + 10% goat serum and incubated for 1h at room temperature. In control stains, the presence of C11orf95-RELA^{FUS} was detected using a rabbit NF-κB p65 antibody (1:800; Cell Signalling Technology). The C11orf95-RELA^{Fus1} specific affinity matured rabbit IgGs were tested using different dilutions (IgG C0040151 at 1:3000, 1:5000; IgG C0040154 at 1:7000 and 1:8000; IgG C0040159 at 1:2000 and 1:3500). While IgG C0040151 works best at a dilution of 1:5000, IgG C0040154 gives best staining results when diluted at 1:8000 and IgG C0040149 at a dilution of 1:3000. DAB substrate was used for signal detection.

Table 2.4: Overview of single chain variable fragments by AAL.

Manufacturer	Matrix Barcode/ Name	Clone No	Concentration in µg/mL	Dilution
AAL	1091012100	C0040007	31	1:60
	1091012101	C0040012	45	1:87
	1091012097	C0040014	40	1:77
	1091012103	C0040018	51	1:98
	1091012095	C0040025	38	1:73
	1091012093	C0040032	122	1:235
	1091012083	C0040036	48	1:92
	1091012091	C0040039	36	1:69
	1091012109	C0040044	90	1:173
	1091012086	C0040045	348	1:669
	1091012111	C0040047	68	1:130
	1091011884	C0040053	32	1:62
	1091011885	C0040054	48	1:92
	1091011886	C0040056	62	1:119
	1091011910	C0040037	51	1:98
	1091011934	C0040038	41	1:79
	1091011958	C0040060	50	1:96
	1091011887	C0040061	35	1:67
	1091011888	C0040062	43	1:83
	1091011889	C0040063	171	1:329
	1091011890	C0040065	45	1:87
	1091011891	C0040066	50	1:96
	1091011892	C0040067	86	1:165
	1091011893	C0040069	55	1:106
	1091011894	C0040072	55	1:106
	1091011895	C0040074	64	1:123
	1091012844	C0040078	59	1:113
	1091012845	C0040040	26	1:50
	-	CEA6 (neg Ctrl)	800	1:1538

Table 2.5: Overview of mature parent IgGs targeting C11orf95-RELA^{Fus1} by AAL.

Manu-facturer	Batch ID	Clone No	Host	Conc. in µg/mL	Cross-reactivity	Assay used	Dilution
AAL	IgG074	NIP228	Rb	440	None	IB	1:440
	IgG075	C0040014	Rb	470	None	IB	1:470
	IgG076	C0040033	Rb	370	Fus2/Fus1	IB	1:370
						IHC	1:10, 1:100, 1:1000
	IgG077	C0040069	Rb	910	None	IB	1:910
	IgG078	C0040012	Rb	238	None	IB	1:238
	IgG079	C0040032	Rb	369	None	IB	1:369
						IHC	1:10, 1:100, 1:1000
	IgG080	C0040035	Rb	323	Fus2	IB	1:323
	IgG081	C0040036	Rb	469	None	IB	1:469
						IHC	1:10, 1:100, 1:1000
	IgG082	C0040037	Rb	531	Fus2	IB	1:531
	IgG083	C0040040	Rb	642	Fus2/ RELA	IB	1:642
	IgG084	C0040045	Rb	559	None	IB	1:559
	IgG085	C0040060	Rb	244	None	IB	1:244
	IgG086	C0040062	Rb	127	None	IB	1:127
	IgG087	C0040074	Rb	248	None	IB	1:248
	IgG088	C0040007	Rb	480	None	IB	1:480
	IgG089	C0040025	Rb	660	None	IB	1:660
	IgG090	C0040034	Rb	730	None	IB	1:730
						IHC	1:10, 1:100, 1:1000
	IgG091	C0040044	Rb	810	Fus2/RELA	IB	1:810
	IgG093	C0040061	Rb	430	Fus2/RELA	IB	1:430
	IgG094	C0040065	Rb	450	None	IB	1:450

	IgG095	C0040066	Rb	950	None	IB	1:950
	IgG096	C0040067	Rb	390	Fus2	IB	1:390
						IHC	1:10, 1:100, 1:1000
	IgG097	C0040072	Rb	540	None	IB	1:540
	IgG099	C0040018	Rb	390	None	IB	1:390
	IgG100	C0040039	Rb	590	None	IB	1:590
	IgG101	C0040063	Rb	180	None	IB	1:180
						IHC	1:10, 1:100, 1:1000

Rb-Rabbit; Fus1- C11orf95-RELAFus1; Fus2- C11orf95-RELAFus2; IB - Immunoblot; IHC-Immunohistochemistry

Table 2.6: Overview of mature parent IgGs targeting C11orf95-RELA^{Fus2} by AAL.

Manu-facturer	Batch ID	Clone No	Host	Conc. in µg/mL	Cross-reactivity	Assay used	Dilution
AAL	IgG130	C0040081	Rb	470	None	IB	1:470
	IgG131	C0040085	Rb	1020	Fus1	IB	1:1020
	IgG132	C0040095	Rb	270	Fus1/ C11orf95 Exon3*	IB	1:270
	IgG134	C0040098 (Germlined)	Rb	650	None	IB	1:650
	IgG135	C0040100	Rb	560	Fus1	IB	1:560
	IgG136	C0040105	Rb	100	Fus1	IB	1:100
	IgG137	C0040108	Rb	280	Fus1	IB	1:280
	IgG138	C0040109	Rb	730	Fus1/ C11orf95 Exon3*	IB	1:730
	IgG139	C0040110	Rb	510	Fus1	IB	1:510
	IgG140	C0040113	Rb	370	Fus1	IB	1:370
	IgG141	C0040115	Rb	380	Fus1	IB	1:380
	IgG142	C0040125	Rb	280	Fus1	IB	1:280
	IgG143	C0040126	Rb	380	Fus1	IB	1:380
	IgG144	C0040127	Rb	610	Fus1	IB	1:610
	IgG145	C0040129	Rb	460	Fus1	IB	1:460
	IgG146	C0040133	Rb	210	Fus1	IB	1:210
	IgG149	C0040135 (Germlined)	Rb	470	Fus1/ C11orf95^{Exon3**}	IB	1:470
	IgG150	C0040136	Rb	180	None	IB	1:180
	IgG152	C0040143 (Germlined)	Rb	600	None	IB	1:600
	IgG153	C0040111	Rb	150	Fus1	IB	1:150

Rb-Rabbit; Fus1- C11orf95-RELAFus1; IB - Immunoblot

Table 2.7: List of affinity matured monoclonal IgGs targeting C11orf95-RELA^{Fus1} by AAL.

Manu-facturer	Parent IgG	Clone No	Host	Conc. in µg/mL	Assay used	Dilution/ volume tested (used)
AAL	34 progeny (IgG90)	C0040150	Rb	870	IHC	1:100-1:1000
		C0040151	Rb	1040	IHC	1:100-1:5500 (1:4000-1:5500)
					IB	1:1040
					IP	10µl
		C0040153	Rb	1160	IHC	1:100-1:1000
		C0040154	Rb	1590	IHC	1:100-1:9000 (1:8000-1:9000)
					IB	1:1590
					IP	10µl
	36 progeny (IgG81)	C0040159	Rb	970	IHC	1:100-1:4000 (1:3500-1:4000)
					IB	1:
					IP	10µl
		C0040161	Rb	1230	IHC	1:100-1:1000

Rb-Rabbit; IB- Immunoblot; IHC-Immunohistochemistry; IP- Immunoprecipitation

Table 2.8: Overview of commercial antibodies used for immunohistochemistry, immunoblotting and immunoprecipitations.

Name of Antibody	Order Number; Manufacturer	Host	Assay used	Conc. in µg/mL	Dilution
Anti-His tag IR Dye680	ab49936; Abcam	Mo	IB	0.35	1:3000
NF-κB p65 (D14E12)	#8242; Cell Signalling Technology	Rb	IB	0.2	1:5000
			IP	10	1:100
			IHC	1.25-0.833	1:800-1:1200
NF-κB p65 (L8F6)	#6956S; Cell Signalling Technology	Mo	IB	1	1:1000
β-actin	ab8226; Abcam	Mo	IB	0.2	1:5000

Mo-Mouse; Rb-Rabbit; IB- Immunoblot; IHC-Immunohistochemistry; IP- Immunoprecipitation

2.3.5. Techniques performed by AAL

2.3.5.1. Peptide design for phage display assay

Biotinylated peptides of C11orf95-RELA^{Fus1}, C11orf95-RELA^{Fus2}, RELA^{WT}, C11orf^{WT} and scrambled protein were prepared by AAL to be used in phage display. In brief, chemical synthesis of peptides in their trifluoracetate salt was performed by Bachem (Switzerland). Purification was completed by analytical High-Performance Liquid Chromatography (HPLC) and Matrix-Assisted Laser Desorption/Ionization-mass spectrometry was used to verify their identities. Linkers in form of 8-amino-3,6-dioxa-octanoic acid flexible spacers were utilized to add biotin groups to the peptides either N-terminally or C-terminally. While figure 3 depicts the structure of the synthesised peptides, Table 2.9 lists the amino acid sequences for each peptide. According to the transcripts for C11orf95-RELA^{Fus1} published by Parker *et al*., the C11orf95-RELA^{Fus1} peptide sequence was spanning the C11orf95-RELA^{Fus1} epitope and included the amino acid sequences described in Table 2.9, of which the first 16 amino acids are encoded by exon two of *C11orf95* and form the N-terminal part of the peptide[40]. The remaining 17 amino acids are encoded by *RELA* exon2 and made up the C-terminal

element of the C11orf95-RELA^{Fus1} peptide. Two variants of the peptide were generated, one with a C-terminal and one with an N-terminal biotin moiety. C11orf95-RELA^{Fus2} were also synthesized in an N-terminal biotinylated and a C-terminal biotinylated form. Attached to the C-terminal RELA sequence was the sequence encoded by exon 3 of *C11orf95.* The C11orf95^{WT} peptide was prepared as an N-terminal biotinylated peptide, while the synthesised RELA^{WT} peptide harboured a biotin moiety at the C-terminus. A C-terminal biotinylated scrambled peptide was included as a further control (Table 2.9; Figure 2.3A-E).

Table 2.9: Overview of amino acid sequences for each synthetic peptide.

Peptide	Amino acid sequence
C11orf95-RELA^{Fus1}	Glu-Glu-Glu-Glu-Gly-Ala-Gly-Val-Pro-Ala-Cys-Pro-Pro-Lys-Gly-Pro-Glu-Leu-Phe-Pro-Leu-Ile-Phe-Pro-Ala-Glu-Pro-Ala-Gln-Ala-Ser-Gly-Pro
C11orf95-RELA^{Fus2}	Trp-Gly-Gly-Gln-Pro-Glu-Ala-Leu-Ser-Glu-Leu-Thr-Gln-Ser-Pro-Pro-Glu-Leu-Phe-Pro-Leu-Ile-Phe-Pro-Ala-Glu-Pro-Ala-Gln-Ala-Ser-Gly-Pro
C11orf95^{WT}	Glu-Glu-Glu-Glu-Gly-Ala-Gly-Val-Pro-Ala-Cys-Pro-Pro-Lys-Gly-Pro-Gly-Lys-Ala-Pro-Ala-Gly
RELA^{WT}	Met-Asp-Glu-Leu-Phe-Pro-Leu-Ile-Phe-Pro-Ala-Glu-Pro-Ala-Gln-Ala-Ser-Gly-Pro
Scrambled	Phe-Ala-Ala-Cys-Pro-Ala-Glu-Pro-Val-Ala-Glu-Pro-Leu-Gly-Ala-Glu-Ser-Pro-Phe-Gly-Pro-Leu-Pro-Gln-Gly-Ile-Pro-Gly-Pro-Glu-Lys

Glu- Glutamate; Gly- Glycine; Ala- Alanine; Val- Valine; Pro-Proline; Cys- Cysteine; Lys- Lysine; Leu- Leucin; Phe- Phenylalanine; Ile- Isoleucine; Gln- Glutamine; Trp- Tryptophan; Ser- Serine; Thr- Threonine; Met- Methionine; Asp- Asparagine

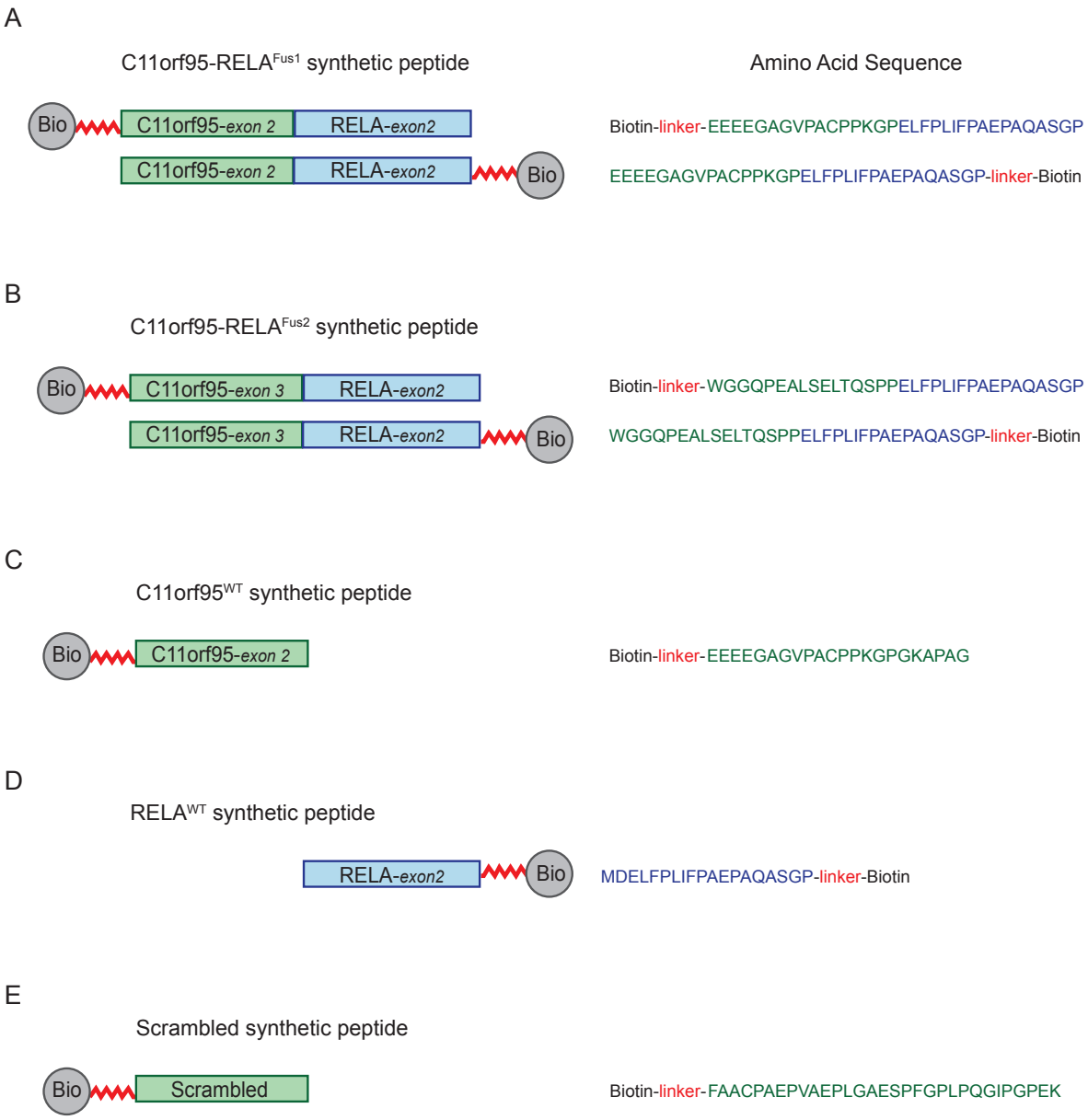

Figure 2.3: Structures and amino acid sequences of synthetic peptides used for phage display, binding assays and ribosome display. A. Synthetic peptides for C11orf95-RELA^{FUS1} with biotin moieties either at the N-terminal or C-terminal end. **B.** Synthetic peptides for C11orf95-RELA^{FUS2} with biotin moieties either at the N-terminal or C-terminal end. **C.** Synthetic peptide for C11orf95^{WT} with a biotinylated N-terminus. **D.** Synthetic peptide for RELA^{WT} with a biotinylated C-terminus. **E.** Synthetic scrambled peptide harbouring a biotin moiety at the N-terminus.

2.3.5.2. Phage display and selection of single chain variable fragments

Phage display selections of scFvs was carried out by AAL as described previously[205,206]. In brief, five naive libraries (nFL, DP47, CS, BMV and EG3) were used to select fragments binding to antigen of interest. ScFvs had been cloned into a phagemid vector based on phage M13 and therefore allowing scFvs to be presented on a phage's surface. Biotinylated peptides described in 2.3.5.1 were used to select for scFv antibodies. Four rounds of selections were carried out changing between C-terminal and N-terminal biotinylated peptides for C11orf95-RELA^{Fus1} or C11orf95-RELA^{Fus2}. Bound scFv fragments were captured using streptavidin-coupled paramagnetic beads, taken through PBST wash cycles to remove non-specific binders and subsequently eluted from beads using Trypsin. *E. coli* TG1 bacteria were infected with eluted phages, which were harvested and used for the following selection round. With each subsequent cycle, the concentration of the antigen was decreased two-fold using a starting concentration of 100nM. Furthermore, N-terminus and C-terminus biotinylated peptides were used interchangeably between the different rounds. To remove binders to peptides of RELA^{WT} and C11orf^{WT}, selection cycles were carried out as described above with WT peptides as well as the bio-scrambled peptide. Fragments bound to beads were discarded and excluded from following selections.

2.3.5.3. Conversion of single chain variable fragments into mature monoclonal immunoglobulins

Reformatting of scFv sequences to mature IgGs was performed by AAL as described previously[207]. Human variable light and heavy chains were cloned into respective vectors encoding whole rabbit constant regions of the light and heavy chains in order to generate hybrid light and heavy chains with human variable domains and constant rabbit domains. Using the ExpiCHO expression system, vectors were transfected into Chinese Hamster Ovary (CHO) cells, which expressed and secreted immunoglobulins into the media. Media was harvested and IgGs purified using a Protein A column. Elution was accomplished using sodium citrate buffer and concentrations were measure spectrophotometrically after a buffer exchange into PBS.

2.3.5.4. Homogenous time-resolved fluorescence binding screens

Homogenous time-resolved fluorescence (HTRF) binding assays were performed by AAL. In brief, binding of selected structures peptides of C11orf95-RELA^{Fus1}, C11orf95-RELA^{Fus2}, C11orf95^{WT} and RELA^{WT} was tested. Testing was done with c-myc tagged unpurified scFvs or purified scFvs and matured IgGs. For c-myc-tagged scFvs, fluorescence resonance energy transfer (FRET) was measured between the tagged scFvs, anti-c-myc detection reagents and the biotinylated peptide that was captured by a streptavidin cryptate. For IgGs, FRET was measured between the europium cryptate labelled streptavidin binding to the biotinylated peptide and an Alexa Fluor 647 labelled anti-rabbit Fc antibody. Assays were performed in black 384-well shallow-well in assay buffer containing PBS and 0.1% BSA under addition of respective clones, anti-c-myc or anti-rabbit IgG and one of the following peptides: C11orf95-RELA^{Fus1}, C11orf95-RELA^{Fus2}, RELA^{WT} or C11orf95^{WT}. Plates were read on a PheraStar plate reader (PerkinElmer, USA) measuring emission at 620nm and 665nm using an excitation wavelength of 320nm. Data was analysed as follows:

$$\%\ \text{Delta F} = \frac{(\text{sample 665nm / 620nm ratio}) - (\text{negative control 665 nm / 620 nm ratio})}{(\text{negative control 665 nm / 620 nm ratio})} \times 100$$

Values for % Delta F determined if clones were binders (>50) or non-binders (<50). Furthermore, only clones binding to C11orf95-RELA^{Fus1} or C11orf95-RELA^{Fus2} but not C11orf95^{WT} or RELA^{WT} were considered binders.

2.3.5.5. Affinity maturation via ribosome display

Ribosome display for affinity maturation was carried out together at AAL and was performed as described previously[208]. In short, parental clones C0040034 (IgG90) and C0040036 (IgG81) were subjected to random error prone mutagenesis to create library of sequences harbouring small changes in comparison to parental sequences. Error prone PCR using a Taq polymerase that induced an average of four changes into the sequence per PCR was performed twice by Denice Chan, thereby yielding a net mutation rate of ~8 per scFv. Libraries of new DNA sequences for variable light and heavy chains of the scFvs were first recombined to combine potential beneficial

mutations and create a larger output selection. Following cycles of PCR amplification and recombination of VH and VL domains into scFvs, their DNA sequences were then transcribed into mRNA. DNA at 50ng/µl was transcribed from the T7 promoter of the library construct using a RiboMax large scale RNA production system for 2-2.5h at 37°C. Following RNA purification, mRNA was amplified in PCRs followed by translation utilizing the *E. coli* S30 translation system. Translation was stalled to generate stable mRNA-ribosome-scFv complexes, that were incubated with biotinylated C11orf95-RELA^{Fus1} peptide overnight at 4°C. Bound complexes were captured using streptavidin-coated magnetic beads and non-binders were removed through various washing cycles. After complex-dissociation, mRNA was resuspended in water, followed reverse transcription PCR (RT-PCR) for conversion of mRNA to DNA. The DNA output was then used for another round of ribosome display. In total, five rounds of affinity maturation were performed, each with a lower concentration of the antigen starting with 60nM and finishing with 0.3nM. Antigens used each round were alternated between N-terminal biotinylated and C-terminal biotinylated peptides.

2.3.5.6. Epitope competition assay

ScFv selections were infected into *E. coli* to generate unpurified scFvs. These unpurified scFvs were then tested towards their affinity for the C11orf95-RELA^{Fus1} epitope by competing with parental clones C0040034 (IgG90) and C0040036 (IgG81). The HTRF assay was used to measure FRET between the biotin-binding streptavidin cryptate and the Alexa Fluor 647 anti-rabbit bound to parental clones. Reduction of FRET in presence of an scFv was an assumed result of successful occupation of the epitope by the scFv. Percentage % F values were calculated as described in 2.3.5.4 and subsequently normalised as follows:

$$\text{Normalised data (\% Control)} = \frac{\text{\% Delta F of sample}}{\text{\% Delta F of Maximum binding control}} \times 100$$

Successful candidates displaying a significant reduction that further exhibited a unique DNA sequence were amplified using *E. coli* followed by purification as described in 2.3.5.2. Purified scFv were subjected to several rounds of competition assays, testing a range of concentrations and calculating the respective normalised values.

2.4. Results

2.4.1. Phage display selections identify candidate C11orf95-RELA^{Fus1}-specific single chain variable fragments

Screening of phage display outputs utilised peptides harbouring epitopes spanning the fusion points of C11orf95 and RELA of C11orf95-RELA^{Fus1} and C11orf95-RELA^{Fus2}, that were generated by the AAL, on the basis of previously published sequences (see Table 2.9) [40]. Biotinylated peptides for wildtype proteins such as RELA^{WT} and C11orf95^{WT} and scrambled protein were further generated to serve as screening controls (Figure 2.3). Screening of phage-display selection outputs from each of the five naïve libraries was undertaken by AAL to test for binding against epitope regions of fusion proteins C11orf95-RELA^{Fus1} and C11orf95-RELA^{Fus2}. ScFv hits from phage display were screened in HTRF assays in multiple rounds towards their binding affinity. Using HTRF screens, C11orf95-RELA^{Fus1}-specific scFvs were classified as binders and provided by AAL. I tested these candidates in molecular assays using mouse ependymoma cell lines as described in 2.4.1.1.

2.4.1.1. Crude scFv fail to recognize C11orf95-RELA^{Fus1} protein in immunoblot assays and require conversion to monoclonal IgGs

Our lab has previously shown that the C11orf95-RELA^{Fus1} protein can be detected in immunoblot assays using NF-κB p65-specific antibodies[40]. Differences in the molecular weight of RELA^{WT} protein (~65kDa) and the C11orf95-RELA^{Fus1} protein (~100kDa) allows the proteins to be resolved by immunoblotting. In the context of antibody development, others have shown that scFv, which harbour the epitope binding side of an antibody, can recognize target proteins in immunoblot assays[209]. Hence, I wanted to investigate if the scFv hits from the phage display library and HTRF screens are able to recognize the fusion protein in immunoblots. This would allow us to triage candidate single chain clones and therefore reduce the numbers of sequences to be matured into IgGs. Thus, 28 scFv hits selected for immunoblot analysis were provided by AAL (see Table 2.4 for list of all scFvs). Besides the C11orf95-RELA^{Fus1}-targeting fragments, AAL further supplied the scFv CEA6, which binds to an unrelated target and served as a negative control (Table 2.4). As all scFvs

were fused to a His-tag, an anti-His-tag IRDye680 secondary antibody was also supplied by AAL to be used for detection of scFvs applied as primary antibodies in immunoblot assays. This anti-His antibody reliably detected to the scFv CEA6 in immunoblot assays, thereby confirming that it could be used to detect the scFvs by AAL (data not shown).

Following this, a commercial NF-κB p65 antibody was used to confirm that expression of C11orf95-RELA^{Fus1} could be detected in lysates of mNSCs that overexpress human C11orf95-RELA^{Fus1} (mSEP-CR[+]) but could not be detected in mNSCs cells overexpressing human RTBDN (mSEP-CR[-]^{RTBDN}) (Figure 2.4A). While endogenous RELA is detected in both samples at a molecular height of ~65kDa, translated C11orf95-RELA^{Fus1} proteins were only detectable in the mSEP-CR(+) sample where it ran at a molecular weight of ~100kDa in accordance with previous results[40]. Following this, the ability of the His-tag-targeting secondary antibody to accurately detect His was tested on His-protein and mSEP-CR(+) lysates. Figure 2.4B shows that, while this antibody does recognize the His-protein, it also recognizes an unspecific band in mSEP-CR(+) cells at a height of ~60kDa (black arrow). This band does not correspond to neither RELA^{WT} (~65kDa) nor C11orf95-RELA^{Fus1} (~100kDa).

All scFvs were subsequently tested in immunoblots of lysates of mSEP-CR(+) cells. None of the 28 C11orf95-RELA^{Fus1}-targeting scFvs detected the target protein in immunoblot assays, but all blots displayed the unspecific bands resulting from secondary antibody incubation (Figure 2.4C). These bands are detectable at a molecular weight of ~60kDa following and since this does not match the size of either RELA^{WT}, nor C11orf95-RELA^{Fus}, it appeared like the scFvs did not bind to C11orf95-RELA^{Fus1} in these assays. Hence, this approach could not determine which scFvs to prioritize for IgG production.

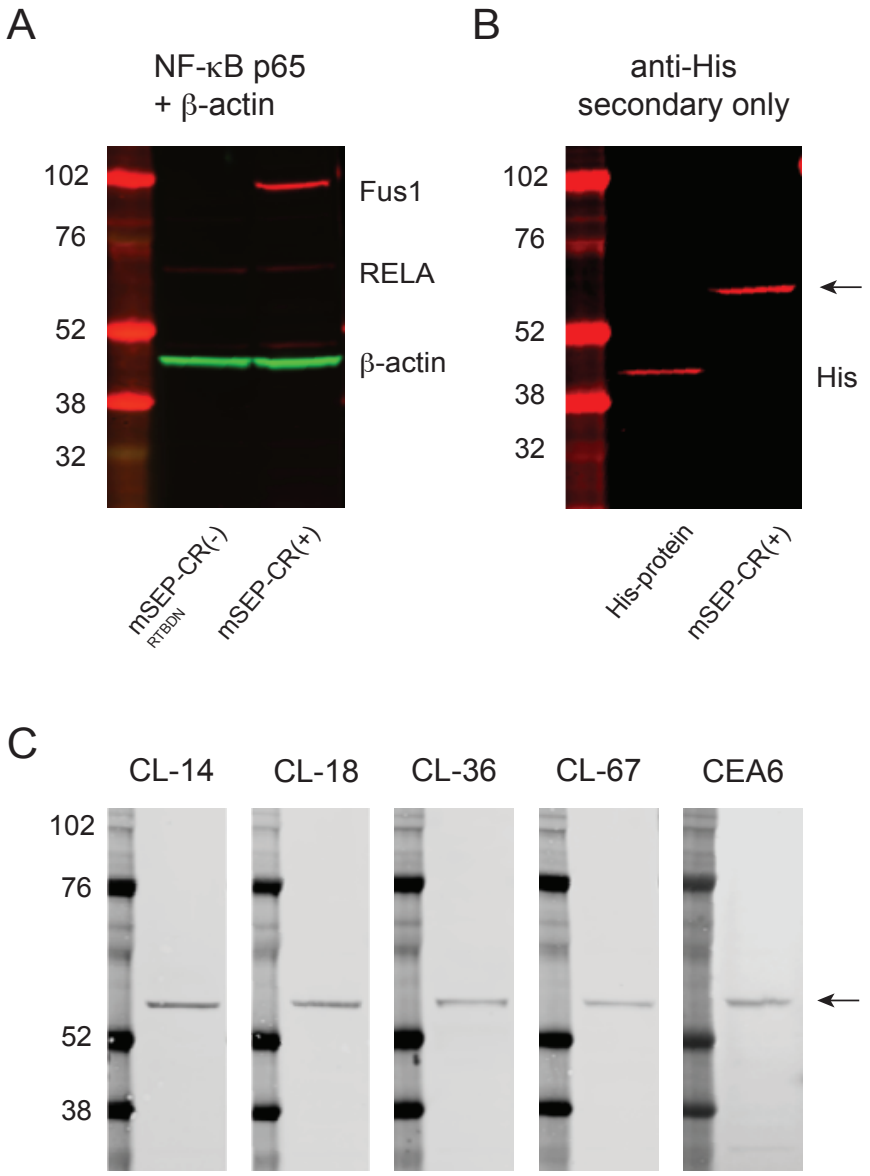

Figure 2.4: Screening of scFv candidate for C11orf95-RELA^{Fus1} recognition in immunoblot assays. A. Immunoblot analysis of C11orf95-RELA^{Fus1} protein in mSEP-CR(+) and mSEP-CR(-)^{RTBDN} lysates using an NF-κB p65 antibody. **B.** Immunoblot analysis of anti-His protein secondary antibody on His-protein and mSEP-CR(+) detects an unspecific band in mouse cell lysate. **C.** Representative images of single chain variable fragments tested in immunoblot assays on whole cell lysates of mSEP-CR(+) cells to investigate their binding of C11orf95-RELA^{Fus1}. Black arrows indicate unspecific bands produced by secondary antibody.

2.4.1.2. Immunoblot analysis identifies lead monoclonal antibodies against C11orf95-RELA^{Fus1} proteins

As previous efforts to triage scFvs candidates via immunoblot assay screening had not been successful, the majority of the crude scFvs were reformatted into monoclonal rabbit antibodies by AAL. In order to achieve this, variable heavy chain (VH) and variable light chain (VL) were subcloned into vectors encoding whole rabbit heavy and light chains to transform candidate scFvs into monoclonal rabbit IgGs. After additional rounds of HTRF binding assays, 25 different C11orf95-RELA^{Fus1}-targeting IgGs were supplied by AAL to be tested in immunoblot assays (see Table 2.5 for list of all 25 IgGs).

Initially, all clones were tested on whole cell lysates of mSEP-CR(+) cells to investigate their ability to bind to C11orf95-RELA^{Fus1}. Most of the antibodies produced multiple bands ranging from 30-150kDa on membranes with mSEP-CR(+) lysates. However, six out of 25 clones (IgG76, IgG79, IgG81, IgG90, IgG96 and IgG101) produced a band at a molecular weight of ~100kDa, lining up with the fusion band as detected in control blots incubated with NF-κB p65 antibody (Figure 2.5A). While IgGs -76, -79, -81, -96 and -101 produced faint bands, membranes stained with IgGs81 and -90 presented prominent bands as indicated by black arrow heads. The six candidate IgGs were taken forward, while the remaining 19 IgGs were excluded from further assays due to their failure to produce a band (data not shown).

To investigate the selectivity of these IgGs towards C11orf95-RELA^{Fus1}, additional immunoblot assays included lysates of a fusion-negative control cell line (mSEP-CR[-]^{RTBDN}). Stained membranes of lysates for mSEP-CR(+) and mSEP-CR(-)^{RTBDN} cells revealed that candidate IgGs produced the bands at a molecular weight of ~100kDa as previously detected in lysates of mSEP-CR(+) also in lysates of mSEP-CR(-)^{RTBDN}. Overlay of membranes stained for IgG81 or IgG90 and membranes incubated with control NF-κB p65 antibody revealed an overlap of bands of interests (Figure 2.5 B&C). On the basis of the results from the overlap analysis, which suggest that the antibodies might be binding to C11orf95-RELA^{Fus1}, six lead antibodies (IgG76, Ig079, IgG81, IgG90, IgG96 and IgG101) were selected to be used in IHC assays using mouse tumour tissues of the respective cell lines.

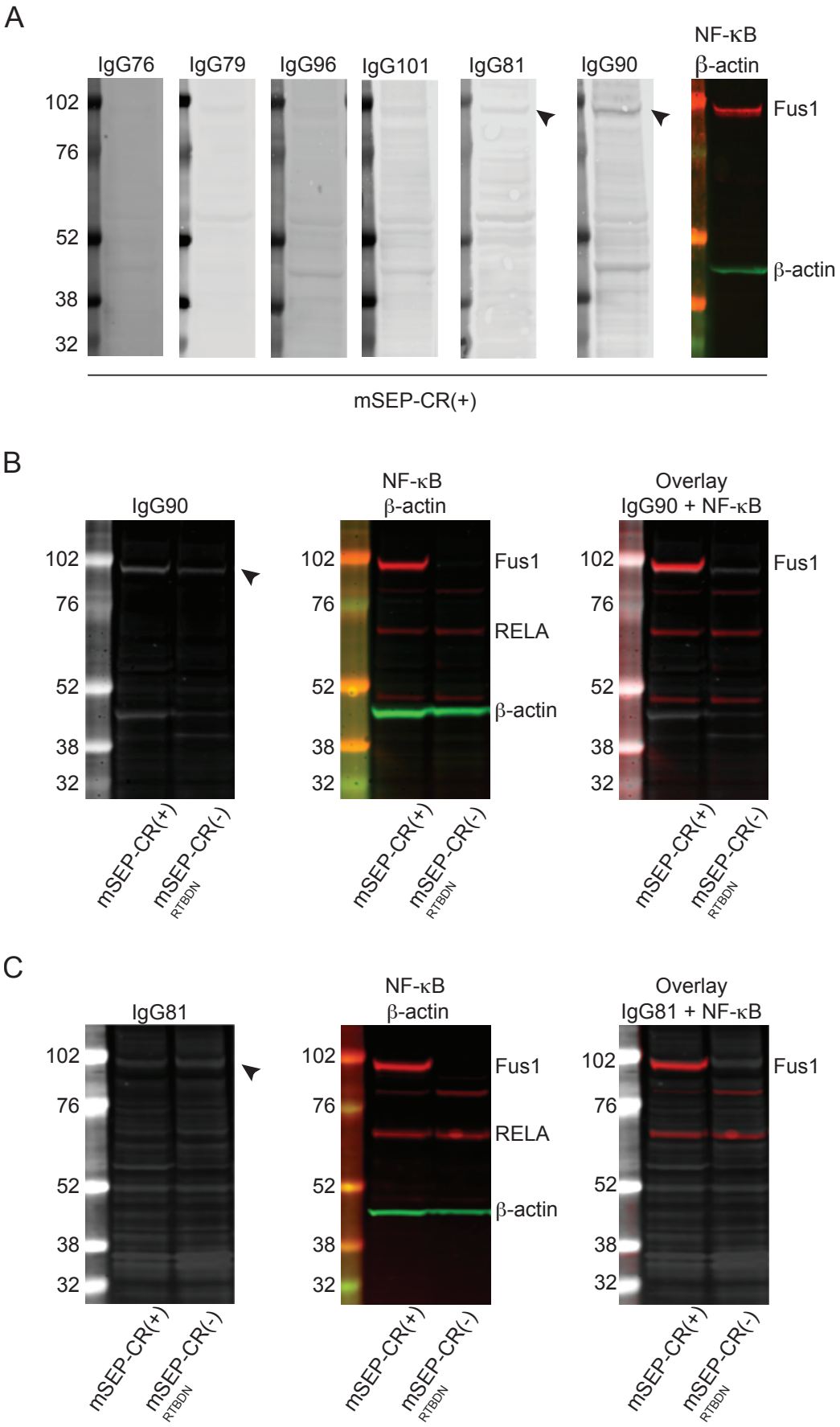
A
IgG76
IgG79
IgG96
IgG101
IgG81
IgG90
NF-κB
β-actin
102
76
52
38
32
Fus1
β-actin
mSEP-CR(+)
B
IgG90
NF-κB
β-actin
Overlay
IgG90 + NF-κB
102
76
52
38
32
Fus1
RELA
β-actin
mSEP-CR(+)
mSEP-CR(-)
RTBDN
C
IgG81
NF-κB
β-actin
Overlay
IgG81 + NF-κB

Figure 2.5: Immunoblot analysis of reformatted C11orf95-RELA^{Fus1}-targeting IgGs. A. Representative images of immunoblot analysis of selected immunoglobulins, which detect C11orf95-RELA^{Fus1} in whole cell lysates of mSEP-CR(+) (n=1). **B+C**. Immunoblot analysis of IgG90 and IgG81 on whole cell lysates of mSEP-CR(+) and mSEP-CR(-)^{RTBDN} reveals that candidate antibodies also produce band at height of C11orf95-RELA^{Fus1} protein mSEP-CR(-)^{RTBDN} cells. Control immunoblot stained with NF-κB p65 antibody confirm expression of C11orf95-RELA^{Fus1} only in lysates of mSEP-CR(+). Overlay of membranes stained with candidate and control antibodies demonstrate co-localization of bands of NF-κB and IgG81 or IgG90 (n=3).

2.4.1.3. Testing C11orf95-RELA^{Fus1}-specific IgGs in immunohistochemistry analysis reveals candidate IgGs for affinity maturation

Results from immunoblot analyses of IgGs targeting C11orf95-RELA^{Fus1} indicated that six IgGs (IgG76, Ig079, IgG81, IgG90, IgG96 and IgG101) were binding to the fusion protein. To test their binding specificity in IHC, they were used in IHC assays of sections from mouse supratentorial ependymoma tissues generated via orthotopic implants of mSEP-CR(+) or mSEP-CR(-)^{RTBDN} cells. In 2014, our lab demonstrated that C11orf95-RELA^{Fus} spontaneously translocates to the nucleus and is therefore mostly located in the nuclei of the tumour cells[40]. Staining of mouse and human supratentorial ependymoma tissue for activated NF-κB p65 (p-RELA^{SER276}) corroborated this finding. These tissues presented a distinct nuclear staining pattern in fusion-positive tissue sections compared to a negative nuclear staining in fusion-negative tissue sections[40]. Hence, we hypothesized that fusion-positive tissues would present a nuclear staining pattern when stained with candidate IgGs.

In order to test the binding potential of the candidate antibodies, tissue sections of mouse brains harbouring tumours of mSEP-CR(+) and mSEP-CR(-)^{RTBDN} cells were stained with the six candidate antibodies. Following an optimisation for epitope retrieval with IgG90, all six antibodies were tested at different dilutions (1:100, 1:500, 1:1000) in a combination with heat-induced epitope-retrieval using Tris-EDTA (TE) buffer to ensure that any potential signal of the antibodies would be detected. An NF-κB p65 antibody from Cell Signaling Technology served as a control antibody.

Neither of the antibodies produced any nuclear staining on fusion-negative mSEP-CR(-)^{RTBDN} tissue. On mSEP-CR(+) tissue, only IgG81 and IgG90 produced a nuclear staining pattern that matched the NF-κB control staining (Figure 2.6). Despite efforts to eradicate background staining by applying different antigen-retrieval methods and higher dilutions, distinct staining patterns were only detectable at lower dilutions of the antibodies, which also resulted in higher background staining. We therefore selected IgG81 and IgG90 to undergo an affinity maturation process in order to enhance binding specificity and affinity of the clones.

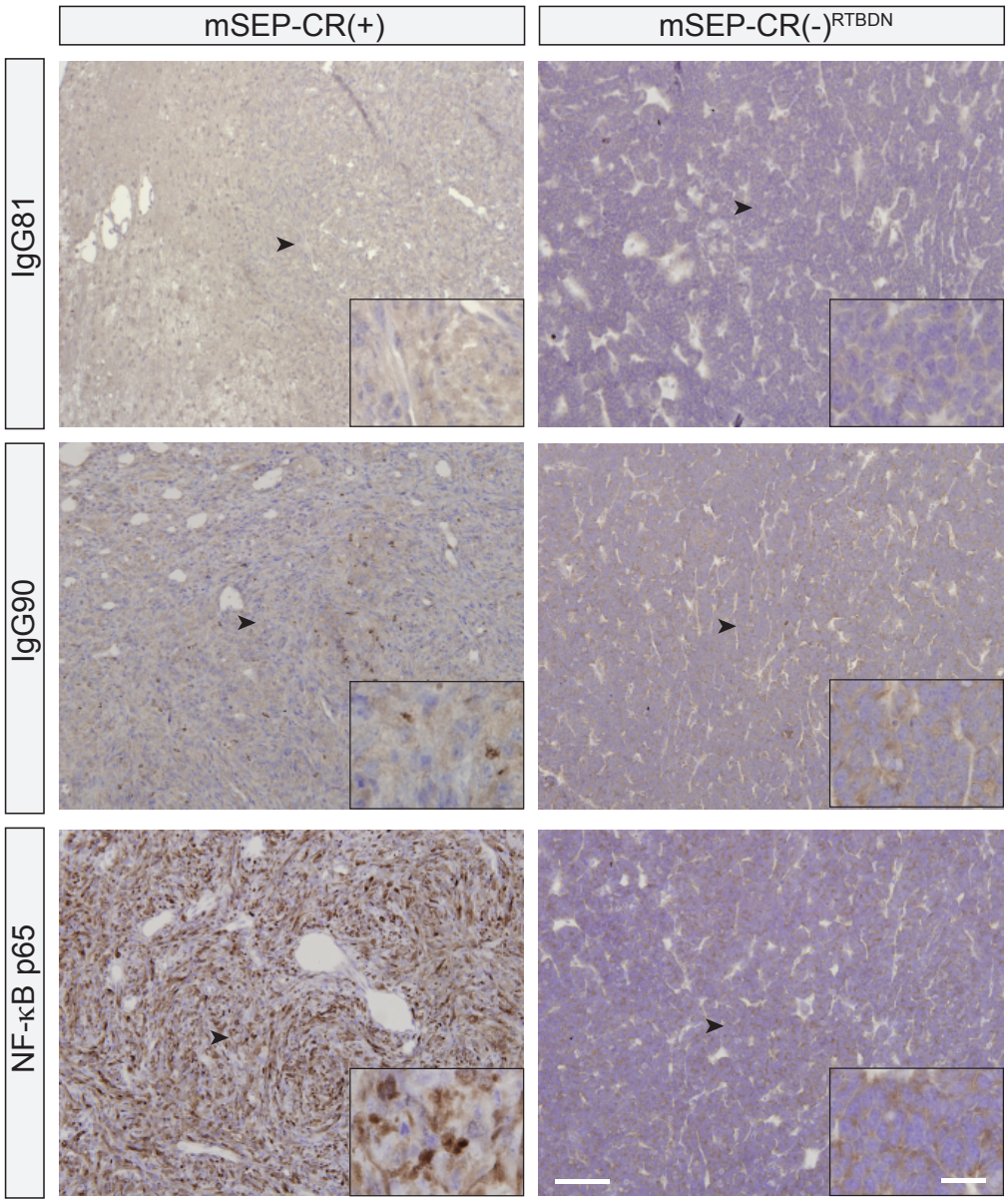

Figure 2.6: Immunohistochemistry analysis of lead C11orf95-RELA^{Fus1}-targeting IgGs on mouse supratentorial ependymoma tissue. Representative images of tissue sections of mSEP-CR(+) and mSEP-CR(-)^{RTBDN} stained with IgG81, IgG90 and control NF-κB p65 antibody post Tris-EDTA-epitope retrieval. All three antibodies present fusion-specific nuclear staining patterns in mSEP-CR(+) sections and display clear nuclei on fusion-negative mSEP-CR(-)^{RTBDN} tissues (n=3). (Large images= x10, small inserts images= 40x. Scale bars=100µm and 20µm, respectively.)

2.4.1.4. C11orf95-RELA^{Fus2}-targeting antibodies do not appear to be binding to C11orf95-RELA^{Fus2} according to immunoblot analysis

In addition to C11orf95-RELA^{Fus1}-targeting antibodies, AAL had also produced monoclonal IgGs that displayed binding affinities to C11orf95-RELA^{Fus2} in HTRF binding assays. Most of them additionally seemed to cross-react with C11orf95-RELA^{Fus1}. Hence, these were also tested in immunoblot to assess their binding affinity to the two most common C11orf95-RELA fusion variants.

In total, 20 monoclonal IgGs were provided by AAL (see Table 2.6 for list of all 20 antibodies). First, a cell line stably overexpressing C11orf95-RELA^{Fus2} had to be generated. However, attempts to produce *Ink4a/Arf*$^{-/-}$ mouse neural stem (Ink$^{-/-}$) cells that stably overexpress C11orf95-RELA^{Fus2} was unsuccessful. While transduction with C11orf95-RELA$^{Fus2\text{-}GFP}$-encoding retroviruses seemed successful 24h post-infection, the cells did not survive long enough to achieve cell numbers required for collection and subsequent use in immunoblot assays (data not shown).

In our lab, we had previously observed that overexpression seemed to be toxic to a range of cells but it appeared to be tolerated in HeLa cells. Thus, I infected HeLa cells with a C11orf95-RELA^{Fus2} encoding lentivirus and confirmed infection by fluorescence microscopy and by immunoblot analysis (Figure 2.7A&B) blotting with an NF-κB p65 antibody. Most of the C11orf95-RELA^{Fus2}-targeting antibodies further seemed to cross-react with C11orf95-RELA^{Fus1} in peptide HTRF screens. Therefore, all antibodies were tested on whole cell lysates of HeLa ^{Fus2} and mSEP-CR(+) cells in immunoblots (Fig. 2.7B&C).

Out of 20 IgGs, two IgGs (IgG141 and IgG142) produced two bands in lysates of both cell lines at heights that seemed to match both proteins, C11orf95-RELA^{Fus1} and C11orf95-RELA^{Fus2}. Overlaid images of membranes for HeLa^{Fus2} whole cell lysates stained with either IgG141 or IgG142 and NF-κB p65, did not confirm the proposed overlay of bands as there appeared to be a slight difference in heights between the bands (Figure 2.7B). Overlay images of membranes with mSEP-CR(+) whole cell lysates suggest that there is an overlay between the lower band produced by both, IgG141 and IgG142, and the band for the C11orf95-RELA^{Fus1} protein detected by the NF-κB p65 antibody (Figure 2.7C).

IgGs141 and 142 were not pursued in their proposed binding affinity towards C11orf95-RELA^{Fus1} as we had already chosen two strong candidates for affinity maturation.

We were further unable to test them on tumour tissue positive for C11orf95-RELA^{Fus2}, as all efforts to generate supratentorial ependymoma tumours driven by C11orf95-RELA^{Fus2} *in vivo* had failed (data not shown).

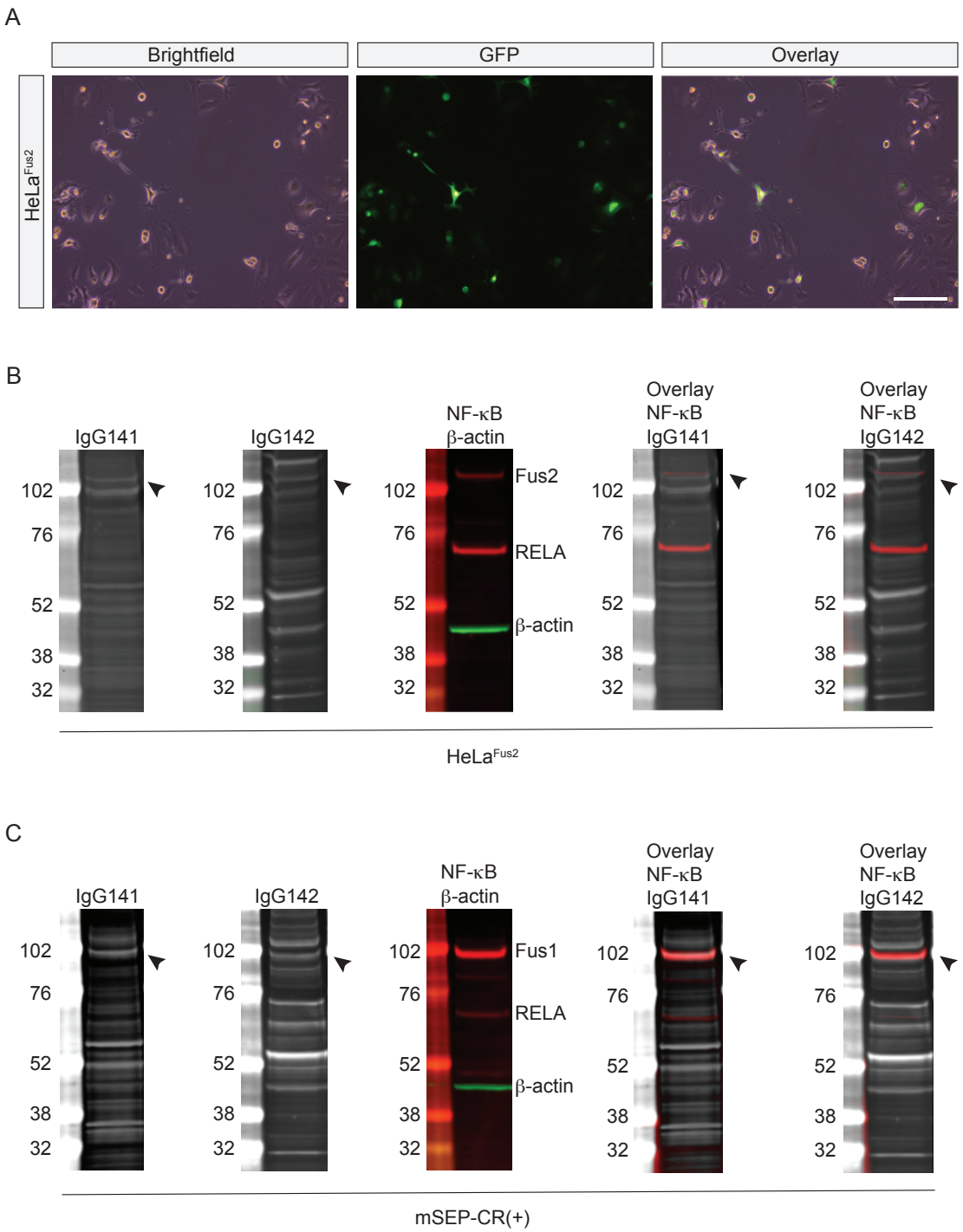

Figure 2.7: Immunoblot analysis of C11orf95-RELA^{Fus2}-targeting IgGs. A. HeLa cells transduced with C11orf95-RELA$^{Fus2\text{-}GFP}$ encoding lentivirus. Fluorescence imaging confirms expression of C11orf95-RELA^{Fus2}. **B.** Immunoblot analysis of IgG141 and IgG142 on whole cell lysates of HeLa^{Fus2} cells. Overlay of NF-κB and 141, or 142 stained membranes does not confirm overlay of bands. **C.** Immunoblot analysis of IgG141 and IgG142 on whole cell lysates of mSEP-CR(+) cells. Overlay of NF-κB and IgG141-, or IgG142-stained membranes suggests overlay of bands. Scale bar=100µm.

2.4.2. Affinity maturation of lead parental clones using ribosome display

Affinity maturation of antibodies via ribosome display has been reported as an efficient approach to optimise the binding affinity of scFvs and thereby generate more efficient antibodies[182]. Previous results of immunoblot and IHC analysis suggested that two of our C11orf95-RELA^{Fus1}-targeting antibodies were binding our protein of interest. However, despite great optimisation efforts, background staining could not be reduced without also losing the distinct staining pattern produced by our candidate antibodies.

To optimise their binding affinity, parental clones IgG90 (C0040034) and IgG81 (C0040036) were enrolled for affinity maturation via ribosome display. Their scFvs were first subjected to two rounds of error prone PCR in order to create libraries of sequences similar to the parental IgGs but with potentially higher affinities towards the target. Following this, ribosome display technique was utilized to narrow down clones with the highest affinity. Five rounds of ribosome display were completed, each round with a lower concentration of the antigen. Concentrations ranged from 60-0.3nM and ribosome display rounds resulted in a number of novel scFvs with higher affinities towards the fusion-epitope. A series of epitope-competition assays followed, in which the affinity of the clones for the epitope was tested by having them compete with their parental clone for the binding to the C11orf95-RELA^{Fus1} peptide.

2.4.3. Analysis of affinity matured candidate antibodies in a variety of assays determines selection of three lead antibodies

With the intention to increase target affinity of selected candidate antibodies, affinity maturation of the two most promising parent IgGs -81 and -90 was performed. After a final round of epitope competition assays, lead sequences of novel scFvs were selected and reformatted to mature rabbit immunoglobulins. We received these IgGs in order to test them in IHC assays on mouse and human samples as well as in molecular assays to gain more insights into the fusion-specificity of the IgGs.

2.4.3.1. Selected affinity matured antibodies produce distinct staining pattern on mouse tissue in immunohistochemistry assays

Following affinity maturation of parental clones, a total of six affinity matured IgG clones were supplied by AAL (see Table 2.7 for details). Four out of these six were progeny of IgG91 (IgG150, IgG151, IgG153 and IgG154) and two were progeny of IgG81 (IgG159 and IgG161). To test if the increased affinity of the novel clones produces different staining results, all affinity-matured antibodies were tested in IHC assays on tissues of mSEP-CR(+) and mSEP-CR(-)^{RTBDN} tumours.

At first, all antibodies were tested in three different dilutions (1 in 100, 1 in 500 and 1 in 1000) in combination with TE buffer antigen due to prior results. C11orf95-RELA^{Fus}-negative tissues stained with any of the candidate IgGs or the control NF-κB antibody did not display any specific nuclear staining pattern. On fusion-positive mouse tumour tissue, however, staining with IgGs -154 and -151 resulted in a distinct nuclear signal. Furthermore, staining of mSEP-CR(+) tissue with IgG159 also revealed a positive staining pattern, albeit much weaker than the one produced by IgG151 and IgG154 (Figure 2.8). IHC assays conducted with IgGs -150, -153, and -161 did not give any positive staining results on mSEP-CR(+) or mSEP-CR(-)^{RTBDN} tissues (data not shown).

Original dilutions resulted in high background signals and therefore further dilutions were tested and optimized with sodium citrate epitope retrieval for the three candidate antibodies -151, -154 and -159. Figure 2.5 shows representative images of mSEP-CR(+) and mSEP-CR(-)^{RTBDN} tissue stained with optimized dilutions for candidate antibodies. On mouse tissue, optimal dilutions for IgG151 are between 1:4000-1:5500, for IgG154 lie between 1:8000 and 1:9000 and for IgG159 between 1:3000-1:4000 (Figure 2.8).

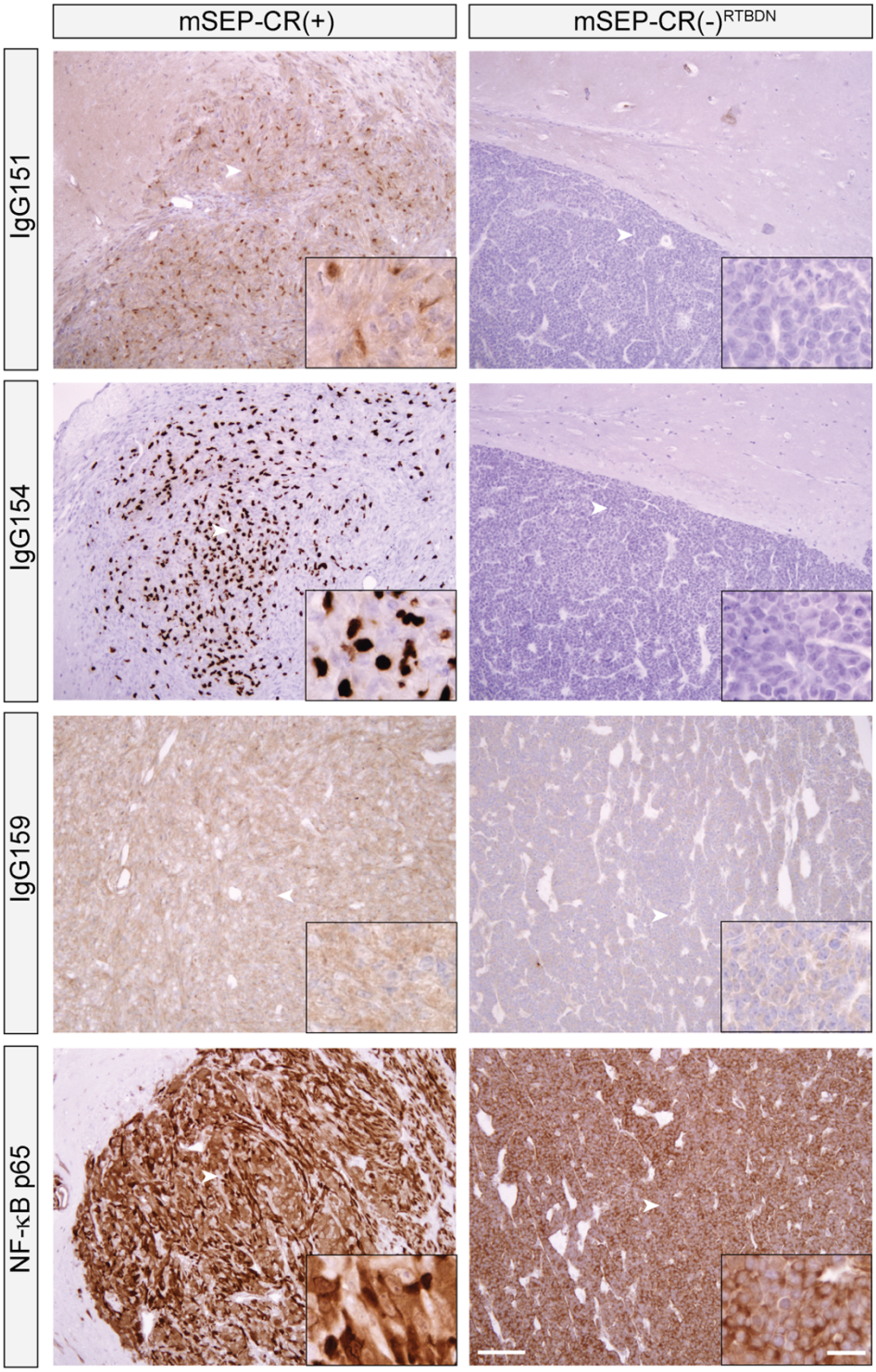

Figure 2.8: Selection of affinity-matured IgGs show nuclear-specific staining pattern on fusion-positive mouse tumour tissues. Representative images of mouse C11orf95-RELAFus1 positive (mSEP-CR[+]) and -negative tissues (mSEP-CR[-]RTBDN) stained with IgGs -151, -154, -159 and CST antibody NF-κB p65 as a control. Antigen retrieval was performed with sodium citrate buffer (n=10). (Large images= x10, small inserts images= 40x. Scale bars=100μm and 20μm, respectively.)

2.4.3.2. Antibody testing in molecular assays demonstrates fusion-specific selectivity of candidate IgGs

To further investigate if the binding of candidate IgGs observed in IHC assays is fusion-specific, molecular assays such as immunoblotting and immunoprecipitations were performed.

Immunoprecipitation (IP) is a method generally used to investigate protein-protein interaction by pulling down protein using targeted antibodies. However, this technique can also be utilized to test binding of antibodies to proteins of interest. For this, the protein of interest is purified through pulldown assays using the protein-specific antibody and proteins captured by candidate antibodies can be detected using immunoblot analysis[204].

First, IgGs -151, -154 and -159 were tested in immunoblot analysis of IPs with an NF-κB p65 antibody. For these, mSEP-CR(+) and human embryonic kidney (HEK) 293 cells overexpressing C11orf95-RELA^{Fus1} (293^{Fus1}) were used for fusion-positive cells and INK$^{-/-}$ mouse neural stem cells (INK) and HEK293 cells overexpressing empty vector (293^{EV}) served as controls. IP on whole cell lysates was performed with the control NF-κB antibody. Captured proteins were detected using immunoblot analysis through staining with candidate IgGs and the NF-κB p65 antibody. Immunoblots of IPs as shown in Figure 2.9 demonstrate that captured fusion proteins were successfully bound by candidate IgGs. All three candidate antibodies produce a band at the height of the fusion protein that co-localizes with the band generated by the p65 antibody. However, Figure 2.9 also shows that in immunoblots of whole cell lysates, IgG151 and IgG154 produce bands for both, fusion-positive and fusion-negative samples. IgG159 also produces bands at the molecular weight of C11orf95-RELA^{Fus1}, albeit much less distinct than the bands produced by IgG151 and IgG154.

Next, we wanted to explore if the antibodies were able to pull down the fusion protein themselves. Since the fusion protein is mainly present in the nucleus, nuclear fractions of mouse ependymoma cell lines were used[210]. Hence, nuclear fractions of mSEP-CR(+), mSEP-CR(-)^{EPHB2} and mSEP-CR(-)^{RTBDN} cells were subjected to IPs with candidate IgGs 151, 154 and 159. Figure 2.10 shows that IPs of candidate IgGs efficiently bind the fusion protein in mSEP-CR(+) cells but do not bind anything in mSEP-CR(-) cells as confirmed by immunoblot analysis with control NF-κB p65 antibody. Immunoblot analysis of nuclear fraction proves that C11orf95-RELA^{Fus1} is only expressed in mSEP-CR(+) cells. However, it also reveals that IgGs appear to be binding a protein of the same molecular weight in mSEP-CR(-)^{EPHB2} and mSEP-CR(-)^{RTBDN} as shown in blots stained with IgG151, IgG154, IgG159 (Figure 2.10).

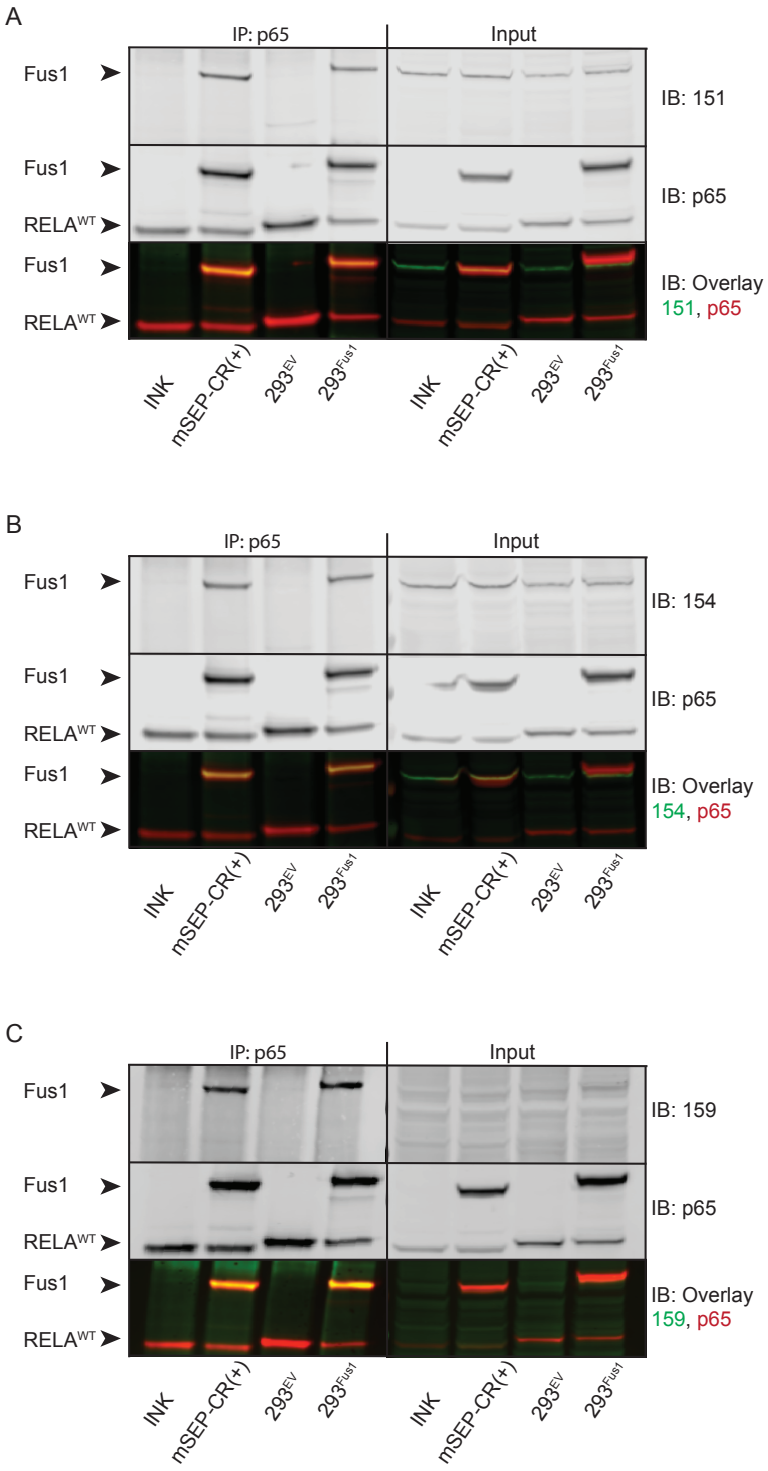

Figure 2.9: Immunoprecipitation and immunoblot analysis of candidate antibodies on mouse and human cell lysates. A-C. IP from whole cell lysates of INK, mSEP-CR(+), 293^{EV}, 293^{Fus1} cells with a commercial NF-κB p65 antibody. **A.** Immunoblot stained with NF-κB and IgG151 confirms expression of C11orf95-$RELA^{Fus1}$ (Fus1) in mSEP-CR(+) and 293^{Fus1} cells. **B.** Immunoblot stained with IgG154 confirms expression of C11orf95-$RELA^{Fus1}$ in mSEP-CR(+) and 293^{Fus1} cells. **C**. Immunoblot stained with NF-κB and IgG159 confirms expression of fusion protein in mSEP-CR(+) and 293^{Fus1} cells. (n=2 replicates for IPs).

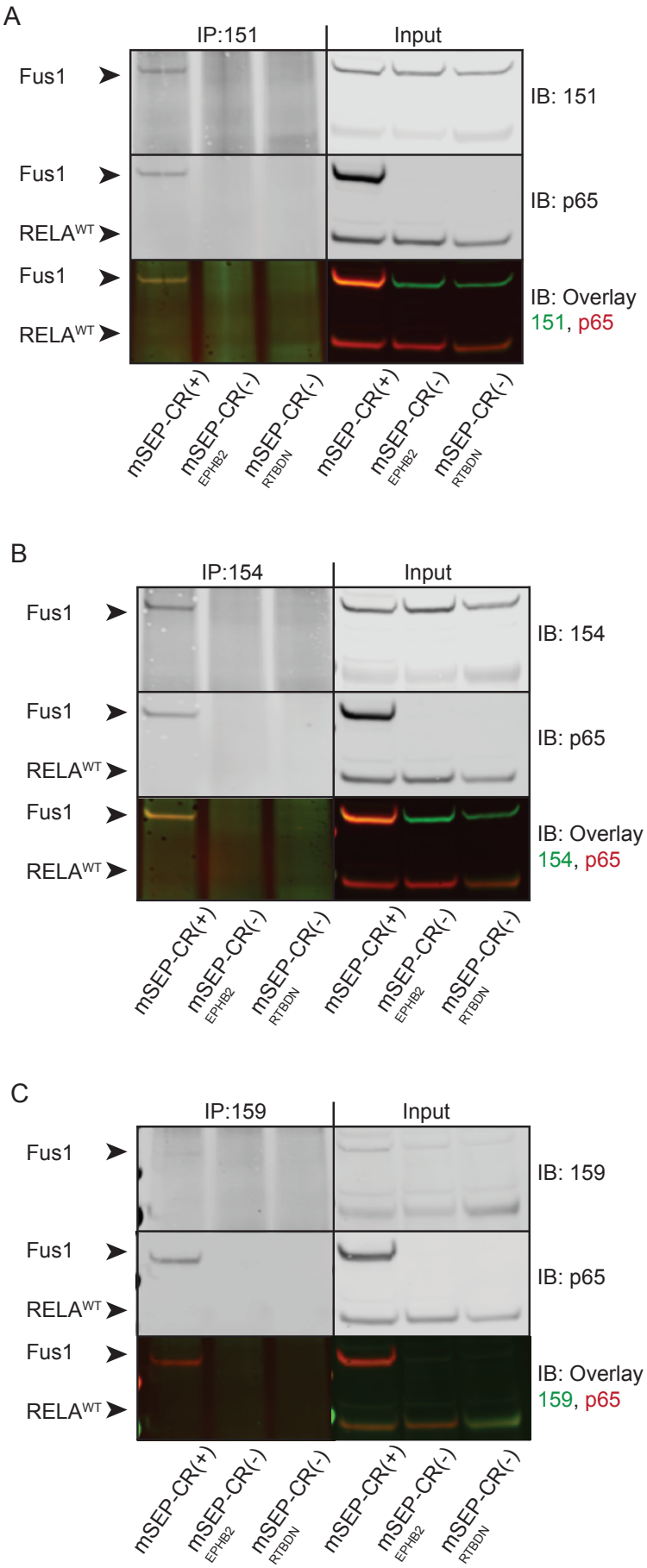
A
IP:151
Input
Fus1
Fus1
RELA^WT
Fus1
RELA^WT
IB: 151
IB: p65
IB: Overlay
151, p65
mSEP-CR(+)
mSEP-CR(-) EPHB2
mSEP-CR(-) RTBDN
mSEP-CR(+)
mSEP-CR(-) EPHB2
mSEP-CR(-) RTBDN
B
IP:154
Input
Fus1
Fus1
RELA^WT
Fus1
RELA^WT
IB: 154
IB: p65
IB: Overlay
154, p65
mSEP-CR(+)
mSEP-CR(-) EPHB2
mSEP-CR(-) RTBDN
mSEP-CR(+)
mSEP-CR(-) EPHB2
mSEP-CR(-) RTBDN
C
IP:159
Input
Fus1
Fus1
RELA^WT
Fus1
RELA^WT
IB: 159
IB: p65
IB: Overlay
159, p65
mSEP-CR(+)
mSEP-CR(-) EPHB2
mSEP-CR(-) RTBDN
mSEP-CR(+)
mSEP-CR(-) EPHB2
mSEP-CR(-) RTBDN

Figure 2.10: Immunoprecipitation and immunoblot analysis of IgG151, 154 and 159 on mouse nuclear fractions. A. IP from nuclear fractions of mSEP-CR(+), mSEP-CR(-)^{EPHB2} and mSEP-CR(-)^{RTBDN} cells with IgG 151. Immunoblot of cell lysates confirms expression of fusion protein in mSEP-CR(+) nuclear fractions. **B.** IgG154-IP from nuclear fractions of mSEP-CR(+), mSEP-CR(-)^{EPHB2} and mSEP-CR(-)^{RTBDN} cells. Immunoblot of cell lysates confirms expression of fusion protein in mSEP-CR(+) nuclear fractions. **C.** IP with IgG159 from nuclear fractions of mSEP-CR(+), mSEP-CR(-)^{EPHB2} and mSEP-CR(-)^{RTBDN} cells. Immunoblot of cell lysates confirms expression of fusion protein in mSEP-CR(+) nuclear fractions.

2.4.4. Immunohistochemistry analysis of lead antibodies on human tissue sections reveals ambiguous staining patterns in fusion-negative ependymoma

Previous IHC analysis of ependymoma mouse tissue sections showed that candidate IgGs produce a distinct nuclear staining pattern in fusion-positive tissues, while nuclei in fusion-negative tissues remain clear. We now wanted to investigate if the same staining patterns can be observed when staining tissues from ependymoma patients.

FFPE sections of human ST-EP and PF-EP were kindly provided by Dr. Ulrich Schüller from UKE Hamburg, Germany. Overall, sections from 13 fusion-positive ST-EP and nine fusion-negative PF-EP patients were used for immunohistochemistry analysis. Validation of fusion status for ependymoma tissues had previously been performed in the lab of Ulrich Schüller. For samples N2875/18 1B, E56/2003 B, E142/05, N13/5 a combination of 850K-methylation assay, FISH and RT-PCR was used to confirm fusion status. RT-PCR was used to confirm fusion-status of samples 3226/17, E300/15 1B, N223/70, E527/06, E117/06, E1014/12 and 94/645. For samples E225/94 and E545/10, IHC was used to validate the fusion-positive status. C11orf95-RELA^{Fus} -negative status in PF-EP tissues had been confirmed via the 850k-methylation assay for all samples except N3430/17. Here, the fusion-negative status had been confirmed via IHC (Table 2.3).

Sections were stained using the three lead antibodies with an NF-κB p65 antibody serving as a control (Figure 2.11, 2.12). Generally, IHC analysis of ST-EP sections revealed positive nuclear staining patterns for all antibodies. Tissues stained with IgG151 displayed the most distinct nuclear staining. IgG154 also produced a visible,

albeit less intense staining pattern. The weakest pattern was generated by IgG159. The amount of positively stained nuclei varied across tissues. Figure 2.11 shows representative images for positively stained ST-EP patient tissues.

PF-EP tissues stained with IgGs presented varying results among the different samples (Figure 2.12). Only one third of PF-EP patient tissues displayed entirely negative nuclei. In two-thirds of the fusion-negative samples, all four antibodies were found to visibly stain nuclei. The left panel of IHC-staining in Figure 2.12 shows representative images from negatively stained tissues. The right panel demonstrates the staining patterns observed in the remaining two-thirds of samples. These display positive nuclei that are stained by all four antibodies – the AAL IgGs as well as the NF-κB control antibody, confirming that the staining pattern is not an effect produced only by our candidate antibodies.

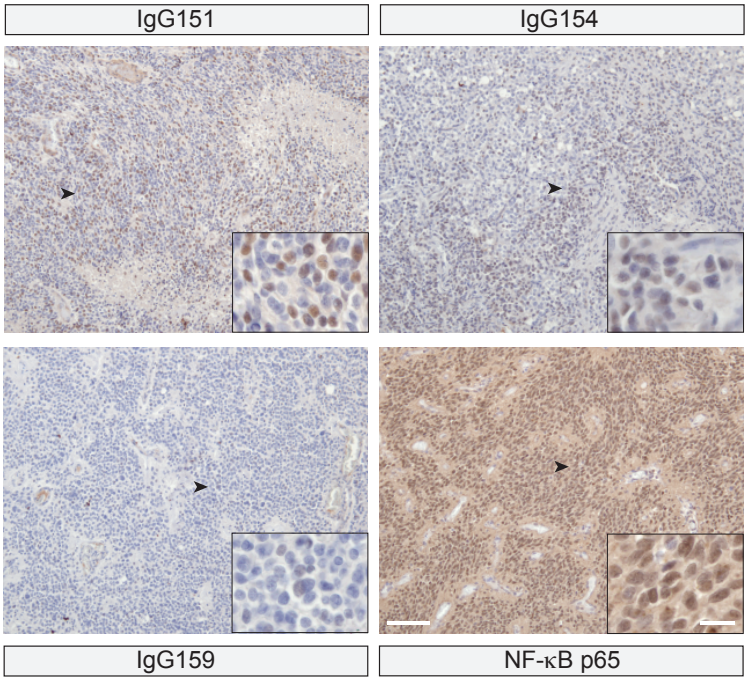

Figure 2.11: Immunohistochemistry analysis of lead antibodies on human supratentorial ependymoma tissues. Representative images of fusion-positive supratentorial patients tissue sections stained positively for fusion and present a distinct nuclear staining pattern. FFPE sections were stained with IgG151, IgG154 and IgG159 after epitope retrieval with sodium citrate buffer. An NF-κB p65 specific antibody served as control. (Large images= x10, small inserts images= 40x. Scale bars=100μm and 20μm, respectively).

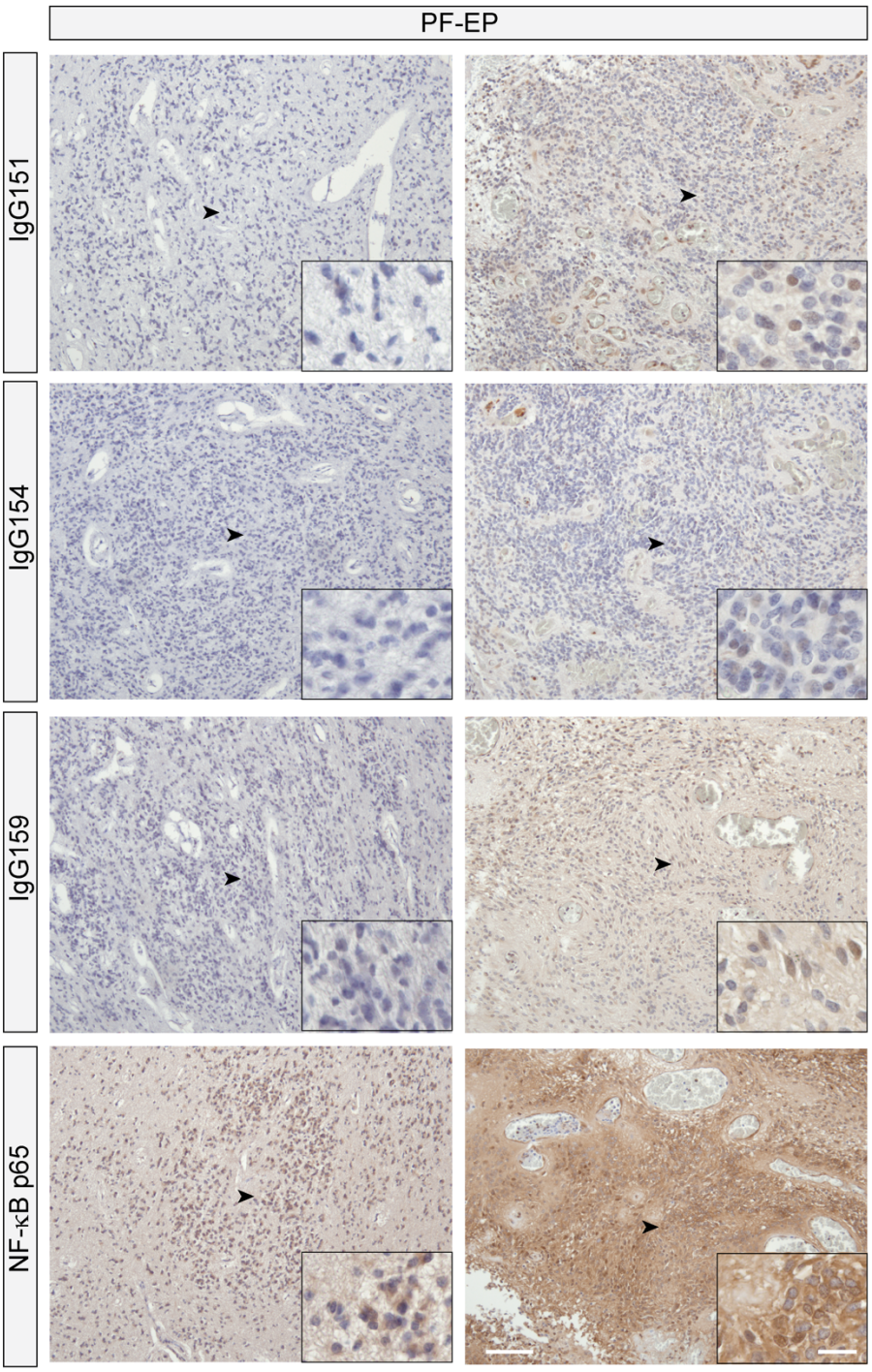

Figure 2.12: Immunohistochemistry analysis of lead antibodies on human posterior fossa ependymoma tissues. Representative images of fusion-negative posterior fossa patients tissue sections. FFPE sections were stained with IgG151, IgG154 and IgG159 post-sodium citrate epitope retrieval. NF-κB p65 specific antibody served as control. Left panel represents one third of tissue sections that present negative nuclei. Right panel presents two thirds of tissue sections, which display positively stained nuclei for all four antibody stains. (Large images= x10, small inserts images= 40x. Scale bars=100μm and 20μm, respectively).

2.5. Discussion

Research efforts have identified several tumour subgroups in a variety of cancers, all of which are characterised by subgroup-specific features. In many cases, subgroups also display differences in their progression or response to therapies[211–213]. Brain tumours in particular are often to be subdivided further into molecular subgroups that are associated with different prognoses[39,102]. Hence, diagnostic antibodies targeting subgroup-specific markers can play a crucial role in the clinical management of a patient.

In ST-EP, over two thirds are characterised by the presence of C11orf95-RELA^{Fus}. As it serves not only as a prognostic but also as a diagnostic marker, the C11orf95-RELA^{Fus}, in particular C11orf95-RELA^{Fus1}, was selected as a target for development of a diagnostic antibody [40,43]. Here, we present the generation of three candidate antibodies targeting C11orf95-RELA^{Fus1}. Our approach was based on phage-display screening and affinity maturing-ribosome display techniques selecting antigen-binding fragments, validated through a range of assays including immunoblotting and IHC[182].

Generally, selection outputs from phage-display assays are commonly tested in high-throughput binding screens and ELISA[182,187]. During antibody validation, matured IgGs are frequently tested in immunofluorescence, IPs or immunoblot analysis, starting with the latter, to confirm their binding affinity[214,215]. Hence, our scFvs targeting C11orf95-RELA^{Fus1} provided by AAL were first tested in immunoblot analysis on fusion-expressing cells (Figure 2.4). All 25 scFvs failed to recognize the fusion protein expressed in mSEP-CR(+) cells.

Although it has been shown before that scFvs can be used as therapeutics or for diagnostic purposes with similar affinities to the matured monoclonal IgG, it has been proposed that fused scFvs display a higher stability and avidity due to multiple binding sites. Developing them further into full immunoglobulins can have a positive effect on their avidity[216–218]. Hence, scFvs were matured into twenty-five rabbit IgGs, which were tested in immunoblot assays again, this time on mSEP-CR(+) and mSEP-CR(-)^{RTBDN} cells (Figure 2.5). Overall, the IgGs seemed to produce numerous bands at various sizes with different intensity. However, six antibodies produced bands at the size of

the fusion protein on both, mSEP-CR(+) and mSEP-CR(-)^{RTBDN} cell lysates. The generation of multiple bands in immunoblots is commonly associated with either cross-reaction of the antibody, protein degradation by proteases or degradation of post-translational modifications (PTMs)[219,220]. We ruled out the latter as immunoblots were performed with freshly prepared samples containing protease inhibitors, thereby reducing the likelihood of protease-mediated degradation. Furthermore, the control antibody did not produce multiple bands rendering degradation of PTMs a less likely explanation for the multiple bands. To further exclude contamination of mSEP-CR(-)^{RTBDN} cells with C11orf95-RELA fusion, end point PCR was performed and confirmed absence of the protein in these cells (data not shown). Nevertheless, the band produced at the size of the fusion protein appeared rather specific, especially for IgG81 or IgG90. Since overlay images of staining for NF-κB p65 and IgGs -81 and -90 suggested a co-localization of bands detected in mSEP-CR(+), six antibodies were chosen to be tested in IHC on tumour tissue generated by implantation of the same cell line.

Staining of tumour sections in IHC assays, revealed that IgG81 and IgG90 produced distinct nuclear staining patterns in mSEP-CR(+) tissue, while stained mSEP-CR(-)^{RTBDN} tissue sections remained negative (Figure 2.6). This nuclear staining pattern in fusion expressing tumours matches the pattern displayed in tissue sections stained with NF-κB antibody but also corresponds to previous findings showing that the C11orf95-RELA fusion spontaneously translocates into the nucleus as demonstrated by Parker *et al.* and Kupp *et al.*[40,210]. Furthermore, staining of fusion-positive patient tissue with antibodies targeting NF-κB p65 or activated NF-κB (p-RELA^{Ser276}) has revealed a nuclei-specific staining pattern[40,72]. The selected IgGs produced a high background in both, mSEP-CR(+) and mSEP-CR(-)^{RTBDN} tissues. It is assumed that background staining in IHC, among other reasons, occurs due to non-specific binding of the antibody as a result of low selectivity or low specificity for the target epitope[221,222]. Various efforts to reduce background staining in our IHC using different approaches failed and high background staining is undesirable for diagnostic antibodies for clinical applications. As a result, the two most promising parent IgGs were chosen to undergo affinity maturation[223,224].

Ribosome display is a technique commonly used to increase affinity of antibodies[187,225–227]. Following five rounds of ribosome display and HTRF competition assays to confirm that selections displayed higher affinities than their parent IgGs, six novel clones were tested in IHC assays of mouse fusion-positive and fusion-negative tissue.

Binding affinity values of clones measured by AAL matched their respective results in IHC (Supplementary Tables 2.10-2.13). Clones -151 and -154, which had demonstrated high affinity towards the target and low affinity towards $RELA^{WT}$, produced very distinct nuclear staining pattern with no or little background staining. While IgG154 displays fusion-specific staining even when used at very high dilutions, IgG151 also generates nuclear staining, although at a lower intensity than IgG154, and has therefore been used at slightly lower dilutions. Both IgGs are derived from the IgG90 parent. C11orf95-$RELA^{Fus}$-positive mouse tissues stained with IgG159, which was derived from IgG81 also exhibited positively-stained nuclei although the staining was much weaker with a higher background. This suggests that the selected candidates can efficiently be applied in IHC assays to confirm presence of C11orf95-$RELA^{Fus1}$ protein on mouse tissue sections (Figure 2.8).

To corroborate these findings on patient tissue, sections from human PF-EP and ST-EP were stained with IgG151, IgG154, IgG159 as well as NF-κB p65 as a control. Upon staining with IgG151, the majority of the 13 fusion-positive ST-EP cases presented with distinct nuclear staining patterns. The staining pattern was comparable to that observed on NF-κB p65-stained sections. Staining with IgG154 resulted in lower numbers of positive nuclei along with no background. Even fewer nuclei were stained by IgG159. These results suggest that for diagnosis on human tissue, IgG151 or IgG154 would be the preferred choice (Figure 2.11).

In contrast, staining of fusion-negative tissue gave inconclusive results. Out of nine patient samples tested, only three were deemed fusion-negative according to staining with any of the antibodies (Figure 2.12). The other six samples stained positively for all four antibodies (including the control NF-κB antibody) with different incidence rates and staining intensities. This could be for a number of reasons. Firstly, NF-κB p65-

positive nuclei can be an indicator of activated RELA in tumour tissue or can confirm the presence of the C11orf95-RELA fusion[40,71,228,229]. Hence, assumed PF-EP-A cases could be fusion-positive rather than fusion-negative. However, the lab of Professor Schüller had confirmed the diagnosis of all but one of the PF-EP-A cases using 850k methylation. This highly sensitive approach has previously been shown to allow distinct clustering of the different ependymoma subgroups[65,150]. It is therefore rather unlikely that these PF-EP cases are in fact misdiagnosed fusion-positive ST-EP cases. Nevertheless, they might still be chance that these have originated as ST-EP and migrated towards the posterior fossa prior to tumour progression. Another possible explanation for the positive staining is that the antibodies are binding to another protein with a similar sequence to our fusion epitope, which is also commonly found in the nucleus.

To gain more insight into the binding of the antibodies, we performed IPs and immunoblot analysis. Here, we could show that, in IPs, IgGs bind solely to the fusion protein. This was confirmed by capturing the fusion protein using the NF-κB control antibody and use the IgGs in subsequent immunoblot analysis and vice versa (Figure 2.9, 2.10). In immunoblots following protein-denaturing SDS-page, candidate IgGs produced bands corresponding to the size of the C11orf95-RELA^{Fus1} protein in both, fusion-negative and fusion-positive cell lysates. The difference between these two techniques is the state of the protein.

In IPs, the protein is in its native state when it is captured by antibodies. Although bound proteins are then separated on a denaturing gel followed by immunoblot analysis, only the captured proteins are present on the blot. For normal immunoblot analysis, the protein is separated from others on a denatured gel and is therefore in its linear form when it is detected. However, as all proteins present in the cells at the point of cell lysis have been blotted on to the membranes and subsequently stained with IgGs, the antibodies can bind sequences occurring anywhere in the protein sequence independent of their location in the folded protein. On the contrary, in IPs, the antibody needs to be able to bind to the protein in its folded state and can consequently only bind to epitopes accessible in the proteins' native state. The sequence, to which the candidate antibodies are binding in normal immunoblots could

therefore be “shielded” when the unknown protein is in its native state. To identify the proteins that could have a similar sequence to the fusion epitope, the online alignment tool for proteins “Protein BLAST” was used[230]. Protein BLAST analysis of the fusion epitope sequence did not generate any useful results as the only sequences found to be aligning with the peptide sequence were sequences from NF-κB p65.

Besides the development of an antibody targeting C11orf95-RELA^{Fus1}, we initially also wanted to explore the potential of C11orf95-RELA^{Fus2}-targeting antibodies. C11orf95-RELA^{Fus2} is the second most common fusion variant and is detectable in ~37% of ST-EP cases[40]. AAL had developed antibodies that bound to C11orf95-RELA^{Fus2} and most of them also appeared to cross-react with C11orf95-RELA^{Fus1} ^{in} binding assays. In immunoblot analysis, these IgGs failed to demonstrate binding to C11orf95-RELA^{Fus2} (Figure 2.7). While two out of 20 IgGs (IgG141, IgG142) seemed to produce bands at the correct sizes for C11orf95-RELA^{Fus1} and C11orf95-RELA^{Fus2}, overlay images of stainings with NF-κB and the respective IgGs did not confirm co-localization of the bands. However, it is generally acknowledged that not all antibodies universally work in all assays but might rather just be applicable in one of them. Hence, I wanted to test the two antibodies on C11orf95-RELA^{Fus2}-positive tissue. Unfortunately, this analysis was not possible as no tumour tissue derived from cells overexpressing C11orf95-RELA^{Fus2} could be generated (data not shown). We therefore did not pursue the development of antibodies raised against C11orf95-RELA^{Fus2} but focused on C11orf95-RELA^{Fus1}-targeting antibodies.

Altogether, I have presented the generation of three promising candidate antibodies specific for C11orf95-RELA^{Fus1}, the most common form of C11orf95-RELA fusion. Their ability to bind to the target epitope has been demonstrated in IP assays in addition to IHC analysis on mouse fusion- positive and -negative tissue. Results of IHC analysis on human ST-EP tissue are promising too. Based on these results, the monoclonal antibodies hold great potential as research tools against the fusion protein.

Future experiments need to focus on the identification of the protein that seems to be bound in immunoblots and in human fusion-negative tissue. A non-denaturing gel could help prove the hypothesis of the shielded epitope of the unknown protein in its folded state. In line with publications about validation of antibodies, IP mass spec should be carried out to investigate any other proteins that the antibodies are binding to[215,231]. With regards to tissue samples, increasing the number of specimens of PF-EP and ST-EP cases will be necessary to draw more precise conclusions towards the specificity and selectivity of the promising antibodies.

2.6. Supplementary Material

Table 2.10: Values of HTRF competition assay for clones competing with C0040034.

Lineage	IgG ID	N=1, IC_{50} nM	N=2, IC_{50} (nM)	Mean IC_{50} (nM)	Fold over parent
C0040034	C0040150	17.1	16.2	16.6	1.2
	C0040151	5.8	5.7	5.8	3.5
	C0040153	4.9	3.8	4.3	4.7
	C0040154	5.8	5.0	5.4	3.7
C0040036	C0040159	44.5	43.9	44.2	0.5
	C0040161	47.4	41.1	44.3	0.5

Table 2.11: Values of HTRF competition assay for clones competing with C0040036.

Lineage	IgG ID	N=1, IC_{50} (nM)	N=2, IC_{50} (nM)	Mean IC_{50} (nM)	Fold over parent
C0040034	C0040150	3.6	3.5	3.5	30.1
	C0040151	1.6	1.1	1.3	79.0
	C0040153	1.3	0.9	1.1	96.3
	C0040154	2.3	1.6	2.0	53.2
C0040036	C0040159	10.4	10.3	10.3	10.2
	C0040161	10.5	10.5	10.5	10.1

Table 2.12: Overview of peptide specificity of affinity matured clones derived from C0040034 lineage.

	C0040034 lineage IgGs					
	Max Delta F%				Top conc. Tested (nM)	Comment
Clone ID	Bio Target^{FUS1}	RELA	Scrambled	Bio C11orf95^{Fus1}		
C0040150	13377.9	111.5	2.4	1.0	67	No RELA binding
C0040151	13482.6	117.2	1.0	0.8	317	No RELA binding
C0040153	14040.2	183.2	2.2	1.9	100	Weak RELA binding
C0040154	10321.1	364.6	0.6	0.9	83	Weak RELA binding
C0040034	12655.0	49.9	-1.0	1.9	1018	Parent

Values from HTRF binding assays performed by AAL. Maximum delta F% values were calculated as described in 2.3.5.4

Table 2.13: Overview of peptide specificity of affinity matured clones derived from C0040036 lineage.

	C0040036 lineage IgGs					
	Max Delta F%				Top conc. Tested (nM)	Comment
Clone ID	Bio Target^{FUS1}	RELA	Scrambled	Bio C11orf95^{Fus1}		
C0040159	9216.7	43.2	1.3	0.0	467	No RELA binding
C0040161	8606.4	70.8	3.1	0.3	6300	No RELA binding
C0040036	5031.5	8.7	-1.3	2.4	1280	Parent

Values from HTRF binding assays performed by AAL. Maximum delta F% values were calculated as described in 2.3.5.4

3. Comprehensive drug screens identify novel compounds that selectively target ependymoma cells

3.1. Attributions

Analogues used in in 3.4.1, were developed by Prof. Richard Gilbertson, Dr. Anang Shelat and Dr. Jamie Jarusiewicz at St Jude Children's Research Hospital, Memphis, US. They further generated data on ADME properties and screened BJ cells as indicated in the chapter. Natural products were obtained from Dr Muhammed Ilias (National Centre for Natural Products Research, Mississippi, US). The new chemical entities used in 3.4.3 were supplied by Sentinel Oncology, Cambridge, UK.

3.2. Introduction

Current standard of care treatment for ependymoma comprises surgical resection followed by irradiation[23,232]. While research efforts have focused on identifying suitable chemotherapeutic treatments for ependymoma, most have yielded disappointing results either at the preclinical or clinical stage[76,107,233,234]. To identify novel compounds suitable for chemotherapy in ependymoma, we developed drug screening approaches which include target-agnostic and target-directed cell screening assays for ependymoma-specific therapeutic development. This chapter focuses on target-agnostic screens. I also present data on novel compounds with known mechanism and high activity in ependymoma cells.

3.2.1. Drug development approaches for cancer

High throughput drug screens (HTS) of cancer cells have proved useful to identify cancer therapeutics[235]. For example, FDA-approved chemotherapeutics such as trametinib used to treat malignant melanoma or vismodegib used to treat basal cell carcinoma were identified in cell-based HTS[236–240].

Screening approaches can be divided into target-specific or target-agnostic assays, also commonly referred to as phenotypic assays[235,241]. Target-based assays focus on discovering compounds active against specific targets that drive the malignant phenotype e.g., amplified oncogenes e.g, HER2 or hormone receptors in breast cancer[242,243]. Numerous anticancer drugs are cytotoxic compounds interfering with cell proliferation, which, in its unlimited state is a hallmark of cancer[244,245].

Target-agnostic assays screen large numbers of compounds without necessarily knowing the targets and/ or molecular mechanisms of action (MMOA)[246]. This approach was commonly used in the early ages of drug development before target-based screens became more available. However, it has recently become a more sought after approach[114,247]. Drugs discovered in these screens are generally distinguished into small molecules or biologics[114,248]. Due to their unknown MMOA, these novel structures are frequently tested in assays analysing specific phenotypic outcomes such as decreased cell viability. These include techniques assessing metabolic activity like the 3-(4,5-dimethylthiazol-2-yl)-2,5-diphenyl-2H-tetrazolium bromide (MTT) assay or the CellTiterGlo® assays, which measure mitochondria activity or the ATP concentration, respectively[249–252]. The identification of active compounds with unknown MMOA should be followed up by assays designed to understand the MMOA of the drug[247]. An identification of the compounds' MMOA holds potential in fostering understanding of the tumour biology[253]. Hence, it is of particular importance that these screens employ systems that accurately recapitulate the disease[247]. In this context, recent evidence suggests that phenotypic screens are more accurate in 3D versus 2D cultures, which allow more accurate prediction of the tumour response to therapeutics, possibly because of preservation of cell-cell communication[254–256].

De novo drug development is predicted to take between 10 and 17 years from initial compound discovery to clinical approval[257]. In order for a drug to be efficacious and subsequently receive clinical approval, it needs to exhibit specific properties. These include solubility and stability, as well as Absorption, Distribution, Metabolism, Excretion and Toxicity (ADMET) properties. Such properties are tested *in vitro* and *in vivo* to gain insight on the disposition of the respective compound within an organism[258–260].

3.2.2. Novel chemical entities and natural products are commonly used in target-agnostic approaches

In anticancer drug discovery, natural products and new chemical entities (NCEs) play a crucial role in target-agnostic approaches. HTS of these compounds deploys the cancer cell of interest and the closest proximity to the normal cell type as controls[241]. Over the last decades, a range of NCEs have been developed and approved by the FDA for the use as a chemotherapeutic for specific types of cancer (reviewed in[261]).

NCEs are either the natural, synthetic or modified version of a natural compound[261]. Of 175 anticancer drugs developed between 1940-2010, 48.6% were either derived from natural products or are the original natural structure. Natural products for medicinal chemistry are typically derived from plants, marine organisms or microbes[262]. Commonly used anticancer drugs such as paclitaxel, topotecan or doxorubicin were originally derived from a natural product structure[262,263]. Paclitaxel and topotecan are derived from plants with paclitaxel harbouring the original natural structure, while topotecan is a derivative of the original structure. Paclitaxel is a microtubule stabilizer and was originally isolated from the bark of *Taxus brevifolia* (Pacific Yew Tree)[264]. Paclitaxel is, among others, used for the treatment of breast cancer and non-small cell lung cancer[265,266]. Topotecan, is a DNA topoisomerase I inhibitor and derived from the cytotoxic alkaloid Camptothecin isolated from the bark and stem *Camptotheca acuminate* (Camptotheca). Due to unfavourable ADMET properties, the original structure was modified to create a compound displaying more favourable properties[262,267]. Topotecan is used to treat ovarian cancer, small cell lung cancer and cervical cancer[268–270]. Doxorubicin, a cytostatic chemotherapy that is used in a range of cancers including breast, stomach and lung cancer, was originally isolated in 1969 from the mutant bacteria strain *Streptomyces peucetius* subsp. *caescius* ATCC 27952[271,272]. Doxorubicin formation is a result of C-14 hydroxylation of its immediate precursor daunorubicin (DNR)[272].

These examples demonstrate how natural product structures can either be directly applied as cancer therapeutics or be further modified to generate a derivate with preferred properties for drug development. Especially in *de novo* drug development, which includes the testing of several different analogues, thorough investigation of

ADMET properties of each active analogue is important to lower the risk of compounds failing in preclinical *in vivo* studies.

3.2.2.1. Atropisomerism in drug development

In *de novo* drug development, it is essential to minimise the risk of toxicity and optimise its formulation prior to testing it on humans in clinical trials. In the context of drug stability, particularly important is the potential of chirality due to atropisomerism of the novel compounds[273]. Atropisomerism describes the ability of a molecule to exist as two enantiomers, which is the consequence of a slow hindered rotation along a bond axis[273]. In drug development, this is important to identify as these enantiomers can have very different properties such as different target-binding affinity or toxicity[273]. A key example of this is thalidomide, that was originally marketed for morning sickness, but in which an unknown enantiomer caused phocomelia in unborn children[274]. With appropriate studies, properly controlled atropisomers can be approved by the FDA[275].

3.2.3. Novel compounds with known mechanisms of action are screened in target-informed approaches

Since the 2000s, the number of cancer therapies against a specific target approved by the FDA has increased tremendously. Targeted therapies include monoclonal antibodies, inhibitors of signal transduction proteins, apoptosis inducing drugs, gene expression modulators and hormone therapies[245]. The increase in these therapies is due largely to the explosion in data generated by genome-wide studies of cancer [245,276,277].

The development of tyrosine kinase inhibitor imatinib (Glivec) for the treatment of chronic myelogenous leukaemia (CML) is an example of an FDA-approved drug produced via a target-driven drug screen[278]. In the case of chronic myelogenous leukaemia (CML), it was found that a reciprocal translocation of chromosomes 9 and 22 produced a shortened chromosome 22, also referred to as Philadelphia chromosome, resulted in the generation of the *Bcr-Abl* fusion which encoded a protein with constitutive tyrosine-kinase activity[279–281]. Another example is gefitinib (Iressa™),

which is an inhibitor of epidermal growth factor receptor tyrosine kinase (EGFR-TK) activity[282]. It has been developed from an originally selected anilinoquinazoline structure into its final structure, that was approved by the FDA for the treatment of non-small cell lung cancer[283]. Another examples for a structurally modified compound approved chemotherapeutic is vismodegib[235]. Originally selected in a screen of synthetic small molecules, it underwent chemical modifications to improve its properties and make it suitable for translation into the clinic [237]. Prior to its approval in 2012 for the use in metastatic or recurrent basal cell carcinoma, it had also been shown to be active in preclinical studies on medulloblastoma mouse models[239,284,285].

Within the scope of targeted therapies, drugs directed against tumour-specific markers are of great interest for the treatment of paediatric tumours; particularly paediatric brain tumours. Since common cell cycle inhibitors do not selectively target cancer cells but inhibit proliferation in all dividing cells, they eliminate normal cycling cells too. Multiple reviews have focused on the long-term effects these types of chemotherapies can have on the CNS of the patient [286–288].

With increasing insights into tumour oncogenes or upregulated potential targets, target-based drug screen approaches are becoming more straightforward. For ependymoma, high-throughput screens testing different compounds on ependymoma cell lines have identified drugs with specific MMOAs as particularly active. Atkinson *et al.* have shown in 2011 that among others, inhibitors of the mitotic Polo-like kinase 1 (PLK1) exhibit specific activity in supratentorial ependymoma cells *in vitro*[115]. PLK1 is important in cell cycle progression as it is involved in mitotic entry, centrosome maturation, spindle assembly, chromosome segregation and cytokinesis[289,290]. It is reportedly upregulated in an array of tumours including glioma, breast and colon cancer[291–293]. While the crucial role of PLK1 in the cell cycle also renders PLK-1-targeting drugs inhibitors of the cell-cycle, it has been shown that PLK1 depletion has a severe effect in cancer cells but does not affect normal cells (reviewed in [294]).

Another drug screen previously performed by our lab, assessed 1.2 Million compounds against choroid plexus carcinoma and ependymoma cells. Included in the single-point screen were marine compounds, natural products (NATPROs), NCEs, a small selection library, a company library as well as the St. Jude house library. From

these, a range of NCEs could be identified as active in mouse choroid plexus carcinoma cells. This cell line was used for the initial screen as choroid plexus carcinoma cells are highly aggressive and resistant towards chemotherapies and therefore used as a proxy. Any compounds displaying high activity in choroid plexus carcinoma cells were subsequently tested against ependymoma cells. Further analysis of the compounds' structures revealed that these NCEs can be classified into four different scaffolds. Follow up drug screens examining dose-related activity included supratentorial ependymoma cells (mSEP-CR[-]^{EPHB2}) and revealed that an aminopyrimidine scaffold was the most promising lead (unpublished).

3.3. Material and Methods

3.3.1. *In vitro* methods

3.3.1.1. Cell culture

Mouse and human ependymoma cells were cultured exactly as described in 2.3.1.1. Briefly, cells were cultured as neurospheres in neurobasal media supplemented with L-Glutamine, Penicillin, Streptomycin, N2, B27, EGF, FGF, and BSA. Cells were cultured in ultra-low attachment plates at 37°C and 5% CO_2 and passaged every 3-5 days.

3.3.1.2. *In vitro* dose-response drug screens

For drug treatment studies, cells were cultured as described in 2.3.1.1 and 3.3.1.1. Using an automated Multidrop™ (Thermo Fisher), cells were seeded in 100µl of culture media in 96-well plates. Previous growth curve experiments have determined optimal cell numbers for each cell line (see Table 3.2). Twenty-four hours post-plating, cells were treated with 500nl of solution containing the compounds of choice dissolved in DMSO. Transfer of drug solution was performed using an automated ClipTip™ multichannel pipette (ThermoFisher). Cells treated with DMSO alone served as vehicle controls in each plate. To generate dose-response curves, cells were drugged with decreasing drug concentrations. Cell Titer Glo® (Promega) was used to determine cell viability. Seventy-two hours post-drugging, cell viability was measured by incubating with 60µl CellTiterGlo® (Promega) per well for 10min and measuring luminescence signal using a PheraStar PlateReader (BMG Labtech). Data were analysed using MARS Software (BMG Labtech) and Prism (Version 7). Cell viability was determined by normalizing the luminescence signal of drugged cells to DMSO-treated control cells.

For NCEs, dilutions had been prepared at St Jude Children's Research Hospital and each drug had a different concentration range. Concentrations reached in wells ranged from 98µM being the highest concentration tested and 0.00047µM being the lowest concentration (see Supplementary Table 3.2). Drug plates for natural products were prepared in DMSO, diluting the compounds 1:3 with concentrations ranging from 10mM to 5.08E-10mM. Drug plates for Sentinel Oncology compounds were prepared

in DMSO, diluting the compounds either in 1:2, 1:3 or semi-log dilutions from well 1-11 (see Supplementary Tables 3.3).

Table 3.1: Overview of cell lines used in *in vitro* drug screens.

Cell line	Origin	Cell of Origin	Oncogene	Tumour subgroup	Cell no./well in 96-well plate
mSEP-CR(+)[40]	Mus musculus	Ink4-/- neural stem cells	*C11orf95-RELA*	ST-EP-CR	4,000
mSEP-CR(-) RTBDN, 47	Mus musculus	Ink4-/- neural stem cells	*RTBDN*	ST-EP-CR(-)	1,500
mSEP-CR(-) EPHB2, 38	Mus musculus	Ink4-/- neural stem cells	*EPHB2*	ST-EP-CR(-)	2,500
xSEP-CR(+), [101]	Homo sapiens	supratentorial ependymoma cells	*C11orf95-RELA*	ST-EP-CR	5,000
mNSC	Mus musculus	cortical stem cells from CD1® nude mice	-	-	4,000

ST-EP-CR- C11orf95-RELA^{Fus} positive supratentorial ependymoma; ST-EP-CR(-)- C11orf95-RELA^{Fus} negative supratentorial ependymoma

3.3.1.3. *In vitro* radiation of cells

For irradiation *in vitro* studies, cells were radiated using a γ-irradiator with a Caesium-137 sealed source. Depending on the drugging regimen, cells were irradiated with 2Gy either 1h pre- or post-drugging of cells.

3.3.2. *In vivo* methods

3.3.2.1. Mouse models and husbandry

Eight-week-old immunodeficient CD1 ® female nude mice were purchased from Charles River (strain code 086) and housed in compliance with the UK Home Office license (license No. P6787677F). They were housed under pathogen-free conditions in groups of 2-5 mice per cage on a 12h light cycle in air-filtered laminar flow racks with laboratory chow and water *ad libitum*.

3.3.2.2. Orthotopic allografts of mouse tumours

Orthotopic allografts of mouse tumours were performed as described in 2.3.2.2. Briefly, mSEP-CR(+) cells resuspended in Matrigel® were implanted at 50,000 cells per mouse into the cortices of CD1 ® nude female mice using a stereotax (Kopf, Model 902). Tumour growth was measured using bioluminescence imaging (BLI; see below). Upon reaching BLI signals of 10^7 photons/sec, mice were randomised into treatment groups according to their signal.

3.3.2.3. Bioluminescent imaging of allograft tumours

Mice with growing tumour allografts were subjected to bioluminescence imaging (BLI) 1-2 times per week. Five minutes prior to imaging, mice were injected intraperitoneally with 150µg/kg of D-Luciferin (Perkin-Elmer). Isoflurane-anaesthetized mice were imaged using a XENOGEN IVIS200 (Caliper Lifesciences) within 5-10min post-Luciferin injection.

3.3.2.4. *In vivo* maximum tolerated dose studies

Non-tumour bearing CD1® nude females (Charles River) were enrolled in a maximum tolerated dose (MTD) studies testing Sentinel Oncology compounds SOL288 and SOL686. For the MTD study of SOL288, mice were dosed with 125mg/kg via oral gavage at a Q3D schedule (every three days). Drug was formulated in 10% DMSO and 90% of 20% w/v hydroxypropyl-beta-cyclodextrin (HPCD; Sigma-Aldrich). Over

the course of a week, mice received three doses and were kept alive for additional seven days to monitor for toxic side effects.
The MTD study for Sentinel Oncology compound SOL686 included two treatment arms. Drug was formulated as SOL288 (see above). Five non-tumour bearing mice per treatment group were treated with either 100mg/kg or 125mg/kg of SOL686. The drug was administered via oral gavage at a dosing schedule of Q7D (every 7 days) over a course of two weeks. In total, animals received three doses and were left for 7 additional days following the final dose to monitor them for toxic effects. Weights were measured three times per week.

3.3.2.5. *In vivo* preclinical efficacy study of lead compound

Mice harbouring mSEP-CR(+) tumours were enrolled into a preclinical efficacy study of SOL288 (Sentinel Oncology). Mice received 125mg/kg of SOL288 at a volume of 5mL/kg via oral gavage. Drug was dissolved in 10% DMSO and 90% HPCD. SOL288 was administered at a Q3D schedule for six doses of the course of 15 days. A solution of 10% DMSO and 90% HPCD served as the vehicle control. Mice displaying adverse effects such as domed heads, hunched backs or weight loss were subjected to schedule 1 killing method using an overdose of CO_2 followed by confirmation of death.

Previous power calculations had revealed that 10 mice for control groups and 15 mice for treatment groups would be necessary in order for the two-sided 5% level Wilcoxon test to have an 80% power to detect a setting in which there is an 80% probability that a random animal from the treatment group survives longer than an animal from the control group. In order to save mice, we started with a smaller number of mice per treatment group and observed the groups. If a trend was detectable, more mice would have been subjected to the treatments. As the Wilcoxon test has poor properties if the sample size is <7, preclinical efficacy studies were started with 7 mice per treatment group.

3.3.2.6. Collection of brains and haematoxylin and eosin staining

Once mice displayed clinical symptoms, brains were dissected and fixed in 10% NBF for 24h, prior to placement into 70% ethanol for 24-72h. Following this, 5micron sagittal sections of paraffin embedded brains were stained with H&E by the Histopathology core at the Cancer Research UK Cambridge Institute. H&E-stained sections were scanned with a Leica Aperio AT2 digital whole slide scanner and uploaded onto the Aperio eSlide manager software.

3.3.3. Data analysis

Cell Titer Glo® measurements in cell viability assays that had been performed in triplicates for each drug per cell line, were analysed using MARS software followed by GraphPad Prism version 7 (v.7). R Studio was used for the presentation of IC_{50} values. The extra sum-of-squares F-test was performed to compare non-linear regressions of dose-response curves and the respective log IC50 values of all cell lines in each dose-response graph.

Data from *in vivo* studies were plotted using GraphPad Prism v.7. Statistical analyses were conducted using GraphPad Prism v.7. Weight loss between treatment groups were analysed using unpaired t-tests. Paired t-tests with or without Welch's correction, depending on the SD values for the different groups, were applied for weight loss analysis within treatment groups. Log-rank tests were carried out for analysis of survival curves.

H&E-stained slides were analysed using Aperio eSlide manager and Aperio Image Scope (both Leica). GraphPad Prism v.7 was used for plotting and statistical analysis of data (unpaired t-test).

3.3.4. Workflow of project

This chapter describes the maturation of NCEs and NATPROs screens. Previous high-throughput drug screens had identified selections of NCEs and NATPROs active against ependymoma cell lines and choroid plexus carcinoma cells *in vitro,* respectively (unpublished). The maturation of these compounds was achieved by testing NCE analogues of an aminopyrimidine scaffold towards their activity against ependymoma cell lines. Hits from the screens described in this chapter were selected for further development.

Moreover, PLK1 inhibitors were assessed as targeted therapy against ependymoma cells. A previous drug screen had identified PLK1 inhibitors as particularly active against ependymoma cells. While repurposed PLK1 inhibitors were examined in Chapter 4, Chapter 3 describes the *in vitro* and *in vivo* screen of novel PLK1 inhibitors developed by Sentinel Oncology, Cambridge, UK.

3.4. Results

3.4.1. *In vitro* drug screens of novel compounds and natural products with unknown mechanisms of actions

Previous high-throughput drug screens performed in our lab identified an aminopyrimidine scaffold as a lead scaffold in the quest for an ependymoma chemotherapy. To investigate how modifications of the chemical structure affect the cytotoxicity and advanced ADME properties, Dr. Jamie Jarusiewicz and Dr. Anang Shelat from St Jude Children's Research Hospital (Memphis, US) generated analogues of the aminopyrimidine scaffold. Figure 3.1 shows the chemical structure of aminopyrimidine scaffold. Red dotted lines indicate groups subjected to modifications for the generation of the analogues.

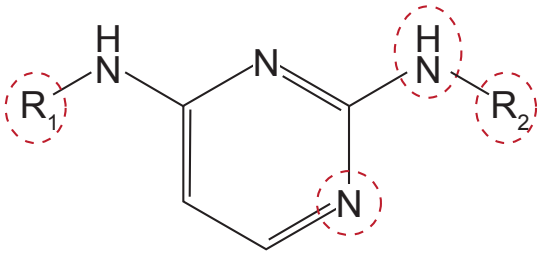

Figure 3.1: Structure of aminopyrimidine scaffold. Scaffold was chemically modified at functional residue groups R1 and R2 as well as at the amino group and the nitrogen group circled by red dotted lines.

3.4.1.1. *In vitro* drug screens of aminopyrimidine scaffold analogues reveal candidate drugs for further development

In total, 86 different analogues with unique modifications of the aminopyrimidine-side chains were developed at St Jude Children's Research Hospital. We received them in previously prepared dilution series in 96-well plates. All 86 analogues were tested towards their *in vitro* efficacy against three different mouse ependymoma cell lines (mSEP-CR[+], mSEP-CR[-]^{EPHB2}, mSEP-CR[-]^{RTBDN}) and a mouse neural stem cell line (mNSC). Each compound was tested in triplicates against each cell line in Cell Titer Glo® assays to measure cell viability. DMSO served as a negative control and the activity of the DMSO-resolved compounds was calculated by normalising the log

values for the different drug concentrations to the log values of the DMSO_control. Activities of each compound against every cell line was calculated as IC_{50}s (half maximal inhibitory concentrations). Drugs producing IC_{50}s below a threshold of 1µM were selected for testing in a fusion-positive human ependymoma cell line (xSEP-CR[+]). Figure 3.2A displays the entirety of the compounds tested in all different cell lines with their respective IC_{50} values. Figure 3.2B illustrates the number of drugs below the selected threshold for each ependymoma cell line.

Across all cell lines, a total of 42 compounds produced IC_{50}s below the threshold of 1µM and were therefore considered active. Analysis of IC_{50}s per cell line demonstrates that the number of compounds deemed potent varies among the different ependymoma cells (Figure 3.2). Overall, 36 drugs were considered active in mSEP-CR(-)$^{EPHB2\ cells}$, while 30 compounds were active in mSEP-CR(-)^{RTBDN} cells. Three compounds efficiently reduced cell viability of mSEP-CR(+) cells and one analogue achieved this in xSEP-CR(+) cells. No drug was potent in all four ependymoma cell lines. Three compounds were potent in all three mouse ependymoma cell lines (SJ000869779-1, SJ000869791-1, SJ000869792-1; Figure 3.3A-C), one compound was potent in both fusion-negative mouse ependymoma cell lines and the human fusion-positive cell line (SJ000865776-1; Figure 3.3D). Another 19 compounds were potent in both, mSEP-CR(-)^{EPHB2} and mSEP-CR(-)^{RTBDN} cells. Furthermore, 14 compounds were active on mSEP-CR(-)^{EPHB2} and eight further analogues were considered active only in mSEP-CR(-)^{RTBDN} cells (Figure 3.2B).

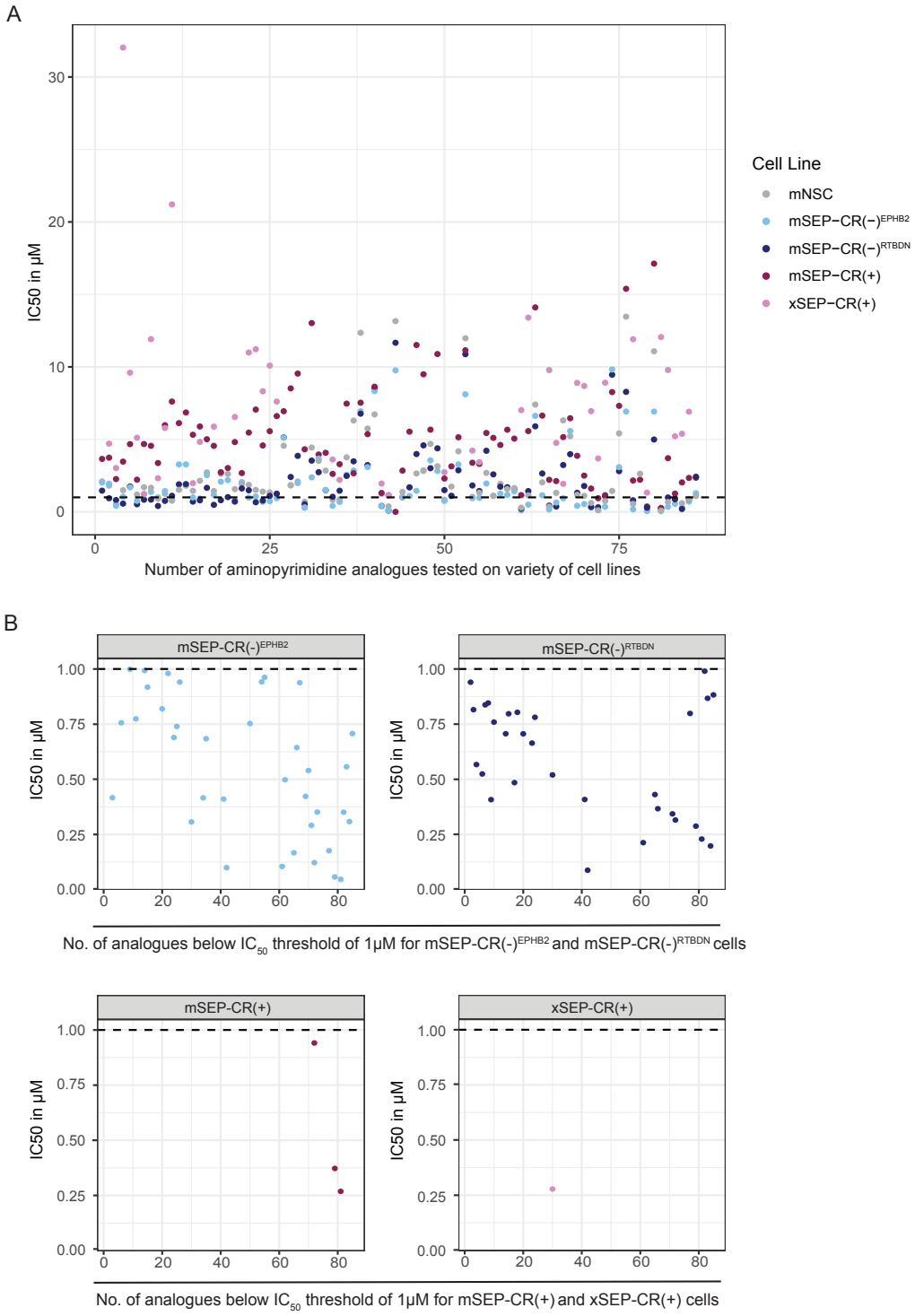

Figure 3.2: Overview of IC_{50} values for new chemical entities tested *in vitro*. A. Overview of analogues of aminopyrimidine scaffold tested in a range of cells. These included mouse ependymoma cell lines (mSEP-CR(+), mSEP-CR[-]^{RTBDN}, mSEP-CR[-]^{EPHB2}), a human ependymoma cell line (xSEP-CR[+]) and mouse neural stem cells (mNSCs). IC_{50}s in µM are plotted against number of drugs. A threshold of 1µM for IC_{50}s was applied for drugs to be included for further development (n= 3). **B.** Selection of new chemical entities with IC_{50}s below threshold of 1µM displayed for each ependymoma cell line.

Figure 3.3 shows the dose-response curves for the four selected lead compounds as well as their chemical structure. Comparison of dose-response curves between the different cell lines for each drug revealed a significant difference in logIC_{50}s (Figure 3.3. extra sum-of-squares F test; $p<0.0001$). Moreover it was observed that xSEP-CR(+) cells display a significantly higher logIC_{50} than all the other cell lines for compounds SJ000869779-1, SJ000869791-1, SJ000869792-1 (Figure 3.3, Supplementary Table 3.4; one-way ANOVA with Tukey's multiple comparisons test). This, coupled with the observation that only one NCE analogue was considered active against xSEP-CR(+) cells, could be an indication that this human ependymoma cell line is more resistant than the mouse ependymoma cell lines (Figures 3.2 and 3.3).

Following my drug screens, the analogues identified as active in our ependymoma cell lines were subjected to further tests. These assessed solubility, permeability and toxicity of analogues on human fibroblast cells (BJ cells). This data was produced at St Jude Children's Research Hospital. It showed that, except for analogue SJ000869792-1, which displayed an IC_{50} on BJ cells in the nanomolar range, the other three lead candidates were inactive in BJ cells with IC_{50}s of 12μM and above.

Compound SJ000869779-1 belongs to the group of analogues harbouring a constant aminopyrimidine group, a cyclopentyl group at pyrimidine-4-position and a benzene and pyridine group at pyrimidine-2-position (Figure 3.3A). For SJ000869791-1, a benzene ring and a benzoic acid were linked at the pyrimidine-2-position, while two methyl groups were linked at pyrimidine-4-position (Figure 3.3B). Compound SJ000869792-1 also harbours a benzene ring and a benzoic acid at the pyrimidine-2-position but a cyclohexane group at pyrimidine-4-position (Figure 3.3C). Analogue SJ000865776-1 has the same structure as SJ000869791-1 with another benzene ring linked at the position of the benzoic acid in SJ000869791-1 (Figure 3.3D).

A

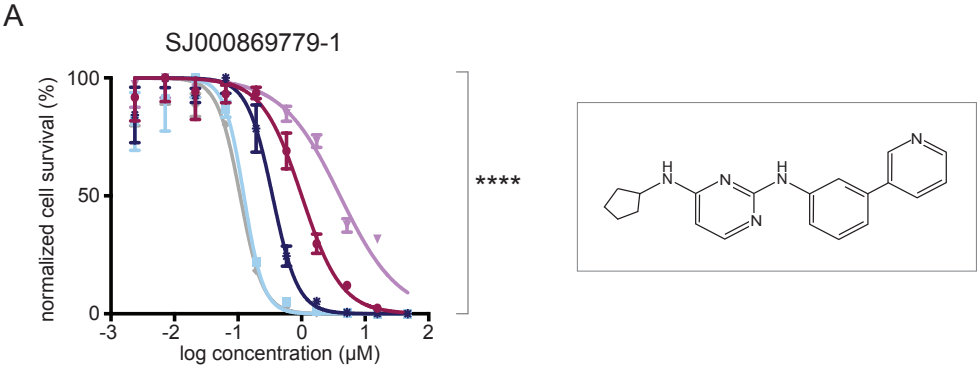

B

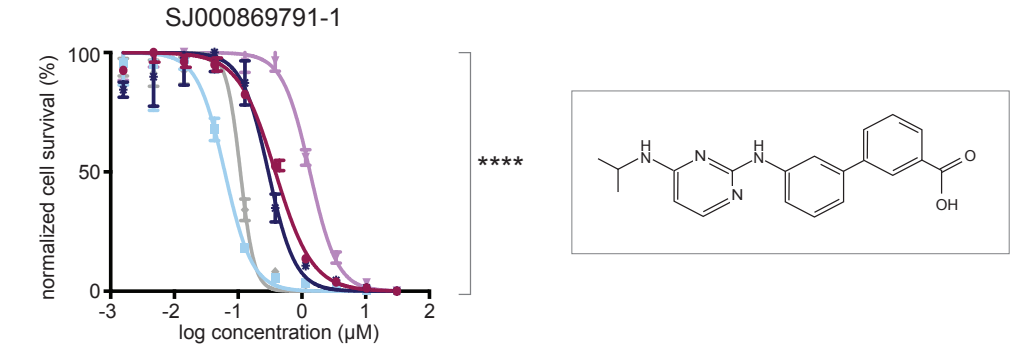

C

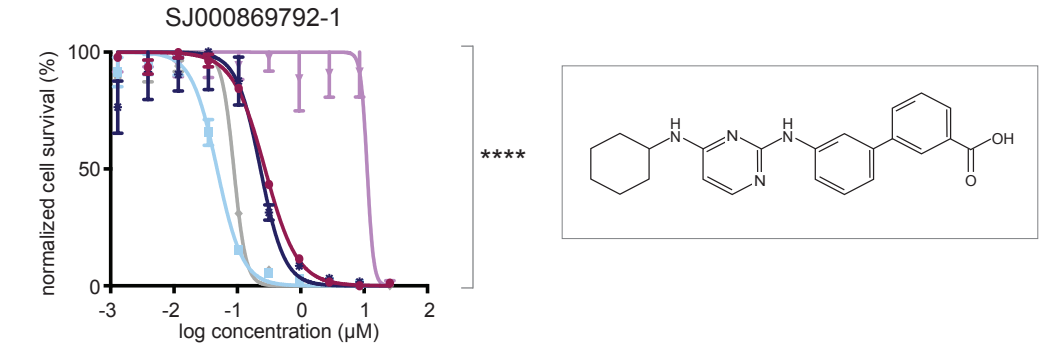

D

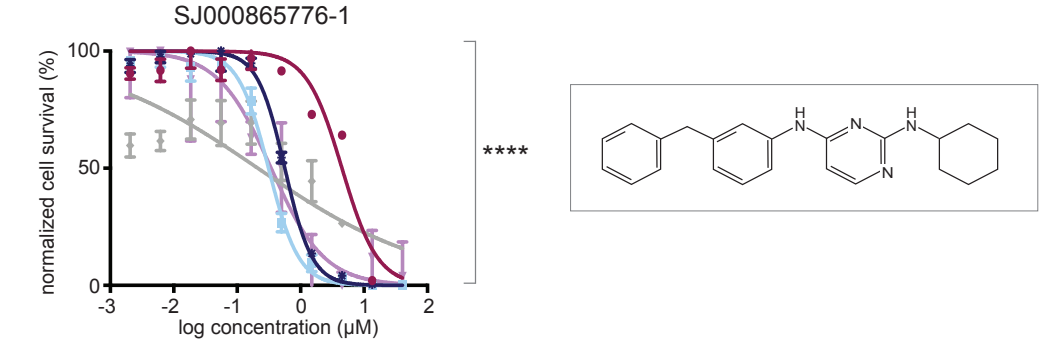

xSEP-CR(+) mSEP-CR(+) mSEP-CR(-)^{RTBDN} mSEP-CR(-)^{EPHB2} mNSC

Figure 3.3: Selection of lead aminopyrimidine analogues identified in mid-throughput drug screen. Drugs were tested on mouse ependymoma cell lines (mSEP-CR[-]^{RTBDN}, mSEP-CR[-]^{EPHB2}, mSEP-CR[+]), mouse neural stem cells (mNSC) and a human ependymoma cell line (xSEP-CR[+]). Dose response-curves and 2D chemical structure are shown for: **A**. SJ000869779-1. Analogue was considered active in mouse ependymoma cell lines and mNCSs. **B**. SJ000869791-1. Analogue was considered active in mouse ependymoma cells lines **C**. SJ000869792-1. Analogue displays particular activity in mouse ependymoma cell lines and mNSCs. **D**. SJ000865776-1 This compound was considered active in mSEP-CR(-)^{RTBDN}, mSEP-CR(-)^{EPHB2} and xSEP-CR(+). (n=3). Comparison of nonlinear regressions and logIC_{50}s with extra sum-of-squares F-test (****: $p<0.0001$).

Following the identification of compounds active against ependymoma cell lines, analogues SJ000869779-1, SJ000869791-1 and SJ000869792-1 are now being matured in a collaboration with the laboratory of Professor Ian Collins at the Institute of Cancer Research, London. Through the application of structure-activity relationship assays of further analogues, the laboratory is currently testing analogues of the lead compounds to determine modifications important for the activity of the compounds.

3.4.1.2. Selection of natural products do not exhibit ependymoma-specific activity

The high-throughput drug screen conducted in our lab also included natural products (NATPROs) in the form of crude plant extracts. These NATPROs were supplied from the National Centre for Natural Products Research, University of Mississippi, USA. From 14,406 NATPROs originally included in the screen, 16 fractions from eight different plants showed activity in choroid plexus carcinoma cells. In previous screens, nine of these drugs had displayed high activity in choroid plexus carcinoma cells with IC_{50}s in the nanomolar range (unpublished). Hence, we were interested if these were also active in ependymoma cells. The five most potent compounds (SD-11-2, SD-11-4, SD-15-6, Diosgenin and JBLL-1016) were chosen to be tested in ependymoma cell lines.

Three of them (SD-11-2, SD-11-4 and SD-15-6) were isolated from S. nigrum Tiogenon (aglycone) and their structures are based on the tiogenin (C-25R spirostane) aglycone. Diosgenin is further based on an aglycone structure, while JBLL-1016 was an extract from Ludovia lancifolia.

NATPROs were tested in our mouse and human ependymoma cell lines with mNSCs serving as controls. Every NATPRO was tested in triplicates on each cell line. Dose-response curves for each compound are shown in Figure 3.4. As described in 3.4.1.1, log values of treated cells were normalised to log values of DMSO-treated cells (control). Nonlinear regressions were used to determine IC_{50} values for each cell line. Analysis of the NATRPO activity against ependymoma cells revealed that the NATPROs are not considered active in ependymoma cells according to their IC_{50}s. All compounds displayed IC50s above 2µM, with IC_{50}s ranging from 2.094µM for SD-15-6 on xSEP-CR(+) cells to 2.203µM for SD-11-4 on mSEP-CR(-)^{EPHB2} cells. Statistical analysis of nonlinear regression curves and logIC50s further revealed that these do not differ significantly between the different cell lines for NATPRO (extra sum-of-squares F test; ns: $p>0.999$) (Figure 3.4).

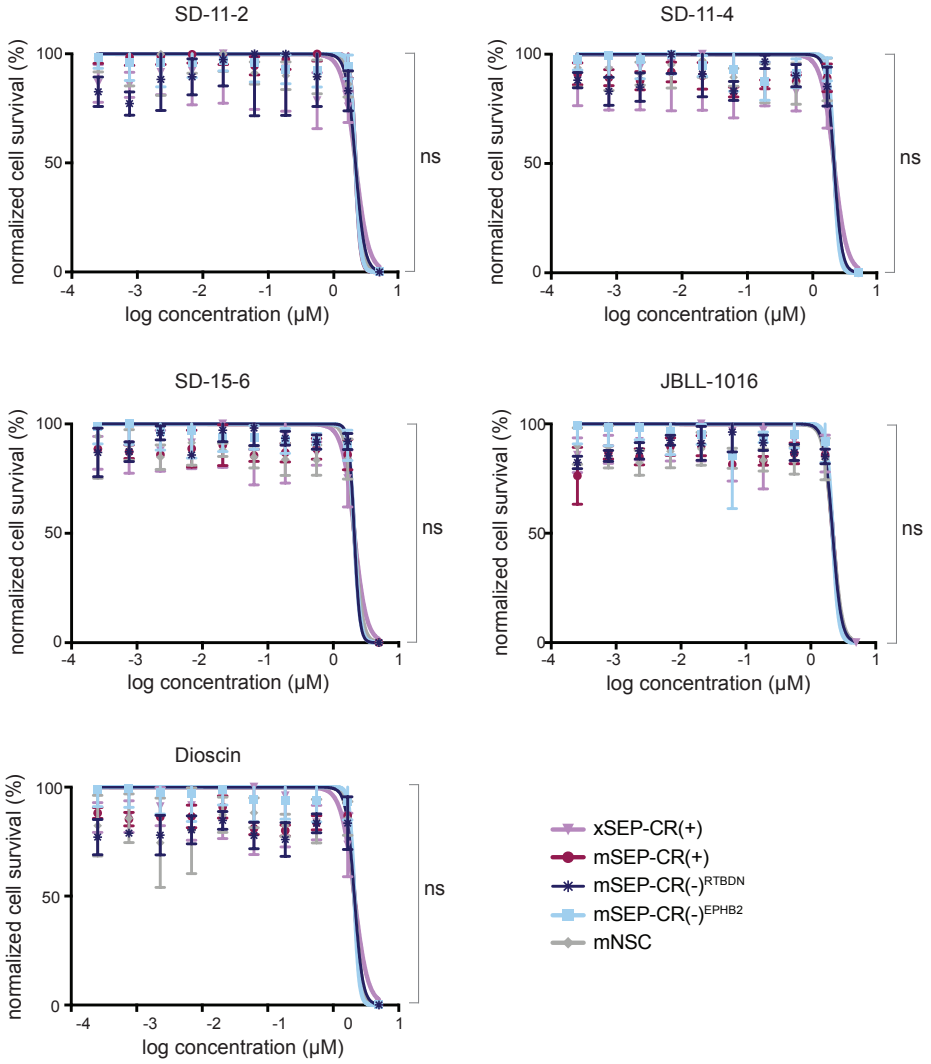

Figure 3.4: Dose-response curves of natural products tested in ependymoma cell lines. Mouse ependymoma (mSEP-CR[-]^{RTBDN}, mSEP-CR[-]^{EPHB2}, mSEP-CR[+]) and human ependymoma cell lines (xSEP-CR[+]) alongside mouse neural stem cells (mNSCs) were treated with decreasing concentrations of five different NATPROs. Dose-response curves are shown for SD-11-2, SD-11-4, SD15-6, JBLL-1016 and Dioscin. Error bars represent SD (n=3). Statistical comparison of nonlinear regression curves and logIC_{50}s using sum-of-squares F-test (ns: p>0.999).

3.4.2. Novel PLK1 inhibitors are promising candidates as novel therapeutics for supratentorial ependymoma

A high-throughput drug screen carried out in our lab had previously identified inhibitors of PLK1 as potent inhibitors of cell proliferation of mSEP-CR(-)^{EPHB2} cells[115]. While FDA-approved PLK1 inhibitors were pursued in combination with novel delivery techniques (see Chapter 4), there was a great interest in novel PLK1 inhibitors with favourable drug properties. Sentinel Oncology has specialised on the development of novel therapeutics that can be delivered directly to the tumour. This is of particular interest for brain tumours due to the BBB, which prevents the majority of drugs from entering the brain[98]. In their developmental programme, Sentinel Oncology have generated a number of BBB penetrable drugs with varying mechanisms of action. These include inhibitors of the Polo-box domain (PBD) of PLK1[295] and CHK1 inhibitors (unpublished). Due to the promising activity of PLK1 inhibitors in previous experiments, we collaborated with Sentinel Oncology to screen their compounds.

Overall, five compounds including inhibitors of PLK1 (SOL288, SOL322, SOL3582-1-A, SOL3614-11B) as well as a Chk1 inhibitor (SOL578) were screened on a variety of ependymoma cell lines (Figure 3.5). Compounds were tested on mSEP-CR(-)^{RTBDN} (n=3) and on mSEP-CR(+), xSEP-CR(+), mSEP-CR(-)^{EPHB2} alongside mNSC (n=4) in CellTiterGlo® cell viability assays. As described for drug screens performed with NCEs and NATPROs, DMSO served as a negative control and activity of compounds was calculated as IC_{50}s by normalizing log values of treated cells to log values of DMOS-treated control cells. Overall, all drugs displayed high activity in ependymoma cell lines with nearly all IC_{50}s for the compounds reaching values below 1µM (Figure 3.5A).

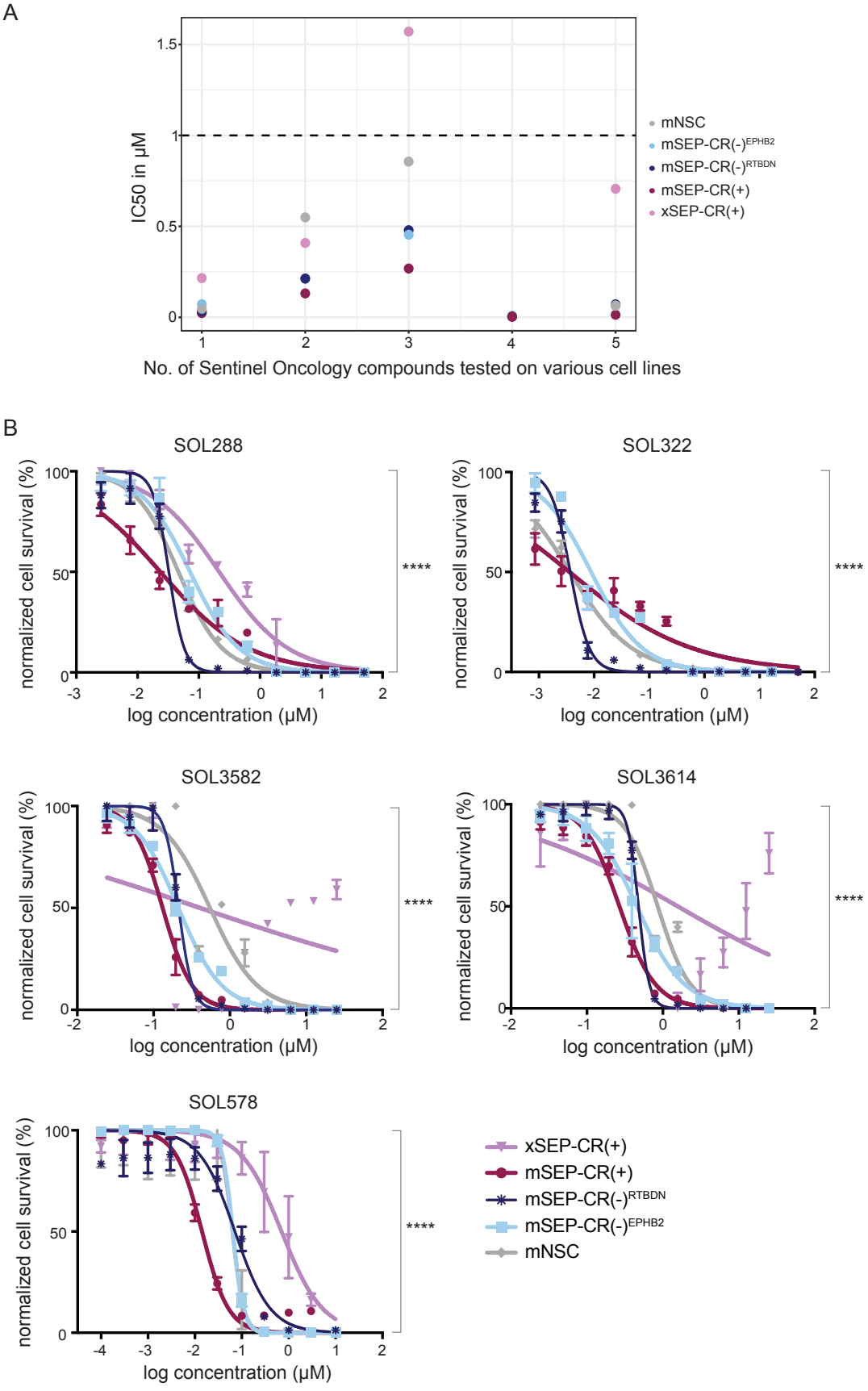
A
IC50 in µM
1.5
1
0.5
0
1
2
3
4
5
No. of Sentinel Oncology compounds tested on various cell lines
mNSC
mSEP-CR(-)EPHB2
mSEP-CR(-)RTBDN
mSEP-CR(+)
xSEP-CR(+)
B
SOL288
SOL322
SOL3582
SOL3614
SOL578
normalized cell survival (%)
log concentration (µM)
****
xSEP-CR(+)
mSEP-CR(+)
mSEP-CR(-)RTBDN
mSEP-CR(-)EPHB2
mNSC

Figure 3.5: Novel compounds with known mechanisms are highly active in ependymoma cells *in vitro.* A. A total of five compounds with known mechanisms developed by Sentinel Oncology were tested in ependymoma cell lines. Except for one, all IC_{50} values fall below the threshold of 1µM. **B** Dose-response curves of different compounds tested in different cell lines (n=3 for mSEP-CR(-)^{RTBDN} cells, n=4 for all other cell lines). Comparison of nonlinear regressions and logIC_{50}s with extra sum-of-squares F-test (****: p<0.0001).

IC_{50}s for SOL288 ranged from 24nM in mSEP-CR(+) cells to 216nM in xSEP-CR(+) cells. For S3582-1A, IC_{50} values ranged from 131.5nM for mSEP-CR(+) and 549.3nM for mNSCs. IC_{50} values for compound S3614-1B were determined to lie between 268.2nM in mSEP-CR(+) cells and 1.571µM for xSEP-CR(+) cells. Particularly high activity was achieved by SOL288 with IC_{50}s ranging from 3.5nM in mSEP-CR(+) cells to 8.8nM in xSEP-CR(+) cells. CHK1 inhibitor SOL578 produced IC_{50} values in the range of 14nM in mSEP-CR(+) and 700nM in xSEP-CR(+) cells (Figure 3.5B). Extra-sum-of-squares F-test showed that there is a significant difference between dose-response curves and logIC_{50} values of the different ependymoma cell lines (****: p<0.0001). It was further observed that xSEP-CR(+) appeared to be more resistant towards treatment with these compounds as the logIC_{50} values of the different drugs were significantly higher in xSEP-CR(+) cells compared to the mouse ependymoma cell lines (one-way ANOVA with Tukey's multiple comparisons test; ****) (Supplementary Table 3.5).

Previous experiments of SOL288 conducted by Sentinel Oncology had confirmed that the compound is highly active in a glioblastoma (GBM) models *in vitro* and *in vivo* and also appeared to be BBB penetrable in mice (data not shown). Hence, SOL288 was taken forward for *in vivo* testing in our fusion-positive ependymoma mouse model.

3.4.2.1. Systemic delivery studies of lead PLK1 inhibitor compound in ependymoma mouse models

Due to its high efficiency in reducing ependymoma cell viability *in vitro*, SOL288 was moved to *in vivo* studies. Since SOL288 had been shown to be BBB penetrable, we administered the drug systemically. In a study on a subcutaneous model of GBM in male CD1® nude mice, oral gavage dosing at a Q3D schedule with 125mg/kg had proven to be efficacious (unpublished). Hence, we started by testing the dose of 125mg/kg on female nude CD1® mice in an MTD study.

Non-tumour bearing mice received three doses of SOL288 via oral gavage every three days over the course of a week (Figure 3.6A). To identify potential toxic side effects of the drug, mouse weights were taken daily. Weight loss was calculated by normalizing weights to start weight. Figure 3.6B depicts the weight loss of mice over time and shows that on Day 9 of the study, mice had lost an average of 4.61 ± 4.2%. Statistical analysis of the weight loss between Day 0 and Day 9 revealed no significant difference (Paired t-test; ns: p=0.3) (Figure 3.6B).

As no other toxicity-related side effects were observed, this drug was assessed in a preclinical efficacy study on the mSEP-CR(+) mouse model. For this, mice were implanted with mSEP-CR(+) tumour cells on Day1 of the experiment and tumour growth was monitored using BLI. On Day12 post-implants mice presented with established tumours (average BLI signal of $>2x10^6$ photons/sec) and the tumours showed signs of growth with the BLI tumour signal increasing over time (Figure 3.6E). Hence, mice were randomised into two treatment groups according to their BLI tumour signal. The randomisation ensured that both treatment groups had the same tumour sizes on averages prior to treatment, which allowed for statistical analysis of the study data. Following randomisation, mice were dosed every three days with either 125mg/kg SOL288 (n=7) or a vehicle (n=7) (Figure 3.6C). The initial study plan included a total number of 7 doses over the course of 18days. However, due to significant weight loss over time, it was not possible to administer the final dose (paired t-test; control group: ** p=0.005; SOL288 group: ** p=0.008) (Figure 3.6D). The weight loss is most likely the result of a combination of drug toxicity and tumour burden.

Throughout the course of the study, tumour growth was monitored via BLI (Figure 3.6E). Kaplan-Meier survival curves present the OS of the two treatment groups (Figure 3.6F).

Analysis of cumulative BLI tumour signal over time revealed that no difference in tumour growth was detectable between the two treatment groups (Mann-Whitney test; ns= $p>0.99$; Figure 3.6E). Survival analysis further demonstrated that there was not significant difference in survival between the treatment groups (p value=0.98, Log-rank relative to control; Figure 3.6F). Once mice displayed clinical symptoms, the mice were culled, brains were harvested and processed for paraffin embedding. Treatment of tumour-harbouring mice also did not appear to have an effect the tumour size. For this analysis, the size of the tumour area was measured on H&E-stained sections and normalised to overall brain size (p value=0.64, unpaired t-test) (Figure 3.6G).

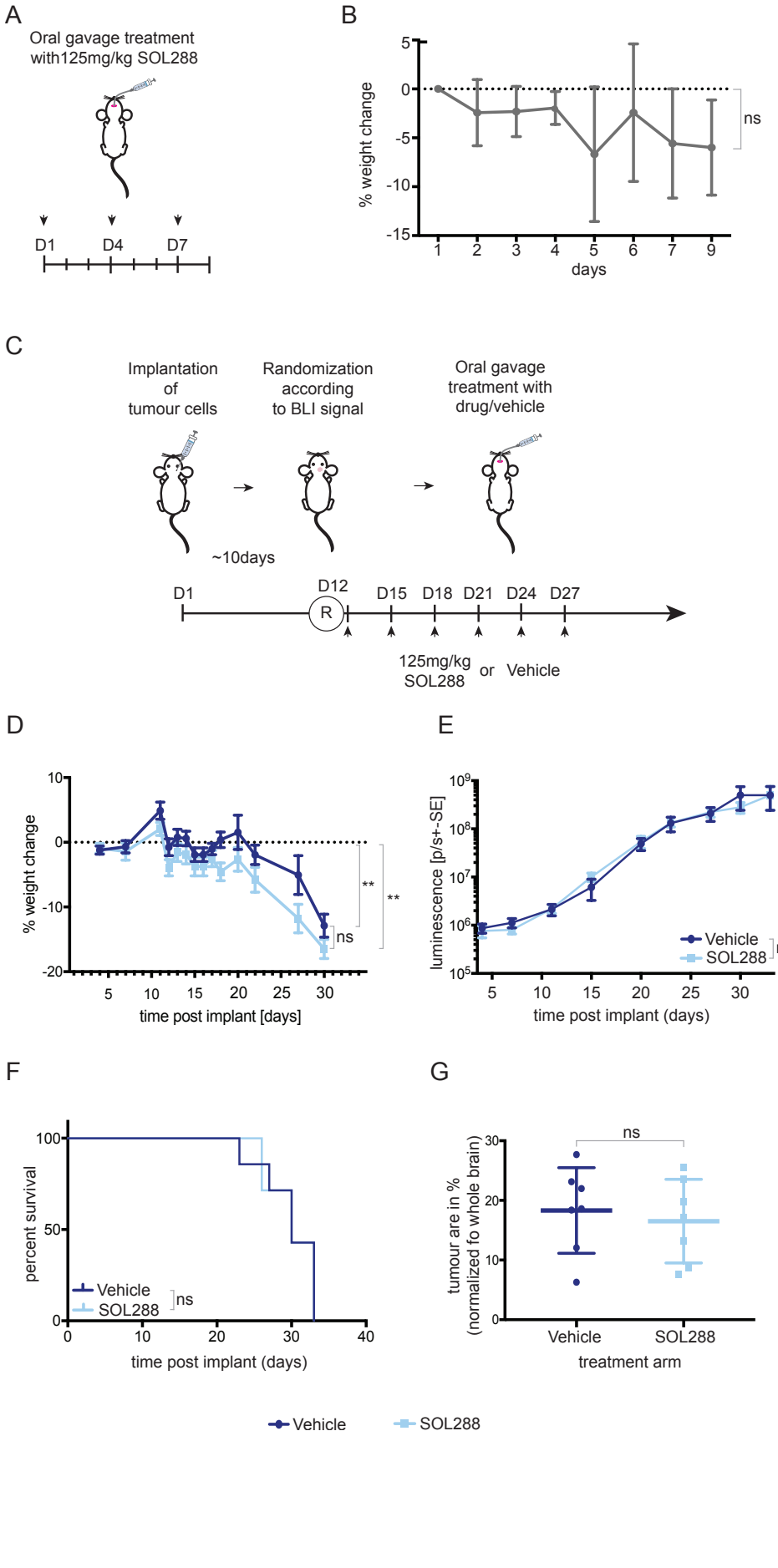
A
Oral gavage treatment
with125mg/kg SOL288
D1
D4
D7
B
% weight change
ns
days
C
Implantation
of
tumour cells
Randomization
according
to BLI signal
Oral gavage
treatment with
drug/vehicle
~10days
D1
D12
R
D15
D18
D21
D24
D27
125mg/kg
SOL288
or
Vehicle
D
% weight change
**
**
ns
time post implant [days]
E
luminescence [p/s+-SE]
Vehicle
SOL288
ns
time post implant (days)
F
percent survival
Vehicle
SOL288
ns
time post implant (days)
G
tumour are in %
(normalized to whole brain)
ns
Vehicle
SOL288
treatment arm
Vehicle
SOL288

Figure 3.6: *In vivo* studies of novel PLK1 inhibitor compound SOL288. A. Treatment schedule for maximum tolerated dose study. Mice received 3 doses of 125mg/kg SOL288 on Day1 (D1), D4 and D7 following a Q3D dosing regimen (n=3 mice). **B.** Percentage of weight loss normalised to start weights (paired t-test; ns: p=0.33). Error bars represent SD. **C.** Treatment schedule for mice enrolled in SOL288-preclinical efficacy study. Mice were orthotopically implanted with mouse ependymoma cells on D1 and randomised according to their bioluminescence tumour signal on D13. Treatment at a Q3D schedule with either 20mg/kg SOL288 (n=7) or vehicle (n=7) started on D13 for 7 doses. **D.** Percentage of weight loss normalised to start weights for vehicle-treated or SOL288-treated mice. (Significance in weight change between treatment groups determined by unpaired t-test; ns=0.22). (Significance in weight change between D0 and D30 for vehicle- or SOL288-treated group determined by paired t-test; **: p=0.005 and 0.008, respectively). Error bars represent SD (n=7). **E.** Graph depicts cumulative luminescence for each treatment group (vehicle; SOL288) over time (Mann-Whitney test; ns= p>0.99). Error bars represent SD. **F.** Kaplan-Meier survival curve (Log-rank test; ns: p=0.98). **G.** Tumour area was measured and normalised to whole brain. There were significant differences between the two treatment groups for either of the measurements (n=7 per treatment group) (unpaired t-test; ns: p=0.65).

3.4.2.2. SOL288-atropisomer SOL686 is highly active against ependymoma cells *in vitro*

During the course of my research, tests of SOL288 by Sentinel Oncology discovered that the structure of SOL288 was an interconverting atropisomer, thereby rendering the compound a mix of two atropisomer structures. Atropisomers are henceforth referred to as SOL685 and SOL686. Further screens revealed that there was a difference in therapeutic activity between the two atropisomers against tumour cells (unpublished).

Hence, I repeated studies testing SOL685 and SOL686 separately against ependymoma cells. Figure 3.7C demonstrates a clear difference in activity between SOL685 and SOL686 after 72 hours incubation. In order to better understand their activity over time, they were tested in decreasing doses (dilution ranges 1:5) with different incubation periods of 24h, 48h and 72h (n=3 per drug per timepoint). Here, mouse ependymoma (mSEP-CR[+], mSEP-CR[-]^{RTBDN}, mSEP-CR[-]^{EPHB2}) cells as well as mNSCs were used in CellTiterGlo® cell viability assays. While drugging

ependymoma cells with SOL685 resulted in IC_{50} values above 1µM, treatment of cells with SOL686 achieved IC_{50} values of below 200nM ranging from 160nM in mSEP-CR(-)^{RTBDN} cells to 38nM in mNSC cells. Figure 3.7 displays the effects of the drugs over time. Non-linear regression curves of SOL686 24h-72h all differ significantly between cell lines. Treatment with SOL685 only resulted in highly significant differences between cell lines after 24- and 48 hours incubation (extra sum-of-squares F-test; ****: $p<0.0001$). After 72h incubation with SOL685, there is no significant difference detectable between dose-response curves and logIC_{50}s of the different cell lines (extra sum-of-squares F-test; ns $p>0.999$).

As standard of care treatment for ependymoma patients includes irradiation, the combination of SOL686 and irradiation (IR) was investigated. Cell viability assays were performed testing the effects of drug only (Figure 3.8A) IR of cells with 2Gy 1h prior to drugging (Figure 3.8B) and drug + IR 1h post-treatment (Figure 3.8C) CellTiterGlo® was applied to measure cell viability 72h post-drugging (n=4 for each condition per cell line). Dose-response curves are displayed in Figure 3.8. Comparison of the logIC_{50} of the different cell lines for each condition was performed (extra sum-of-squares F-test). It revealed that for all conditions except SOL685 72h, the logIC_{50}s between cell lines differed significantly (extra sum-of-squares F-test; ns: $p>0.05$, **: $p<0.01$, ****: $p<0.0001$).

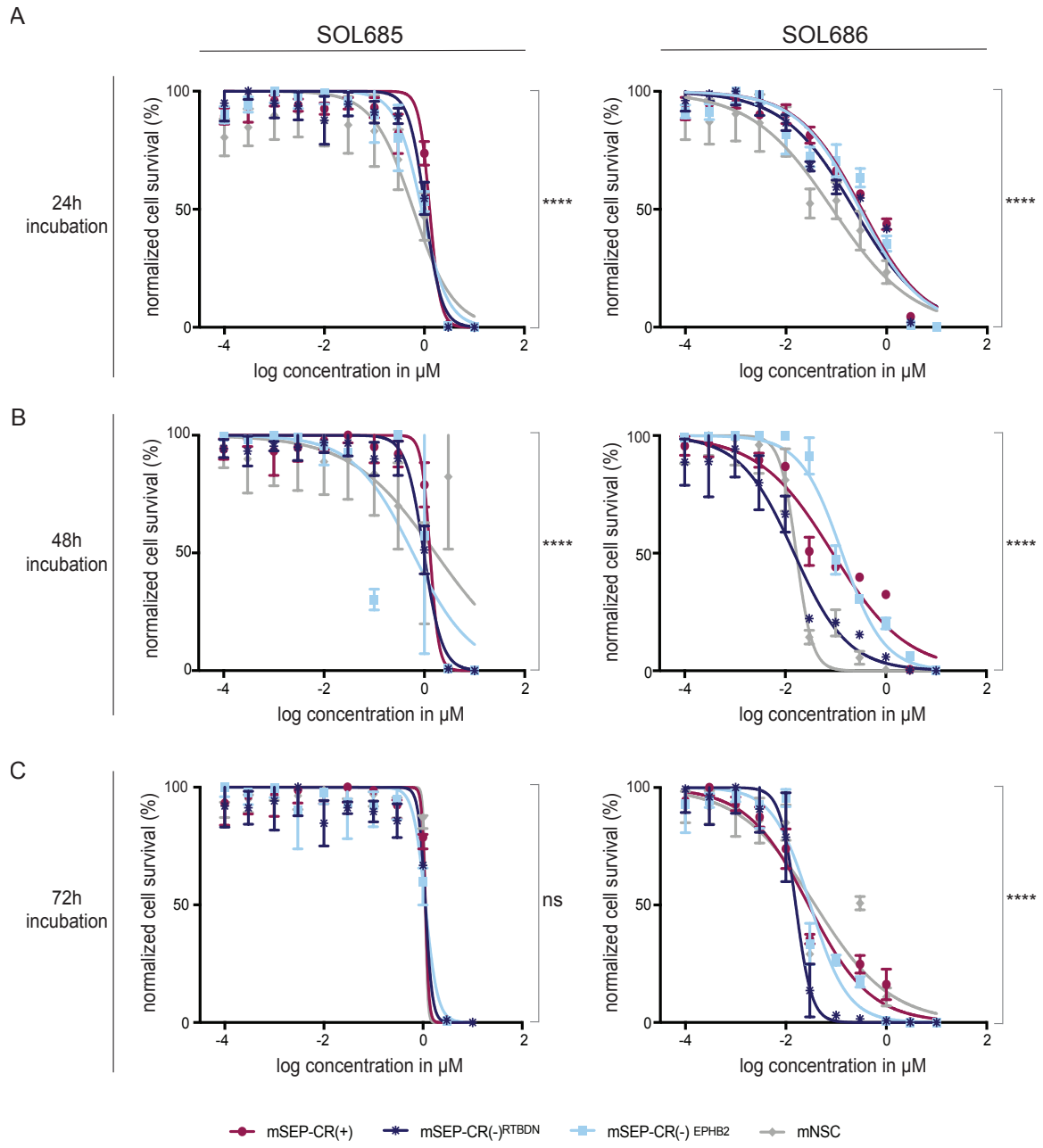

Figure 3.7: Effects of atropisomers SOL685 and SOL686 over time. Mouse ependymoma cells (mSEP-CR[+], mSEP-CR[-]^{RTBDN}, mSEP-CR[-]^{EPHB2} and mouse neural stem cells (mNSCs) were drugged with decreasing concentrations of either SOL685 or SOL686. **A.** Dose-response curves for cells drugged with SOL685 or SOL686 for 24h. **B.** Dose-response curve for cell lines treated for 48h with either SOL685 or SOL686. **C.** Dose-response curves for cells treated with either SOL685 or SOL686 for 72h. Error bars represent SD, n=4. Comparison of nonlinear regressions with extra sum-of-squares F-test (****: $p<0.0001$; ns: $p>0.999$).

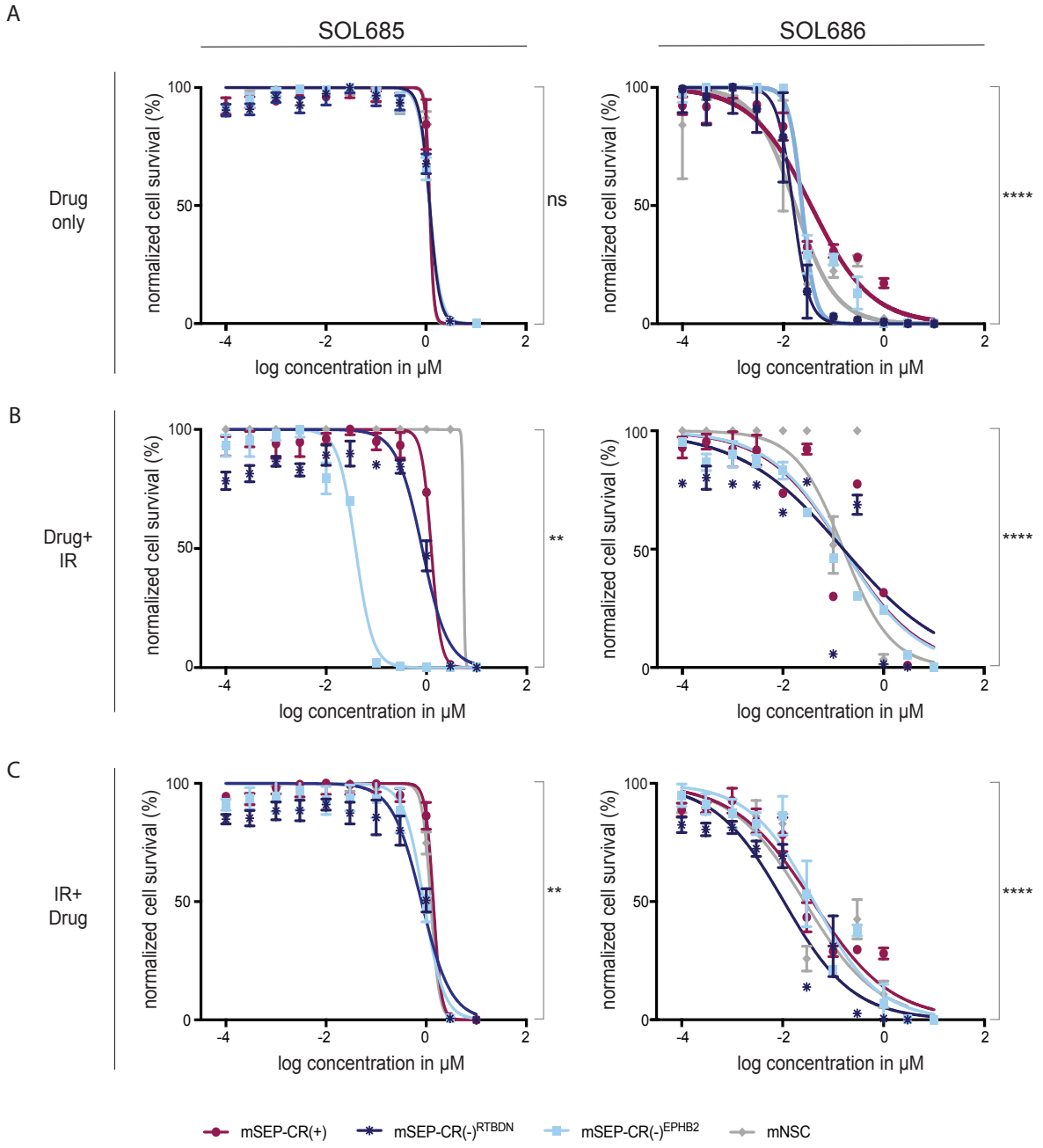

Figure 3.8: Combination therapy of irradiation with SOL atropisomers. Mouse ependymoma cells mSEP-CR[+], mSEP-CR[-]^{RTBDN}, mSEP-CR[-]^{EPHB2} and mouse neural stem cells (mNSCs) were treated with either SOL685 or SOL686 with or without irradiation over 72h. **A.** Dose-response curves for cells treated with drug only for 72h. **B.** Dose-response curves of cells treated with atropisomers followed by irradiation with 2Gy 1h post-irradiation. **C.** Dose-response curves of cells irradiated with 2Gy, 1h prior to treatment with atropisomers. Cell viabilities were measured 72h post-drugging. Error bars represent SD, n=4. Comparison of nonlinear regressions with extra sum-of-squares F-test (ns: p>0.999, **: p< 0.01; ****: p<0.0001).

3.4.2.3. Systemic delivery of SOL686 in mouse ependymoma models is not toxic

Due to its very low IC_{50} values on our ependymoma cell lines, SOL686 was progressed to *in vivo* studies. To assess toxicity of the compound on non-tumour bearing mice, we performed an MTD study. Ten mice were subjected to treatment with either 100mg/kg or 125mg/kg of SOL686 (5 mice per treatment group) using a dosing schedule of Q7D (every 7 days). Dosing schedule is presented in Figure 3.9A. Weights were measured two-three times a week and are displayed in Figure 3.9B, which shows that no significant weight loss is observed in either of the treatment groups throughout the course of the MTD study. Instead, mice treated with 100mg/kg SOL686 display a significant weight gain of over time averaging at 10.4 ± 2.57g on Day 22 of the study (paired t-test; **: p= 0.004). Mice treated with 125mg/kg also displayed an average weight gain of 1.96 ± 4.5% after 22 days, but when compared to the start weight, the weight gain in % is not significant (paired t-test; ns: p= 0.38). As a result of this difference in weight gain between the two different treatment groups, there is also a significant difference in weight gain in % between mice treated with 100mg/kg SOL686 and 125mg/kg SOL686 (unpaired t-test with Welch's correction; p= 0.38).

Based on these results, future preclinical efficacy studies will be performed using a dose of 100mg/kg SOL686. Pharmacokinetic studies will be applied to assess the BBB penetrability of the compound.

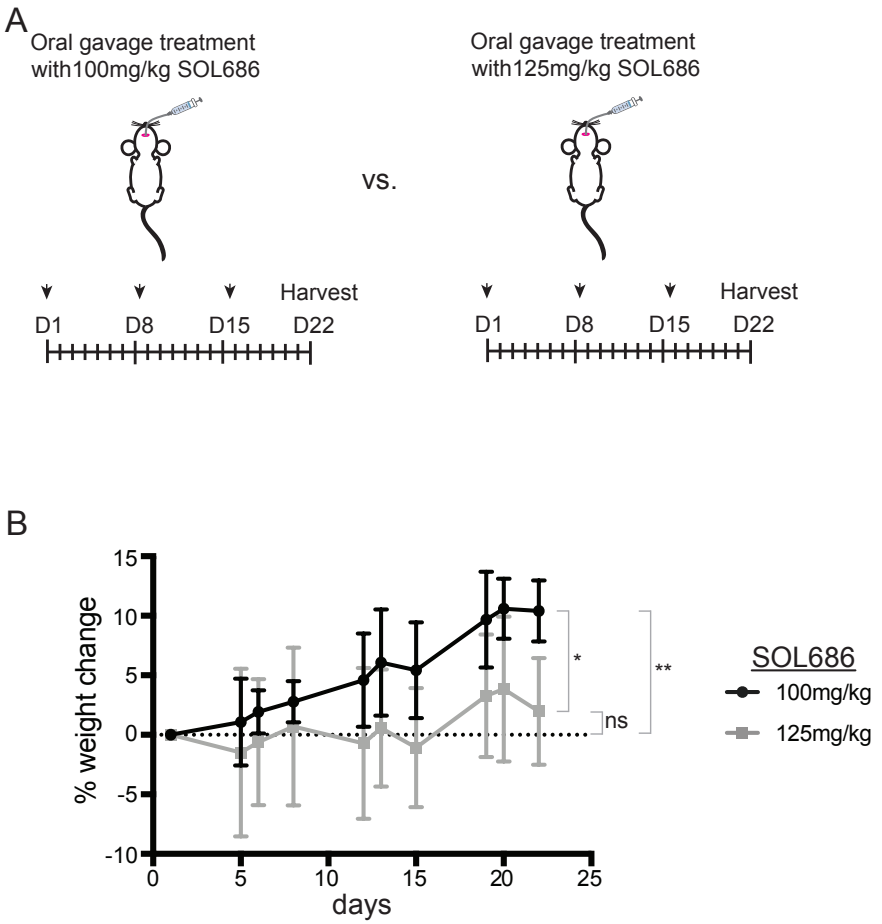

Figure 3.9: Maximum-tolerated dose study of SOL686 determines dose for future preclinical efficacy studies. A. Dosing schedule for mice enrolled in maximum tolerated dose (MTD) study for SOL686. Five mice received 100mg/kg SOL686 via oral gavage, while five mice were treated with 125mg/kg of SOL686. Dosing was performed according to the Q7D dosing scheme every 7 days. Mice were left for another 7 days before brains were harvested. **B.** Weight loss normalised to start weights shown in percentage for both treatment groups (Statistical analysis for weight gain within treatment groups performed with paired t-test; **: p= 0.004; *: p=0.01;) (Statistical analysis comparing weight gain for different treatment groups with unpaired t-test with Welch's correction ns: p=0.38). Error bars represent SD.

3.5. Discussion

Current ependymoma standard of care treatment regimen include resection, followed by adjuvant therapy, which, in most cases, is limited to irradiation[296]. Due to devastating long-term effects of RT in children, there is a need for treatment alternatives[17,18,297,298].

Novel target-agnostic molecules are frequently tested in drug screens to explore their potential as new cancer therapeutics. Particularly in cancers where commonly used chemotherapeutics do not appear to be beneficial, chemicals with unknown targets harbour the potential to reveal novel, druggable pathways in these hard-to-cure cancers[253]. Hence, NCEs were included in the search for a novel chemotherapeutic for ST-EP. Several rounds of high-throughput drug screens identified an aminopyrimidine scaffold as a lead scaffold (Figure 3.1). Pyrimidine analogues are commonly used as antineoplastic agents in chemotherapy as they can act as nucleoside analogues[299]. They include standard of care drugs like gemcitabine and 5-fluorouracil used for the treatment of various cancers such as pancreatic adenocarcinoma and colorectal or breast cancer[300,301]. Preclinical studies had demonstrated a survival benefit of ST-EP mouse models treated with 5-Fluorouracil[115]. Nevertheless, in a Phase I clinical study, this effect was not observed in patients receiving the drug[302].

Analogues of aminopyrimidines have been studied extensively with regards to their anticancer properties with several studies demonstrating strong activity on cancer cell lines[303,304]. Here, a range of 86 aminopyrimidine analogues generated to enhance general activity and ADMET properties was tested in cell viability assays on four different ependymoma cell lines. Amongst these, over 30 compounds displayed activity in ependymoma cell lines (Figure 3.2). Four of these were selected as lead scaffolds due to their activity in mSEP-CR(+) and xSEP-CR(+) cells (Figure 3.3). Analysis of ADMET properties at St Jude's further revealed that structures SJ000869791-1 and SJ000869792-1 have favourable properties, thereby rendering them lead candidates for further development (data not shown). To further enhance ADMET and BBB permeability properties of the compounds, analogues of these lead compounds and an additional two analogues have been prepared by the laboratory of

Ian Collins at the Institute of Cancer Research, London and are now thoroughly tested by the Ian Collins' lab and our lab.

IC_{50} values of compounds tested against xSEP-CR(+) cells were significantly higher compared to the other cell lines, suggesting that these might be less sensitive. Since this is the only human PDX cell line used in the screen, future screens should include more human PDX cell lines in their screens.

Overall, there was a difference in activity for drugs tested against the various ependymoma cell lines and the mouse neural stem cell line. The neural stem cells have previously been isolated from the cortex of a CD-1® nude female mouse (unpublished). As these mice are used for *in vivo* preclinical efficacy studies, the NSCs are included in drug screens in order to determine how the compounds could affect NSCs in our preclinical models. While the drugs tested here appear to also display a high activity on NSCs, future experiments will need to investigate if these compounds display a general toxicity towards normal brain cells.

The difference in activity of compounds between the different ependymoma cell lines was expected as these cell lines are representing different ependymoma subgroups, which have previously been suggested to react differently to treatments[43]. In order to develop a pan-active therapeutic that can be used to treat all patients suffering from supratentorial ependymoma, it will be important to continue screening compounds on a variety of ependymoma cell lines throughout the drug development process to monitor their activity across the ependymoma subgroups.

As the 1.2 million compound drug screen also triaged NATPROs, I tested the structures that were most potent in mouse choroid plexus carcinoma cells. Despite their high activity in mouse choroid plexus carcinoma cells, the NATPROs tested on ependymoma cells did not display favourable IC_{50}s and were therefore not chosen for follow-up screens (Figure 3.4). This difference in response between the cancer cell lines is in concordance with former observations that different brain tumour types respond differently to treatments[101].

Besides the target-agnostic screening approaches, I also tested compounds with known targets. Atkinson *et al.* previously demonstrated that PLK1 inhibitors efficiently decrease cell viability of ependymoma cells *in vitro*[115].

Sentinel Oncology previously developed Poloppin I, a compound inhibiting the Polo-box domain (PBD) of mitotic PLKs with distinct activity on KRAS-mutant cancer cell lines. Poloppin II- an analogue of Poloppin I was shown to be active in xenografts of these cell lines[295]. Further development of these resulted in the generation of novel BBB penetrable PLK1 inhibitors, which were tested on ependymoma cell lines in cell viability assays (Figure 3.5.). All compounds displayed high activity with IC_{50} values in the low nanomolar range. Due to its strong activity, most developed compound SOL288 was subsequently tested *in vivo*. An MTD study demonstrated that no toxic effects were observed on mice treated with 125mg/kg SOL288. Preclinical study of SOL288 on mSEP-CR(+) mouse model did not reveal any significant difference in tumour growth or survival between SOL288-treated and vehicle-treated mice (Figure 3.6). In this study, we did not collect brains for PK analysis but only for histopathology. Analysis of the tumour area normalised to the whole brain on H&E-stained sections from collected brains further revealed that there was no measurable difference in final tumour sizes (Figure 3-6). Sentinel Oncology had previously collected data of brain exposure for SOL288, in which the compound reached the brain, thereby leading to the hypothesis that systemic delivery of SOL288 would be sufficient for drug delivery in our orthotopic tumour model. Furthermore, during a preclinical efficacy study on a subcutaneous GBM model they observed that tumour growth had been slowed down in animals treated with SOL288 (unpublished). However, despite former data showing that SOL288 was BBB penetrable, it is possible that the drug either did not penetrate the brain at all in our model or that the amounts of drug required to actively interfere with tumour growth were not reached. To confirm if SOL288 crosses the BBB, a PK study would need to be carried out, in which tumour and brain tissues are collected at specific timepoints post-drugging. Mass-spectrometric analysis can then be applied to detect the compound in samples.

However, at the time of the preclinical study, during analysis of the compound by Sentinel Oncology, they discovered that SOL288 is in fact a mixture of two atropisomers- SOL685 and SOL686, which display different activities. As this is

commonly observed in drugs exhibiting atropisomerism, it is important to assess the properties of each enantiomer. Due to the interconverting nature of the structure, we concentrated on the investigation of the activity of the different enantiomers (SOL685, SOL686) on ependymoma models.

Consequently, isolated atropisomers were tested on ependymoma cell lines towards their effect on cell viability (Figure 3.7). The tremendously active atropisomer SOL686 is of particular interest due to its very low IC_{50} values in mSEP-CR(+) and xSEP-CR(+) cells. As fusion-positive ependymoma comprise 70% of all ST-EP cases and are associated with a poor prognosis, it is crucial for active therapeutics to be developed[40,41]. Due to the current standard of care protocol involving radiotherapy, the effect of combination therapy consisting of SOL686 and irradiation was examined (Figure 3.8). No significant effect of the combination therapy was observed. This will be further investigated in preclinical efficacy studies examining the effect of combination therapy. Moreover, the significant differences in $logIC_{50}$ values between cell lines for the drug could be an indication that cells with different genetic backgrounds react differently to the drug *in vivo*. This, too, will need to be monitored in future *in vivo* preclinical efficacy studies.

An MTD study of SOL686 further demonstrated that dosing of mice with 100mg/kg or 125mg/kg does not have any toxic effect on the mice (Figure 3.9). As mice treated with 100mg/kg displayed significant weight gain over time, SOL686 will be tested in preclinical efficacy studies at a dose of 100mg/kg. Pharmacokinetic studies will be performed to investigate the brain exposure of the compound at different timepoints after dosing.

Overall, this chapter underlines the potential of novel chemical compounds with known or unknown mechanisms of actions as possible therapeutics for ST-EP. While natural products did not pass *in vitro* efficacy tests, aminopyrimidine analogues are a promising lead for *de novo* drug development.

As several studies in the drug discovery field have highlighted, thorough examination of structural analogues *in vitro* and *in vivo* are important to provide all requirements for a successful translation of the candidate drug into the clinic[282,305]. Hence, for further

development of candidate NCEs, future experiments will focus on structure-activity relationship assays, investigation of the MMOA and enhancement of the compounds' ADMET properties *in vivo*.

Novel PLK1 inhibitors developed by Sentinel Oncology further display promising activity on ependymoma models *in vitro* and will be translated into preclinical efficacy studies. Furthermore, within the scope of our preclinical mouse hospital described in 1.4, the novel PLK1 inhibitors will be tested in the context of standard of care treatment for ependymoma[101]. The BBB-penetrability will be assessed in pharmacokinetic and pharmacodynamic studies.

3.6. Supplementary Material

Table 3.2: Overview of drug plate numbers, compound names, dilution factors, and concentration ranges for aminopyrimidine analogues.

Plate No.	Compound Name	Dilution factor	Highest concentration in drug plate (mM)	Lowest concentration in drug plate (nM)
SJCH0069834	SJ000865748-1	3	7.76	394
SJCH0069834	SJ000865747-1	3	6.8	345
SJCH0069834	SJ000865746-1	3	5.8	295
SJCH0069834	SJ000865745-1	3	7.7	391
SJCH0069834	SJ000859878-2	3	5.6	285
SJCH0069834	SJ000865778-1	3	7.3	371
SJCH0069834	SJ000519614-2	3	8.2	417
SJCH0069834	SJ000865753-1	3	6.9	351
SJCH0069845	SJ000865754-1	3	6.1	310
SJCH0069845	SJ000865756-1	3	7	356
SJCH0069845	SJ000865757-1	3	8.9	452
SJCH0069845	SJ000865758-2	3	3.12	159
SJCH0069845	SJ000865759-1	3	3.52	179
SJCH0069845	SJ000865760-1	3	6.16	313
SJCH0069845	SJ000865761-1	3	6.32	321
SJCH0069845	SJ000865762-1	3	7	356
SJCH0069846	SJ000865763-1	3	8.1	412
SJCH0069846	SJ000865764-1	3	3.6	183
SJCH0069846	SJ000865765-1	3	3.68	187
SJCH0069846	SJ000865766-1	3	6.2	315
SJCH0069846	SJ000865767-1	3	3.52	179
SJCH0069846	SJ000865768-1	3	19.6	996
SJCH0069846	SJ000865769-1	3	8.32	423
SJCH0069846	SJ000865770-1	3	6.88	350
SJCH0069847	SJ000546270-2	3	6.4	325
SJCH0069847	SJ000546281-2	3	7.2	366
SJCH0069847	SJ000865773-1	3	2.4	122
SJCH0069847	SJ000865774-1	3	7.6	386
SJCH0069847	SJ000865775-1	3	7.84	398

SJCH0069847	SJ000865776-1	3	8.1	412
SJCH0069847	SJ000865777-1	3	8.5	432
SJCH0069847	SJ000868936-1	3	1.84	93.48
SJCH0069848	SJ000868937-1	3	3.2	163
SJCH0069848	SJ000868938-1	3	2.8	142
SJCH0069848	SJ000868938-2	3	2.56	130
SJCH0069848	SJ000868939-1	3	9	457
SJCH0069848	SJ000868940-1	3	3.9	198
SJCH0069848	SJ000868941-1	3	6.1	310
SJCH0069848	SJ000868942-1	3	2.9	147
SJCH0069848	SJ000868943-1	3	4.8	244
SJCH0069849	SJ000868944-1	3	1.84	93.5
SJCH0069849	SJ000868945-1	3	2.08	106
SJCH0069849	SJ000868946-1	3	10	508
SJCH0069849	SJ000868947-1	3	3.5	178
SJCH0069850	SJ000865750-1	3	8.2	417
SJCH0069850	SJ000865749-1	3	10.56	537
SJCH0069850	SJ000519699-2	3	9	457
SJCH0069850	SJ000865751-1	3	6.5	330
SJCH0069850	SJ000865752-1	3	7.92	402
SJCH0069850	SJ000865755-1	3	2.333	119
SJCH0069850	SJ000865771-1	3	2.24	114
SJCH0069850	SJ000865772-1	3	5.68	289
SJCH0069851	SJ000859879-1	3	11.6	589
SJCH0069851	SJ000862533-3	3	3.12	159
SJCH0069851	SJ000862530-1	3	4.8	244
SJCH0069851	SJ000862535-1	3	8.56	435
SJCH0069851	SJ000519199-2	3	7.9	401
SJCH0069851	SJ000862284-1	3	7.9	401
SJCH0069851	SJ000862532-1	3	5.2	264
SJCH0069851	SJ000862538-1	3	5.84	297
SJCH0083043	SJ000869783-1	3	8	406
SJCH0083043	SJ000869784-1	3	8.56	435
SJCH0083043	SJ000869782-1	3	9.04	459
SJCH0083043	SJ000869785-1	3	9.68	492

SJCH0083043	SJ000869781-1	3	8.88	451
SJCH0083043	SJ000869786-1	3	7.5	381
SJCH0083043	SJ000869787-1	3	3.6	183
SJCH0083043	SJ000869797-1	3	3.12	159
SJCH0083044	SJ000869788-1	3	10.4	528
SJCH0083044	SJ000862535-2	3	8.64	439
SJCH0083044	SJ000869780-1	3	7.68	390
SJCH0083044	SJ000869779-1	3	9.36	476
SJCH0083044	SJ000869778-1	3	7.2	366
SJCH0083044	SJ000869789-1	3	5.68	289
SJCH0083044	SJ000861391-2	3	7.4	376
SJCH0083044	SJ000869796-1	3	7.8	396
SJCH0083045	SJ000869777-1	3	16.48	837
SJCH0083045	SJ000869790-1	3	3.92	199
SJCH0083045	SJ000869791-1	3	6.2	315
SJCH0083045	SJ000869795-1	3	9.6	488
SJCH0083045	SJ000869792-1	3	5.1	259
SJCH0083045	SJ000869776-1	3	5.429	276
SJCH0083045	SJ000869775-1	3	9.68	492
SJCH0083046	SJ000869793-1	3	7.3	371
SJCH0083046	SJ000869794-1	3	9.12	463
SJCH0083046	SJ000869774-1	3	8.2	417

Table 3.3: Overview of dilutions for novel compounds by Sentinel Oncology.

Compound Name	Dilution factor	Highest concentration in drug plate in mM	Lowest concentration in drug plate in µM
SOL288	3	10	0.508
SOL322	3	10	0.169
SOL3582-1-A	2	5	4.883
SOL3614-11B	2	5	4.883
SOL578	Semi-log	2	0.02
SOL685	Semi-log	2	0.02
SOL686	Semi-log	2	0.02

Table 3.4: Overview of statistical analysis of dose-response curves of mouse ependymoma cell lines vs. human ependymoma cell line in candidate NCEs.

Test	Drug	Comparison of cell lines	Significance level	P value
One-way ANOVA with Dunnett's multiple comparisons test	SJ000869779-1	xSEP-CR(+) vs. mSEP-CR(+)	****	<0.0001
		xSEP-CR(+) vs. mSEP-CR(-)^{RTBDN}	****	<0.0001
		xSEP-CR(+) vs. mSEP-CR(-)^{EPHB2}	****	<0.0001
	SJ000869791-1	xSEP-CR(+) vs. mSEP-CR(+)	****	<0.0001
		xSEP-CR(+) vs. mSEP-CR(-)^{RTBDN}	****	<0.0001
		xSEP-CR(+) vs. mSEP-CR(-)^{EPHB2}	****	<0.0001
	SJ000869792-1	xSEP-CR(+) vs. mSEP-CR(+)	****	<0.0001
		xSEP-CR(+) vs. mSEP-CR(-)^{RTBDN}	****	<0.0001
		xSEP-CR(+) vs. mSEP-CR(-)^{EPHB2}	****	<0.0001
	SJ000865776-1	xSEP-CR(+) vs. mSEP-CR(+)	****	<0.0001
		xSEP-CR(+) vs. mSEP-CR(-)^{RTBDN}	****	<0.0001
		xSEP-CR(+) vs. mSEP-CR(-)^{EPHB2}	ns	0.2986

Table 3.5: Overview of statistical analysis of dose-response curves of mouse ependymoma cell lines vs. human ependymoma cell line in Sentinel Oncology compounds.

Test	Drug	Comparison of cell lines	Significance level	P value
One-way ANOVA with Dunnett's multiple comparisons test	SOL288	xSEP-CR(+) vs. mSEP-CR(-)RTBDN	****	<0.0001
		xSEP-CR(+) vs. mSEP-CR(-)EPHB2	****	<0.0001
		xSEP-CR(+) vs. mSEP-CR(+)	****	<0.0001
	SOL3582	xSEP-CR(+) vs. mSEP-CR(-)RTBDN	****	<0.0001
		xSEP-CR(+) vs. mSEP-CR(-)EPHB2	****	<0.0001
		xSEP-CR(+) vs. mSEP-CR(+)	****	<0.0001
	SOL3614	xSEP-CR(+) vs. mSEP-CR(-)RTBDN	****	<0.0001
		xSEP-CR(+) vs. mSEP-CR(-)EPHB2	****	<0.0001
		xSEP-CR(+) vs. mSEP-CR(+)	****	<0.0001
	SOL578	xSEP-CR(+) vs. mSEP-CR(-)RTBDN	****	<0.0001
		xSEP-CR(+) vs. mSEP-CR(-)EPHB2	****	<0.0001
		xSEP-CR(+) vs. mSEP-CR(+)	****	<0.0001

4. Hyaluronic acid-based hydrogels as a novel drug delivery method for ependymoma

4.1. Attributions

Preparation of the hyaluronic-acid based polymer and the cucurbit[8]uril (CB8) was performed by Chris Parkins (former PhD Student, Melville Laboratory of Polymer Synthesis at the Department of Chemistry, University of Cambridge) (for FITC-labelled gels) and Paraskevi Kasapidou (Postdoctoral Fellow, Melville Laboratory) (for all other gels used in this chapter). I carried out the gel preparation prior to *in vitro* or *in vivo* experiments. Ultra-High Performance Liquid Chromatography-Mass Spectrometry (UHPLC-MS) was performed by Lee Mendil, Maria Pawula and Dorentina Bexheti from the Pharmacokinetics/ Bioanalytics Core at the CRUK CI. Power calculations for *in vivo* preclinical efficacy studies of drug-loaded hydrogels were performed by statistician Dominique-Laurent Couturier. I performed all other experiments including data analysis.

4.2. Introduction

The BBB represents a major obstacle to the delivery of systemic therapies to brain tumours. Many compounds with promising anti-cancer cell activity *in vitro* have failed translation into the clinic due to unfavourable BBB penetration properties. This problem is compounded by the fact that drug companies typically design drugs not to cross the BBB since this significantly reduces the risk of neurotoxicity. Therefore, research efforts have focused on the development ways of delivering drugs directly into the brain. Additionally, repurposing of FDA-approved drugs has proven efficient in cancer drug development. As these drugs have been tested extensively in preclinical and clinical studies, there is a large quantity of data on their safety and toxicity, which would allow for accelerated testing of these at the preclinical and clinical stages. As most of these drugs display unfavourable BBB penetration properties but are highly active in tumour cells *in vitro*, they need to be combined with approaches that allow for circumvention of the BBB.

This chapter presents the optimisation of a novel local drug delivery approach combined with FDA-approved drugs selected for repurposing in ependymoma mouse models.

4.2.1. The role of repurposed compounds in the quest for a brain tumour cure

The development of novel drugs originally discovered in high-throughput drug screens usually takes one to two decades before receiving final approval from the FDA or the European Medicines Agency (EMA)[257,306]. This is not only a costly process but many drugs fail the transition from *in vitro* to *in vivo* at preclinical or clinical stages (reviewed in[307,308]). Therefore, repurposing, also referred to as repositioning, of FDA- or EMA-approved drugs is highly attractive alternate strategy to identify drugs with anticancer activity that can be used for other distinct tumour subgroups[257,309]. Repurposed compounds include non-cancer drugs or chemotherapeutics used in other cancer types and are either screened alone or in combination with other existing or novel compounds[310,311]. When repurposed as a monotherapy, their development is accelerated due to the availability of data on toxicity and side-effects from previous clinical safety studies. Successfully repurposed drugs include thalidomide, raloxifene and aspirin, which were originally approved for morning sickness, osteoporosis and analgesia, respectively. Thalidomide and aspirin have shown to be beneficial for the survival of multiple myeloma and colorectal cancer patients, while raloxifene was approved by the FDA for the treatment of breast cancer in 2016[312].

Our group has identified promising candidates for drug repurposing in the treatment of ependymoma[47,101,115]. Specifically, Mohankumar and colleagues identified that the cholesterol synthesis pathway is suppressed in ST-EP[47]. Moreover, they demonstrated that ependymoma cells are particularly sensitive against further inhibition of the pathway through the use of statins[47]. Statins are inhibitors of the 3-Hydroxy-3-methylglutaryl-Coenzyme A Reductase (HMGR), a rate-limiting step in the cholesterol synthesis pathway, which reduces HMG-CoA to mevalonic acid[313]. They are commonly used to treat hypercholesterolemia and thereby prevent cardiovascular diseases[314,315]. Additionally, previous studies have suggested statins may reduce the risk of developing glioma and gastric cancer[316,317]. And, they have been proposed as

potential treatments for patients diagnosed with glioma, ovarian cancer and melanoma[318–321].

Our high-throughput drug screens have identified several candidate repurposed drugs active against a range of ependymoma cells *in vitro*[101,115]. They include PLK1 inhibitors, and chemotherapeutics such as gemcitabine. PLK1 inhibitors can be distinguished into non-ATP-competitive and ATP-competitive, with the latter often showing pan-selectivity for other Polo-like kinases[294]. Volasertib (BI6727), an ATP-competitive inhibitor, has efficiently reduced tumour growth in various preclinical studies across several different tumour models. Clinical trials with volasertib on acute myeloid leukaemia patients showed such a significant survival benefit that the drug was awarded the 'Breakthrough Therapy' status by the FDA[294,322,323]. Rigosertib (ON01910), a non-ATP-competitive PLK1-inhibitor, displays dual activity by inhibiting PLK1 and phosphatidylinositide 3 kinase (PI3K). Rigosertib has demonstrated efficacy in various xenograft cancer mouse models and has exhibited promising effects in phase I and II clinical trials[324–327]. Of statins and PLK1 inhibitors, neither rigosertib nor fluvastatin exhibit favourable BBB penetrance properties when tested in preclinical studies[328], making them ideal candidates for testing alternative routes of delivery such as by local drug delivery.

Our lab also showed previously that gemcitabine, a nucleoside analogue first approved by the FDA in 1996, significantly increases survival of mice with ST-EP[101,329]. Gemcitabine is standard of care for pancreatic cancer and has been proposed for the treatment of brain tumours either as a radiosensitizer or in combination with pemetrexed[330,331]. However, prolonged systemic treatment with gemcitabine can result in the development of gemcitabine-resistance (reviewed in [301,332]). This challenge and the short half-life of gemcitabine suggest local delivery approaches for gemcitabine might be of use in brain tumours. In 2017, Bastiancich *et al.* reported how the intratumoural injection of gemcitabine-loaded lipid nanocapsule based hydrogels can prolong survival in a PDX-model for GBM[333].

Moreover, analysis of RNA sequencing data of ependymoma cell lines performed by Birgit Nimmervoll had shown anaplastic lymphoma kinase (ALK), platelet-derived growth factor receptor α and β (PDGFRα/β) and cyclin-dependent kinases (CDK) to

be upregulated in ependymoma cells suggesting these pathways might be important in ependymoma (Figure 4.16). ALK is a tyrosine kinase that is frequently overexpressed in neuroblastoma and whose inhibitors lorlatinib and crizotinib successfully prolong PFS in ALK-positive NSCLC with brain metastases[334–336]. PDGFR, which is commonly expressed in a variety of tumours, is inhibited by crenolanib, which in turn has been tested in clinical trials for paediatric DIPG (NCT01393912) and recurrent and refractory GBM (NCT02626364)[10,337–339]. CDK7 is not only a therapeutic target in ependymoma but also in high-grade glioma and DIPG. The covalent CDK7 inhibitor THZ1 has been found to induce a significant but modest increase in survival in DIPG-xenografts[340,341].

4.2.2. Local drug delivery systems for the treatment of brain tumours include injectable hydrogels

Hydrogels are 3D cross-linked structures composed of hydrophilic polymer chains, which can be moulded into different forms such as films, coatings nano- and microparticles[342]. These gels have been utilised in tissue engineering, wound dressings, drug delivery and as 3D cell cultures[343]. One of their biggest advantages is their property to resemble biological tissues once they are exposed to aqueous environments. This biocompatibility reduces inflammation and interference with surrounding normal tissue. These gels can also be cross-linked through a number of external triggers such as temperature or pH or covalently cross-linked through physicochemical interactions like hydrogen bond formation or the functionalizing of reactive functional groups[342–344].

Due to their large pores, hydrogels can be loaded with cargo, with their drug release properties being modifiable[149]. Thus, they present the ideal drug delivery method as they can produce sustained drug release over a desired amount of time. Their biodegradability further aids drug release and simultaneously means that they do not have to be removed.

With all these advantageous features, they have become of great interest for the treatment of brain tumours as they can be injected intratumoural or into post-resection cavities where they deliver the drug at a controlled rate[345].

4.2.3. Hyaluronic acid-based hydrogels as novel drug delivery methods for the treatment brain tumours

A biodegradable hyaluronic acid-based hydrogel has previously been reported as a novel local drug delivery technique for the treatment of brain tumours[149,346]. Its modifiable properties allow gel viscosity to be altered in order to match its stiffness to the brain parenchyma and brain tumour tissue. It is thought to be used as a local drug delivery method post-surgical resection of the tumour. Due to its viscosity, the gel can mould into tumour cavities allowing for total coverage of the cavity walls[149]. Its backbone is formed of hyaluronic acid (HA), a major component of the brain extracellular matrix. HA is naturally degraded by hyaluronidase, therefore rendering it biodegradable[347,348]. The mechanical features of the gel can further be modified to adjust drug release to a desired rate. All these characteristics mean it presents several advantages over available delivery systems such as the Gliadel® wafers, whose rigid structure does not match the flexibility of the brain parenchyma.

In this chapter, the novel local drug delivery method based on HA-hydrogels was combined with FDA-approved drugs, which were selected for repurposing for treatment of ependymoma. The approach was optimised *in vitro* and *in vivo. In vivo,* the drug delivery technique was implemented into our preclinical mouse hospital, where multimodality treatments representing the standard of care treatment for human ependymoma patients are modelled in mice. Here, each novel treatment method is tested in the context of ependymoma standard of care treatment. The mainstay of treatment remains gross total resection. Hence, drug-loaded hydrogels were implemented into standard-of-care post-resection surgery[101] (Figure 4.1). Directly after debulking the tumour, they were injected into the post-resection cavity in the mouse brain and drug release as well as efficacy was examined.

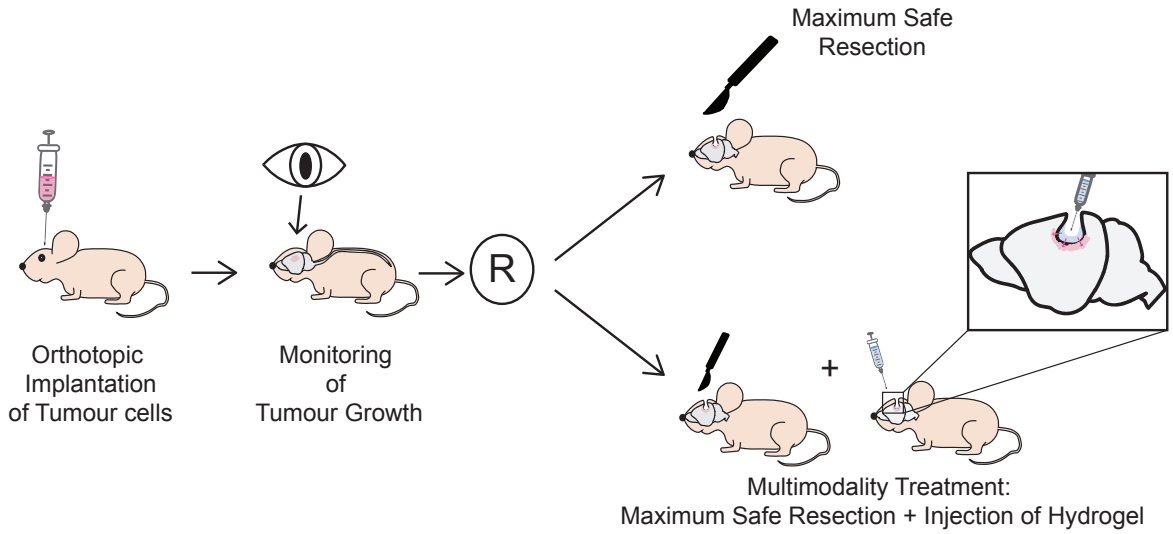

Figure 4.1: Overview of hydrogel as a local drug delivery in a preclinical mouse hospital. Schematic overview of treatment regimen for ependymoma mouse models to include injection of hydrogels. Following implantation of tumour cells, tumour growth is monitored until reaching a certain bioluminescent signal (ranging from $2x10^6$ to $5x10^7$, dependent on tumour model). Mice are randomised into different treatment groups including maximum safe resection and multimodality treatment consisting of maximum safe resection and injection of hydrogels. Once injected, the hydrogel releases drug into the surrounding tissue.

4.3. Methods

4.3.1. *In vitro* assays

4.3.1.1. Cell culture

Ependymoma cells were cultured exactly as described in 2.3.1.1 (see Table 3.1 for an overview of cell lines used). Briefly, they were cultured as neurospheres in ultra-low attachment plates with Neurobasal media supplemented with penicillin-streptomycin, L-glutamine, B27, N2, EGF, FGF and BSA. Cells were passaged every 3-4 days.

4.3.1.2. Drug treatment and cell viability studies

For drug treatment studies, cells were cultured and plated as described in 2.3.1.1 and 3.3.1.2. Briefly, cells were seeded with an automated Multidrop™ in 100µLNeurobasal culture media in 96-well plates. Previous growth curve experiments have determined optimal cell numbers for each cell line (see Table 3.1). Twenty-four hours after plating, cells were treated with 500nl of solution containing the compounds of choice dissolved in DMSO. Cells treated with DMSO only served as negative controls in each plate. Cell viability was determined with CellTiterGlo®. To generate dose-response curves, cells were drugged with decreasing drug concentrations ranging from 25µM to 0.024µM, 25µM to $1.7x10^{-5}$µM or 2.5µM to 0.0024µM (see Supplementary Table 4.4).

4.3.2. Hydrogel assays

4.3.2.1. Hydrogel preparation and drug loading

UV-sterilised peptide-functionalized hyaluronic acid polymer (HA_{CF}) was kindly supplied by Chris Parkins and Paraskevi Kasapidou from the Melville laboratory of Polymer Synthesis at the Department of Chemistry, University of Cambridge and has been formulated as described previously by Rowland *et al*. 2018[149].

Experimental hydrogels were prepared under sterile conditions, 24-48h prior to use and preparation was performed as follows. For a 2wt% gel, in compliance with protocol one, drugs were dissolved in respective amounts of PBS, depending on the desired

final concentration, and vortexed to allow for complete resolving of the drug. For a 2wt% gel, 20mg of HA_{CF} and 5mg CB8 were dissolved in 1mL of either PBS only for unloaded hydrogels or PBS- drug solution for drug-loaded hydrogels.

In accordance with protocol two, CB8 was first dissolved in PBS for 20min at 37°C. Afterwards, the HA_{CF} polymer and either gemcitabine, fluvastatin or rigosertib were added at different concentrations. Continuous stirring at 400-600rpm for 18-48h resulted in a homogenous hydrogel.

4.3.2.2. FITC labelling of polymer

FITC labelling of HA_{CF} was performed by Chris Parkins as described previously[149]. Briefly, fluorescein isothiocyanate (FITC; 1mg) was stirred overnight into a solution of 100mg HA_{CF} and 25mL water. Following several water changing steps, the polymer was recovered by lyophilisation once the dialysis solution did not stain yellow anymore.

4.3.2.3. Time-release basket assays

24-well microplates were filled with 600µL of cell culture media per well. Cell culture inserts (Greiner) were placed into each well and filled with 20-250µL of drug-loaded or unloaded control hydrogel. At specific timepoints (1h, 2h, 3h, 4h, 5h, 6h, 7h, 8h, 10h, 24h, 48h, 72h, 96h, 145h, 168h, 264h, 336h), total volume of media was collected and wells were re-filled with new culture media. At the last collection timepoint (336h), hydrogels from 24-well cell inserts were sampled along with media from within the 24-wells. Collected media was flash-frozen and stored at -80°C until processed by PK-D core at the CRUK Cambridge Institute.

4.3.2.4. Drug release basket assays

Cells were cultured as described in 2.3.1.1. For drug release studies, ependymoma cells were seeded into 24-well microplates plates (Perkin-Elmer) at previously determined cell densities (mSEP-CR(+)= 24,000 cells/well; mSEP-CR(-)^{EPHB2} =15,000 cells/well) in 600µL Neurobasal media containing the relevant growth factors. After 24h, cell culture inserts were placed into each well and filled with 50-100µL of drug-loaded or unloaded hydrogel. After another 72h, images of neurospheres grown under the different conditions were acquired using a brightfield microscope (Axio Vert.A1, Zeiss).

4.3.2.5. Sample preparation for UHPLC-MS

Ultra-high-performance liquid chromatography (UHPLC) followed by mass-spectrometry (MS) (UHPLC-MS) was used to detect residues in samples of media, cells and hydrogels. This was performed by Maria Pawula, Lee Mendil and Dorentina Bexheti as specified in 4.1.

Prior to the measurement of the samples, calibration standards were prepared for each drug for *in vitro* and *in vivo* assays (see Table 4.1). For gemcitabine samples, media and plasma were treated with 1µL of THU to prevent enzymatic degradation. For all drugs, media and plasma samples were then prepared as follows: Briefly, internal standard solution was added (20µL sample, 10µL standard solution), followed by 150µL methanol. Samples were mixed via vortexing, centrifuged (6800g for 12min) and evaporated to dryness. Reconstitution of samples was achieved with water: methanol (9:1), followed by mixing and centrifugation before samples were loaded onto LC-MS/MS.

Hydrogels were first diluted in water:methanol (9:1) and then processed as outlined above. Unloaded hydrogels served as controls.

Following accurate weighing of the brain samples, they were homogenised in appropriate amounts of water:methanol (9:1) to generate a 200mg/mL homogenate solution. Afterwards, samples were described as above.

Table 4.1: Overview of mass-spectrometry calibration standards for gemcitabine, fluvastatin and rigosertib.

Sample/ Drug	Gemcitabine	Fluvastatin	Rigosertib
Media	0.076 – 152μM	0.608-243μM	0.111-221.5μM
Gel	0.076 - 152μM	0.122-243μM	0.111-221.5μM
Plasma	0.00190 - 0.378μM	0.0608-243μM	0.00111-2.21 μM
Brain	0.00475 - 1.90μM	0.003-121.5μM	0.005-11.05μM

4.3.3. *In vivo* studies

4.3.3.1. Mice used and husbandry

Eight to twelve- week-old immunodeficient CD1® female nude mice were purchased from Charles River (strain code 086) and housed in compliance with the UK Home Office license (P6787677F). They were housed under pathogen-free conditions in groups of 2-5 per cage on a 12h light cycle in air-filtered cages and received regular food and water *ad libitum*.

4.3.3.2. Orthotopic allografts and xenografts

Orthotopic allografts of ependymoma cells were performed as described in 2.3.2.2. Briefly, mouse or human ependymoma cells were resuspended in 5 or 7μL Matrigel®, respectively, and implanted using a stereotax into the cerebral cortex of brains of 8 to 12-week-old CD1 nude. Table 4.1 lists cell line, species, driver oncogenes, tumour subgroup and implanted cell number for each tumour model. Bioluminescence imaging was applied to assess tumour growth throughout the course of each study. Mice were further assessed regarding neurological symptoms 2-3 times a week.

Table 4.2: Overview of mouse and human cells used for allografts and xenografts.

Cell line	Species	Driver Oncogene	Tumour Subgroup	Implanted cell number
mSEP-CR(+)[101]	*Mm*	*C11orf95-RELA fusion*	ST-EP-CR	50,000
mSEP-CR(-)$^{RTBDN, 47}$	*Mm*	*RTBDN*	ST-EP-CR(-)	10,000
mSEP-CR(-)$^{EPHB2, 38}$	*Mm*	*EPHB2*	ST-EP-CR(-)	5,000
xSEP-CR(+)	*Hs*	*C11orf95-RELA fusion*	ST-EP-CR	1,000,000

Mm- Mus musculus, Hs- Homo sapiens; ST-EP-CR- C11orf95-RELA fusion-positive supratentorial ependymoma; ST-EP-CR(-) C11orf95-RELA fusion-negative supratentorial ependymoma

4.3.3.3. Bioluminescence imaging

Tumour sizes of tumour-bearing mice were measured via bioluminescence imaging once to twice per week. All tumour cell lines were expressing a firefly luciferase reporter linked to a yellow fluorescent protein (YFP) tag, thereby enabling tumour visualisation in live animals. To image tumour cells, mice were injected intraperitoneally with 200µL of D-Luciferin (Perkin-Elmer) and imaged within 5-10min post-Luciferin injection under anaesthesia. Imaging was performed using a XENOGEN IVIS200 (Caliper Lifesciences). The average cumulative bioluminescence was plotted using GraphPad Prism v.7.

4.3.3.4. Preclinical efficacy studies of systemic fluvastatin

Preclinical efficacy studies of systemic fluvastatin were performed as described previously[101]. Briefly, mice implanted with mSEP-CR(+), mSEP-CR(-)^{RTBDN} or xSEP-CR(+) cells were subjected to treatment with 20mg/kg of fluvastatin treatment via oral gavage. Prior to treatment, fluvastatin sodium was dissolved in 0.5% carboxymethylcellulose. Mice treated with 0.5% carboxymethylcellulose served as controls. Both, fluvastatin and the vehicle control were administered in a 5-days-on, 2-days-off treatment regimen starting on Day 4 post-implant. On Day 4 post-implants, all mice displayed BLI tumour signals representative for established tumours ranging

from 10^5 photons/seconds for mSEP-CR(-)^{RTBDN} models to 10^7 photons/seconds for xSEP-CR(+) models. Mice were randomised according to their signals and allocated into different treatment groups (20mg/kg fluvastatin; vehicle control). Mice of mSEP-CR(+) and mSEP_CR(-)^{RTBDN} models received the treatments over three weeks, while mice of the xSEP-CR(+) model were subjected to the treatment over 16 weeks. Tumour growth was measured via BLI and mice were sacrificed once they displayed clinical symptoms. Previous power calculations had revealed that 10 mice for control groups and 15 mice for treatment groups would be necessary in order for the two-sided 5% level Wilcoxon test to have an 80% power to detect a setting in which there is an 80% probability that a random animal from the treatment group survives longer than an animal from the control group. In order to save mice, we started with a smaller number of mice per treatment group and observed the groups. If a trend was detectable, more mice would have been subjected to the treatments. As the Wilcoxon test has poor properties if the sample size is <7, preclinical efficacy studies were started with 7 mice per treatment group.

4.3.3.5. Preclinical neurosurgery and post-op care

In accordance with previously published studies, mice with established tumours with BLI signals of >2x10^6 photons/seconds were subjected to preclinical neurosurgery[101]. Preclinical neurosurgery of tumour-bearing mice was performed in compliance with aseptic technique. Prior to surgery, mice were injected with 0.3mg/mL of buprenorphine. Anaesthetised mice were fixed into a stereotactic frame and surgery site on the head was cleaned using iodine and 70% EtOH. Surgery was performed under a surgical microscope (Leica F40). A small incision was made to open the scar from the previous tumour implant. The periosteum covering the cranial window was removed using sterile cotton swabs. Bipolar forceps attached to a bipolar cutting electrosurgical unit (both MEGADYNE™, Ethicon) were then used to break apart the cortical tissue at the side of the cranial window. Upon exposure of the brain parenchyma, brain tumour tissue was removed using 24-26 Gauge suction tubes (Miltex). Haemorrhage was stopped either with small pieces of Lyostypt® (Braun) or SURGICEL® (Ethicon) and by cauterizing vessels using bipolar forceps. Once haemostasis was achieved, the resection cavity was optionally rinsed with warm PBS

to clean it from clotted blood. Optimisation surgeries included optional filling of the cavity using a small piece of SURGICEL® to prevent post-operative bleeding. It further included the sealing of the resection cavity using a small piece of artificial dura (TissuePatchDural™, TissueMed). The dura was cut into shape for each cavity individually (typically squares sized ~3x3mm) and pressed onto the window using a damped cotton swab for 30sec. Incision was closed with 3-4 stitches. To confirm successful resection, animals were subjected to BLI as described in 4.3.3.3.

For the first 72h post-surgery, animals were monitored closely for any post-operative complications. During this time, animals received an injection of a "post-op care drug mix" intraperitoneally every 6 hours (Q6H). Table 4.2 lists dilutions, doses and mechanism of action for each drug.

Table 4.3: Overview of drugs contained in the post-operative care drug mix.

Name of drug / fluid	Manufacturer	Dilution	Typical dose per animal (Total volume per dose= 0.5mL)	Description
Depo-medrone	Star Pharmaceuticals	1:50	0.1mL = 0.08mg	Anti-inflammatory Glucocorticoid
Dexa-methasone	Aspen Pharma	1:20	0.1mL = 0.018mg	Corticosteroid
Mannitol (20%)	Fresenius Cabi	-	0.13mL = 0.026g	Osmotic Diuretic
Saline	Vetivex	-	0.17mL	

4.3.3.6. Preclinical neurosurgery and hydrogel injection

Preclinical neurosurgery was performed as described in 4.3.2.4. Prior to surgery, hydrogels were filled into 2mL Hamilton syringes and subsequently pushed into 1mL Hamilton syringes. Upon successful resection and achieved haemostasis, hydrogels were injected into resection cavities through a sterile 25 Gauge needle. Gel was left to set for 1-2min before cavity in optimised resection surgeries was sealed with a fitted patch of TissuePatchDural™ (Tissuemed). Afterwards, the wound was closed as described in 4.3.3.5.

Based on historical survival data from different treatments in our ependymoma mouse models, biostatistician Dominique-Laurent Couturier has calculated that each treatment group containing drug-loaded hydrogels will need mouse numbers of at least 13 mice per group. This is necessary in order for the two-sided 5% level Wilcoxon test to have an 80% power to detect a setting in which there is an 80% probability that a random animal from the treatment group survives longer than an animal from the control group.

4.3.3.7. Brain Sample collection and Haematoxylin & Eosin staining

Mice that displayed neurological symptoms were euthanised via CO_2, followed by second confirmation of death. Brains were dissected, cut in half along the midline and fixed in neutral buffered formalin (NBF) for 24h prior to submersion in 70% EtOH. Brains were embedded in paraffin and 5µm thick sagittal sections were prepared and stained for H&E at the Histopathology core at the Cancer Research UK Cambridge Institute.

4.3.3.8. Fluorescent imaging of mouse brains

For fluorescence imaging of FITC-labelled gels in cavities, freshly dissected brains were placed into 6mm dishes and coated with PBS. Imaging of FITC-labelled gel was performed using a Leica M205 FA fluorescent microscope. Post-imaging, brains were fixed and processed as described in 4.3.3.7.

4.3.3.9. Pharmacokinetic studies

Blood samples and brains were collected at specific timepoints (1h, 8h, 24h, 72h, 144h) post gel-injection from three animals at each timepoint. Blood was collected via cardiac puncture following euthanasia with CO_2 and second confirmation of death via severing of the femoral artery. Syringes coated with 0.5M EDTA were used to collect blood which was transferred into 1.5mL Eppendorf tubes containing 20µL of 0.5M EDTA. Following a short centrifugation step of 3min at 14,800rpm, plasma was transferred into new tubes and probes were stored at -80°C until processed by PK-D

core at the CRUK Cambridge Institute. Brains were dissected and cut into four different sections and flash frozen on dry ice before being stored at -80 until processed further. Samples were processed as described in 4.3.2.6.

4.3.4. Data analysis

Cell Titer Glo® measurements in cell viability assays that had been performed in triplicates for each drug per cell line, were analysed using MARS software followed by GraphPad Prism version 7 (v.7). R Studio was used for the presentation of IC_{50} values. Extra sum-of-squares F-test was performed to compare dose-response curves of cell lines for each drug. One-way ANOVA with Tukey's multiple comparison test was further applied to specifically analyse statistical significance between dose-response curves of different cell lines.

Data from *in vivo* studies were plotted using GraphPad Prism v.7. Statistical analyses were conducted using GraphPad Prism v.7. Weight loss between treatment groups were analysed using unpaired t-tests. Paired t-tests with or without Welch's correction, depending on the SD values for the different groups, were applied for weight loss analysis within treatment groups. Log-rank tests were carried out for analysis of survival curves.

H&E-stained slides were analysed using Aperio eSlide manager and Aperio Image Scope (both Leica). GraphPad Prism v.7 was used for plotting and statistical analysis of data (unpaired t-test).

4.3.5. Workflow of project

Hydrogels were established as novel drug delivery technique in ependymoma models following several different steps *in vitro* and *in vivo*. Figure 4.2 displays workflow of the project.

1) *In vitro* drug screens of FDA-approved drugs

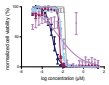

2) Preclinical efficacy study of systemically delivered fluvastatin

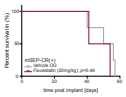

3) *In vitro* time-course drug release study for candidate drugs

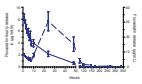

4) Effects of drugs-released from hydrogel on ependymoma cells *in vitro*

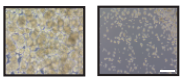

5) Pilot study of hydrogel injection post resection surgery

6) Identification of challenges for hydrogel-based drug delivery *in vivo*

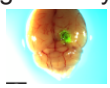

7) Optimisation of resection surgery technique to involve injection of hydrogel

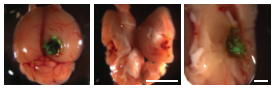

8) Pharmacokinetic study for hydrogel-based drug release *in vivo*

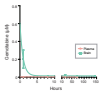

9) Preclinical efficacy study of gemcitabine-loaded hydrogels in ependymoma models

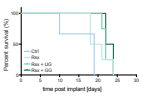

Figure 4.2: Overview of workflow for establishment of hydrogels as novel drug delivery in ependymoma models. 1) *In vitro* drug screens of FDA-approved drugs to select candidate compounds for repurposing. **2)** Efficacy study of systemically delivered fluvastatin in preclinical ependymoma models. **3)** Time-course drug release studies for gemcitabine, fluvastatin and rigosertib *in vivo*. **4)** *In vitro* efficacy study of drugs released from hydrogel on ependymoma cells. **5)** Pilot study of hydrogel injection into post-resection cavities in ependymoma mouse models *in vivo*. **6)** Identification of challenges that could affect hydrogel-based drug delivery in resection cavities. **7)** Optimisation of resection technique to resolve challenges identified previously. **8)** Pharmacokinetic studies of hydrogels loaded with gemcitabine, fluvastatin or rigosertib in ependymoma mouse model. **9)** Preclinical efficacy study of gemcitabine-loaded gel in mSEP-CR(-)^{EPHB2} ependymoma mouse model.

4.4. Results

Standard-of-care treatment for ependymoma has not changed over 40 years and is limited to surgical resection and irradiation occasionally with chemotherapy. This treatment results in significant side-effects and up to 40% of patients ultimately succumb to their disease.

There are different approaches in drug development to identify candidate drugs for brain tumour therapy. While chapter 3 of this thesis focuses on the screening of novel compounds, this chapter describes the identification of FDA-approved drugs for drug repurposing, which will be used in combination with a novel drug delivery.

4.4.1. Anticancer and non-oncology drugs identified as lead compounds for drug repurposing

To identify FDA-approved drugs with activity in ependymoma cell lines, I tested a variety of cell cycle inhibitors, antineoplastic drugs and anticancer drugs selected from previous high-throughput screens and tumour biology studies (see 4.2.1). These included statins, PLK1 inhibitors as well as a range of anticancer drugs such as carboplatin, crizotinib, crenolanib, doxorubicin, etoposide, gemcitabine, lorlatinib, temozolomide and THZ1.

The activity of these thirteen drugs was tested against five different cell lines including one human ependymoma cell line (xSEP-CR[+]),three mouse ependymoma cell lines (mSEP-CR[+], mSEP-CR[-]^{RTBDN}, mSEP-CR[-]^{EPHB2}) and mNSCs (Figure 4.1). Compounds were tested in dose-response cell viability assays (CellTiterGlo®) and IC_{50} values calculated from four biological replicates.

Based on the results for IC_{50} values from previous screens, most drugs were tested in dose-responses with concentrations ranging from 24nM to 25µM (Supplementary Table 4.4)[47,101,115]. Due to their very high activity in ependymoma cells, doxorubicin and gemcitabine were tested in extended dose-responses with concentrations ranging from 11.9pM to 25µM. As THZ1 displayed high activity in xSEP-CR(+) cells, it was

tested in lower dilutions ranging from 2.4nM to 2.5µM to determine accurate IC_{50} values for xSEP-CR(+) cells.

As previously applied for drugs screened in chapter 2, a 1µM threshold for IC_{50}s was set to with all drugs displaying IC_{50}s below 1µM being classified as active. Figure 4.3 presents IC_{50} values for all drugs across all cell lines.

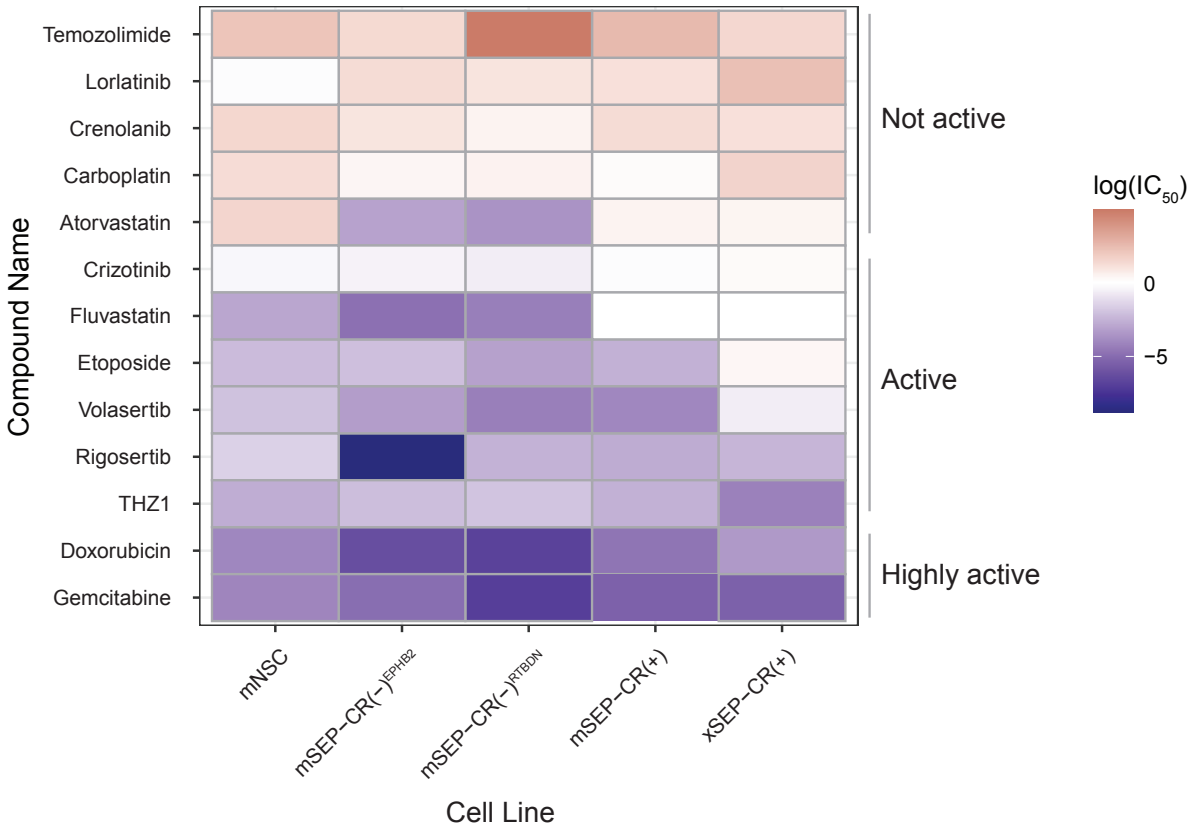

Figure 4.3: Activity of repurposed drugs against ependymoma cell lines *in vitro*. Selection of FDA-approved drugs included a range of anticancer drugs, PLK1 inhibitors and statins. Drugs were tested against a range of mouse ependymoma cells (mSEP-CR[+], mSEP-CR[-]^{RTBDN}, mSEP-CR[-]^{EPHB2}), a human ependymoma cell line (xSEP-CR[+]). Mouse neural stem cells (mNSCs) served as controls. Heat-map represents log IC_{50} across all drugs and cell lines. Compounds with IC_{50} values above 1µM were classified as not active, while drugs reaching IC_{50}s below 1µM were considered active. Highly active compounds achieved IC_{50} values of 0.05µM and below. (n=4)

In total, five drugs (temozolomide, lorlatinib, crenolanib, carboplatin, atorvastatin) were considered not active based on their IC_{50} values (Figure 4.3). Six compounds (crizotinib, fluvastatin, etoposide, volasertib, rigosertib, THZ1) were classified as active as they produced IC_{50} values below 1µM in all ependymoma cell lines. Gemcitabine and doxorubicin were classified as highly active due to their IC_{50} values laying below 0.05µM in ependymoma cell lines.

For the establishment of local drug delivery via hydrogels in ependymoma mouse models, we wanted to select drugs that displayed high activity on ependymoma cells *in vitro* but had demonstrated poor BBB penetrability properties following systemic delivery *in vivo*. On the basis of this, we selected fluvastatin and rigosertib. Both showed high activity in ependymoma cell lines (Figure 4.3 and 4.4) and had previously been reported to present BBB-penetration properties unfavourable for brain tumour therapeutics[328,349].

In order to include a control drug that would allow for proper examination of the feasibility of hydrogel-based drug delivery gemcitabine was included. Gemcitabine not only displayed high activity on ependymoma models *in vitro* but also significantly increased survival *in vivo* following systemic delivery via Alzet pumps[101]. Thus, we hypothesized that gemcitabine would achieve at least the same but potentially even better efficacy when delivered locally in post-resection ependymoma models[101]. Furthermore, local delivery might allow for gemcitabine concentrations to be lowered, thereby reducing side effects.

Figure 4.4 displays the dose-response curves of these compounds tested on a variety of cell lines *in vitro*. Strikingly, a ~10-100x fold change in IC_{50} values for fluvastatin between mSEP-CR(+) and mSEP-CR(-)$^{RTBDN/EPHB2}$ cells was observed. $LogIC_{50}$ values are significantly lower for mSEP-CR(-)^{RTBDN} and mSEP-CR(-)^{EPHB2} cells compared to mSEP-CR(+) and xSEP-CR(+) (one-way ANOVA with Tukey's multiple comparison; ****: $p<0.0001$). For rigosertib, the IC_{50}s for all ependymoma cell lines were below 100nM, while IC_{50} values for gemcitabine were below 8nM for all ependymoma cell lines. Curve comparisons for both drugs further revealed significant

differences between dose-response curves of the different cell lines (extra sum-of-squares F-test; ****: p<0.0001).

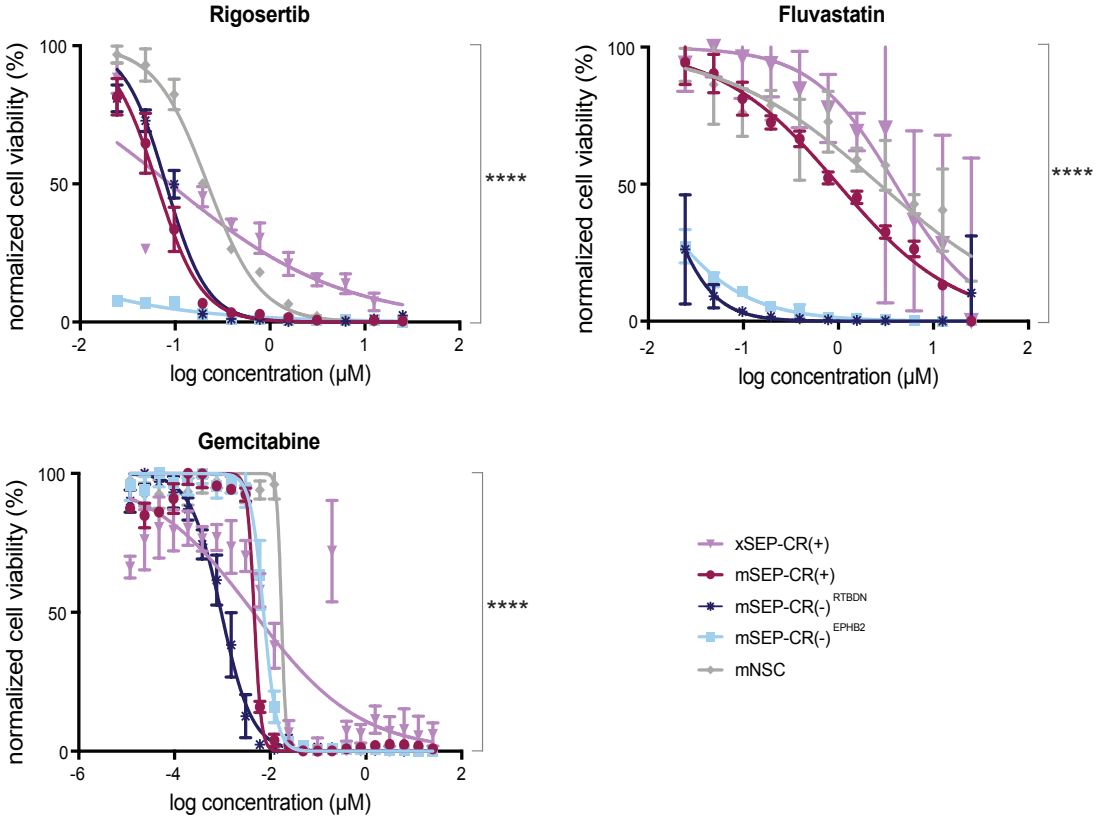

Figure 4.4: Dose-response curves for drugs selected for repurposing. Dose-response curves for fluvastatin, rigosertib and gemcitabine tested on mSEP-CR(+), mSEP-CR(-)^{RTBDN}, mSEP-CR(-)^{EPHB2}, xSEP-CR(+) and mNSC cells. Error bars represent SD, n=4. Extra sum-of squares F-test was applied to compare dose-response curves of the different cell lines for each drug (****: p<0.0001).

In vitro, gemcitabine, fluvastatin and rigosertib displayed high activity in ependymoma cells. To ensure that systemic delivery of selected drugs does not have a beneficial effect on survival in ependymoma mouse models, drug activity *in vivo* had to be assessed.

Data on *in vivo* efficacy of systemically delivered gemcitabine and rigosertib has been published previously[101,328]. Nimmervoll *et al*. showed in 2018 that systemic delivery via pump infusion of gemcitabine, prolongs survival in ependymoma mouse models[101]. Nuthalapti and colleagues investigated *in vivo* activity of systemically administered

rigosertib in a glioma mouse model and found that brain penetrance of systemically delivered rigosertib is unfavourable for the treatment of brain tumours[328].

4.4.1.1. Systemic delivery of fluvastatin does not have an effect on tumour growth or overall survival in ependymoma models

One study published in 1993 demonstrated that systemic fluvastatin displays low BBB-penetrability *in vitro* and *in vivo*[349]. However, there are no studies published more recently on the BBB penetrability of fluvastatin. Hence, we wanted to investigate the effect of systemically delivered fluvastatin on tumour growth and survival in our ependymoma models. Previous maximum tolerated dose studies of orally administered fluvastatin performed in our lab had determined that the clinical dose of 20mg/kg fluvastatin is also tolerated in mice (unpublished). Therefore, in order to examine the effects of systemically administered fluvastatin on tumour growth in our mouse ependymoma models, it was tested in preclinical efficacy studies in three different ependymoma models.

Mice were implanted either with mSEP-CR(-)^{RTBDN} (n=15), mSEP-CR(+) (n=15) or xSEP-CR(+) cells (n=15). Following establishment of tumours, which was confirmed through a BLI signal of >1x10^5, mice were randomised according to their BLI tumour signals on Day 4 post-implant and allocated to two treatment groups receiving either fluvastatin or a vehicle via oral gavage. Mice were subjected to either 20mg/kg fluvastatin or vehicle control (0.5% carboxymethylcellulose) treatment via oral gavage, following a 5-day treatment schedule for 3-16 weeks, depending on the model (Figure 4.5A). While mSEP-CR(-)^{RTBDN} and mSEP-CR(+) mice received treatment over three weeks, the treatment window of xSEP-CR(+) was extended to 16 weeks (Figure 4.5 A&B).

Originally, seven mice of the xSEP-CR(+) model had been allocated to the control group and eight mice were receiving fluvastatin treatment. However, three mice in total (1x control, 2x fluvastatin group) had to be excluded due to health concerns unrelated to tumour burden and were subsequently censored in the survival analysis.

Statistical analysis of survival revealed that no significant difference between the treatment groups in the xSEP-CR(+) model (Log-rank, ns: p=0.23) (Figure 4.5C). Tumour growth for both treatment groups did also not differ significantly (Mann-Whitney Test; ns: p=0.21).

Eight mice of the mSEP-CR(+)model received 20mg/kg fluvastatin, while seven mice were treated with the vehicle. There was no statistical difference in survival between mSEP-CR(+) mice treated with vehicle or fluvastatin (Log-rank; ns: p=0.46). While there is also no overall significant difference in tumour growth for mSEP-CR(+) models treated with either vehicle or fluvastatin (Mann-Whitney Test; ns: p=, there is a significant difference between the BLI curves from Day 40 onwards (Mann-Whitney Test; **: p=0.0079). Here, fluvastatin-treated animals display a significantly slower tumour growth than vehicle-treated models. This is difference in tumour growth would suggest that the fluvastatin might reach the brain and have an effect on tumour growth. This is not reflected in survival as the tumours have already reached sizes where the mice start succumbing to the disease (tumour BLI average >5x10^7 photons/sec).

Of the mSEP-CR(-)^{RTBDN} mice, seven mice received fluvastatin treatment, while vehicle was administered to six mice. Two mice had to be excluded due to health concerns prior to the treatment. This was due to the slow tumour growth of the model (Figure 4.5B). Over the course of the treatment, bioluminescence imaging was applied to monitor tumour growth. Mouse brains were harvested when mice started exhibiting clinical symptoms related to tumour burden such as weight loss or hunched back. Statistical analysis of survival revealed that no significant difference between the treatment groups in the mSEP-CR(-)^{RTBDN} models (Log-rank; ns: p= 0.9) (Figure 4.5E). There was further no significant difference in tumour growth for the different treatments groups of mSEP-CR(-)^{RTBDN} models (Mann-Whitney Test; ns: p=0.39).

On the basis of the result from our study, which were corroborated by results reported in the literature, fluvastatin was chosen to be taken forward for the development of a novel local drug delivery technique.

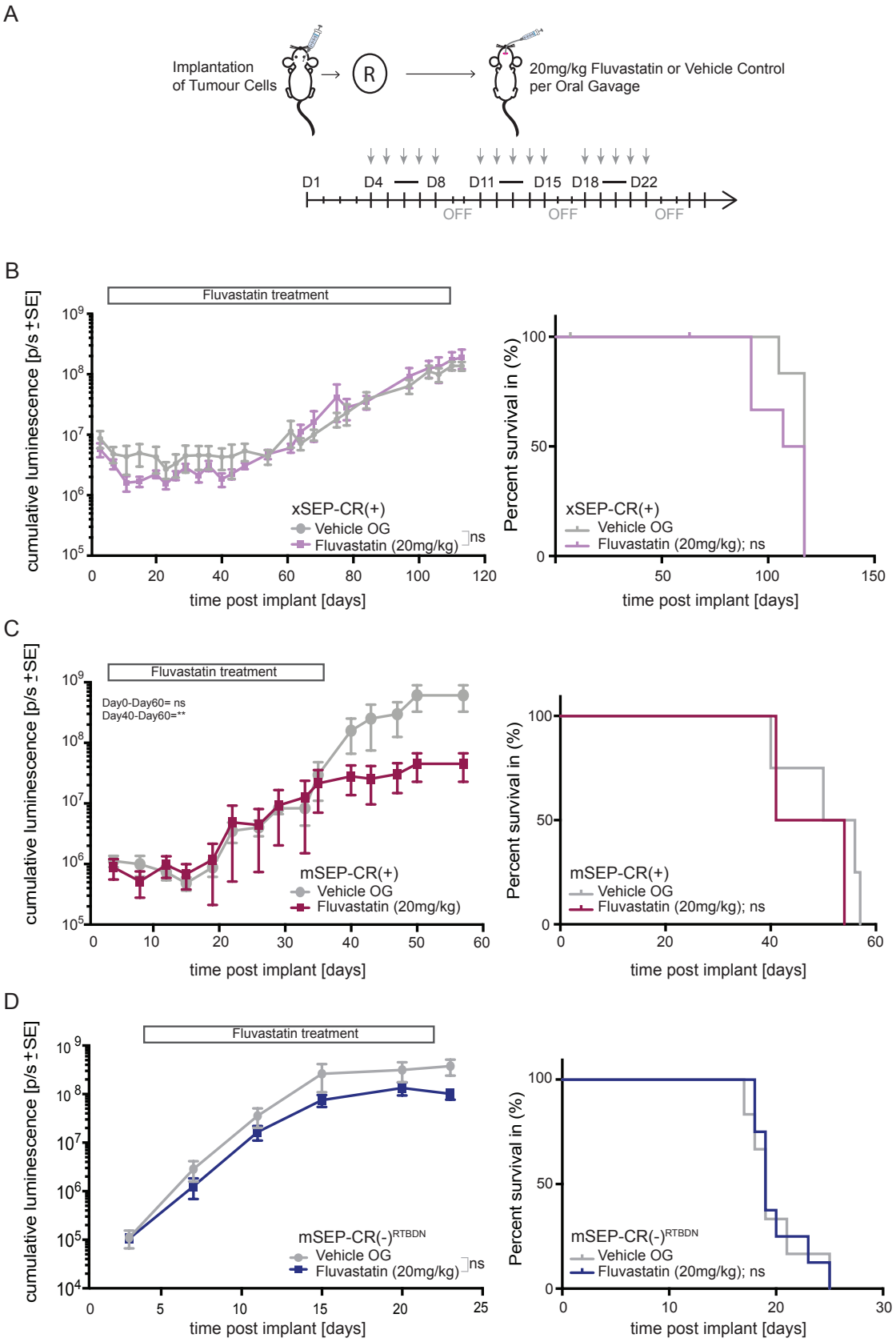
A
Implantation
of Tumour Cells
R
20mg/kg Fluvastatin or Vehicle Control
per Oral Gavage
D1
D4
D8
D11
D15
D18
D22
OFF
OFF
OFF
B
Fluvastatin treatment
cumulative luminescence [p/s ± SE]
time post implant [days]
xSEP-CR(+)
Vehicle OG
Fluvastatin (20mg/kg)
ns
Percent survival in (%)
xSEP-CR(+)
Vehicle OG
Fluvastatin (20mg/kg); ns
time post implant [days]
C
Fluvastatin treatment
Day0-Day60= ns
Day40-Day60=**
cumulative luminescence [p/s ± SE]
time post implant [days]
mSEP-CR(+)
Vehicle OG
Fluvastatin (20mg/kg)
Percent survival in (%)
mSEP-CR(+)
Vehicle OG
Fluvastatin (20mg/kg); ns
time post implant [days]
D
Fluvastatin treatment
cumulative luminescence [p/s ± SE]
time post implant [days]
mSEP-CR(-)RTBDN
Vehicle OG
Fluvastatin (20mg/kg)
ns
Percent survival in (%)
mSEP-CR(-)RTBDN
Vehicle OG
Fluvastatin (20mg/kg); ns
time post implant [days]

Figure 4.5: Systemic delivery does not have any effect on tumour growth or survival in ependymoma *in vivo* models. A. Overview of experimental setup. Mice were implanted with ependymoma cell lines and randomised into treatment groups on Day 4 post-implant. Mice were treated with a 5day schedule for up to 16 weeks with 20mg/kg Fluvastatin or vehicle control. **B.** Bioluminescence imaging and Kaplan-Meier survival curves for xSEP-CR(+) ependymoma models treated with fluvastatin or vehicle. Error bars represent SD, n=6 per treatment group (Statistical analysis of tumour growth using Mann-Whitney test; ns: p=0.21), (Statistical analysis of survival using Log-rank; ns: p=0.23). **C.** Bioluminescence imaging and Kaplan-Meier survival curves for mSEP-CR(+) ependymoma models treated with fluvastatin or vehicle. Error bars represent SD, n=7 for control, n=8 for fluvastatin-treated mice per treatment group (Statistical analysis of tumour growth using Mann-Whitney test; ns: p=0.67; Statistical analysis of tumour growth between Day40 and Day60 using Mann-Whitney test; **: p=0.0079), (Statistical analysis of survival using Log-rank; ns: p=0.46). **D.** Bioluminescence imaging and Kaplan-Meier survival curves for mSEP-CR(-)^{RTBDN} ependymoma models treated with fluvastatin or vehicle. Error bars represent SD, n=6 for control, n=7 for fluvastatin-treated mice per treatment group (Statistical analysis of tumour growth using Mann-Whitney test; ns: p=0.39), (statistical analysis of survival using Log-rank; ns: p=0.9).

4.4.2. Establishing a hyaluronic acid-based hydrogel as novel delivery technique for ependymoma models *in vitro*

As discussed in 1.5.1, a variety of local drug delivery techniques exist to circumvent the BBB. These include nanoparticles, focused ultrasound and implantable wafers[140,350,351]. While some of these have been approved and are used for the treatment of brain tumours, others are still in the development. One of the delivery techniques currently in development is the hyaluronic-acid based hydrogel developed by the Melville laboratory of Polymer Synthesis led by Professor Oren Scherman[149,346]. This technology can be used to line post-resection cavities and therefore deliver drug directly to residual tumour cells post-resection with the aim of achieving cure.

4.4.2.1. Confirmation of hydrogel-based drug-release of gemcitabine, fluvastatin and rigosertib over time *in vitro*

In collaboration with Chris Parkins, we previously studied gemcitabine, fluvastatin and doxorubicin release from hydrogel. This revealed an initial bolus release for drugs in

the first 8h, followed by a slower release reaching a maximum release of 20-30%, depending on the drug (unpublished). These release studies deployed UV/ vis spectroscopy. Since our *in vivo* drug-release studies would deploy UHPLC-MS, we repeated *in vitro* time-course drug-release studies for fluvastatin, gemcitabine and rigosertib utilizing UHPLC-MS.

In order to test the amount and pace of drug-release from hydrogels, 24-well basket assays were performed. Just like in the previous study, each gel was loaded with 1mg/mL of either gemcitabine, fluvastatin or rigosertib. So-called basket cell-inserts loaded with gels were placed into media-filled wells of 24-well plates. Unloaded gels served as controls. Over the course of 336 hours, media samples were collected at 17 different timepoints. Five replicates were collected for each sample. Drug-loaded gel collected prior to the time-course study served as a reference control.

Figure 4.6A displays the relative concentration in percent of drug in gel. This was normalised to the concentration of 1mg/mL for each drug. Figure 4.6B demonstrates the release rate for each drug in µg/mL/h at each collection timepoint. In order to allow comparison of percentage release for drugs between our MS-release experiment and the previous experiments that deployed UV/ vis spectroscopy, the relative cumulative release in percent was calculated and is presented in Figure 4.5C.

Figure 4.6A shows that 92% of the original 1mg/mL gemcitabine concentration was measured in the gemcitabine-loaded gel. Figure 4.6B displays the hourly release rate in µg/mL/h and the release in µg/mL of gemcitabine for each specific timepoint over time. A maximum average release rate of 14.7 ± 0.86µg/mL/h is observed at 1h. Following this, the release rate per hour decreases over time and falls below 1µg/mL/h at 72h. At this timepoint, the average hourly release rate for gemcitabine is 0.44 ± 0.15µg/mL/h. At 145h, the release rate falls below 0.1µg/mL/h and gemcitabine is released with an average of 0.027 ± 0.011µg/mL/h. The average release rate for gemcitabine at 336h is 0.0015 ± 0.0009µg/mL/h. Overall, the highest release rates are observed for the first 24h (Figure 4.6B). The release in µg/mL shows that the highest concentration measured is an average of 55.6 ± 6.7µg/mL. Following the sharp increase in gemcitabine release, the release declines over the next timepoints and reaches an average 0.11 ± 0.06µg/mL.

In the fluvastatin-loaded gel used for the time-course study, only 64.4% of the original 1mg/mL fluvastatin concentration were measured (Figure 4.6A). Possible reasons for this will need to be examined in future experiments in collaboration with the Melville laboratory.

The release rate of fluvastatin from the gel is similar to the release of gemcitabine, with the curve which depicts the release rate over time exhibiting an exponential decrease over time. The highest release rate is observed at 1h with an average release of 8.3 ± 0.5μg/mL/h. Following this, the release slowly decreases over the next 23h, with an average release rate of 2.19 ± 0.45μg/mL/h measured at 24h. Afterwards, the release rate declines and approaches values close to 0. The lowest release rate is determined at 336h with 0.004 ± 0.0007μg/mL/h (Figure 4.6C).

Similar to the gemcitabine release, fluvastatin release from hydrogel peaks at 24h with an average release of 30.6 ± 6.37μg/mL (Figure 4.6C).

A relative concentration of 73.8% rigosertib was measured in the rigosertib-loaded gel (Figure 4.6A). While this is higher than the relative concentration of fluvastatin in the gel, the release of rigosertib is the lowest when compared to release rates for gemcitabine and fluvastatin.

The highest hourly release rate of rigosertib was measured at 1h with an average release of 3.4 ± 0.7μg/mL/h. Between 1h and 2h, the release rate decreases, before a steady hourly release ranging from averages 1.6 ± 0.6μg/mL/h to 1.9 ± 0.6μg/mL/h between 3h and 10h. At 24h, the release rate has declined to 1.08 ± 0.71μg/mL/h. Afterwards, the release rate continues to decline with the release reaching values of 0.002 ± 0.001μg/mL/h at 336h (Figure 4.6D). As for gemcitabine and fluvastatin, analysis of the release of rigosertib reaches a maximum at 24h with an average release of 15.2 ± 9.92%. This is followed by a decrease in release with the minimum average concentration measured at 336h (0.15 ± 0.08μg/mL).

Taken together, the release rates for gemcitabine, fluvastatin and rigosertib display a similar trend with a bolus release in the first 24h and a general decline of release over time that appears to be exponential. However, drug concentrations released into media vary between the different drugs, with gemcitabine-loaded gels displaying the

highest release of drug, followed by fluvastatin-loaded gels. Rigosertib-loaded gels displayed the lowest drug release.

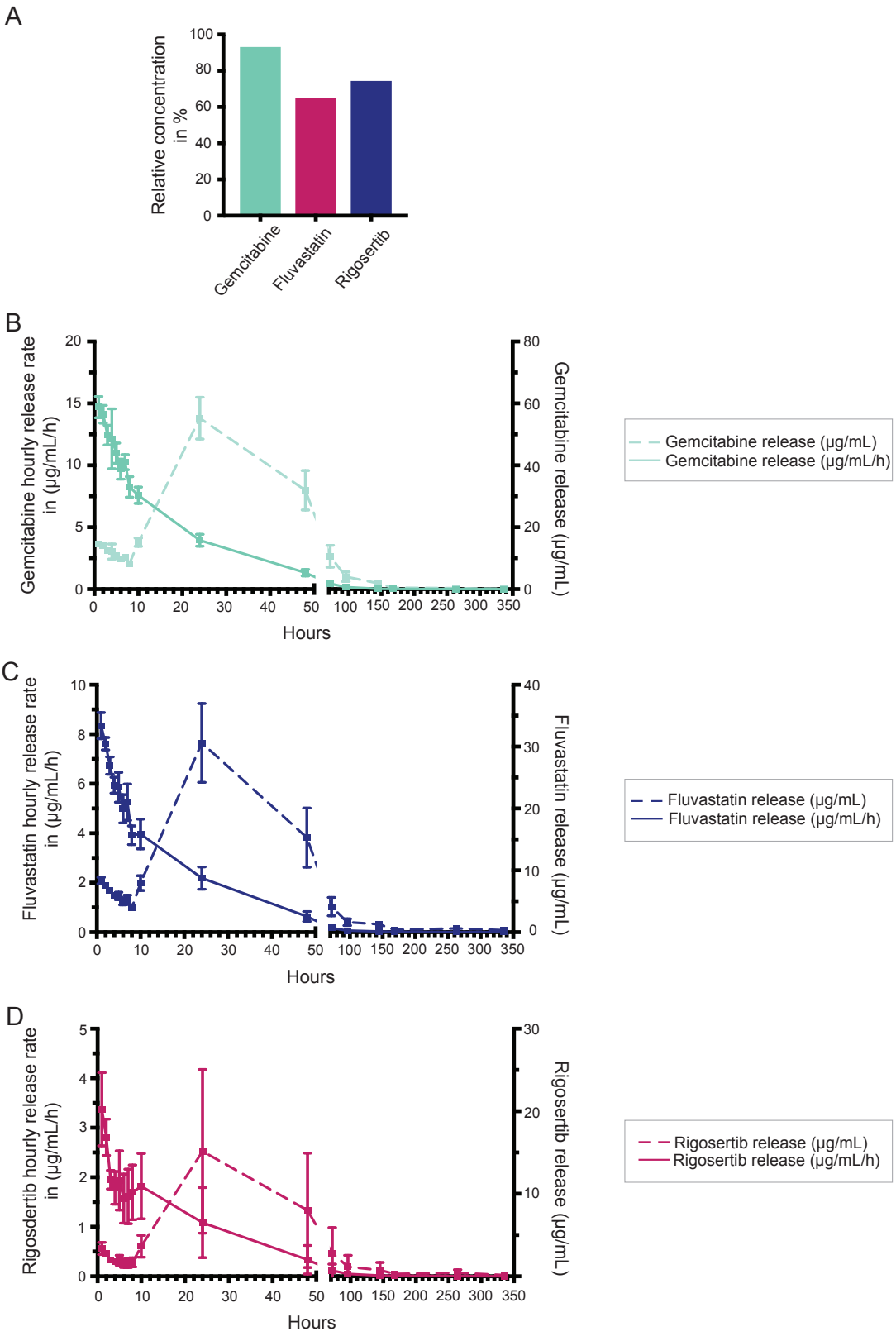

Figure 4.6: Release of gemcitabine, fluvastatin and rigosertib over time. A. Percentage of drug concentration measured in gel (normalised to original concentration of 1mg/mL). **B-D.** Graphs display the release rate per hour (in µg/mL/h) for each drug over the course of time as well as the release in µg/mL for each timepoint. Error bars represent SD, n=5.

4.4.2.2. Gemcitabine and fluvastatin released from hydrogels inhibit ependymoma neurosphere formation *in vitro*

Following the time-course release experiment, the effect of gemcitabine and fluvastatin released from gels on ependymoma cells *in vitro* was tested. Ependymoma cells (mSEP-CR[+] and mSEP-CR[-]^{EPHB2}) cultured in wells were subjected to drug treatment with fluvastatin and gemcitabine released through HA-hydrogels.

First, hydrogels loaded with increasing concentrations of gemcitabine (0.1µM, 1µM and 1.33mM) were tested. The concentrations of 0.1µM and 1µM were chosen based on the results for IC_{10}, IC_{50} and IC_{90} values for mSEP-CR(+) and mSEP-CR(-)^{EPHB2} cells as determined from *in vitro* dose-response screens as well as the results for percentage release from the time-course release studies. Gemcitabine IC_{10}-IC_{90} values range from 0.003-0.0067µM for mSEP-CR(+) and 0.0036-0.146µM for mSEP-CR(-)^{EPHB2} cells (Table S.4.3).

Assuming that up to 20% of gemcitabine are released from the hydrogel over 72h, the concentrations of gemcitabine in the hydrogel needed to be at least 5x higher than the IC_{10}-IC_{90} values. Theoretically, this should be covered by gemcitabine released from a 0.1µM-loaded hydrogel. However, in order to examine the effect of gels loaded with a higher concentration, the 1µM gemcitabine-loaded hydrogel was added. A gel loaded with 1.33mM gemcitabine was further included as this was the concentration of gemcitabine that would be tested in *in vivo* PK studies (Figure 4.7). Gels loaded with this concentration had previously achieved an extension of survival in GBM-PDX mouse models following intratumoural injection[346].

For the experiment, mSEP-CR(+) and mSEP-CR(-)^{EPHB2} cells were cultured in 24-well plates. Basket inserts containing gemcitabine-loaded hydrogels (0.1µM, 1µM and 1.33mM) were added to the wells 24h post plating of the cells in quadruplets. Following

a 72h incubation, images of cells under different conditions were taken and media from each well was sampled.

Figure 4.7A demonstrates the effect of gemcitabine released from hydrogels on sphere formation for mSEP-CR(+) and mSEP-CR(-)^{EPHB2} over 72h. It shows that gels loaded with 1.33mM-gemcitabine had the most visible effect on sphere formation over 72h (Figure 4.7). Figure 4.7B shows the concentration of gemcitabine measured in the cell culture media for mSEP-CR(+) and mSEP-CR(-)^{EPHB2} cells. An average concentration of 0.0015 ± 0.0009µg/mL gemcitabine was detected in mSEP-CR(+) media exposed to 0.1µM gemcitabine-loaded gels. Only in one of the replicates for mSEP-CR(-)^{EPHB2} media gemcitabine could be detected at a concentration of 0.00029µg/mL. For media exposed to gemcitabine released from 1µM-loaded gels, the average concentrations of gemcitabine were 0.030 ± 0.012µg/mL and 0.025 ± 0.007µg/mL for mSEP-CR(+) and mSEP-CR(-)^{EPHB2} media, respectively. Media exposed to 1.33mM gemcitabine-loaded hydrogels contained concentrations of 3.535 ± 0.71µg/mL and 2.983 ± 0.53µg/mL for mSEP-CR(+) and mSEP-CR(-)^{EPHB2} media, respectively. While there is no significant difference in gemcitabine concentrations in media from mSEP-CR(+) and mSEP-CR(-)^{EPHB2} cells (unpaired t-test; ns:p= >0.999), there is a significant difference in gemcitabine concentration in medias exposed to gels loaded with 1µM or 1.33mM gemcitabine (unpaired t-test; ****:p= <0.0001).

Overall, this data demonstrates that gemcitabine released from hydrogels loaded with the highest gemcitabine concentration of 1.33mM displayed the most efficient effect on mouse ependymoma cell lines *in vitro*. Hence, this concentration was selected to be tested in *in vivo* PK studies.

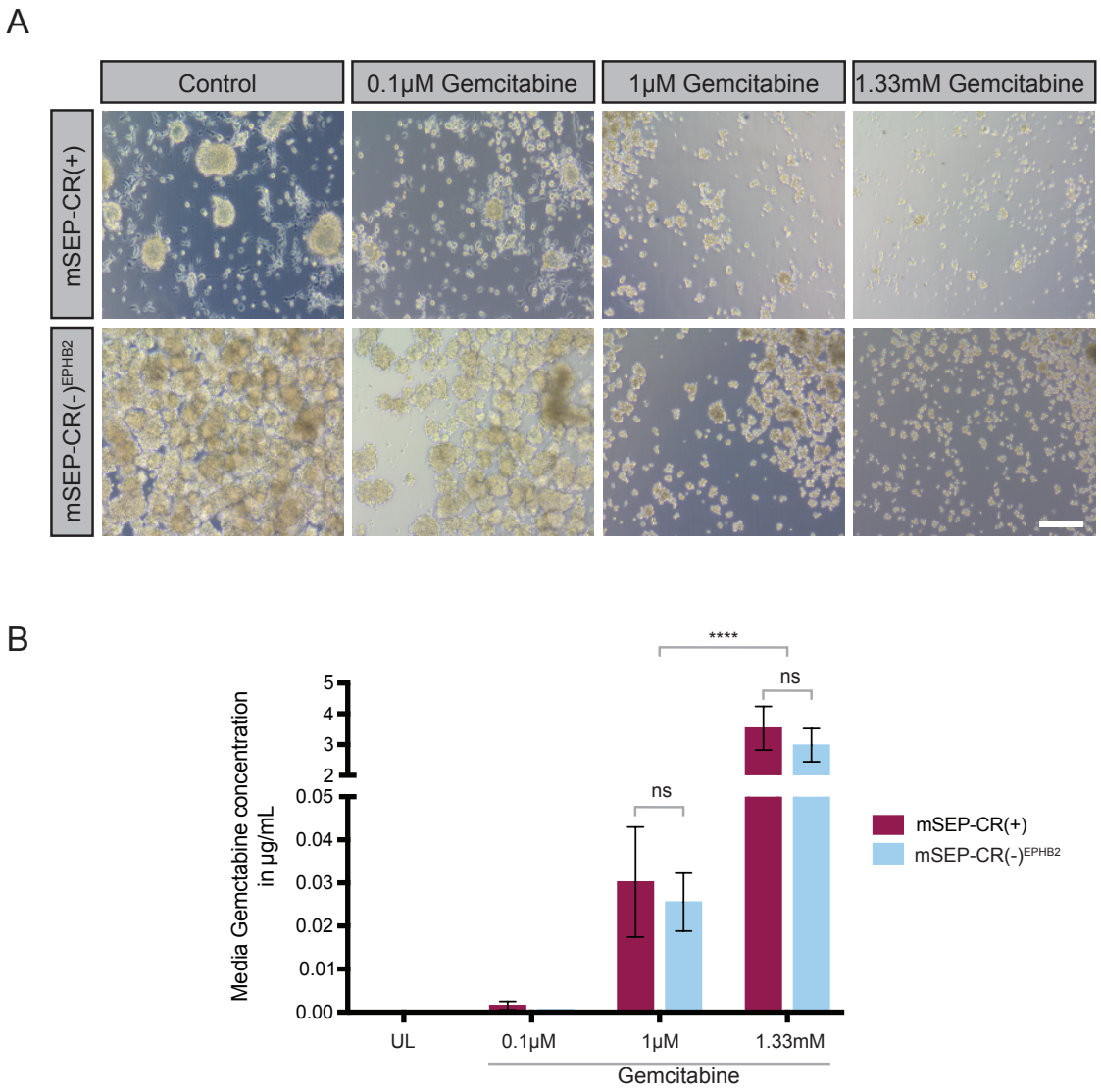

Figure 4.7: Effect of gemcitabine released from hydrogels on ependymoma cells *in vitro*. Mouse ependymoma cells (mSEP-CR[+] and mSEP-CR[-]^{EPHB2}) cultured in 24 well plates were subjected to gemcitabine released from gels harbouring different gemcitabine concentrations (0.1µM, 1µM and 1.33mM). Unloaded gels served as controls. **A.** Representative images demonstrate the effect of hydrogel-based delivery of gemcitabine from differently concentrated gels on sphere formation was examined (scale bar = 100µm). **B.** Graph displays gemcitabine concentration released from gels with different concentrations, which measured in media of mSEP-CR(+) and mSEP-CR(-)^{EPHB2} cells. Error bars represent SD, n=4. (Unpaired t-test; ns:p=0.54 for 1µM, p=0.26 for 1.33mM; ****: p=<0.0001).

Following the study with gemcitabine-loaded hydrogels, the effect of fluvastatin released from hydrogels on neurosphere formation of ependymoma cells was examined. As the gemcitabine released from gels loaded with 1.33mM had the most visible effect on sphere formation, hydrogels were loaded with a similar concentration of fluvastatin (1mM). Hydrogels loaded with this concentration would further be used for *in vivo* PK studies. As before, unloaded hydrogels served as controls. Since IC_{10}-IC_{90} values for fluvastatin in mSEP-CR(+) and mSEP-CR(-)^{EPHB2} range from < 0.007µM- 23µM (see Supplementary Table 4.6), the effect of fluvastatin released from gel was expected to be different on mSEP-CR(+) compared to mSEP-CR(-)^{EPHB2} cells. Representative images in Figure 4.8A demonstrate how fluvastatin released from 1mM fluvastatin-loaded hydrogels affects ependymoma cells in culture. While there seems to be a moderate effect on mSEP-CR(+) cells, sphere formation of mSEP-CR(-)^{EPHB2} is massively interrupted. However, statistical analysis comparing fluvastatin concentration in media from mSEP-CR(+) and mSEP-CR(-)EPHB2 cells reveals no significant differences in concentration (Unpaired t-test; ns: p=0.65) (Figure 4.8B).

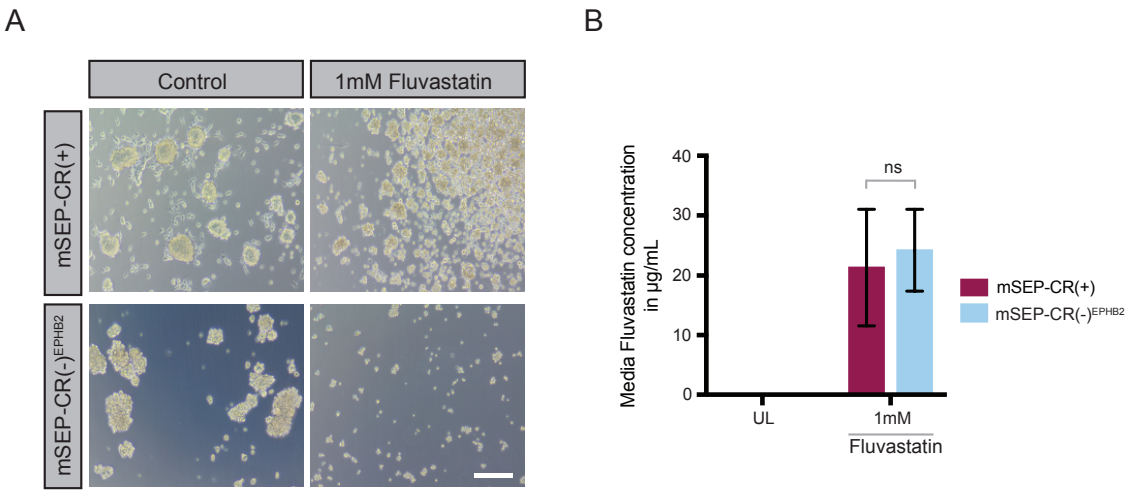

Figure 4.8: Effect of fluvastatin released from hydrogels on ependymoma cells *in vitro.* Mouse ependymoma cells (mSEP-CR[+] and mSEP-CR[-]^{EPHB2}) cultured in 24 well plates were subjected to fluvastatin released from a 1mM-fluvastatin-loaded hydrogel. Unloaded gels (UG) served as controls. **A.** Representative images demonstrate the effect of fluvastatin released from 1mM-fluvastatin loaded gels on sphere formation of ependymoma cells (mSEP-CR[+], mSEP-CR[-]^{EPHB2}) (scale bar =100µm). **B.** Graph displays fluvastatin concentration released from gel with 1mM fluvastatin concentration, which was measured in media of mSEP-CR(+) and mSEP-CR(-)^{EPHB2} cells. Error bars represent SD, n= 3-4. (Unpaired t-test; ns: p=0.65).

4.4.3. Implementation hydrogel-based delivery into preclinical standard of care neurosurgery

Front line treatment of ependymoma includes maximum safe resection; therefore, any novel drugs or drug delivery methods should be tested in the context of this approach. The efficacy of hydrogel-based drug delivery had already been examined *in vivo* on PDX models for GBM by Parkins *et al.*[346]. However, they assessed its effect through intratumoural injection of drug-loaded gels rather than via injection into post-resection cavities[346]. While Parkins *et al.* did not observe any adverse effects in mice injected with unloaded gel, we wanted to investigate if the injection of unloaded hydrogels into post-resection cavities has any toxic effects in our ependymoma mouse models.

4.4.3.1. Injection of unloaded hydrogels into post-resection cavities is not toxic and does not affect tumour recurrence

In order to investigate if the injection of hydrogels into post-resection cavities is toxic or has any effect on tumour growth or survival in mouse ependymoma models, an *in vivo* study was carried out comparing resection alone with resection followed by injection of unloaded hydrogel. For this, six mice were orthotopically implanted with mSEP-CR(-)^{RTBDN} cells. On Day 15 post-implants, tumour-bearing mice were randomised according to their BLI tumour signal and subjected to I) surgical resection followed by observation (Rsx) or II) surgical resection followed by injection of unloaded hydrogel (Rsx+UG). While four mice were injected with hydrogel post-resection, two mice were subjected to surgical resection followed by observation. Tumour growth was monitored using bioluminescence and mice sacrificed once they displayed clinical signs as a result of tumour burden. Statistical analysis of survival revealed that injection of unloaded hydrogel into cavities did not appear to have any significant effect on survival (p value=0.97, Log-rank) (Figure 4.9B). Furthermore, there is no difference in tumour growth detectable between the two treatment groups (Figure 4.9A).

There were also no adverse effects observed in mice injected with unloaded hydrogel. Hence, it was concluded that the injection of unloaded hydrogel does not have any toxic effects and also does not interfere with tumour recurrence or OS in mouse ependymoma models.

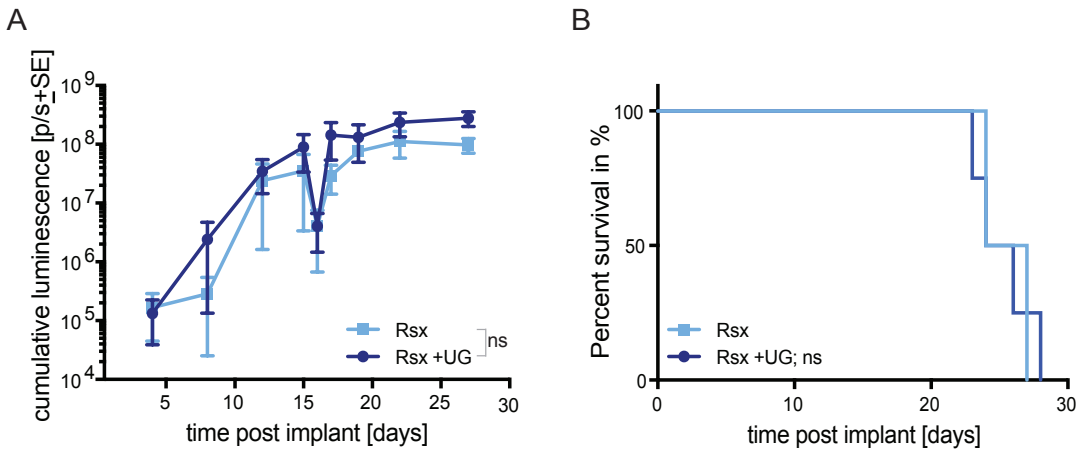

Figure 4.9: Hydrogel injection into surgical resection activities does not affect tumour growth or survival. A. Cumulative bioluminescence measures of tumour growth. Error bars represent SD (Mann-Whitney test; ns: p=0.34). **B.** Kaplan-Meier survival curves of mSEP-CR(-)^{RTBDN} mouse models treated with resection surgery followed by observation (Rsx) or resection surgery with injection of unloaded hydrogel (Rsx+UG) (n=2; n=4 for Rx, Rsx+UG respectively) (Log-rank; ns: p=0.97).

4.4.3.2. Identification of challenges associated with hydrogel delivery in post-resection cavities

Having confirmed that injection of unloaded hydrogels into resection cavities does not appear to be associated with adverse effects in mice, the behaviour of the gel in the cavity was studied over time. For this, preclinical neurosurgery followed by injection of a FITC-labelled hydrogel was carried out in an ependymoma mouse model. In order to examine the location of the gel at different timepoints post-injection, ten mice were implanted with mSEP-CR(-)^{RTBDN} cells, followed by resection on Day 10 post-implant. Three mice were enrolled in the control treatment group and were subjected to resection followed by observation. The remaining seven mice were subjected to injection with FITC-labelled hydrogel post-resection.

During the surgery, the maximum gel volume injectable into cavities was tested. Hydrogel volume was measured via scale markings on the sterile Hamilton syringe used to inject the hydrogel into post-resection cavities. An average volume of 4.25 ± 0.87µL hydrogel was measured (Figure 4.10A). This is a very low volume of the gel

and might have an effect on the efficacy of drug-loaded hydrogels. It therefore represents the first challenge in hydrogel delivery.

Post-surgery, the behaviour of the gel in the cavity was examined over time. First, we investigated if the gel remains in the cavity over 72h or if it moves from the cavity. For this, brains were collected and imaged using a fluorescence microscope at different timepoints: 1h, 6h, 24h, 72h (Figure 4.10B). At each timepoint over the 72h, FITC labelled gel was detected in and around the resection cavity (Figure 4.10B). However, during the imaging of brains with intact skulls, it was also observed that FITC-labelled gel appeared to be present above the skull (as shown in representative images for 6h and 24h). This suggests that some of the gel had moved out of the cavity (Figure 4.10C). Thus, the cavity would need to be closed in future studies to ensure retention of the hydrogel within the resection cavity.

Moreover, a sagittal cut through the resection cavities revealed that resection cavities contain residual blood (Figure 4.10D). As it is unclear if clotted blood in the cavity interferes with drug release from the hydrogel or drug diffusion to the residual tumour cells, the bleeding would need to be controlled better in order to minimise the amount of clotted blood in the resection cavity.

To summarise, while FITC-labelled hydrogel was detectable in the resection cavities over a course of 72h, three challenges associated with hydrogel delivery were identified in this study: I) cavity size and volume of gel injected into cavity II) control of haemostasis during surgery III) retention of gel inside the cavity.

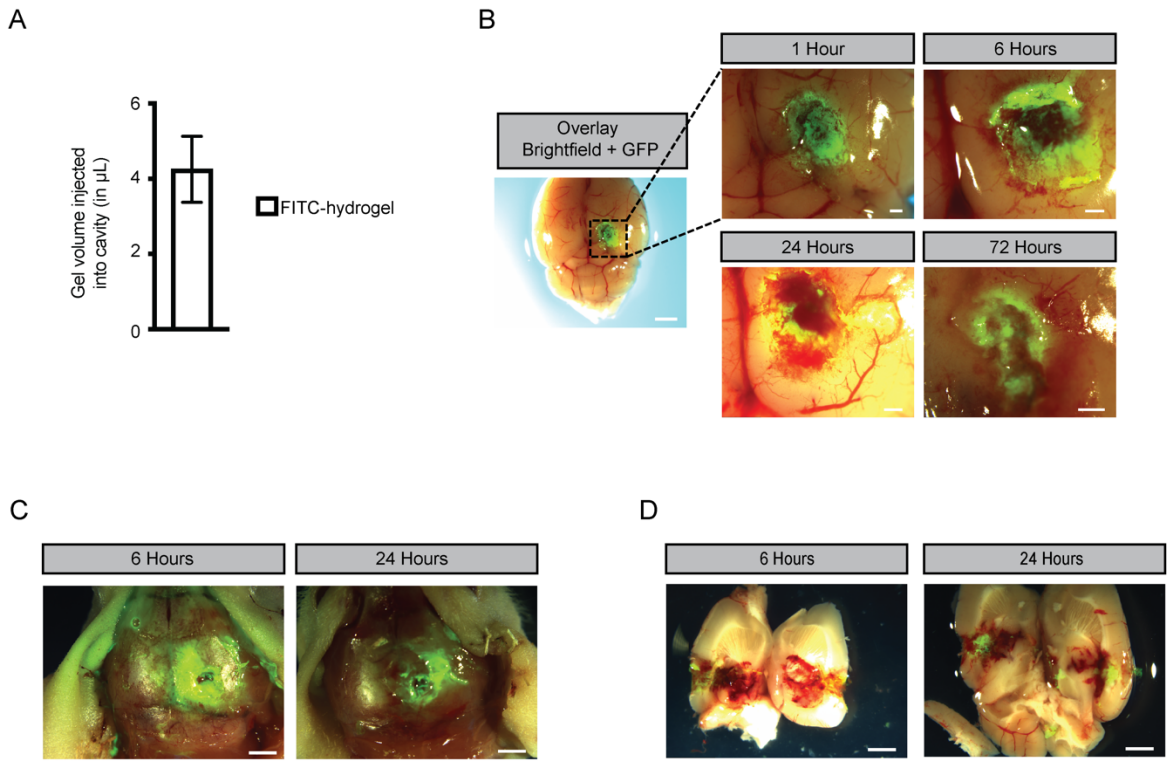

Figure 4.10: Overview of challenges in hydrogel-based drug delivery post-resection. Mice harbouring mSEP-CR(-)^{RTBDN} tumours were resected and injected with FITC-labelled hydrogel. **A.** Graph displays average gel volume injected into post-resection cavities. Error bar represents SD, n=7. **B.** FITC-labelled hydrogel resides in the cavity over 72h. Scale bar overview of brain (2mm) Scale bars enlarged cavities (400µm). **C.** Representative images for FITC-labelled hydrogel detectable on the skull at 6h and 24h post injection. **D.** Representative images for clotted blood residing in resection cavity at 6h and 24h post-surgery.

4.4.4. Optimisation of resection surgery to overcome challenges for hydrogel delivery

Following the identification of challenges for hydrogel delivery, a resection optimisation study was performed aiming to minimise or completely resolve the challenges. Each challenge was addressed using different approaches. For this study, mice were implanted with mSEP-CR(+) cells and subjected to different approaches of resection surgery. These approaches included testing the feasibility of cavity enlargement, improving haemostasis during surgery and closure of the resection cavity to ensure retention of the hydrogel within the cavity.

Mice subjected to these different surgery techniques were sacrificed at different timepoints (3h, Day 6, Day 11 and Day 18) to study and compare the effects of the different surgery techniques in dissected brains. Brains were imaged using a fluorescence microscope as in the previous study.

4.4.4.1. Optimisation of cavity size and hydrogel volume injected into post-resection cavity

The optimisation surgery study involved the optimisation of cavity size and volume of gel injected into the cavity. More rigorous resection of tumours in a previous study had been unsuccessful because mice displayed adverse effects such as tilted heads and displayed strong leaning towards one side so that they had to be culled within a couple of hours post-surgery (data not shown). Hence, in this study, the cavity was carefully expanded and some cavities were flushed with hydrogel prior to hydrogel injection. For the injections, hydrogel volume could be increased marginally to an average volume of 4.5 ± 0.8μL hydrogel (Figure 4.11). In cavities flushed with gel prior to gel injection, the FITC-labelled hydrogel was detectable over the course of 18 days (Figure 4.12B).

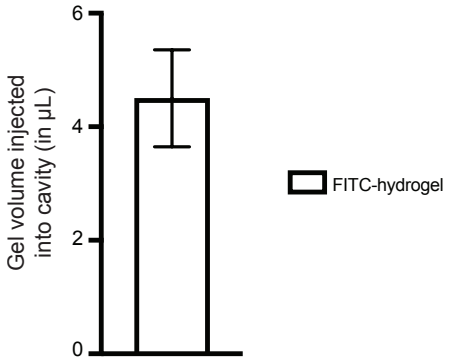

Figure 4.11: Overview of gel volume injected into post-resection cavity. Mice harbouring mSEP-CR(+) tumours were resected and FITC-labelled hydrogel was injected into post-resection cavity. Error bars represent SD, n=14.

An additional study investigated the potential of fluorescence-guided surgery in our ependymoma models. In the clinical setting, protoporphyrin IX (PpIX), a fluorescent metabolite of 5-aminolevulinic acid (5-ALA), can be utilized for fluorescence guided resection surgery for glioblastoma[352]. This allows for more accurate resection with less residual tumour cells post-surgery. The ependymoma cell lines used for our orthotopic ependymoma mouse models express GFP and can therefore be visualised using lasers or specific fluorescence filters without the need to use an imaging agent. Hence, the use of a so-called fluorescent gun (NightSea), which can be utilised to visualise fluorescent cells during resection was tested. I examined if this would allow for better identification of the residual tumour cells and subsequently lead to more successful NTR or even GTR. However, the residual tumour was not large enough and located too far below the brain surface, which meant it could not be visualised with the fluorescence gun (data not shown).

4.4.4.2. Control of haemorrhage during resection surgery involves combination of haemostatic agents and PBS washes

One of the challenges identified for hydrogel delivery were residues of clotted blood in post-resection cavities. To prevent residues of clotted blood from interfering with drug release from hydrogel, two types of haemostatic agent were tested alone and in combination.

In previous resection studies, Lyostypt® was used during the resection surgery to stop tumour-bed haemorrhage. This was achieved by inserting small pieces of the collagen fleece into the cavity. Once haemostasis was complete, Lyostypt® pieces as be removed from wound. However, this removal of the Lyostypt® from the resection cavity frequently led to new bleeding and thereby prolonged the process of haemostasis, which was occasionally accompanied by residues of clotted blood accumulating in the cavity. In order to remove the clotted blood, cavities were flushed with warm PBS in this study prior to the injection of hydrogel. The combination of Lyostypt® and cavity-flushing with PBS represented the first approach to achieve haemostasis.

SURGICEL® was the second type of haemostatic agent tested in this experiment. SURGICEL® is an absorbable oxidized cellulose mesh frequently used in neurosurgery, which can remain in the tumour cavity to achieve haemostasis in the case of post-operative haemorrhage in humans[141,353]. Thus, SURGICEL® was left in the cavity in our preclinical mouse models to test its efficacy to absorb blood during and after surgery.

Alternatively, haemostasis was achieved through a combination of Lyostypt® and SURGICEL® (removed from the cavity) followed by the flushing of the resection cavity with PBS.

All three approaches were compared to each other and the combination of Lyostypt®, SURGICEL® and cavity-flushing appeared to worked best with regards to minimising the amount of clotted blood while retaining enough gel in the cavity that could be detected over time. Figure 4.12B shows representative images for cavities of mice where the bleeding was stopped as described above. Furthermore, these cavities had been flushed with FITC-labelled gel prior to proper hydrogel-injection into the cavity. As demonstrated in Figure 4.12B, cavities filled this way harboured FITC-labelled gel after on Day 18 post-hydrogel injection.

While the use of SURGICEL® did appear to be efficient with regards to blood absorption in the resection cavity, it is not applicable in our mouse resection model as the cellulose mesh fills up the whole cavity rather than lining it (Figure 4.12C). This resulted in very little space remaining for the hydrogel to be injected into. As the volume of hydrogel injected into resection cavities is already low, leaving SURGICEL® in the cavity was not feasible in resection surgeries followed by gel injections.
Representative images in Figure 4.12C demonstrate how SURGICEL® occupies the whole cavity. While there is FITC-labelled gel detectable in the cavity, it appears to be co-localised with pieces of the SURGICEL® mesh.

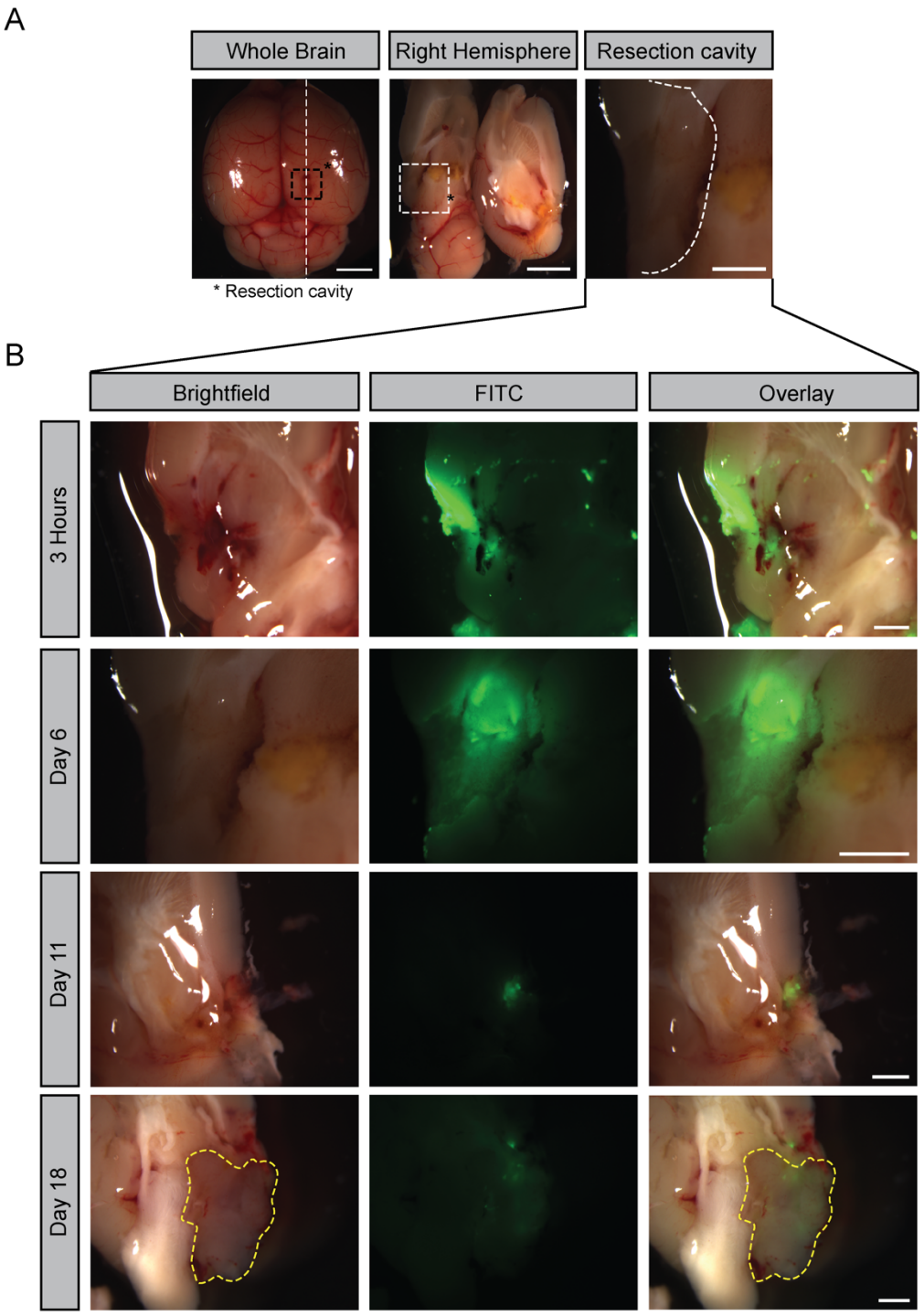
A
Whole Brain
Right Hemisphere
Resection cavity
* Resection cavity
B
Brightfield
FITC
Overlay
3 Hours
Day 6
Day 11
Day 18
C
Whole Brain
Right Hemisphere
Resection Cavity

Figure 4.12: Optimisation of resection surgery technique to resolve challenges regarding hydrogel delivery. Mice harbouring mSEP-CR(+) tumours were resected once tumours were established and injected with FITC-labelled hydrogel. Brains were collected at different timepoints post hydrogel-injection (3h, Day 6, Day 11, Day 18) and brains were examined under a fluorescent microscope **A.** Mouse brains were dissected and imaged as a whole before a sagittal cut was made through the resection cavity in the right hemisphere. Resection cavities were then imaged in higher magnifications. **B.** High magnifications of resection cavities where haemostasis was achieved through a combination of Lyostypt®, SURGICEL® and cavity-flushing with PBS. FITC-labelled gel is detectable at every collection timepoint. **C.** Representative images of cavities filled with SURGICEL® and injected with FITC-labelled hydrogel. Scale bars 2mm-low magnifications, 400µm-high magnifications.

4.4.4.3. Retention of gel within resection cavity achieved through sealing the resection cavity with artificial dura

One of the challenges for hydrogel delivery that had been identified in the previous study was the retention of hydrogel inside the resection cavity. In this study, the cavities were sealed using a sterile biodegradable artificial dura, which can be attached to the skull. Attachment of the dura to the skull appeared to have a beneficial effect regarding the retention of hydrogel within the cavity (Figure 4.13). As sealing of the cavity with this dura further prevents the skin to come in contact with the cavity and the brain and has therefore been implanted into all subsequent resection surgeries.

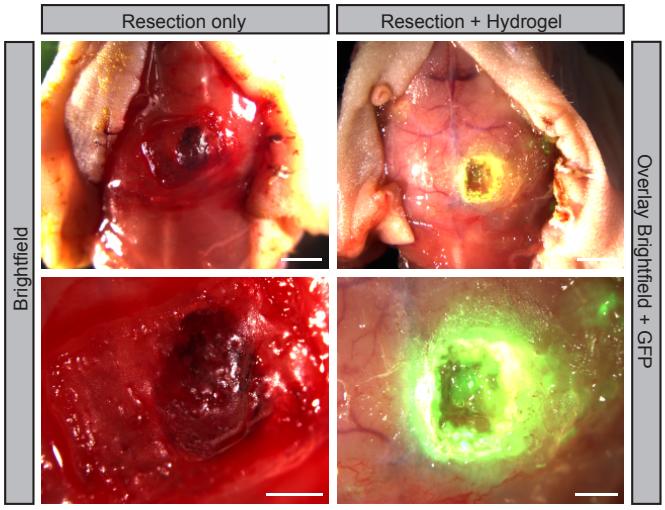

Figure 4.13: Utilization of artificial dura to close of resection cavity. Representative images of mice subjected to resection only or resection followed by injection of FITC-labelled hydrogel. Through sealing of the cavity using artificial dura, FITC-labelled gel is retained in cavity. Scale bars 2mm top panel, 400µm bottom panel.

4.4.5. Utilization of drug-loaded hydrogels as local delivery technique post-surgical resection in ependymoma models *in vivo*

After successful optimisation of the resection surgery technique and validation that injection of hydrogels does not affect tumour re-growth, the hydrogel-based release of selected drugs *in vivo* was examined. *In vivo* pharmacokinetic studies were designed for a mouse ependymoma model and included resection of tumours, followed by injection of hydrogels loaded with either gemcitabine, rigosertib or fluvastatin.

4.4.5.1. *In vivo* pharmacokinetic studies reveal gemcitabine as the candidate drug for repurposing in hydrogels

A crucial step in drug discovery, is the investigation of ADMET properties of the drug in development. *In vivo*, this is achieved through pharmacokinetic (PK) and pharmacodynamic (PD) studies, which can help gain insight into the absorption, distribution, clearance etc[354].

In vivo, absorption can be assessed through blood samples, while distribution to the tissue of interest can either be measured by using radiolabelled compounds in combination with imaging or by harvesting the respective timepoint and evaluate compound metabolites via mass-spectrometry[354]. To select drugs for subsequent preclinical efficacy studies of hydrogel-based drug delivery, PK studies were performed with gels loaded with gemcitabine, fluvastatin and rigosertib. For each study, 15 mice were implanted with mSEP-CR(-)^{EPHB2} cells. Resection of tumours occurred on Day 5 post-implant and gels loaded with either 1.33mM gemcitabine, 1mM fluvastatin or 1mM rigosertib were injected into post-resection cavities. For gemcitabine and fluvastatin-loaded gels, plasma and brain samples were collected at five different timepoints (1h, 8h, 24h, 72h and Day 7) from three mice each. In the PK study for rigosertib-gels, mice were collected at Day 5 instead of Day 7. All probes were analysed using HPLC-MS towards concentrations of the selected drugs. While brains were cut into four different pieces for the UHPLC-MS measurements, analysis of PK data for brain was performed by pooling data for the different brain areas per animal.

Figure 4.14A demonstrates the concentrations of drugs in brain and plasma across time. Displayed are the mean and standard deviation (SD) values as calculated from three replicates per timepoint for both, brain and plasma. Gemcitabine, albeit at low concentrations, is detectable in the brain throughout the whole duration of the study. In the brain, the gemcitabine immediately reaches its maximum concentration (C_{max}) with an average of 0.2 ± 0.1µM 1h post-injection. Afterwards, brain concentration decreases to. Between 8h and 144h post-injection, gemcitabine concentrations remain detectable and vary between 0.01± 0.01µM -0.009 ± 0.008µM. Its half-life in the brain ($T_{1/2}$) is 36min. In plasma, gemcitabine can be detected over 24h post-injection at ~0.002-0.003µM. After 24h, gemcitabine concentrations were below the limit of quantification of the UHPLC-MS. The half-life value of gemcitabine in plasma could not be established due to the steady low concentrations.

Fluvastatin was only detectable in the brain for 8h and fluvastatin concentrations in samples of 24h and older were below the limit of quantification of the UHPLC-MS (Figure 4.14B). Like gemcitabine, fluvastatin reaches its C_{max} (average of 0.5 ± 0.38µM) in the brain 1h post-injection with a half-life of 3.15h. In the plasma, the concentration of fluvastatin reaches its C_{max} of 0.0024 ± 0.0015µM at 1h post-gel injection. A decrease of fluvastatin is visible over the next 7h and the concentration of fluvastatin in the plasma at 8h post-injection is 0.001 ± 0.0001µM. $T_{1/2}$ for fluvastatin in plasma with 6.2h was therefore longer than in the brain. Concentrations of fluvastatin in samples for the older timepoints (72h, 144h) were below the limit of quantification.

Concentrations of rigosertib in the brain were only measurable 1h post-injection (Figure 4.14C). Here, it was detectable with an average concentration of 0.18 ± 0.14µM. Afterwards, brain levels of rigosertib were undetectable using UHPLC-MS. Thus, the brain half-life is particularly short with 22.5min. A similar trend same was observed for the plasma, where rigosertib was detected at a concentration of 0.007 ± 0.001µM at 1h post-injection, followed by very low concentrations of 0.001µM at 8h and 24h. Plasma half-life for rigosertib was 1.14h.

To confirm the concentration of drug in the gel, gels were also analysed using UHPLC-MS. Figure 4.14D reveals that the gemcitabine gel only a very small concentration of

62.7µM was detected. This is only a relative concentration of 4.7%. The relative concentrations for fluvastatin and rigosertib were higher with 23.8% and 73.8%, respectively.

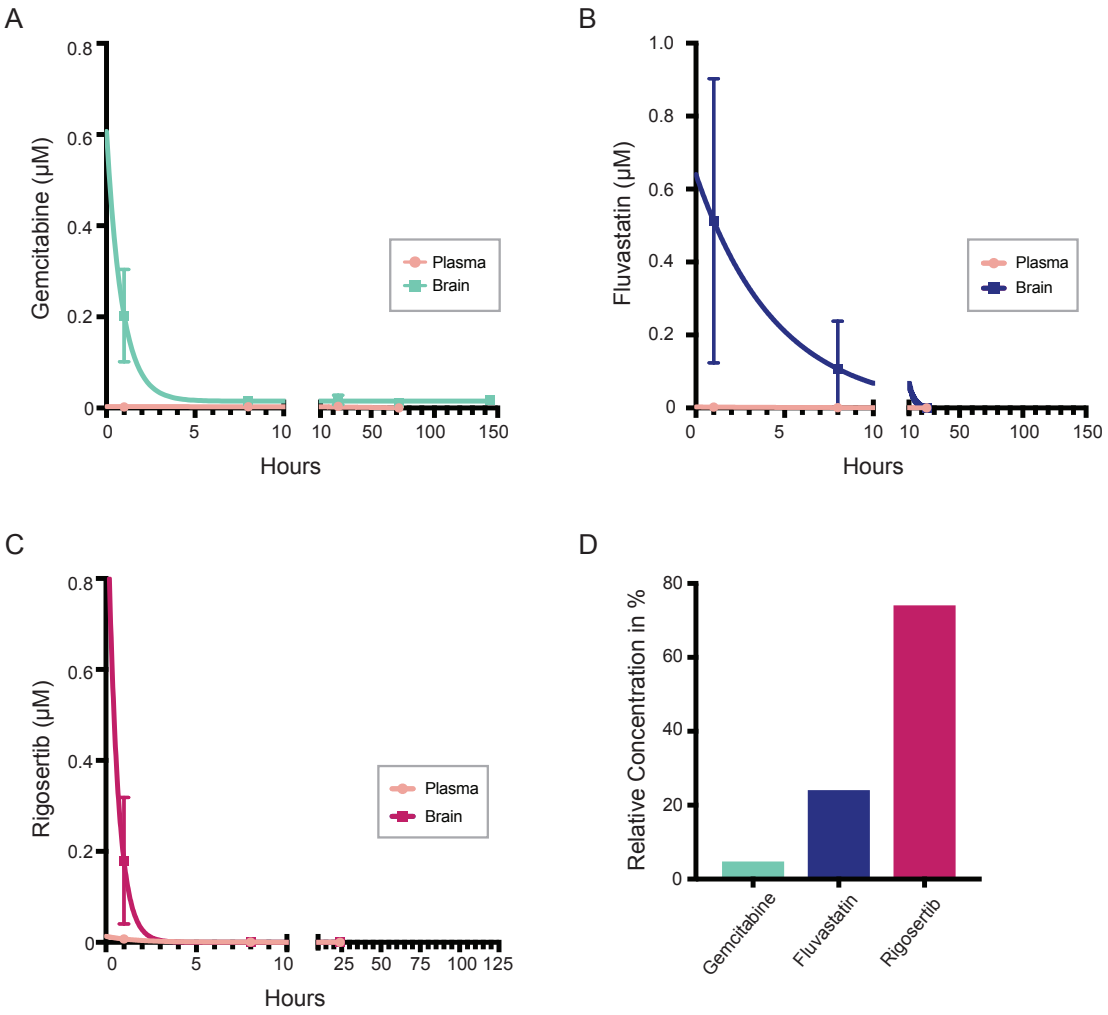

Figure 4.14: Pharmacokinetics for gemcitabine, fluvastatin and rigosertib released from hydrogels in post-resection cavities. A. Mice harbouring mSEP-CR(-)^{EPHB2} tumours were resected on Day5 post-implant and injection with hydrogels loaded with 1.33mM gemcitabine, 1mM fluvastatin or 1mM rigosertib. Blood samples and brains were collected at different timepoints over the course of 1 week from three mice per drug and timepoint. **B.** Gemcitabine concentration in brain and plasma over time. Error bars represent SD, n=3. **C.** Fluvastatin concentration in brain and plasma over time. Error bars represent SD, n=3. **D.** Rigosertib concentration in brain and plasma over time. Error bars represent SD, n=3. **E.** Relative concentration of each drug in gel normalised to intended concentration of drug in gel.

4.4.5.2. Preclinical efficacy study of gemcitabine-loaded hydrogel reveals trend of efficacy for hydrogel-based delivery of gemcitabine

Previously, Parkins *et al.* have demonstrated how injection of gemcitabine-loaded hydrogel correlates with a survival benefit in GBM PDX models[346]. In their studies, injection of a hydrogel containing 1.33mM did not have toxic side effects in a diffusely growing model. Furthermore, *in vitro* experiments on ependymoma cells had validated that 1.33mM gemcitabine gel had an effect on neurosphere formation (Figure 4.7). Thus, the same concentration was used in ependymoma mouse models to examine the effect of hydrogel-based gemcitabine delivery post-resection on tumour growth and survival. For this study, ten mice harbouring *EPHB2*-driven ependymoma were used and once tumours reached sizes of subjected to four different treatment arms: 1) Observation only (Ctrl) 2) Resection only (Rsx only), 3) Resection and unloaded gel (Rsx + UG), 4) Resection and 1.33mM Gemcitabine-loaded gel (Rsx + GG).

Figure 4.15 presents graphs that display tumour growth and survival for all four treatment groups. While there is no significant difference in survival between the different treatment groups (p=0.064, Log-rank), a trend towards a difference can be observed and has been calculated using the Log-rank test for trend (p value= 0.0148). However, due to low numbers of mice (n=2-4) in each treatment group, this study will be repeated with gemcitabine-loaded gels of the same and a higher concentration to allow for accurate statistical analysis. For these studies, mouse numbers in each treatment group will be n=13. It has been calculated that this number is required in order for the two-sided 5% level Wilcoxon test to have an 80% power to detect a setting in which there is an 80% probability that a random animal from the treatment group survives longer than an animal from the control group.

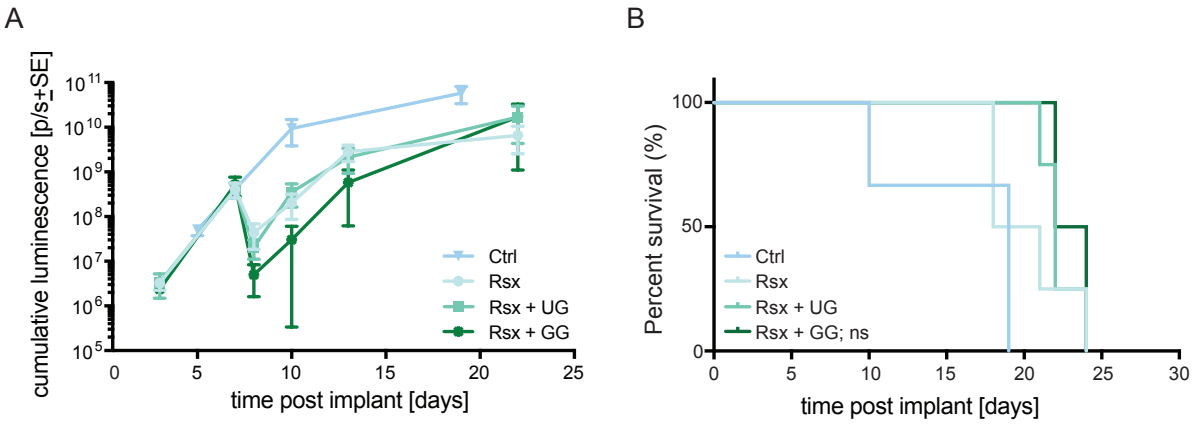

Figure 4.15: Preclinical efficacy study with gemcitabine-loaded gels shows trend of extended survival. Mice of mSEP-CR(-)^{EPHB2} treated with surgery alone (Rsx; n=4), surgery and unloaded hydrogel (Rsx + UG; n=4) and surgery and 1.33mM Gemcitabine-loaded gel (Rsx + GG; n=2). Untreated mice served as untreated controls (n=3). **A.** Bioluminescence tumour growth. Error bars represent SD. **B.** Kaplan-Meier survival curve. Log-rank test; ns: p=0.064.

4.5. Discussion

There is an unmet need for novel therapeutics for ependymoma as the mainstay treatment of resection and RT has not changed over 40years. Due to the chemoresistance of these tumours, 40% of all cases remain incurable[23,24,355]. However, in the quest of a cure for brain tumours, the BBB presents the major bottleneck in drug delivery to brain tumours[98]. Some types of brain tumours exhibit a leaky BBB, which render them more susceptible to treatment with systemic chemotherapies[129]. While the integrity of the BBB in ependymoma remains to be studied, the chemoresistance of these tumours suggest that the BBB is intact. Since many drugs with efficacy in ependymoma models *in vitro* do not efficiently penetrate the BBB, there is a need for local drug delivery method to circumvent the BBB.
Biodegradable hyaluronic acid-based hydrogels have previously been reported as a novel drug delivery technique for the treatment of brain tumours[149,346].

Here, we identified a selection of FDA-approved drugs that displayed activity in *in vitro* dose-response cell viability assays on ependymoma cells (Figure 4.3). Based on results from previous drug screens, statins (fluvastatin, atorvastatin), and PLK1 (rigosertib and volasertib) inhibitors were included as well as anticancer drugs commonly tested in clinical and preclinical trials for brain cancers such as doxorubicin, etoposide, temozolomide, carboplatin and gemcitabine[22,47,101,115,351,356]. Additionally, drugs targeting kinases ALK, CDK7 and PDGFRβ were tested as these had been shown to be upregulated in ependymoma cell lines (data not shown).

A selection of 7 drugs was classified as active in ependymoma cells *in vitro*. Of these, we chose three drugs on the basis of their *in vitro* activity and their BBB-penetrability (Figure 4.4). Fluvastatin and rigosertib were selected as drugs with low BBB penetrability but high activity on ependymoma models *in vivo*.
While fluvastatin demonstrates antitumour effect in xenograft models of human hepatocellular carcinoma, pancreatic and breast cancer, its BBB-penetrability properties remain unclear[357–360]. However, with its hydrophilic properties, it is less likely to sufficiently cross the BBB[361]. Preclinical efficacy studies performed on three different ependymoma models demonstrated that sustained systemic delivery of 20mg/kg fluvastatin did not affect tumour growth or survival (Figure 4.5). This is in

concordance with results from a study published by Guillot *et al.,* which showed low brain penetration of fluvastatin[349].

Systemic rigosertib has demonstrated efficacy in preclinical models of multiple myeloma and breast and pancreatic cancer[324,362]. However, PK studies of systemic delivery of rigosertib in preclinical glioma models revealed low brain and brain tumour distribution[328]. Nuthalapti *et al.* hypothesized that the low lipophilicity of rigosertib might the reason for the poor BBB penetrability of rigosertib[328].

Gemcitabine had been selected as our control drug due to its efficiency of delaying tumour regrowth post-surgery in ependymoma mouse models, when administered systemically via Alzet pump infusion[101].

Following the selection of drugs for repurposing, the release of lead compounds from hydrogel was studied. It was shown that the three drugs display different release rates from hydrogels (Figure 4.6). Gemcitabine was released at the highest concentration, followed by fluvastatin and rigosertib. While the release rate of gemcitabine and fluvastatin are similar to the rates measured before in collaboration with Chris Parkins using UV/ vis spectroscopy. Rigosertib release was measured for the first time and could therefore not be compared to previous studies. It was shown that smaller amounts of rigosertib were released from the gel *in vitro*. As interactions between CB8 and drugs can differ, this could be a result of stronger interactions between rigosertib and CB8 and can potentially be altered by changing the content of CB8 or the general formulation conditions of the hdyrogel[149].

Analysis of the drug concentration in the hydrogels loaded with gemcitabine, fluvastatin and rigosertib further showed that for fluvastatin and rigosertib, only about two thirds of the original concentration was detected. Since the gels appeared to be homogenous and did not feature any visible drug aggregates, the reason for this difference in concentration will need to be investigated in collaboration with the Melville Laboratory.

Additional *in vitro* experiments, which examined the effect of gemcitabine released from differently concentrated gels, showed that gels loaded with 1.33mM gemcitabine had the most effect on neurosphere formation of ependymoma cells (Figure 4.7). Based on the results from the time-course study, we would have expected this effect

to be visible in wells exposed to gemcitabine released from lower concentrated hydrogels. However, to better understand the effect of gemcitabine released from hydrogels in more detail, *in vitro* cell viability studies should be performed. These should include hydrogels with different doses of gemcitabine to identify IC_{50} and IC_{90} values for gemcitabine released from hydrogels.

The effect of fluvastatin released from 1mM-loaded hydrogels was also examined *in vitro*. As observed for gemcitabine, fluvastatin appeared to impact sphere formation of ependymoma cells (Figure 4.8). Here too, the effect of fluvastatin released from differently concentrated hydrogels on ependymoma cells should be examined in cell viability assays.

As drugs released from 1.3mM gemcitabine and 1mM fluvastatin loaded gels had a visible impact on ependymoma cells *in vitro*, these concentrations were selected for *in vivo* PK studies.

However, prior to PK studies with selected drugs, the injection of hydrogel had to be implemented into the first line of treatment for ependymoma- maximum safe resection surgery. In the first *in vivo* study of hydrogel injection post-resection, mice were monitored for potential toxic side effects. It was further analysed if the loading of the resection cavity with hydrogel has any effect on tumour recurrence and OS. We showed that mice injected with unloaded hydrogel display the same pattern of tumour recurrence like mice treated with resection alone (Figure 4.9). Mice injected with unloaded hydrogels further did not exhibit any side effects, suggesting the hydrogel injection is tolerable in our ependymoma mouse models.

Studies investigating the behaviour of FITC-labelled gel in the cavity over a time course of 72h showed that while the gel appeared to mainly reside in the cavity, a number of challenges were identified that could impact hydrogel-based drug delivery. Challenges included leaking of the gel from the cavity, residues of clotted in cavities as well as the limit of hydrogel volume injectable, which is correlated to the small sizes of resection cavities (Figure 4.10).

To overcome these challenges, different resection approaches addressing each challenge were tested. No improvement of cavity sizes could be achieved as mice with bigger cavities started showing adverse effects immediately after surgery. In order to more precisely perform resection surgeries and model resection surgeries of human brain tumours, a bigger model organism would need to be used in these studies. However, the use of rats or even bigger organisms comes with its limitations- the main one being that the ependymoma models and the preclinical hospital are established in mice and not established in larger animals. Nonetheless, marginal extension of the cavities resulted in small increase of average gel volume injected into resection cavities (Figure 4.11).

To address the challenge of residues of clotted blood, different haemostatic agents were tested. A combination of the haemostatic agents Lyostypt® and SURGICEL® followed by PBS washed of the cavity was identified as the most efficient method to reduce the amount of blood in resection cavities (Figure 4.12). SURGICEL® is commonly used in surgeries for CNS tumours, where it is frequently left in the cavity [141,353,363]. Furthermore, studies have reported that SURGICEL® was applied to cover wafers placed in the resection cavity[141,353]. Covering the hydrogel lining the cavity walls in resection cavities with SURGICEL® could be of interest in surgeries in humans. However, this cannot be modelled in mouse ependymoma models as SURGICEL® and or gel usually occupy the whole cavity rather than lining the cavity walls.

The retention of hydrogels within the resection cavity could be ensured by sealing the cavity using an artificial dura. In human brain tumour surgery, if parts of the skull are removed prior to surgery, they are usually placed in their original location once the tumour has been resected. In our mouse models this is not possible as the cranial window used in resection surgery is already prepared during the implantation of tumour cells. The piece of the skull covering the window is usually destroyed in the process of perforating the skull using a dental drill and can therefore not be used to cover the window post-surgery. The closure of the cavity as achieved in humans can be modelled in our surgeries by applying the artificial dura post-resection and has now been implemented into the standard resection protocol (Figure 4.13).

When administered systemically, rigosertib and fluvastatin do not efficiently affect tumour growth in orthotopic models of brain tumours despite high activity *in vitro* (see also Figure 4.5) [328]. This can either be a result of poor BBB penetrability or fast clearance from the tissue into the blood. In the case of both drugs, it is more likely to be due to poor BBB-penetrability as shown previously[328,349].

Pharmacokinetic studies in ependymoma mouse models revealed that fluvastatin was only detectable in the brain for 8h (Figure 4.14). The exponential decrease of fluvastatin concentration in the brain and plasma matches with the release profile generated from the *in vitro* time-course release study. The low half-life of fluvastatin in the brain (3.15h) could be due to fast efflux of fluvastatin out of the brain followed by fast metabolism of fluvastatin in the liver. However, due to the low BBB penetrability of fluvastatin, there is no data available on the efficacy of brain efflux transporters for fluvastatin. While it was shown by Guillot and colleagues that endothelial membranes prevent fluvastatin from entering the brain via anionic microdomains, it is also possible that fluvastatin is a substrate for one more of the many drug efflux transporters expressed on the BBB[349,364,365]. For other statins like pitavastatin and pravastatin, a study has shown that their efflux from the cortex into the blood stream is most likely mediated by the receptors rOat3 and rOatp2[366]. Pitavastatin is further a substrate of, Oatp1a2, the most common Oatp isoform on the BBB[365,367].

In the plasma, fluvastatin is detectable for 8h. An elimination half-life of 1-3h has previously been reported for fluvastatin, along with a very high percentage of plasma protein binding (>98%) following a single oral dose of 40mg (reviewed in [368]). Fluvastatin half-life in plasma in our study was 6.2 hours. This would suggest that there fluvastatin released is sustained over ~3h before the release either stops or decreases to a concentration level that is undetectable.

Data for rigosertib further suggests that, there was an initial drug release from the gel due to it being detected in brain and plasma 1h post-injection. As it could not be detected at any timepoint after that, it was either not released or only released to a very small extent after 1h (Figure 4.14). The low release rate *in vivo* would match the release rate observed in *in vitro* time-course release studies, which saw very low levels of rigosertib released.

Its detection in the plasma at very low levels at 8h and 24h post-injection indicates that drug might still be released from the gel but only at very low levels, which fall below the limit of quantification in UHPLC-MS. As for fluvastatin, drug efflux via BBB transporters of rigosertib remains to be verified. While it was shown by Qin *et al*. that delivery of rigosertib via loaded ApoE-targeting polymersomes has an effect on orthotopic PDX-models for GBM, they did not study the pharmacokinetics of the drug[369]. Other studies have shown that rigosertib is active in drug-resistant cell lines[324]. As shown in multiple cancers, the multidrug-resistance of the cells was mediated by the P-gp, which also play a crucial role in the BBB permeability. Thus, their data implies that rigosertib might not be a substrate of P-gp[370]. However, there are a number of other drug efflux transporters expressed on the BBB that could be responsible for rigosertib efflux.

Pharmacokinetic studies for gemcitabine-loaded hydrogels revealed that it was, albeit at low levels, detectable in the brain up to 144h. This implies that gemcitabine is continuously released from the gel. The lowest concentrations detected (9.8nM-1.018µM) are still in the range of the IC_{50} values determined for ependymoma cell lines *in vitro (*0.9nM-7nM*)*. Technically, the gemcitabine released from the gel should be efficient in eliminating residual tumour cells. However, it was observed that these conclusions cannot be drawn as *in vitro* studies had shown that gemcitabine released from 1.33mM loaded gels do not seem to completely kill off mSEP-CR(+) or mSEP-CR(-)^{EPHB2} cells *in vitro* (Figure 4.6).

The decrease of gemcitabine concentration over time is corroborated by *in vitro* release data (Figure 4.6) and data from a study in an orthotopic PDX-model for DIPG also display a decrease in gemcitabine concentration over time in brain tissue following a single dose[371]. Just like in the data from *in vitro* studies the released concentration of gemcitabine at the 1h timepoint. A combination of decreased release of gemcitabine from the hydrogel and gemcitabine efflux from the brain might be an explanation for the decrease in concentration. In general, gemcitabine is transported into tissues via nucleoside transporters (hENT1, hENT2) due to its hydrophilicity[332]. These transporters are bidirectional and can also promote efflux of gemcitabine. Furthermore, efflux of gemcitabine by the ABCC5 transporter has been reported to promote gemcitabine-resistance in cancer cells[372].

Due to the low concentrations of gemcitabine remaining consistent over time, it is difficult to establish a half-time for gemcitabine in plasma. In the literature, half-life for gemcitabine in rat plasma is reported at 2.6 ± 1.1h[373]. In humans, gemcitabine plasma levels peak 15-30min post infusion with a half time of 5-20min following a 30min infusion[374]. This short half-life is a result of fast metabolism of gemcitabine in the liver by cytidine deaminase[375]. Due to the short half-live of gemcitabine, sustained delivery via hydrogels should be more beneficial for eliminating residual tumour cells than single doses of gemcitabine.

Comparison of the drug concentrations with each other and the *in vitro* release data, reveals that the released concentrations of fluvastatin and rigosertib are higher than the ones for gemcitabine. This is not as it was expected from the results of the *in vitro* drug release study. Here, more gemcitabine is released than fluvastatin or rigosertib. However, a potential reason for this is there appears to be a much lower concentration of gemcitabine in the hydrogel than intended (Figure 4.14). As mentioned above, this will need to be examined in future studies. While there were no drug aggregates visible prior to gel injection, one reason for this could be improper resolving of the drug in the gel.

The degradation of the hyaluronic-acid based hydrogel by hyaluronidases has an additional effect on the drug release rate *in vivo*. There are six different forms of hyaluronidase (HYAL1-6), which are expressed at different levels throughout the body[348]. Brain tumours have been shown to not only highly express hyaluronic acid but also hyaluronidases, which suggests a faster degradation of hydrogel when it is injected near residual tumour cells rather than embedded in brain parenchyma. Analysis of RNA sequencing data from our ependymoma models show that levels of HYAL 2 are highest in mSEP-CR(+) and xSEP-CR(+) (Figure 4.17, one-way ANOVA with Dunnett's multiple comparisons test). As a result of this, hydrogels might be degraded quicker in mSEP-CR(+) and xSEP-CR(+) models compared to mSEP-CR(-)^{EPHB2} mSEP-CR(-)^{RTBDN} models. However, this will need to be analysed further *in vitro* and *ex vivo* and taken into account when tailoring hydrogels in future preclinical efficacy studies.

Following the *in vivo* PK study, a preclinical efficacy study was performed, investigating the effect of gemcitabine released on systemic delivery of gemcitabine. A previous study performed by Nimmervoll *et al.* had shown that systemic delivery of gemcitabine via infusion pumps in the mSEP-CR(-)^{EPHB2} mouse model significantly delays tumour growth and thereby prolongs OS[101]. Based on these results and results from the PK study, we hypothesised an effect on survival and tumour growth.
While injection of gemcitabine-loaded gel does not have a significant effect on survival, a trend towards prolonged survival can be observed (Figure 4.15). As the cohort of mice receiving surgical resection and gemcitabine-loaded hydrogel was very small (n=2), more mice will need to be subjected to this treatment to increase numbers in treatment groups and allow for statistical analysis (n= 13). However, the significant trend observed could be a result of sustained delivery of gemcitabine through the gel as demonstrated in previous PK studies for gemcitabine-loaded hydrogels (Figure 4.12). However, further studies will need to be performed, testing larger cohorts of mice and also testing gels with higher concentrations of gemcitabine to allow for maximum efficacy.

In this chapter, implementation of hyaluronic acid-based hydrogels into the first in line treatment for ependymoma- resection surgery- is demonstrated. *In vitro* and *in vivo* assays further confirmed drug release from hydrogels for three different candidate drugs, which all display high activity towards ependymoma cells *in vitro*. While there is a huge difference in sizes for resection cavities between mice and humans and has to be taken into account when translating this technique into the clinic, the preclinical assessment and establishment of hyaluronic acid hydrogels as a local drug delivery technique presents an important step in its development.

Future studies will focus on the release of gemcitabine and fluvastatin from hydrogels *in vitro* and *in vivo*. As the amount of rigosertib is released from the gels was shown to be very low (Figures 4.6 and 4.14), rigosertib will be excluded from any further experiments.

First, we will examine if loading the gel with higher concentrations of fluvastatin and gemcitabine will automatically lead to a higher release of the drugs. Following up on these *in vitro* studies, *in vivo* maximum tolerated dose studies with gemcitabine and

fluvastatin-loaded gels will be performed to investigate what the highest tolerated dose of gemcitabine and fluvastatin released from hydrogels is in mice. Once that has been confirmed, preclinical efficacy studies will examine the effect of gemcitabine and fluvastatin-loaded hydrogels on tumour growth and survival.

However, with regards to the translation of this treatment to the management of human ependymoma patients, there are some factors that could render the application of hydrogels for the treatment of intracranial ependymoma challenging. Firstly, the slow relapse of ependymoma could be a result of residing dormant tumour cells, which are undetectable after resection surgery in human patients. The hydrogel-based delivery of an antiproliferative agent such as gemcitabine directly after the resection surgery might therefore not be practical as this compound only targets actively proliferating cells and would therefore not have any effect on dormant tumour cells. In order to circumvent this, the drug release would either have to be altered to a late-onset and slower drug release or the drug would have to be replaced by an ependymoma-targeting drug.

Secondly, the diffusion of the drug into the surrounding tissue will need to be investigated. In 2018, Rowland *et al.* have reported a penetration of doxorubicin of up to 900µm following injection of doxorubicin-loaded hydrogel into ex-vivo brain tumour tissue. This was much further than the drug penetration observed from Carmustine wafers[149]. However, resection surgery in both, human and mice, is often accompanied by intracranial haemorrhage (as described in 4.4.3.2), which can result in a layer of clotted blood lining the resection cavity. As this layer is most likely thicker than 900µm, it will be crucial to study the penetration distance of the drug of choice to ensure effective drug delivery to the residing tumour cells. In order to avoid the use of hameostatic agents prior to the injection of the hydrogel, it should be examined if it is possible to transform the hydrogel into a haemostatic agent itself by introduce a haemostasis-inducing compound such as thrombin or its precursor pro-thrombin[376].

Thirdly, since intracranial ependymoma occur in the ventricular space, successful resection surgery might not result in a resection cavity that can subsequently be filled with drug-loaded hydrogel. An alternative to local delivery via hydrogels would therefore be intrathecal delivery, which helps deliver the desired chemotherapeutic

directly into the ventricular system. This has been shown to be efficient in other brain tumour types. Intrathecal delivery of methotrexate is successfully applied in combination with multi-agent chemotherapy in a subset of paediatric medulloblastoma patients (reviewed in [11]).

In summary, this chapter presents the successful establishment of a novel local drug delivery method for a resection model of an ependymoma mouse brain tumour model. However, this delivery technique is not restricted to ependymoma but will be applicable for the treatment of all other brain tumour types, whose standard of care treatment regimen involves surgical resection.

4.6. Supplementary Data

Table 4.4: Overview of dose-response concentrations for repurposed drugs.

Compound Name	Highest concentration in µM	Lowest concentration in µM	concentration range tested in xSEP-CR(+)
Temozolimide	25	$2.44x10^{-2}$	-
Lorlatinib	25	$2.44x10^{-2}$	-
Crenolanib	25	$2.44x10^{-2}$	-
Carboplatin	25	$2.44x10^{-2}$	-
Atorvastatin	25	$2.44x10^{-2}$	-
Crizotinib	25	$2.44x10^{-2}$	-
Fluvastatin	25	$2.44x10^{-2}$	-
Etoposide	25	$2.44x10^{-2}$	-
Volasertib	25	$2.44x10^{-2}$	-
Rigosertib	25	$2.44x10^{-2}$	-
THZ1	25	$2.44x10^{-2}$	2.5-$2.44x10^{-3}$ µM
Doxorubicin	25	$1.19x10^{-7}$	-
Gemcitabine	25	$1.19x10^{-7}$	-

Table 4.5: Overview of IC_{50}s for all drugs tested against variety of ependymoma cell lines.

Compound Name	IC_{50} mSEP-CR(+) in µM	IC_{50} mSEP-CR(-)^{RTBDN} in µM	IC_{50} mSEP-CR(-)^{EPHB2} in µM	IC_{50} xSEP-CR(+)in µM	IC_{50} mNSC in µM
Fluvastatin	0.9906	0.0133	0.0079	0.9311	0.0533
Atorvastatin	1.6840	0.0271	0.0472	1.6200	4.4590
Rigosertib	0.0642	0.0800	0.0002	0.0883	0.2198
Volasertib	0.0180	0.0134	0.0403	0.5407	0.1337
Crizotinib	0.8664	0.5493	0.6260	1.2740	0.7205
Lorlatinib	3.0960	2.7510	3.6090	9.9620	0.8867
Crenolanib	3.5760	1.7130	2.6750	3.0520	4.2850
THZ1	0.0788	0.1455	0.1184	0.0146	0.0660
Doxorubicin	0.0093	0.0011	0.0019	0.0350	0.0176
Gemcitabine	0.0046	0.0009	0.0073	0.0045	0.0172
Etoposide	0.0794	0.0444	0.1275	1.4920	0.1125
Temozolimide	12.9600	142.9000	3.8810	4.1260	8.7180
Carboplatin	1.2310	1.7580	1.5410	4.8960	3.5100

Table 4.6: Overview of IC_{10}, IC_{50} and IC_{90} for gemcitabine and fluvastatin values for mSEP-CR(+) and mSEP-CR(-)^{EPHB2} cells.

Cell line	Drug	IC_{10} in µM	IC_{50} in µM	IC_{90} in µM
mSEP-CR(+)	Gemcitabine	0.00318	0.0046	0.0067
	Fluvastatin	0.04256	0.9906	23.06
mSEP-CR(-)^{EPHB2}	Gemcitabine	0.0036	0.007	0.0146
	Fluvastatin		0.007896	0.09416

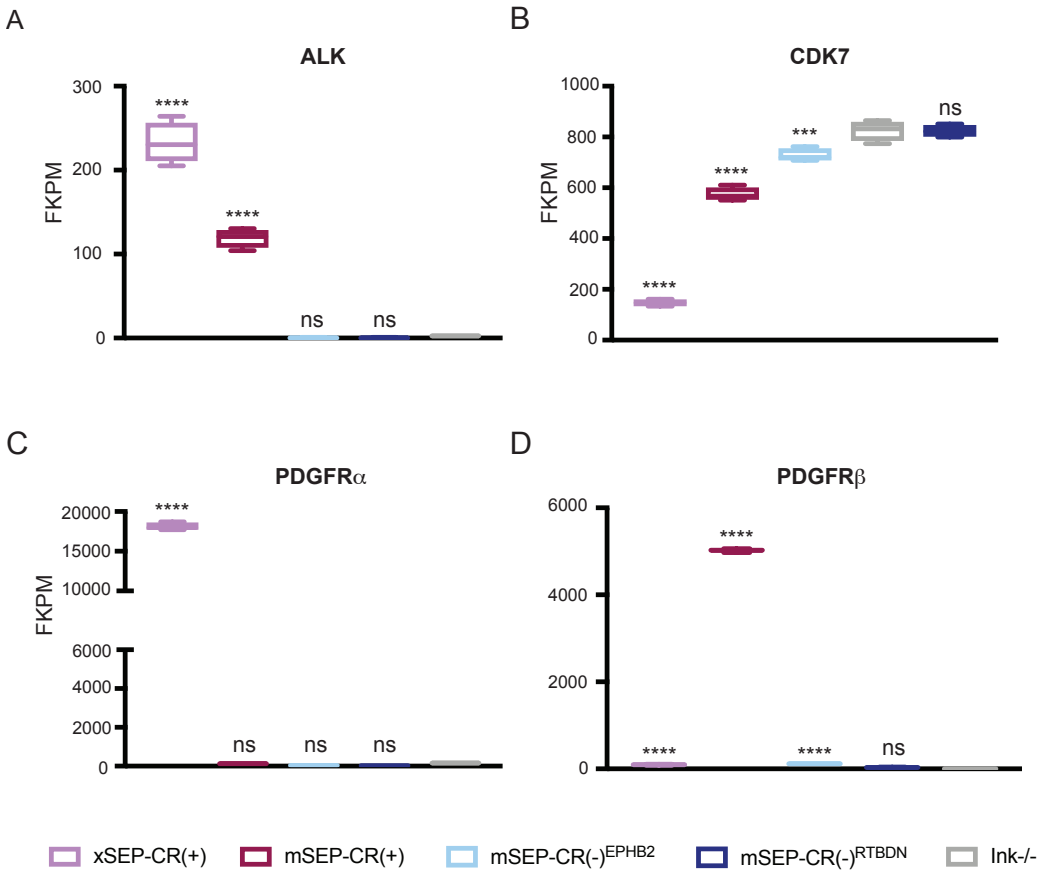

Figure 4.16: Expression analysis of PDGFRα/β, ALK, CDK in ependymoma cell lines. RNA expression analysis of anaplastic lymphoma kinase (ALK), cyclin-dependent kinase 7 (CDK7) and platelet-derived growth factor receptor α and β (PDGFRα/β) in mouse ependymoma cell lines (mSEP-CR[+], mSEP-CR[-]^{RTBDN}, mSEP-CR[-]^{EPHB2}) and a human ependymoma cell line (xSEP-CR[+]). Mouse neural stem cells from INK-/- mice served as control cells. Reads in Fragments Per Kilobase Million (FKPM). Bar plots represent median and standard deviation, n=4. One-way ANOVA with Dunnett's multiple comparison's test comparing to INK$^{-/-}$ control cells (****: p<0.0001, ***p<0.001, ns>0.999).

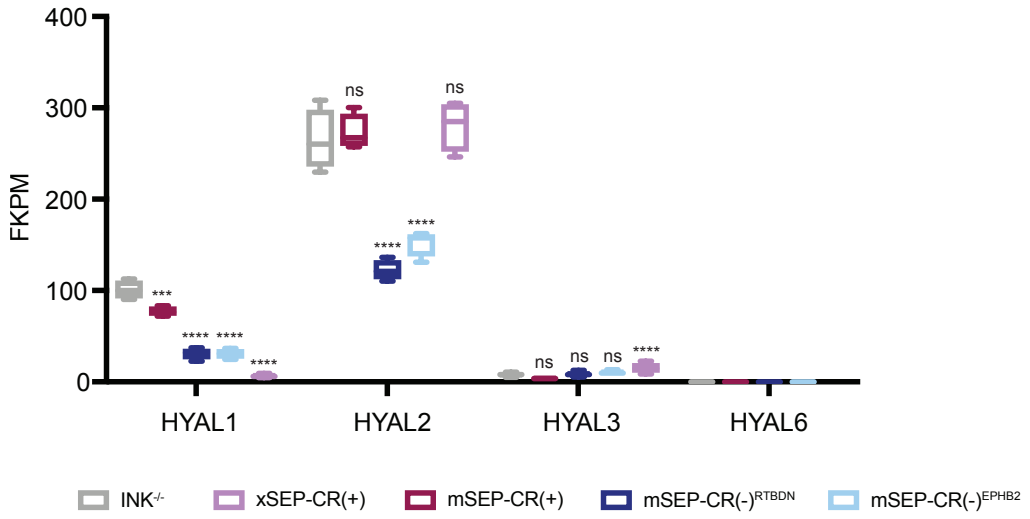

Figure 4.17: Expression analysis of Hyaluronidases 1,2,3 and 6 in ependymoma cell lines. RNA expression analysis of hyaluronidases 1-6 (HYAL1-6) in mouse ependymoma cell lines (mSEP-CR[+], mSEP-CR[-]^{RTBDN}, mSEP-CR[-]^{EPHB2}) and a human ependymoma cell line (xSEP-CR[+]). Mouse neural stem cells from INK-/- mice served as control cells. Reads in Fragments Per Kilobase Million (FKPM). Bar plots represent median and standard deviation, n=4. One-way ANOVA with Dunnett's multiple comparison's test comparing to INK$^{-/-}$ control cells (****: p<0.0001, ***p<0.001, ns>0.999).

5. Conclusion

Although rare, ependymomas are the third most common paediatric brain tumours, which are incurable in over one third of all cases. Ependymomas comprise several unique molecular subgroups characterised by distinct oncogenic drivers and prognoses. Thus, there is a need to create diagnostic tools to easily distinguish molecular subtypes and develop efficacy therapeutics that can be delivered effectively for ependymoma treatment.

Due to the variable clinical behaviour of the ependymoma subtypes, accurate diagnosis of the respective subgroups is crucial for subsequent clinical management of ependymoma patients. C11orf95-RELA^{Fus}-positive tumours define an aggressive subgroup with poor progression-free and overall survival rates. Hence, it is proposed that patients harbouring these tumours would need an equally aggressive treatment regimen compared to subgroups with more favourable prognoses. Accurate diagnosis for ST-EP-CR is currently still limited to tedious and sophisticated approaches like methylation profiling and break-apart fish, which are not widely available. Here, the generation of three candidate antibodies that specifically bind to C11orf95-RELA^{Fus} was reported. These antibodies show potential as diagnostic antibodies, which can be utilized in IHC assays that are performed in clinics worldwide. An accurate diagnostic tool such as these antibodies will transform the management of patients with supratentorial ependymoma.

Following tumour diagnosis, patients are subjected to standard-of-care treatments, which have not changed over four decades. The benefit of chemotherapy in the management of ependymoma has yet to be proven. *De novo* drug development allows for specific tailoring of the drug towards the tumour type throughout the developmental process. Hence, it consists of various stages of drug modifications and screens. Here, we report a mid-throughput drug screen of aminopyrimidine analogues variants, which have previously been identified as a candidate scaffold for ependymoma drug development (unpublished). Three lead structures were selected for further development.

In addition to the screens, we also investigated the efficacy of novel PLK1 inhibitors, which had been identified as candidate drugs for ependymoma treatment in a previous

drug screen[47]. This thesis therefore further describes the identification and development of active novel PLK1 inhibitors as a treatment for ependymoma mouse models. The identification of specific aminopyrimidine analogues and a novel PLK1 inhibitor, which are active in ependymoma *in vitro* and also display favourable drug properties for BBB penetrance presents an important step in the drug development for a novel ependymoma chemotherapy.

To accelerate the development of a chemotherapy for ependymoma that can be translated into the clinic, this thesis further demonstrates the use of alternative routes of drug delivery to circumvent the BBB bottleneck. In particular, we have established a hyaluronic acid-based hydrogel in the context of standard-of-care treatment for ependymoma. Hydrogels were successfully implemented following surgical removal of tumours in ependymoma mouse models by being injected into post-resection cavities. It was further confirmed *in vitro* and *in vivo* that gemcitabine-loaded hydrogels present the most effective combination of novel drug delivery and repurposed drug to treat ependymoma preclinically.
In general, hyaluronic-acid based hydrogels are a promising novel technique, which allows for the local delivery of drugs that display high activity against brain tumour cells but poor blood-brain barrier penetrability. In combination with selected FDA-approved drugs, this approach can be accelerated as a novel treatment option to be tested in clinical trials on ependymoma patients.

Taken together, this thesis presents the development of promising candidates for diagnostic antibodies targeting C11orf95-RELA^{Fus}, candidate compounds for the development of a novel chemotherapy and the utilisation of a novel drug delivery technique as part of multimodality treatments for ependymoma.

6. Patent application

6.1. Patent application for antibodies targeting C11orf95-RELA^{Fus1}

C11orf95-RELAFus1-targeting IgGs: 151, 154 and 159 and any similar IgGs were subject of a patent application filed in 2020 by Cancer Research Technology & MedImmune Limited.

Patent application PCT/EP2020/063096: Detection of fusion protein (C11orf95-RELAFUS1)

References

1. American Cancer Society. Facts & Figures 2019. *Am. Cancer Soc.* 1–76 (2019).
2. UK, C. R. Children's cancers incidence statistics. https://www.cancerresearchuk.org/health-professional/cancer-statistics/childrens-cancers/incidence#heading-Onetle.
3. AMERICAN CANCER SOCIETY. Key Statistics for Childhood Cancers. 2018 https://www.cancer.org/cancer/cancer-in-children/key-statistics.html (2020).
4. Public Health England. Childhood Cancer Statistics, England Annual Report 2018. *Public Heal. Engl.* 31 (2018).
5. Siegel, R. L., Miller, K. D. & Jemal, A. Cancer statistics, 2020. *CA. Cancer J. Clin.* **70**, 7–30 (2020).
6. Capasso, M. *et al.* Genetic Predisposition to Solid Pediatric Cancers. *Front. Oncol.* **10**, 1–22 (2020).
7. Huse, J. T. & Holland, E. C. Targeting brain cancer: advances in the molecular pathology of malignant glioma and medulloblastoma. *Nat. Rev. Cancer* **10**, 319–331 (2010).
8. Azzarelli, R., Simons, B. D. & Philpott, A. The developmental origin of brain tumours: A cellular and molecular framework. *Dev.* **145**, (2018).
9. Girardi, F., Allemani, C. & Coleman, M. P. Worldwide trends in survival from common childhood brain tumors: A systematic review. *J. Glob. Oncol.* **2019**, 1–25 (2019).
10. Glod, J. *et al.* Paediatric Brain Tumours: Current Knowledge and Therapeutic Opportunities. *J Pediatr Hematol Oncol.* **28**, 249–260 (2016).
11. Pollack, I. F., Agnihotri, S. & Broniscer, A. Childhood brain tumors: Current management, biological insights, and future directions. *J. Neurosurg. Pediatr.* **23**, 261–273 (2019).
12. Nejat, F., El Khashab, M. & Rutka, J. T. Initial Management of Childhood Brain Tumors: Neurosurgical Considerations. *J Child Neurol* **23**, 1136–1148 (2008).
13. Merchant, T. E., Pollack, I. F. & Loeffler, J. S. Brain tumors across the age spectrum: biology, therapy, and late effects. *Semin Radiat. Oncol* **20**, 58–66 (2010).

14. Pollack, I. F., Claassen, D., Al-Shboul, Q., Janosky, J. E. & Deutsch, M. Low-grade gliomas of the cerebral hemispheres in children: An analysis of 71 cases. *J. Neurosurg.* **82**, 536–547 (1995).
15. Cappelli, C. *et al.* Long term follow up of 69 patients treated for optic pathway tumours before the chemotherapy era. *Arch. Dis. Child.* **79**, 334–338 (1998).
16. Fouladi, M. *et al.* Survival and functional outcome of children with Hypothalamic/Chiasmatic tumors. *Cancer* **97**, 1084–1092 (2003).
17. Benesch, M. *et al.* Late sequela after treatment of childhood low-grade gliomas: A retrospective analysis of 69 long-term survivors treated between 1983 and 2003. *J. Neurooncol.* **78**, 199–205 (2006).
18. Laprie, A. *et al.* Paediatric brain tumours: A review of radiotherapy, state of the art and challenges for the future regarding protontherapy and carbontherapy. *Cancer/Radiotherapie* **19**, 775–789 (2015).
19. Evans, A. E. *et al.* The treatment of medulloblastoma. **72**, 572–582 (1990).
20. Tait, D. M., Thornton-Jones, H., Bloom, H. J., Lemerle, J. & Morris-Jones, P. Adjuvant chemotherapy for medulloblastoma: the first multi-centre control trial of the International Society of Paediatric Oncology (SIOP I). *Eur. J. Cancer* **26**, 464–469 (1990).
21. Duffner, P. K. *et al.* Prognostic Factors in Infants and Very Young Children with Intracranial Ependymomas. *Pediatr. Neurosurg.* **28**, 215–222 (1998).
22. Grill, J. *et al.* Postoperative chemotherapy without irradiation for ependymoma in children under 5 years of age: A multicenter trial of the French Society of Pediatric Oncology. *J. Clin. Oncol.* **19**, 1288–1296 (2001).
23. Merchant, T., Li, C., Xiong, X. & Kun, L. A Prospective Study of Conformal Radiation Therapy for Pediatric Ependymoma. *Lancet Oncol.* **10**, 258–266 (2009).
24. Ostrom, Q. T. *et al.* Alex's Lemonade stand foundation infant and childhood primary brain and central nervous system tumors diagnosed in the United States in 2007-2011. *Neuro. Oncol.* **16**, x1–x35 (2014).
25. Paulino, A. C. *et al.* Intracranial ependymomas: an analysis of prognostic factors and patterns of failure. *Am. J. Clin. Oncol.* **25**, 117–122 (2002).
26. Louis, D. N. *et al.* The 2007 WHO classification of tumours of the central nervous system. *Acta Neuropathol.* **114**, 97–109 (2007).

27. Wu, J., Armstrong, T. S. & Gilbert, M. R. Biology and management of ependymomas. *Neuro. Oncol.* **18**, 902–913 (2016).
28. Ross, G. W. & Rubinstein, L. J. Lack of histopathological correlation of malignant ependymomas with postoperative survival. *J. Neurosurg.* **70**, 31–36 (1989).
29. James, C. D. *et al.* Loss of genetic information in central nervous system tumors common to children and young adults. *Genes, Chromosom. Cancer* **2**, 94–102 (1990).
30. Ransom, D. T. *et al.* Cytogenetic and loss of heterozygosity studies in ependymomas, pilocytic astrocytomas, and oligodendrogliomas. *Genes, Chromosom. Cancer* **5**, 348–356 (1992).
31. Weremowicz, S., Kupsky, W. J., Morton, C. C. & Fletcher, J. A. Cytogenetic evidence for a chromosome 22 tumor suppressor gene in ependymoma. *Cancer Genet. Cytogenet.* **61**, 193–196 (1992).
32. Wernicke, C. *et al.* Involvement of chromosome 22 in ependymomas. *Cancer Genet. Cytogenet.* **79**, 173–176 (1995).
33. Carter, M. *et al.* Genetic abnormalities detected in ependymomas by comparative genomic hybridisation. *Br. J. Cancer* **86**, 929–939 (2002).
34. Ebert, C. *et al.* Molecular genetic analysis of ependymal tumors: NF2 mutations and chromosome 22q loss occur preferentially in intramedullary spinal ependymomas. *Am. J. Pathol.* **155**, 627–632 (1999).
35. Korshunov, A. *et al.* Gene Expression Patterns in Ependymoma correlate with Tumor Location , Grade , and Patient Age. *Am. J. Pathol.* **163**, 1721–1727 (2003).
36. Dyer, S. *et al.* Genomic imbalances in pediatric intracranial ependymomas define clinically relevant groups. *Am. J. Pathol.* **161**, 2133–2141 (2002).
37. Taylor, M. D. *et al.* Radial glia cells are candidate stem cells of ependymoma. *Cancer Cell* **8**, 323–335 (2005).
38. Johnson, R. a *et al.* Cross-species genomics matches driver mutations and cell compartments to model ependymoma. *Nature* **466**, 632–636 (2010).
39. Pajtler, K. W. *et al.* Molecular Classification of Ependymal Tumors across All CNS Compartments, Histopathological Grades, and Age Groups. *Cancer Cell* **27**, 728–743 (2015).
40. Parker, M. *et al.* C11orf95–RELA fusions drive oncogenic NF-kB signalling in ependymoma. *Nature* **506**, 451–554 (2014).

41. Pajtler, K. W., Pfister, S. M. & Kool, M. Molecular dissection of ependymomas. *Oncoscience* **2**, 827–828 (2015).
42. Gajjar, A., Pfister, S. M., Taylor, M. D. & Gilbertson, R. J. Molecular Insights into Pediatric Brain Tumours Have the Potential to Transform Therapy. *Biophys. Chem.* **20**, 5630- (2014).
43. Pajtler, K. W. *et al.* The current consensus on the clinical management of intracranial ependymoma and its distinct molecular variants. *Acta Neuropathol.* **133**, 1–8 (2016).
44. Ramaswamy, V. *et al.* Therapeutic impact of cytoreductive surgery and irradiation of posterior fossa ependymoma in the molecular era: A retrospective multicohort analysis. *J. Clin. Oncol.* **34**, 2468–2477 (2016).
45. Fukuoka, K. *et al.* Significance of molecular classification of ependymomas: C11orf95-RELA fusion- negative supratentorial ependymomas are a heterogeneous group of tumors. *Acta Neuropathol. Commun.* **22**, 134 (2018).
46. Zschernack, V. *et al.* Supratentorial ependymoma in childhood: more than just RELA or YAP. *Acta Neuropathol.* **141**, 455–466 (2021).
47. Mohankumar, K. M. *et al.* An in vivo screen identifies ependymoma oncogenes and tumor-suppressor genes. *Nat. Genet.* **47**, 878–887 (2015).
48. Serrano, M. *et al.* Role of the INK4a locus in tumor suppression and cell mortality. *Cell* **85**, 27–37 (1996).
49. Sherr, C. J. Cancer cell cycles. *Science (80-.).* **274**, 1672–1674 (1996).
50. Dodelet, V. C. & Pasquale, E. B. Eph receptors and ephrin ligands: Embryogenesis to tumorigenesis. *Oncogene* **19**, 5614–5619 (2000).
51. Wilkinson, D. G. Multiple roles of eph receptors and ephrins in neural development. *Nat. Rev. Neurosci.* **2**, 155–164 (2001).
52. Nakada, M. *et al.* The Phosphorylation of EphB2 Receptor Regulates Migration and Invasion of Human Glioma Cells. *Cancer Res.* **64**, 3179–3185 (2004).
53. Wang, S. D. *et al.* EphB2 receptor controls proliferation/migration dichotomy of glioblastoma by interacting with focal adhesion kinase. *Oncogene* **31**, 5132–5143 (2012).
54. Husa, A. M., Magic, Ž., Larsson, M., Fornander, T. & Pérez-Tenorio, G. EPH/ephrin profile and EPHB2 expression predicts patient survival in breast cancer. *Oncotarget* **7**, 21362–21380 (2016).

55. Chen, P. *et al.* EphB2 activation is required for ependymoma development as well as inhibits differentiation and promotes proliferation of the transformed cell. *Sci. Rep.* **5**, (2015).
56. Kelley, R. A., Al-Ubaidi, M. R. & Naash, M. I. Retbindin is an extracellular riboflavin-binding protein found at the photoreceptor/retinal pigment epithelium interface. *J. Biol. Chem.* **290**, 5041–5052 (2015).
57. Louis, D. N. *et al.* The 2016 World Health Organization Classification of Tumors of the Central Nervous System: a summary. *Acta Neuropathol.* **131**, 803–820 (2016).
58. Forment, J. V., Kaidi, A. & Jackson, S. P. Chromothripsis and cancer: Causes and consequences of chromosome shattering. *Nat. Rev. Cancer* **12**, 663–670 (2012).
59. Luijten, M. N. H., Lee, J. X. T. & Crasta, K. C. Mutational game changer: Chromothripsis and its emerging relevance to cancer. *Mutat. Res. - Rev. Mutat. Res.* **777**, 29–51 (2018).
60. Stephens, P. J. *et al.* Massive genomic rearrangement acquired in a single catastrophic event during cancer development. *Cell* **144**, 27–40 (2011).
61. Taniguchi, K. & Karin, M. NF-kB, inflammation, immunity and cancer: Coming of age. *Nat. Rev. Immunol.* **18**, 309–324 (2018).
62. Ozawa, T. *et al.* A De Novo Mouse Model of C11orf95-RELA Fusion-Driven Ependymoma Identifies Driver Functions in Addition to NF-κB. *Cell Rep.* **23**, 3787–3797 (2018).
63. Kim, G. B. *et al.* Rapid generation of somatic mouse mosaics with locus-specific stably-integrated transgenic elements. **179**, 251–267 (2019).
64. Pajtler, K. W. *et al.* YAP1 subgroup supratentorial ependymoma requires TEAD and nuclear factor I-mediated transcriptional programmes for tumorigenesis. *Nat. Commun.* **10**, 1–16 (2019).
65. Capper, D. *et al.* Practical implementation of DNA methylation and copy-number-based CNS tumor diagnostics: the Heidelberg experience. *Acta Neuropathol.* **136**, 181–210 (2018).
66. Wani, K. *et al.* BI-30. Characterization of L1CAM as a clinical marker for the C11orf95-RELA fusion in supratentorial ependymomas. *Neuro. Oncol.* **16**, 23–31 (2014).

67. Pietsch, T. *et al.* Supratentorial ependymomas of childhood carry C11orf95-RELA fusions leading to pathological activation of the NF-κB signaling pathway. *Acta Neuropathol.* **127**, 609–611 (2014).
68. Malgulwar, P. B. *et al.* C11orf95-RELA fusions and upregulated NF-KB signalling characterise a subset of aggressive supratentorial ependymomas that express L1CAM and nestin. *J. Neurooncol.* **138**, 29–39 (2018).
69. Chavali, P. *et al.* L1CAM Immunopositivity in Anaplastic Supratentorial Ependymomas: Correlation With Clinical and Histological Parameters. *Int. J. Surg. Pathol.* **27**, 251–258 (2019).
70. Gessi, M. *et al.* Role of immunohistochemistry in the identification of supratentorial C11ORF95-RELA fused ependymoma in routine neuropathology. *Am. J. Surg. Pathol.* **43**, 56–63 (2017).
71. Sasaki, A. *et al.* Review of ependymomas: assessment of consensus in pathological diagnosis and correlations with genetic profiles and outcome. *Brain Tumor Pathol.* **36**, 92–101 (2019).
72. Pagès, M. *et al.* Diagnostics of pediatric supratentorial RELA ependymomas: integration of information from histopathology, genetics, DNA methylation and imaging. *Brain Pathol.* **29**, 325–335 (2019).
73. Marinoff, A. E. *et al.* Rethinking childhood ependymoma: a retrospective, multi-center analysis reveals poor long-term overall survival. *J. Neurooncol.* **135**, 201–211 (2017).
74. Evans, A. E., Anderson, J. R., Lefkowitz-Boudreaux, I. B. & Finlay, J. L. Adjuvant chemotherapy of childhood posterior fossa ependymoma: Cranio-spinal irradiation with or without adjuvant CCNU, vincristine, and prednisone: A Childrens Cancer Group study. *Med. Pediatr. Oncol.* **27**, 8–14 (1996).
75. Timmermann, B. *et al.* Combined postoperative irradiation and chemotherapy for anaplastic ependymomas in childhood: Results of the German prospective trials HIT 88/89 and HIT 91. *Int. J. Radiat. Oncol. Biol. Phys.* **46**, 287–295 (2000).
76. Bouffet, E. & Foreman, N. Chemotherapy for intracranial ependymomas. *Child's Nerv. Syst.* **15**, 563–570 (1999).
77. Bouffet, E. *et al.* Intracranial ependymomas in children: A critical review of prognostic factors and a plea for cooperation. *Med. Pediatr. Oncol.* **30**, 319–329 (1998).

78. Rodríguez, D. *et al.* Outcomes of Malignant CNS Ependymomas: An Examination of 2408 Cases Through the Surveillance, Epidemiology, and End Results (SEER) Database (1973-2005). *J. Surg. Res.* **156**, 340–351 (2009).
79. Han, Z. *et al.* Prognostic value of H3K27me3 in children with ependymoma. *Pediatr. Blood Cancer* 1–7 (2019) doi:10.1002/pbc.28121.
80. Zacharoulis, S. *et al.* Treatment and outcome of children with relapsed ependymoma: A multi-institutional retrospective analysis. *Child's Nerv. Syst.* **26**, 905–911 (2010).
81. Denunzio, N. J. & Yock, T. I. Modern radiotherapy for pediatric brain tumors. *Cancers (Basel).* **12**, 1–16 (2020).
82. Merchant, T. E. *et al.* Conformal radiation therapy for pediatric ependymoma, chemotherapy for incompletely resected ependymoma, and observation for completely resected, supratentorial ependymoma. *J. Clin. Oncol.* **37**, 974–983 (2019).
83. Byer, L. *et al.* A systematic review and meta-analysis of outcomes in pediatric, recurrent ependymoma. *J. Neurooncol.* **144**, 445–452 (2019).
84. Lillard, J. C. *et al.* Pediatric Supratentorial Ependymoma: Surgical, Clinical, and Molecular Analysis. *Clin. Neurosurg.* **85**, 41–49 (2019).
85. Hidalgo, E. T. *et al.* Subgroup-specific outcomes of children with malignant childhood brain tumors treated with an irradiation-sparing protocol. *Child's Nerv. Syst.* **36**, 133–144 (2020).
86. Kurt, E. *et al.* Identification of relevant prognostic histopathologic features in 69 intracranial ependymomas, excluding myxopapillary ependymomas and subependymomas. *Cancer* **106**, 388–395 (2006).
87. Xi, S. *et al.* Clinical significance of the histological and molecular characteristics of ependymal tumors: A single institution case series from China. *BMC Cancer* **19**, 1–9 (2019).
88. Li, A. M. *et al.* EZH2 expression is a prognostic factor in childhood intracranial ependymoma: A Canadian Pediatric Brain Tumor Consortium study. *Cancer* **121**, 1499–1507 (2015).
89. Robertson, P. L. *et al.* Survival and prognostic factors following radiation therapy and chemotherapy for ependymomas in children: A report of the children's cancer group. *J. Neurosurg.* **88**, 695–703 (1998).

90. Rousseau, P. *et al.* Treatment of intracranial ependymomas of children: review of a 15-year experience. *Int. J. Radiat. Oncol. Biol. Phys.* **28**, 381–386 (1994).
91. Grundy, R. G. *et al.* Primary postoperative chemotherapy without radiotherapy for intracranial ependymoma in children: the UKCCSG/SIOP prospective study. *Lancet Oncol.* **8**, 696–705 (2007).
92. Smith, A. *et al.* ACNS0831: A children's oncology group phase III randomized trial of post-radiation chemotherapy in patients with newly diagnosed ependymoma ages 1 to 21 years. *Pediatr. Blood Cancer* **60**, (2013).
93. Witt, D. A. *et al.* Specific expression of PD-L1 in RELA-fusion supratentorial ependymoma: Implications for PD-1-targeted therapy. *Pediatr. Blood Cancer* e26960 (2018) doi:10.1002/pbc.26960.
94. de Almeida Magalhães, T. *et al.* Notch pathway in ependymoma RELA-fused subgroup: upregulation and association with cancer stem cells markers expression. *Cancer Gene Ther.* 4–7 (2019) doi:10.1038/s41417-019-0122-x.
95. Ferguson, S. D. *et al.* Ependymomas overexpress chemoresistance and DNA repair- related proteins. **9**, 7822–7831 (2018).
96. Phan, T. G. & Croucher, P. I. The dormant cancer cell life cycle. *Nat. Rev. Cancer* **20**, 398–411 (2020).
97. Aldape, K. *et al.* Challenges to curing primary brain tumours. *Nat. Rev. Clin. Oncol.* **16**, 509–520 (2019).
98. Pardridge, W. M. The blood-brain barrier: Bottleneck in brain drug development. *NeuroRX* **2**, 3–14 (2005).
99. Banks, W. A. Characteristics of compounds that cross the blood-brain barrier. *BMC Neurol.* **9**, S3 (2009).
100. Mak, I. W., Evaniew, N. & Ghert, M. Lost in translation: animal models and clinical trials in cancer treatment. *Am. J. Transl. Res.* **6**, 114–8 (2014).
101. Nimmervoll, B. V. *et al.* Establishing A Preclinical Multidisciplinary Board for Brain Tumors. **24**, 1654–1666 (2018).
102. Northcott, P. A. *et al.* Medulloblastoma comprises four distinct molecular variants. *J. Clin. Oncol.* **29**, 1408–1414 (2011).
103. Merino, D. M. *et al.* Molecular Characterization of Choroid Plexus Tumors Reveals Novel Clinically Relevant Subgroups. *Clin. Cancer Res.* **21**, 184–192 (2015).

104. Tong, Y. *et al.* Cross-Species Genomics Identifies TAF12, NFYC and RAD54L as Choroid Plexus Carcinoma and RAD54L as Choroid Plexus Carcinoma Oncogenes. *Cancer Cell* **27**, 712–727 (2015).
105. Park, J. *et al.* Transcriptome profiling-based identification of prognostic subtypes and multi-omics signatures of glioblastoma. *Sci. Rep.* **9**, 1–11 (2019).
106. Schüller, U. *et al.* Acquisition of Granule Neuron Precursor Identity Is a Critical Determinant of Progenitor Cell Competence to Form Shh-Induced Medulloblastoma. *Cancer Cell* **14**, 123–134 (2008).
107. Morfouace, M. *et al.* Preclinical studies of 5-fluoro-2'-deoxycytidine and tetrahydrouridine in pediatric brain tumors. *J. Neurooncol.* **126**, 225–234 (2016).
108. Nicolaides, T. P. *et al.* Targeted therapy for BRAF V600E malignant astrocytoma. *Clin. Cancer Res.* **17**, 7595–7604 (2011).
109. Singh, D. *et al.* Transforming Fusions of FGFR and TACC Genes in Human Glioblastoma. *Science (80-.).* **337**, 1231–1235 (2012).
110. Taylor, K. R. *et al.* Recurrent activating ACVR1 mutations in diffuse intrinsic pontine glioma. *Nat. Genet.* **46**, 457–461 (2014).
111. Basu, A. *et al.* An interactive resource to identify cancer genetic and lineage dependencies targeted by small molecules. *Cell* **154**, 1151–1161 (2013).
112. Mack, S. C. *et al.* Therapeutic targeting of ependymoma as informed by oncogenic enhancer profiling. *Nature* **553**, 101–105 (2017).
113. Tsoli, M. *et al.* Integration of genomics, high throughput drug screening, and personalized xenograft models as a novel precision medicine paradigm for high risk pediatric cancer. *Cancer Biol. Ther.* **19**, 1078–1087 (2018).
114. Swinney, D. C. Phenotypic vs. Target-based drug discovery for first-in-class medicines. *Clin. Pharmacol. Ther.* **93**, 299–301 (2013).
115. Atkinson, J. M. *et al.* An Integrated In Vitro and In Vivo High-Throughput Screen Identifies Treatment Leads for Ependymoma. *Cancer Cell* 384–399 (2011) doi:10.1016/j.ccr.2011.08.013.
116. Ashby, L. S. & Shapiro, W. R. Intra-arterial cisplatin plus oral etoposide for the treatment of recurrent malignant glioma: a phase II study. *J. Neurooncol.* **51**, 67–86 (2001).
117. Chamberlain, M. C. & Johnston, S. K. Temozolomide for recurrent intracranial supratentorial platinum-refractory ependymoma. *Cancer* **115**, 4775–4782 (2009).

118. Deeken, J. F. & Löscher, W. The blood-brain barrier and cancer: Transporters, treatment, and trojan horses. *Clin. Cancer Res.* **13**, 1663–1674 (2007).
119. Persidsky, Y., Ramirez, S. H., Haorah, J. & Kanmogne, G. D. Blood-brain barrier: Structural components and function under physiologic and pathologic conditions. *J. Neuroimmune Pharmacol.* **1**, 223–236 (2006).
120. Ballabh, P., Braun, A. & Nedergaard, M. The blood-brain barrier: An overview: Structure, regulation, and clinical implications. *Neurobiol. Dis.* **16**, 1–13 (2004).
121. Wong, A. D. *et al.* The blood-brain barrier: an engineering perspective. **6**, 1–22 (2013).
122. Levin, V. a. Relationship of octanol/water partition coefficient and molecular weight to rat brain capillary permeability. *J. Med. Chem.* **23**, 682–684 (1980).
123. Eiseman, J. L. *et al.* Plasma pharmacokinetics and tissue distribution of paclitaxel in CD2F1 mice. *Cancer Chemother. Pharmacol.* **34**, 465–471 (1994).
124. Heimans, J. J. *et al.* Paclitaxel (TAXOL®) concentrations in brain tumor tissue. *Ann. Oncol.* **5**, 951–953 (1994).
125. Kemper, E. M. *et al.* Increased penetration of paclitaxel into the brain by inhibition of P-glycoprotein. *Clin. Cancer Res.* **9**, 2849–2855 (2003).
126. Demeule, M. D. *et al.* Expression of multidrug-resistance p-glycoprotein (MDR1) in human brain tumours. **66**, 62–66 (2001).
127. Henrique, R. *et al.* Epigenetic regulation of MDR1 gene through post-translational histone modifications in prostate cancer. *BMC Genomics* **14**, 1–12 (2013).
128. Badowska-Kozakiewicz, A. M., Sobol, M. & Patera, J. Expression of multidrug resistance protein P-glycoprotein in correlation with markers of hypoxia (HIF-1α, EPO, EPO-R) in invasive breast cancer with metastasis to lymph nodes. *Arch. Med. Sci.* **13**, 1303–1314 (2017).
129. Phoenix, T. N. *et al.* Medulloblastoma Genotype Dictates Blood Brain Barrier Phenotype. *Cancer Cell* **29**, 508–522 (2016).
130. Gilhuis, H. J. *et al.* Three-dimensional (3D) reconstruction and quantitative analysis of the microvasculature in medulloblastoma and ependymoma subtypes. *Angiogenesis* **9**, 201–208 (2006).
131. Duda-Szymańska, J. & Papierz, W. Morphological analysis of vascular density in ependymomas. *Folia Neuropathol.* **45**, 115—119 (2007).

132. Ginguené, C. *et al.* P-glycoprotein (ABCB1) and breast cancer resistance protein (ABCG2) localize in the microvessels forming the blood-tumor barrier in ependymomas. *Brain Pathol.* **20**, 926–935 (2010).
133. Laquintana, V. *et al.* New strategies to deliver anticancer drugs to brain tumors. *Expert Opin Drug Deliv.* **6**, 1017–1032 (2009).
134. Haumann, R., Videira, J. C., Kaspers, G. J. L., van Vuurden, D. G. & Hulleman, E. Overview of Current Drug Delivery Methods Across the Blood–Brain Barrier for the Treatment of Primary Brain Tumors. *CNS Drugs* (2020) doi:10.1007/s40263-020-00766-w.
135. Zhang, F., Xu, C. L. & Liu, C. M. Drug delivery strategies to enhance the permeability of the blood–Brain barrier for treatment of glioma. *Drug Des. Devel. Ther.* **9**, 2089–2100 (2015).
136. Choi, J. J., Wang, S., Tung, Y. S., Morrison, B. & Konofagou, E. E. Molecules of Various Pharmacologically-Relevant Sizes Can Cross the Ultrasound-Induced Blood-Brain Barrier Opening in vivo. *Ultrasound Med. Biol.* **36**, 58–67 (2010).
137. Ananthanarayanan, B., Kim, Y. & Kumar, S. Elucidating the mechanobiology of malignant brain tumors using a brain matrix-mimetic hyaluronic acid hydrogel platform. *Biomaterials* **32**, 7913–7923 (2011).
138. Mangraviti, A., Gullotti, D., Tyler, B. & Brem, H. Nanobiotechnology-based delivery strategies: New frontiers in brain tumor targeted therapies. *J. Control. Release* **240**, 443–453 (2016).
139. Lesniak, M. S. & Brem, H. Targeted therapy for brain tumours. *Nat. Rev. Drug Discov.* **3**, 499–508 (2004).
140. Bota, D. A., Desjardins, A., Quinn, J. A., Affronti, M. L. & Friedman, H. S. Interstitial chemotherapy with biodegradable BCNU (Gliadel®) wafers in the treatment of malignant gliomas. *Ther. Clin. Risk Manag.* **3**, 707–715 (2007).
141. Subach, B. R. *et al.* Morbidity and survival after 1,3-bis(2-chloroethyl)-1-nitrosourea wafer implantation for recurrent glioblastoma: a retrospective case-matched cohort series. *Neurosurgery* **45**, 17–22 (1999).
142. Bregy, A. *et al.* The role of Gliadel wafers in the treatment of high-grade gliomas. *Expert Rev. Anticancer Ther.* **13**, 1453–1461 (2013).
143. Chaichana, K. L. *et al.* Risk of surgical site infection in 401 consecutive patients with glioblastoma with and without carmustine wafer implantation. *Neurol. Res.* **37**, 717–726 (2015).

144. Mechleb, B., Khater, F., Eid, A., David, G. & Moorman, J. P. Late onset Ommaya reservoir infection due to Staphylococcus aureus: Case report and review of Ommaya infections. *J. Infect.* **46**, 196–198 (2003).
145. Von Bueren, A. O. *et al.* Treatment of young children with localized medulloblastoma by chemotherapy alone: Results of the prospective, multicenter trial HIT 2000 confirming the prognostic impact of histology. *Neuro. Oncol.* **13**, 669–679 (2011).
146. Peyrl, A. *et al.* Safety of Ommaya reservoirs in children with brain tumors: A 20-year experience with 5472 intraventricular drug administrations in 98 patients. *J. Neurooncol.* **120**, 139–145 (2014).
147. Mead, P. A., Safdieh, J. E., Nizza, P., Tuma, S. & Sepkowitz, K. A. Ommaya reservoir infections: A 16-year retrospective analysis. *J. Infect.* **68**, 225–230 (2014).
148. Szvalb, A. D. *et al.* Ommaya reservoir-related infections: Clinical manifestations and treatment outcomes. *J. Infect.* **68**, 216–224 (2014).
149. Rowland, M. J. *et al.* An adherent tissue-inspired hydrogel delivery vehicle utilised in primary human glioma models. *Biomaterials* **179**, 199–208 (2018).
150. Capper, D. *et al.* DNA methylation-based classification of central nervous system tumours. *Nature* **555**, 469–474 (2018).
151. Chaplin, D. D. Overview of the Immune Response. *J Allergy Clin Immunol* **125**, 3–23 (2010).
152. Bonilla, F. A. & Oettgen, H. C. Adaptive immunity. *J. Allergy Clin. Immunol.* **125**, 33–40 (2010).
153. Joseph, S. B. *et al.* LXR-dependent gene expression is important for macrophage survival and the innate immune response. *Cell* **119**, 299–309 (2004).
154. Malisan, F. *et al.* Interleukin-10 induces immunoglobulin G isotype switch recombination in human CD40-activated naive B lymphocytes. *J. Exp. Med.* **183**, 937–947 (1996).
155. Jacob, J., Kelsoe, G., Rajewsky, K. & Weiss, U. Intraclonal generation of antibody mutants in germinal centres. *Nature* **354**, 389–392 (1991).
156. Berek, C., Berger, A. & Apel, M. Maturation of the immune response in germinal centers. *Cell* **67**, 1121–1129 (1991).

157. Harriman, W., Völk, H., Defranoux, N. & Wabl, Ma. Immunoglobulin class switch recombination deficiencies. *Annu. Rev. Immunol.* **1**, 361–384 (1993).
158. Schroeder Jr, H. W. & Cavacini, L. Structure and Function of Immunoglobulins. *J Allergy Clin Immunol* **125**, 1–7 (2010).
159. Glockshuber, R., Malia, M., Pfitzinger, I. & Plückthun, A. A Comparison of Strategies To Stabilize Immunoglobulin Fv-Fragments. *Biochemistry* **29**, 1362–1367 (1990).
160. Leong, S. S. J. & Chen, W. N. Preparing recombinant single chain antibodies. *Chem. Eng. Sci.* **63**, 1401–1414 (2008).
161. Amlot, P. L. *et al.* Prolonged action of a chimeric interleukin-2 receptor (CD25) monoclonal antibody used in cadaveric renal transplantation. *Transplantation* **60**, 748–756 (1995).
162. Behring, E. von & Kitasato, S. Ueber das Zustandekommen der Diphtherie-Immunität und der Tetanus-Immunität bei Thieren. *Dtsch. Medizinische Wochenschrift* **49**, (1890).
163. Köhler, G., Milstein, C. Continuous cultures of fused cells secreting antibody of predefined specificity. *Nature* **256**, 495–497 (1975).
164. Courtenay-Luck, N. S. *et al.* Development of Primary and Secondary Immune Responses to Mouse Monoclonal Antibodies Used in the Diagnosis and Therapy of Malignant Neoplasms. *Cancer Res.* **46**, 6489–6493 (1986).
165. Tjandra, J. J., Ramadi, L. & McKenzie, I. F. C. Development of human anti-murine antibody (HAMA) response in patients. *Immunol. cell Biol.* **68**, 367–376 (1990).
166. Legouffe, E. *et al.* Human anti-mouse antibody response to the injection of murine monoclonal antibodies against IL-6. *Clin. Exp. Immunol.* **98**, 323–329 (1994).
167. Osbourn, J., Groves, M. & Vaughan, T. From rodent reagents to human therapeutics using antibody guided selection. *Methods* **36**, 61–68 (2005).
168. Frenzel, A., Schirrmann, T. & Hust, M. Phage display-derived human antibodies in clinical development and therapy. *MAbs* **8**, 1177–1194 (2016).
169. Smith, G. P. Filamentous fusion phage: Novel expression vectors that display cloned antigens on the virion surface. *Science (80-.).* **228**, 1315–1317 (1985).
170. Parmley, S. F. & Smith, G. P. Antibody-selectable filamentous fd phage vectors: affinity purification of target genes. *Gene* **73**, 305–318 (1988).

171. De Haard, H. J. *et al.* A large non-immunized human Fab fragment phage library that permits rapid isolation and kinetic analysis of high affinity antibodies. *J. Biol. Chem.* **274**, 18218–18230 (1999).
172. Clackson, T., Hoogenboom, H. R., Griffiths, A. D. & Winter, G. Making antibody fragments using phage display libraries. *Nature* **352**, 624–628 (1991).
173. Hoogenboom, H. R. *et al.* Multi-subunit proteins on the surface of filamentous phage: Methodologies for displaying antibody (Fab) heavy and light chains. *Nucleic Acids Res.* **19**, 4133–4137 (1991).
174. Vaughan, T. J. *et al.* Human Antibodies with Sub-nanomolar Affinities Isolated from a Large Non-inmmunized Phage Display Library. *Nat. Med.* **2**, 534–539 (1996).
175. Marks, J. D. *et al.* By-passing Immunization- Building High Afifnity Human Antibodies by Chain Shuffling. *Nature* **10**, 779–782 (1992).
176. Skerra, A. & Plückthun, A. Assembly of a functional immunoglobulin Fv fragment in Escherichia coli. *Science (80-.).* **240**, 1038–1041 (1988).
177. Griffiths, A. D. *et al.* Human anti-self antibodies with high specificity from phage display libraries. *EMBO J.* **12**, 725–734 (1993).
178. Hanyu, Y. & Kato, M. Screening antibody libraries with colony assay using scFv-alkaline phosphatase fusion proteins. *Molecules* **25**, 1–12 (2020).
179. Hoet, R. M. *et al.* Generation of high-affinity human antibodies by combining donor-derived and synthetic complementarity-determining-region diversity. *Nat. Biotechnol.* **23**, 344–348 (2005).
180. Hawkins, R. E., Russell, S. J. & Winter, G. Selection of phage antibodies by binding affinity. Mimicking affinity maturation. *J. Mol. Biol.* **226**, 889–896 (1992).
181. McCafferty, J., Griffiths, A., Winter, G. & DJ, C. Phage antibodies: filamentous phage dispalying antibody variable domains. *Nature* **348**, 552 (1990).
182. Groves, M. *et al.* Affinity maturation of phage display antibody populations using ribosome display. *J. Immunol. Methods* **313**, 129–139 (2006).
183. Hust, M. *et al.* A human scFv antibody generation pipeline for proteome research. *J. Biotechnol.* **152**, 159–170 (2011).
184. Irving, R. A., Coia, G., Roberts, A., Nuttall, S. D. & Hudson, P. J. Ribosome display and affinity maturation: From antibodies to single V-domains and steps towards cancer therapeutics. *J. Immunol. Methods* **248**, 31–45 (2001).

185. Amstutz, P., Forrer, P., Zahnd, C. & Plückthun, A. In vitro display technologies: Novel developments and applications. *Curr. Opin. Biotechnol.* **12**, 400–405 (2001).
186. Lewis, L. & Lloyd, C. Ribosome Display and Related Technologies. **805**, 75–85 (2012).
187. Chan, D. T. Y. *et al.* Extensive sequence and structural evolution of Arginase 2 inhibitory antibodies enabled by an unbiased approach to affinity maturation. *Proc. Natl. Acad. Sci. U. S. A.* **117**, 16949–16960 (2020).
188. Attarwala, H. Role of antibodies in cancer targeting. *J. Nat. Sci. Biol. Med.* **1**, 53–56 (2010).
189. Pierpont, T. M., Limper, C. B. & Richards, K. L. Past, present, and future of Rituximab-The world's first oncology monoclonal antibody therapy. *Front. Oncol.* **8**, (2018).
190. Zhang, J. Y. *et al.* Enhancement of antibody detection in cancer using panel of recombinant tumor-associated antigens. *Cancer Epidemiol. Biomarkers Prev.* **12**, 136–143 (2003).
191. Saadi, H. *et al.* Development of an ELISA detecting Tumor Protein 53-Induced Nuclear Protein 1 in serum of prostate cancer patients. *Results Immunol.* **3**, 51–56 (2013).
192. Agnolon, V. *et al.* ELISA assay employing epitope-specific monoclonal antibodies to quantify circulating HER2 with potential application in monitoring cancer patients undergoing therapy with trastuzumab. *Sci. Rep.* **10**, 1–12 (2020).
193. Cressey, R. *et al.* Simplified approaches for the development of an ELISA to detect circulating autoantibodies to p53 in cancer patients. *BMC Biotechnol.* **8**, 1–12 (2008).
194. Jin, Y. *et al.* Use of autoantibodies against tumor-associated antigens as serum biomarkers for primary screening of cervical cancer. *Oncotarget* **8**, 105425–105439 (2017).
195. Brennan, D. J. & Gallagher, W. M. Prognostic ability of a panel of immunohistochemistry markers - retailoring of an 'old solution'. *Breast Cancer Res.* **10**, 10–12 (2008).
196. Heo, C. K., Bahk, Y. Y. & Cho, E. W. Tumor-associated autoantibodies as diagnostic and prognostic biomarkers. *BMB Rep.* **45**, 677–685 (2012).

197. Zaha, D. C. Significance of immunohistochemistry in breast cancer. *World J. Clin. Oncol.* **5**, 382–392 (2014).
198. Melling, N. *et al.* High Ki67 expression is an independent good prognostic marker in colorectal cancer. *J. Clin. Pathol.* **69**, 209–214 (2016).
199. Molina, R. *et al.* Assessment of a combined panel of six serum tumor markers for lung cancer. *Am. J. Respir. Crit. Care Med.* **193**, 427–437 (2016).
200. Carneiro, A. *et al.* The Role of Immunohistochemical Analysis as a Tool for the Diagnosis, Prognostic Evaluation and Treatment of Prostate Cancer: A Systematic Review of the Literature. *Front. Oncol.* **8**, 1–9 (2018).
201. Stratton, M. R., Campbell, P. J. & Futreal, P. A. The cancer genome. *Nature* **458**, 719–724 (2009).
202. Brien, G. L., Stegmaier, K. & Armstrong, S. A. Targeting chromatin complexes in fusion protein-driven malignancies. *Nat. Rev. Cancer* **19**, 255–269 (2019).
203. Kadoch, C. & Crabtree, G. R. Reversible Disruption of mSWI/SNF (BAF) Complexes by the SS18-SSX Oncogenic Fusion in Synovial Sarcoma. *Cell* **153**, 71–85 (2013).
204. Baranov, E. *et al.* A Novel SS18-SSX Fusion-specific Antibody for the Diagnosis of Synovial Sarcoma. *Am. J. Surg. Pathol.* **44**, 922–933 (2020).
205. Vaughan, T. J. *et al.* Human Antibodies with Sub-nanomolar Affinities Isolated from Large Non-immunized Phage Display Library. *Nat. Med.* **2**, 534–539 (1996).
206. Lloyd, C. *et al.* Modelling the human immune response: Performance of a 1011 human antibody repertoire against a broad panel of therapeutically relevant antigens. *Protein Eng. Des. Sel.* **22**, 159–168 (2009).
207. Persic, L. *et al.* An integrated vector system for the eukaryotic expression of antibodies or their fragments after selection from phage display libraries. *Gene* **187**, 9–18 (1997).
208. Groves, M. A. & Nickson, A. A. Affinity Maturation of Phage Display Antibody Populations Using Ribosome Display. in *Ribosome Display and Related Technologies: Methods and Protocols* vol. 805 75–85 (2012).
209. Wang, R. *et al.* Engineering production of functional scfv antibody in E. coli by co-expressing the molecule chaperone skp. *Front. Cell. Infect. Microbiol.* **4**, 1–9 (2013).

210. Kupp, R. *et al.* C11orf95 translocations constitute aberrant chromatin remodeling and transcription factors in ependymoma. *Cancer Discov.* **accepted**,.
211. Carbone, A., Gloghini, A., Kwong, Y. L. & Younes, A. Diffuse large B cell lymphoma: Using pathologic and molecular biomarkers to define subgroups for novel therapy. *Ann. Hematol.* **93**, 1263–1277 (2014).
212. Liu, L. *et al.* The Combination of the Tumor Markers Suggests the Histological Diagnosis of Lung Cancer. *Biomed Res. Int.* **2017**, (2017).
213. Ramaswamy, V. *et al.* Risk stratification of childhood medulloblastoma in the molecular era: The Current Consensus. *Acta Neuropathol* **131**, 821–831 (2017).
214. Bordeaux, J. *et al.* Antibody validation. *Biotechniques* **48**, 197–209 (2010).
215. Taussig, M. J., Fonseca, C. & Trimmer, J. S. Antibody validation: a view from the mountains. *N. Biotechnol.* **45**, 1–8 (2018).
216. Kerschbaumer, R. J. *et al.* Single-chain Fv fusion proteins suitable as coating and detecting reagents in a double antibody sandwich enzyme-linked Immunosorbent assay. *Anal. Biochem.* **249**, 219–227 (1997).
217. Afanasieva, T. A. *et al.* Single-chain antibody and its derivatives directed against vascular endothelial growth factor: Application for antiangiogenic gene therapy. *Gene Ther.* **10**, 1850–1859 (2003).
218. Holliger, P. & Hudson, P. J. Engineered antibody fragments and the rise of single domains. *Nat. Biotechnol.* **23**, 1126–1136 (2005).
219. Mahmood, T. & Yang, P. C. Western blot: Technique, theory, and trouble shooting. *N. Am. J. Med. Sci.* **4**, 429–434 (2012).
220. Pillai-Kastoori, L. *et al.* Antibody validation for Western blot: By the user, for the user. *J. Biol. Chem.* **295**, 926–939 (2020).
221. Buchwalow, I., Samoilova, V., Boecker, W. & Tiemann, M. Non-specific binding of antibodies in immunohistochemistry: Fallacies and facts. *Sci. Rep.* **1**, 1–6 (2011).
222. Kim, S. W., Roh, J. & Park, C. S. Immunohistochemistry for pathologists: Protocols, pitfalls, and tips. *J. Pathol. Transl. Med.* **50**, 411–418 (2016).
223. Goldstein, N. S. *et al.* Recommendations for improved standardization of immunohistochemistry. *Appl. Immunohistochem. Mol. Morphol.* **15**, 124–133 (2007).

224. Shi, Z. & Stack, Ms. An Update on Immunohistochemistry in Translational Cancer Research. *Cancer Transl. Med.* **1**, 115 (2015).
225. Hanes, J., Jermutus, L., Weber-Bornhauser, S., Bosshard, H. R. & Plückthun, A. Ribosome display efficiently selects and evolves high-affinity antibodies in vitro from immune libraries. *Proc. Natl. Acad. Sci. U. S. A.* **95**, 14130–14135 (1998).
226. Hanes, J., Schaffitzel, C., Knappik, A. & Plückthun, A. Picomolar affinity antibodies from a fully synthetic naive library selected and evolved by ribosome display. *Nat. Biotechnol.* **18**, 1287–1292 (2000).
227. Zahnd, C. *et al.* Directed in Vitro Evolution and Crystallographic Analysis of a Peptide-binding Single Chain Antibody Fragment (scFv) with Low Picomolar Affinity. *J. Biol. Chem.* **279**, 18870–18877 (2004).
228. Sasaki, N. *et al.* Nuclear factor-κB p65 (RelA) transcription factor is constitutively activated in human colorectal carcinoma tissue. *Clin. Cancer Res.* **7**, 4136–4142 (2001).
229. Weichert, W. *et al.* High expression of RelA/p65 is associated with activation of nuclear factor-κB-dependent signaling in pancreatic cancer and marks a patient population with poor prognosis. *Br. J. Cancer* **97**, 523–530 (2007).
230. Altschul, S. F., Gish, W., Miller, W., Myers, E. W. & Lipman, D. J. Basic local alignment search tool. *J. Mol. Biol.* **215**, 403–410 (1990).
231. Uhlen, M. *et al.* A proposal for validation of antibodies. *Nat. Methods* **13**, 823–827 (2016).
232. Chiu, J. K. *et al.* Intracranial ependymoma in children: analysis of prognostic factors. *J. Neurooncol.* **13**, 283–90 (1992).
233. Gramatzki, D. *et al.* Chemotherapy for intracranial ependymoma in adults. *BMC Cancer* **16**, 287 (2016).
234. Nuño, M. *et al.* Treatment and survival of supratentorial and posterior fossa ependymomas in adults. *J. Clin. Neurosci.* **28**, 24–30 (2016).
235. Coussens, N. P. *et al.* Small-molecule screens: A gateway to cancer therapeutic agents with case studies of food and drug administration–approved drugs. *Pharmacol. Rev.* **69**, 479–496 (2017).
236. Abe, H. *et al.* Discovery of a highly potent and selective MEK inhibitor: GSK1120212 (JTP-74057 DMSO solvate). *ACS Med. Chem. Lett.* **2**, 320–324 (2011).

237. Williams, J. A. *et al.* Identification of a small molecule inhibitor of the hedgehog signaling pathway: Effects on basal cell carcinoma-like lesions. *Proc. Natl. Acad. Sci. U. S. A.* **100**, 4616–4621 (2003).
238. Sekulic, A. *et al.* Efficacy and Safety of Vismodegib in Advanced Basal-Cell Carcinoma. *N Engl J Med* **366**, 2171–2179 (2012).
239. Hoffmann L, L. R. L. FDA approves Erivedge (vismodegib) capsule, the first medicine for adults with advanced basal cell carcinoma. *Media Release* 88–91 (2012).
240. Flaherty, K. T. *et al.* Improved Survival with MEK Inhibition in BRAF-Mutated Melanoma. *N. Engl. J. Med.* **367**, 107–114 (2012).
241. Lage, O. M. *et al.* Current screening methodologies in drug discovery for selected human diseases. *Mar. Drugs* **16**, 1–31 (2018).
242. Platet, N., Cathiard, A. M., Gleizes, M. & Garcia, M. Estrogens and their receptors in breast cancer progression: A dual role in cancer proliferation and invasion. *Crit. Rev. Oncol. Hematol.* **51**, 55–67 (2004).
243. Rugo, H. S. *et al.* Endocrine therapy for hormone receptor-positive metastatic breast cancer: American society of clinical oncology guideline. *J. Clin. Oncol.* **34**, 3069–3103 (2016).
244. Hanahan, D. & Weinberg, R. A. The Hallmarks of Cancer. *Cell* **100**, 57–70 (2000).
245. Sun, J. *et al.* A systematic analysis of FDA-approved anticancer drugs. *BMC Syst. Biol.* **11**, (2017).
246. Croston, G. E. The utility of target-based discovery. *Expert Opin. Drug Discov.* **12**, 427–429 (2017).
247. Moffat, J. G., Vincent, F., Lee, J. A., Eder, J. & Prunotto, M. Opportunities and challenges in phenotypic drug discovery: An industry perspective. *Nat. Rev. Drug Discov.* **16**, 531–543 (2017).
248. Mullard, A. 2019 FDA drug approvals. *Nat. Rev. Drug Discov.* **19**, 79–84 (2020).
249. Florento, L. *et al.* Comparison of cytotoxic activity of anticancer drugs against various human tumor cell lines using in vitro cell-based approach. *Int. J. Biomed. Sci.* **8**, 76–80 (2012).
250. Riva, G. *et al.* In vitro anticancer drug test: A new method emerges from the model of glioma stem cells. *Toxicol. Reports* **1**, 188–199 (2014).

251. Gautam, P. *et al.* Identification of selective cytotoxic and synthetic lethal drug responses in triple negative breast cancer cells. *Mol. Cancer* **15**, 1–16 (2016).
252. Folkesson, E. *et al.* High-throughput screening reveals higher synergistic effect of MEK inhibitor combinations in colon cancer spheroids. *Sci. Rep.* **10**, 1–14 (2020).
253. Eder, J., Sedrani, R. & Wiesmann, C. The discovery of first-in-class drugs: Origins and evolution. *Nat. Rev. Drug Discov.* **13**, 577–587 (2014).
254. Riedl, A. *et al.* Comparison of cancer cells in 2D vs 3D culture reveals differences in AKT-mTOR-S6K signaling and drug responses. *J. Cell Sci.* **130**, 203–218 (2017).
255. Melissaridou, S. *et al.* The effect of 2D and 3D cell cultures on treatment response, EMT profile and stem cell features in head and neck cancer 11 Medical and Health Sciences 1112 Oncology and Carcinogenesis. *Cancer Cell Int.* **19**, 1–10 (2019).
256. Fontoura, J. C. *et al.* Comparison of 2D and 3D cell culture models for cell growth, gene expression and drug resistance. *Mater. Sci. Eng. C* **107**, 110264 (2020).
257. Zhang, Z. *et al.* Overcoming cancer therapeutic bottleneck by drug repurposing. *Signal Transduct. Target. Ther.* **5**, (2020).
258. Li, A. P. Preclinical in vitro screening assays for drug-like properties. *Drug Discov. Today Technol.* **2**, 179–185 (2005).
259. Di, L. & Kerns, E. H. Biological assay challenges from compound solubility: strategies for bioassay optimization. *Drug Discov. Today* **11**, 446–451 (2006).
260. Legehar, A., Xhaard, H. & Ghemtio, L. IDAAPM: Integrated database of ADMET and adverse effects of predictive modeling based on FDA approved drug data. *J. Cheminform.* **8**, 1–11 (2016).
261. Swinney, D. C. & Anthony, J. How were new medicines discovered? *Nat. Rev. Drug Discov.* **10**, 507–519 (2011).
262. Mushtaq, S., Abbasi, B. H., Uzair, B. & Abbasi, R. Natural products as reservoirs of novel therapeutic agents. *EXCLI J.* **17**, 420–451 (2018).
263. Butler, M. S. The role of natural product chemistry in drug discovery. *J. Nat. Prod.* **67**, 2141–2153 (2004).
264. Weaver, B. A. How Taxol/paclitaxel kills cancer cells. *Mol. Biol. Cell* **25**, 2677–2681 (2014).

265. Clegg, A., Scott, D. A., Hewitson, P., Sidhu, M. & Waugh, N. Clinical and cost effectiveness of paclitaxel, docetaxel, gemcitabine, and vinorelbine in non-small cell lung cancer: A systematic review. *Thorax* **57**, 20–28 (2002).
266. Crown, J., O'Leary, M. & Ooi, W.-S. Docetaxel and Paclitaxel in the Treatment of Breast Cancer: A Review of Clinical Experience. *Oncologist* **9**, 24–32 (2004).
267. Nirmala, M. J., Samundeeswari, A. & Sankar, P. D. A gene encoding autoclavable superoxide dismutase and its expression in E. coli. *Res. Plant Biol.* **1**, 1–14 (2011).
268. Möbus, V., Kieback, D. G. & Kaubitzsch, S. K. Duration of chemotherapy with topotecan influences survival in recurrent ovarian cancer: A meta-analysis. *Anticancer Res.* **27**, 1581–1587 (2007).
269. Quoix, E. Topotecan in the treatment of relapsed small cell lung cancer. *Onco. Targets. Ther.* 79 (2008) doi:10.2147/ott.s3689.
270. Coronel, J. *et al.* Weekly topotecan as second- or third-line treatment in patients with recurrent or metastatic cervical cancer. *Med. Oncol.* **26**, 210–214 (2009).
271. Arcamone, F. *et al.* Adriamycin, 14-hydroxydaunomycin, a new antitumor antibiotic from S. peucetius var. caesius. *Biotechnol. Bioeng.* **11**, 1101–1110 (1969).
272. Malla, S., Prasad Niraula, N., Singh, B., Liou, K. & Kyung Sohng, J. Limitations in doxorubicin production from Streptomyces peucetius. *Microbiol. Res.* **165**, 427–435 (2010).
273. Laplante, S. R., Edwards, P. J., Fader, L. D., Jakalian, A. & Hucke, O. Revealing Atropisomer Axial Chirality in Drug Discovery. *ChemMedChem* **6**, 505–513 (2011).
274. Franks, M. E., Macpherson, G. R. & Figg, W. D. Thalidomide. *Lancet* **363**, 1802–1811 (2004).
275. Toenjes, S. T. & Gustafson, J. L. Atropisomerism in medicinal chemistry: Challenges and opportunities. *Future Med. Chem.* **10**, 409–422 (2018).
276. Hoelder, S., Clarke, P. A. & Workman, P. Discovery of small molecule cancer drugs: Successes, challenges and opportunities. *Mol. Oncol.* **6**, 155–176 (2012).
277. Winkler, G. C., Barle, E. L., Galati, G. & Kluwe, W. M. Functional differentiation of cytotoxic cancer drugs and targeted cancer therapeutics. *Regul. Toxicol. Pharmacol.* **70**, 46–53 (2014).

278. Capdeville, R., Buchdunger, E., Zimmermann, J. & Matter, A. Glivec (ST1571, imatinib), a rationally developed, targeted anticancer drug. *Nat. Rev. Drug Discov.* **1**, 493–502 (2002).
279. Hungerford, D. A. & Nowell, P. C. A minute chromosome in human chronic granulocytic leukemia. *Science (80-.).* **132**, 1497–1499 (1960).
280. Rowley, J. D. A New Consistent Chromosomal Abnormality in Chronic Myelogenous Leukaemia identified by quinacrine Fluorescence and Giemsa Staining. *Nature* **243**, 290–293 (1973).
281. Lugo, T. G., Pendergast, A.-M., Muller, A. J. & Witte, O. N. Tyrosine Kinase Activity and Transformation Potency of bcr-abl Oncogene Products. *Science (80-.).* **24**, 1079–1082 (1990).
282. Barker, A. J. *et al.* Studies leading to the identification of ZD1839 (Iressa^{TM}): An orally active, selective epidermal growth factor receptor tyrosine kinase inhibitor targeted to the treatment of cancer. *Bioorganic Med. Chem. Lett.* **11**, 1911–1914 (2001).
283. Websites, A. *AstraZeneca - IRESSA® (gefitinib) approved by the U.S. Food and Drug Administration for first-line treatment of advanced EGFR mutation-positive non-small cell lung cancer*. http://www.astrazeneca-us.com/media/press-releases/Article/20150713-iressa-approved-by-the-fda (2015).
284. Romer, J. T. *et al.* Suppression of the Shh pathway using a small molecule inhibitor eliminates medulloblastoma in Ptc1+/-p53-/- mice. *Cancer Cell* **6**, 229–240 (2004).
285. Von Hoff, D. D. *et al.* Inhibition of the Hedgehog Pathway in Advanced Basal-Cell Carcinoma. *N. Engl. J. Med.* **361**, 1164–1172 (2009).
286. Karajannis, M., Allen, J. C. & Newcomb, E. W. Treatment of pediatric brain tumors. *J. Cell. Physiol.* **217**, 584–589 (2008).
287. Anderson, F. S. & Kunin-Batson, A. S. Neurocognitive Late Effects of Chemotherapy in Children: The Past 10 Years of Research on Brain Structure and Function. *Pediatr. Blood Cancer* **52**, 159–164 (2009).
288. Ikonomidou, C. Chemotherapy and the pediatric brain. *Mol. Cell. Pediatr.* **5**, (2018).
289. Barr, F. A., Silljé, H. H. W. & Nigg, E. A. Polo-like kinases and the orchestration of cell division. *Nat. Rev. Mol. Cell Biol.* **5**, 429–440 (2004).

290. De Cárcer, G., Manning, G. & Malumbres, M. From Plk1 to Plk5: Functional evolution of Polo-like kinases. *Cell Cycle* **10**, 2255–2262 (2011).
291. Weichert, W. *et al.* Polo-like kinase 1 expression is a prognostic factor in human colon cancer. *World J. Gastroenterol.* **11**, 5644–5650 (2005).
292. Cheng, M. W., Wang, B. C., Weng, Z. Q. & Zhu, X. W. Clinicopathological significance of Polo-like kinase 1 (PLK1) expression in human malignant glioma. *Acta Histochem.* **114**, 503–509 (2012).
293. Donizy, P. *et al.* Augmented expression of polo-like kinase 1 is a strong predictor of shorter cancer-specific overall survival in early stage breast cancer at 15-year follow-up. *Oncol. Lett.* **12**, 1667–1674 (2016).
294. Liu, Z., Sun, Q. & Wang, X. PLK1, A potential target for cancer therapy. *Transl. Oncol.* **10**, 22–32 (2017).
295. Narvaez, A. J. *et al.* Modulating Protein-Protein Interactions of the Mitotic Polo-like Kinases to Target Mutant KRAS. *Cell Chem. Biol.* **24**, 1017-1028.e7 (2017).
296. Khatua, S., Ramaswamy, V. & Bouffet, E. Current therapy and the evolving molecular landscape of paediatric ependymoma. *European Journal of Cancer* vol. 70 34–41 (2017).
297. Klein, M. *et al.* Effect of radiotherapy and other treatment-related factors on mid-term to long-term cognitive sequelae in low-grade gliomas: A comparative study. *Lancet* **360**, 1361–1368 (2002).
298. Bhansali, A. *et al.* Radiation-induced brain disorders in patients with pituitary tumours. *Australas. Radiol.* **48**, 339–346 (2004).
299. Brockman, R. W. & Anderson, E. P. Pyrimidine Analogues. *Liver Tox: Clinical and Research Information on Drug-Induced Liver Injury. Bethesda (MD): National Institute of Diabetes and Digestive and Kidney Diseases* 239–285 (2012) doi:10.1016/b978-0-12-395622-4.50012-4.
300. Longley, D. B., Harkin, D. P. & Johnston, P. G. 5-Fluorouracil: Mechanisms of action and clinical strategies. *Nat. Rev. Cancer* **3**, 330–338 (2003).
301. Cavalcante, L. D. S. & Monteiro, G. Gemcitabine : Metabolism and molecular mechanisms of action , sensitivity and chemoresistance in pancreatic cancer. *Eur. J. Pharmacol.* **741**, 8–16 (2014).
302. Wright, K. D. *et al.* Phase I study of 5-fluorouracil in children and young adults with recurrent ependymoma. *Neuro. Oncol.* **17**, 1620–1627 (2015).

303. Lee, S. & Lee, J. Synthesis of 2-Thio-4-aminopyrimidine Derivatives as Anti-cancer Agent. *J. Exp. Biomed. Sci.* **15**, 105–112 (2009).
304. Wang, C. *et al.* Anticancer activity evaluation of indazolyl-substituted piperidin-4-yl-aminopyrimidines. *Med. Chem. Res.* **29**, 910–915 (2020).
305. Huang, S. *et al.* Synthesis and biological study of 4-aminopyrimidine-5-carboxaldehyde oximes as antiproliferative VEGFR-2 inhibitors. *Bioorganic Med. Chem. Lett.* **16**, 6063–6066 (2006).
306. Ashburn, T. T. & Thor, K. B. Drug repositioning: Identifying and developing new uses for existing drugs. *Nat. Rev. Drug Discov.* **3**, 673–683 (2004).
307. Seyhan, A. A. Lost in translation: the valley of death across preclinical and clinical divide – identification of problems and overcoming obstacles. *Transl. Med. Commun.* **4**, 1–19 (2019).
308. Munos, B. Lessons from 60 years of pharmaceutical innovation. *Nat. Rev. Drug Discov.* **8**, 959–968 (2009).
309. Armando, R. G., Gómez, D. L. M. & Gomez, D. E. New drugs are not enough-drug repositioning in oncology: An update. *Int. J. Oncol.* **56**, 651–684 (2020).
310. O'Neil, J. *et al.* An unbiased oncology compound screen to identify novel combination strategies. *Mol. Cancer Ther.* **15**, 1155–1162 (2016).
311. Perry, J. M. *et al.* Overcoming Wnt–β-catenin dependent anticancer therapy resistance in leukaemia stem cells. *Nat. Cell Biol.* **22**, 689–700 (2020).
312. Pushpakom, S. *et al.* Drug repurposing: Progress, challenges and recommendations. *Nat. Rev. Drug Discov.* **18**, 41–58 (2018).
313. Goldstein, J. L. & Brown, M. S. Regulation of the mevalonate pathway. *Nature* **343**, 425–430 (1995).
314. Shepherd, J. *et al.* Prevention of coronary heart disease with pravastatin in men with hypercholesterolemia. *N. Engl. J. Med.* **333**, 1301–1307 (1995).
315. Collins, R., Armitage, J., Parish, S., Sleight, P. & Peto, R. MRC/BHF Heart Protection Study of cholesterol lowering simvastatin in 5963 people with diabetes: a randomized controlled trial. Heart Protection Study Collaborative Group. *Lancet* **361**, 2005–2016 (2003).
316. Gaist, D. *et al.* Use of statins and risk of glioma: a nationwide case-control study in Denmark. *Br. J. Cancer* **108**, 715–20 (2013).

317. Singh, P. P. & Singh, S. Statins are associated with reduced risk of gastric cancer: A systematic review and meta-analysis. *Ann. Oncol.* **24**, 1721–1730 (2013).
318. Shellman, Y. G. *et al.* Lovastatin-induced apoptosis in human melanoma cell lines. *Melanoma Res.* **15**, 83–89 (2005).
319. Yanae, M. *et al.* Statin-induced apoptosis via the suppression of ERK1/2 and Akt activation by inhibition of the geranylgeranyl-pyrophosphate biosynthesis in glioblastoma. *J. Exp. Clin. Cancer Res.* **30**, 74 (2011).
320. Gaist, D., Hallas, J., Friis, S., Hansen, S. & Sørensen, H. T. Statin use and survival following glioblastoma multiforme. *Cancer Epidemiol.* **38**, 722–727 (2014).
321. Stine, J. E. *et al.* The HMG-CoA reductase inhibitor, simvastatin, exhibits anti-metastatic and anti-tumorigenic effects in ovarian cancer. *Oncotarget* **1**, 946–960 (2015).
322. Gjertsen, B. T. & Schöffski, P. Discovery and development of the Polo-like kinase inhibitor volasertib in cancer therapy. 11–19 (2015) doi:10.1038/leu.2014.222.
323. Van den Bossche, J. *et al.* Spotlight on Volasertib: Preclinical andClinical Evaluation ofa Promising Plk1 Inhibitor. *Med. Res. Rev.* **36**, 749–786 (2016).
324. Gumireddy, K. *et al.* ON01910 , a non-ATP-competitive small molecule inhibitor of Plk1 , is a potent anticancer agent. **7**, 275–286 (2005).
325. Anderson, R. T. *et al.* The Dual Pathway Inhibitor Rigosertib Is Effective in Direct Patient Tumor Xenografts of Head and Neck Squamous Cell Carcinomas. *Mol. Cancer Ther.* **12**, 1994–2005 (2013).
326. Raza, A., Mukherjee, S., Eisenberger, A., Mears, J. G. & Wilhelm, F. Phase II study of orally administered rigosertib (ON 01910.Na) in transfusion-dependent lower-risk myelodysplastic syndrome (MDS) patients. *J. Clin. Oncol.* **31**, 7031 (2013).
327. Bowles, D. W. *et al.* Phase I Study of oral rogisertib (ON 01910.Na), a dual inhibitor of the Pl3k and Plk1 pathways, in adult patients with advanced solid malignancies. *Clin. Cancer Res.* **20**, 1656–1665 (2014).

328. Nuthalapati, S. *et al.* Preclinical Pharmacokinetic and Pharmacodynamic Evaluation of Novel Anticancer Agents , ON01910 . Na (Rigosertib , Estybon ™) and ON013105 , for Brain Tumor Chemotherapy. 2499–2511 (2012) doi:10.1007/s11095-012-0780-y.
329. Parker, W. B. Enzymology of purine and pyrimidine antimetabolites used in the treatment of cancer. *Chem. Rev.* **109**, 2880–2893 (2009).
330. Sigmond, J. *et al.* Gemcitabine uptake in glioblastoma multiforme: Potential as a radiosensitizer. *Ann. Oncol.* **20**, 182–187 (2009).
331. Morfouace, M. *et al.* Pemetrexed and gemcitabine as combination therapy for the treatment of Group3 medulloblastoma. **25**, 516–529 (2015).
332. Zhang, J. *et al.* The role of nucleoside transporters in cancer chemotherapy with nucleoside drugs. *Cancer Metastasis Rev.* **26**, 85–110 (2007).
333. Bastiancich, C. *et al.* Injectable nanomedicine hydrogel for local chemotherapy of glioblastoma after surgical resection. *J. Control. Release* **264**, 45–54 (2017).
334. Holla, V. R. *et al.* ALK: a tyrosine kinase target for cancer therapy. *Mol. Case Stud.* **3**, a001115 (2017).
335. Wang, W., Sun, X. & Hui, Z. Treatment Optimization for Brain Metastasis from Anaplastic Lymphoma Kinase Rearrangement Non-Small-Cell Lung Cancer. *Oncol. Res. Treat.* **42**, 599–606 (2019).
336. Shaw, A. T. *et al.* First-Line Lorlatinib or Crizotinib in Advanced *ALK* -Positive Lung Cancer. *N. Engl. J. Med.* **383**, 2018–2029 (2020).
337. Cao, Y. Multifarious functions of PDGFs and PDGFRs in tumor growth and metastasis. *Trends Mol. Med.* **19**, 460–473 (2013).
338. Shergalis, A., Bankhead, A., Luesakul, U., Muangsin, N. & Neamati, N. Current challenges and opportunities in treating glioblastomas. *Pharmacol. Rev.* **70**, 412–445 (2018).
339. Staedtke, V., Bai, R.-Y. & Laterra, J. Investigational New Drugs for Brain Cancer. *Expert Opin Investig Drugs* **25**, 937–956 (2016).
340. Greenall, S. A. *et al.* Cyclin-dependent kinase 7 is a therapeutic target in high-grade glioma. *Oncogenesis* **6**, e336-13 (2017).
341. Nagaraja, S. *et al.* Transcriptional Dependencies in Diffuse Intrinsic Pontine Glioma. *Cancer Cell* **31**, 635-652.e6 (2017).
342. Hoare, T. R. & Kohane, D. S. Hydrogels in drug delivery: Progress and challenges. *Polymer (Guildf).* **49**, 1993–2007 (2008).

343. Wang, K. *et al.* Functional Hydrogels and Their Application in Drug Delivery, Biosensors, and Tissue Engineering. *Int. J. Polym. Sci.* **2019**, (2019).
344. Basso, J. *et al.* Hydrogel-Based Drug Delivery Nanosystems for the Treatment of Brain Tumors. *Gels* **4**, 62 (2018).
345. Bastiancich, C., Danhier, P., Préat, V. & Danhier, F. Anticancer drug-loaded hydrogels as drug delivery systems for the local treatment of glioblastoma. *J. Control. Release* **243**, 29–42 (2016).
346. Parkins, C. C. *et al.* Increasing Drug Bioavailability by Mechanically Matching the Rheological Properties of Brain Tissue in Human Glioblastoma Models. *Biomaterials* **submitted**, (2020).
347. Laurent, T. C. & Fraser, J. R. E. Hyaluronan 1 . *FASEB J.* **6**, 2397–2404 (1992).
348. Toole, B. P. Hyaluronan: From extracellular glue to pericellular cue. *Nat. Rev. Cancer* **4**, 528–539 (2004).
349. Guillot, F., Misslin, P. & Lemaire, M. Comparison of Fluvastatin and Lovastatin Blood-Brain Barrier Transfer Using In Vitro and In Vivo Methods. 339–346 (1993).
350. Wohlfart, S., Gelperina, S. & Kreuter, J. Transport of drugs across the blood-brain barrier by nanoparticles. *J. Control. Release* **161**, 264–273 (2012).
351. Bunevicius, A., McDannold, N. J. & Golby, A. J. Focused Ultrasound Strategies for Brain Tumor Therapy. *Oper. Neurosurg.* **19**, 9–18 (2020).
352. Hadjipanayis, C. G. *et al.* What is the Surgical Benefit of Utilizing 5-ALA for Fluroscence-Guided-Surgery of Malignant Gliomas? *Neurosurgery* **143**, 951–959 (2015).
353. Brem, H. *et al.* Placebo-controlled trial of safety and efficacy of intraoperative controlled delivery by biodegradable polymers of chemotherapy for recurrent gliomas. *Lancet* **345**, 1008–1012 (1995).
354. Tuntland, T. *et al.* Implementation of pharmacokinetic and pharmacodynamic strategies in early research phases of drug discovery and development at novartis institute of biomedical research. *Front. Pharmacol.* **5 JUL**, 1–16 (2014).
355. Marinoff, A. E. *et al.* Rethinking childhood ependymoma: a retrospective, multi-center analysis reveals poor long-term overall survival. *J. Neurooncol.* **135**, 201–211 (2017).

356. Norouzi, M. *et al.* Doxorubicin-loaded iron oxide nanoparticles for glioblastoma therapy: a combinational approach for enhanced delivery of nanoparticles. *Sci. Rep.* **10**, 1–18 (2020).
357. Bocci, G. *et al.* Fluvastatin synergistically enhances the antiproliferative effect of gemcitabine in human pancreatic cancer MIAPaCa-2 cells. *Br. J. Cancer* **93**, 319–30 (2005).
358. Gao, J. *et al.* Combined Inhibitory Effects of Celecoxib and Fluvastatin on the Growth of Human Hepatocellular Carcinoma Xenografts in Nude Mice. *J. Int. Med. Res.* **38**, 1413–1427 (2010).
359. Vintonenko, N. *et al.* Transcriptome analysis and in vivo activity of fluvastatin versus zoledronic acid in a murine breast cancer metastasis model. *Mol. Pharmacol.* **82**, 521–8 (2012).
360. Jiang, P. *et al.* In vitro and in vivo anticancer effects of mevalonate pathway modulation on human cancer cells. *Br. J. Cancer* **111**, 1562–1571 (2014).
361. Haag, M. D. M., Hofman, A., Koudstaal, P. J., Stricker, B. H. C. & Breteler, M. M. B. Statins are associated with a reduced risk of Alzheimer disease regardless of lipophilicity. The Rotterdam Study. *J. Neurol. Neurosurg. Psychiatry* **80**, 13–17 (2009).
362. Zangari, M. *et al.* Rigosertib, a Pan RAS Inhibitor, Decreases Mouse and Human Myeloma Cell Growth in Preclinical Models. *Blood* **128**, 5664 (2016).
363. Chen, S. L., Zhang, G. L., Zhang, H. W., Lei, T. & Hu, C. C. Arachnoid adhesion caused by SURGICEL after operation for ventral spinal schwannoma. *Chin. Med. J. (Engl).* **123**, 3167–3168 (2010).
364. Sun, H., Dai, H., Shaik, N. & Elmquist, W. F. Drug efflux transporters in the CNS. *Adv. Drug Deliv. Rev.* **55**, 83–105 (2003).
365. Williams, E. I., Betterton, R. D., Davis, T. P. & Ronaldson, P. T. Transporter-mediated delivery of small molecule drugs to the brain: A critical mechanism that can advance therapeutic development for ischemic stroke. *Pharmaceutics* **12**, (2020).
366. Kikuchi, R., Kusuhara, H., Abe, T., Endou, H. & Sugiyama, Y. Involvement of multiple transporters in the efflux of 3-hydroxy-3- methylglutaryl-CoA reductase inhibitors across the blood-brain barrier. *J. Pharmacol. Exp. Ther.* **311**, 1147–1153 (2004).

367. Kalliokoski, A. & Niemi, M. Impact of OATP transporters on pharmacokinetics. *Br. J. Pharmacol.* **158**, 693–705 (2009).
368. Neuvonen, P. J., Backman, J. T. & Niemi, M. Pharmacokinetic comparison of the potential over-the-counter statins simvastatin, lovastatin, fluvastatin and pravastatin. *Clin. Pharmacokinet.* **47**, 463–474 (2008).
369. Qin, H., Jiang, Y., Zhang, J., Deng, C. & Zhong, Z. Oncoprotein Inhibitor Rigosertib Loaded in ApoE-Targeted Smart Polymersomes Reveals High Safety and Potency against Human Glioblastoma in Mice. *Mol. Pharm.* **16**, 3711–3719 (2019).
370. Persidis, A. Cancer multidrug resistance. *Nat. Biotechnol.* **18**, 18–20 (2000).
371. Green, A. L. *et al.* Preclinical and clinical investigation of intratumoral chemotherapy pharmacokinetics in DIPG using gemcitabine. *Neuro-Oncology Adv.* **2**, 1–9 (2020).
372. Oguri, T. *et al.* The determinants of sensitivity and acquired resistance to gemcitabine differ in non-small cell lung cancer: A role of ABCC5 in gemcitabine sensitivity. *Mol. Cancer Ther.* **5**, 1800–1806 (2006).
373. Wang, G. *et al.* Development and validation of a UPLC–MS/MS assay for the determination of gemcitabine and its L-carnitine ester derivative in rat plasma and its application in oral pharmacokinetics. *Asian J. Pharm. Sci.* **12**, 478–485 (2017).
374. Ciccolini, J., Serdjebi, C., Peters, G. J. & Giovannetti, E. Pharmacokinetics and pharmacogenetics of Gemcitabine as a mainstay in adult and pediatric oncology: an EORTC-PAMM perspective. *Cancer Chemother. Pharmacol.* **78**, 1–12 (2016).
375. Guchelaar, H. J., Richel, D. J. & Van Knapen, A. Clinical, toxicological and pharmacological aspects of gemcitabine. *Cancer Treat. Rev.* **22**, 15–31 (1996).
376. Crawley, J. T. B., Zanardelli, S., Chion, C. K. N. K. & Lane, D. A. The central role of thrombin in hemostasis. *J. Thromb. Haemost.* **5**, 95–101 (2007).